Title

Tool-Building and Mechanistic Insights for Cytosolic and Nuclear Delivery of Therapeutic Proteins

Author

Zoltek, Madeline Abby

Publication Date

2024

Peer reviewed|Thesis/dissertation

Tool-Building and Mechanistic Insights for Cytosolic and Nuclear Delivery of Therapeutic Proteins

By

Madeline Zoltek

A dissertation submitted in partial satisfaction of the

requirements for the degree of

Doctor of Philosophy

in

Molecular and Cell Biology

in the

Graduate Division

of the

University of California, Berkeley

Committee in charge:

Professor Alanna Schepartz, Chair
Professor Jennifer Doudna
Professor Randy Schekman
Professor Roberto Zoncu

Summer 2024

Tool-Building and Mechanistic Insights for Cytosolic and Nuclear Delivery of Therapeutic Proteins

By

Madeline Zoltek

Abstract

Tool-Building and Mechanistic Insights for Cytosolic and Nuclear Delivery of Therapeutic Proteins

By

Madeline Zoltek

Doctor of Philosophy in Molecular and Cell Biology

University of California, Berkeley

Professor Alanna Schepartz, Chair

Macromolecular therapeutics like proteins and RNAs have immense potential to impact human health. Relative to small molecules, their architecture is significantly more complex and structurally diverse, enabling high-affinity and high-specificity interactions in the crowded cell interior. However, macromolecules (or biologics) are also typically charged and hydrophilic, and thus cannot directly cross a lipid bilayer. This results in cellular uptake through active pathways such as endocytosis which result in significant degradation unless the macromolecule can escape an endosome. Endosomal escape has been a bottleneck to the clinical application of biologics for decades, spurring the development of a multitude of delivery vehicles and assays to optimize them.

Here, we begin by providing a detailed review of the current state of the protein and RNA delivery field. We discuss techniques to establish absolute quantitation of exogenously delivered macromolecules in discrete locations within the cell, as well as an overview of delivery modalities that promote cytosolic and nuclear delivery of a variety of biologics. Next, we present a thorough interrogation of the mechanisms governing delivery of a cell-permeant miniature protein designed by the Schepartz lab called ZF5.3. Using a highly quantitative technique called fluorescence correlation spectroscopy (FCS), we establish molecular design rules for optimal cargos that expand the therapeutic scope of ZF5.3 and provide insights into its endosomal escape pathway. These findings are followed by the development of a highly sensitive tool to track the intracellular trafficking of ZF5.3. We exploit the increasing acidity of the endocytic pathway to design an assay that uses fluorescence lifetime as a readout for the pH microenvironment of ZF5.3. We apply this assay toward tracking both endosomal maturation and cytosolic localization of ZF5.3 to gain insights into the relationship between pH and intracellular delivery. Finally, we apply FCS to the nuclear delivery of a high-impact biologic, the Cas9 ribonucleoprotein complex (RNP), to establish a quantitative relationship between nuclear concentration and gene editing outcomes in multiple mammalian cell lines. We conclude with an outlook on the future of macromolecular delivery and the challenges that lie ahead. Together, the projects presented in this dissertation will contribute to the growing understanding of intracellular delivery pathways and provide a framework to optimize and quantify delivery strategies for biologics.

Table of Contents

ACKNOWLEDGMENTS

Having finished my PhD, I feel the enormous gravity of sufficiently thanking the many people who, directly or indirectly, guided me toward and through it. It has been the most challenging, transformative, and genuinely fulfilling experience of my life.

First and foremost, I want to thank my PhD advisor, Alanna Schepartz, for everything she has given me. Some mentoring relationships just click, and ours did from the very start. I have always felt that Alanna saw my potential as a scientist before I was ever confident enough to believe in it myself. She encouraged me, pushed me, gave me freedom to explore and make mistakes, and provided a brilliant and fierce example of the kind of scientist I wanted to become. Alanna has taught me how to give a sharp and charismatic scientific talk, to always look at the raw data, to be precise with how I speak and write, and of course, to design a rigorous experiment with all the appropriate controls. Looking back, I see that I owe so much of the confidence I've gained as a scientist and a person to how much she believed in me. Above all else, I hope I have made her proud.

Thanks to Alanna, I was introduced to the incredibly supportive Schepartz lab who have defined my PhD experience in so many amazing ways. Karen has been an indispensable member of the Schepartz lab who answered more questions on Slack than I can count over the years. I am thankful to all the members of the delivery subgroup, both alums (Xizi, Pixie, and Susan) and current members (Dan, Angel, Jonathan, Abe, Teresia, Diego, Jess, Lizzy, and Aurora), who have provided sounding boards for new ideas, given nearly endless feedback and support, and both helped me become a better mentor and taught me so much at the same time. I will actually miss subgroup meetings with all of them. I am also so thankful to have met Cameron, Neville, and Isaac, who joined the lab with me as the first class of Berkeley students in Alanna's lab (during a global pandemic), and all of my other Schepartz lab friends who have been an irreplaceable source of commiseration, chats about science, chats about life, coffee runs, and many, many laughs over the past four years. I owe so much of my growth as a scientist to everyone in the Schepartz lab, past and present, who have shown me how special it is to work with people that make you excited and inspired to show up each day.

I am so grateful to all of my collaborators and especially my qualifying exam committee (Prof. Randy Schekman, Prof. Roberto Zoncu, Prof. Susan Marqusee, and Prof. Ellen Lumpkin) and my thesis committee (Prof. Randy Schekman, Prof. Roberto Zoncu, and Prof. Jennifer Doudna) for their invaluable feedback on my scientific progress over the years. It's been such a privilege to present to and be mentored by such a brilliant group of scientists. I also want to thank everyone that led me to graduate school, of which there are too many to name individually – but especially Paul Gignilliat, who truly made all my academic dreams at Yale and beyond possible, and Prof. Matthew Simon and Dr. Tyler Smith, who were wonderful mentors and the first to encourage me to apply for a PhD.

I owe so much gratitude to my parents for their FaceTime calls, care packages, frozen food shipments, visits, and encouraging texts that made me feel so supported and loved from two thousand miles away. I can't express how lucky I am to have had my sister, Mo, living ten minutes away from me for three years of grad school – thanks for all the meals and desserts you cooked for me when I was too busy to feed myself (and for providing

Henry as an unofficial emotional support dog who I love so much). I can't imagine my PhD without the support of my unbelievably amazing friends, both old and new, who have listened to me complain about the same things for five years now. I want to thank the phenomenal people I lived with for the first four years, especially Shari, Nikki, Brenna, Kailey, and Karen; I met my very best friends in grad school in that house. I will never forget the positivity, Yogurt Park runs, dance parties, deep conversations, and camaraderie that got us through a pandemic and inspired me to push through every late night and hard day knowing I had such incredible women in my corner.

Finally, a paragraph is not nearly enough to express my love and appreciation for Rob Howle. We met as I was starting my second year of grad school, when finishing this PhD seemed like a lifetime away. Now that it's here, I can't imagine getting through this degree without him. Our inside jokes and constant laughs have put a smile on my face even on the longest days. Rob, thank you for all the dinners you made when I was too stressed, the pep talks that made me feel on top of the world, the relaxed nights on the couch, the adventures both near and far, and the unconditional support you have shown me these past years. I can't describe how much I appreciate the sacrifices you have made to support me through my PhD and to move to Boston for our next adventure. I love you with my whole heart.

CHAPTER ONE

Recent Advances in Techniques and Vehicles for the Intracellular Delivery of Macromolecules

This chapter is based in part on a manuscript in preparation “Recent Advances in Quantitative Techniques to Detect Intracellular Delivery” and has been adapted with permission from all co-authors.

1.1 Overview

There is an urgent and unmet need to enhance the "deliverability" of protein- and RNA-based therapeutics. Such therapies have immense implications in vaccine development,[1,2] gene editing,[3,4] modulation of gene expression,[5,6] and replacement of disease-causing enzymes,[7] among many others (Fig. 1.1). Direct delivery of intact proteins and RNAs (henceforth referred to as biologics) has the potential to overcome immunogenicity challenges faced by many gene therapy approaches[8] and provide tunable control over intracellular lifetime and dosage. Biologics reaching targets in the extracellular space, cell surface, or endocytic pathway have already achieved massive clinical success, comprising six of the ten top-selling drugs of 2023.[9] Enzyme replacement therapies have revolutionized the treatment of lysosomal storage disorders, pancreatic enzyme deficiencies, and even cardiovascular disease,[7] while antibody therapeutics have transformed the management of autoimmune disorders and cancers.[10] However, FDA-approved biologics with activity in the cell interior are lacking. To reach a target in the cytosol or nucleus, a biologic must overcome the energetic unfavorability of crossing a hydrophobic lipid bilayer (Fig. 1.2). The inability to efficiently circumnavigate biological membranes severely limits the activity of biologics whose function demands cytosolic or nuclear localization.

There are two ways a hydrophilic biologic can enter the cell: direct penetration across the plasma membrane or endocytosis. If endocytosed, the biologic must then traverse the endosomal membrane before lysosomal degradation, a major bottleneck referred to as "endosomal escape". The engineering of vehicles that enable delivery alongside quantitative techniques to detect intracellular sublocalization are equally critical to develop next-generation protein- and RNA-based therapeutics. A thorough interrogation of mechanisms exploited by different delivery strategies, including their route of cellular entry and trafficking, is also necessary for the iterative improvement of their efficacy.

In this chapter, we highlight recent progress in two facets of intracellular protein and RNA delivery: 1) techniques to measure the success of a given delivery strategy and 2) vehicles purported to enhance the delivery of macromolecules. We conclude by briefly discussing notable macromolecular therapeutics currently in preclinical or clinical development. These advances provide relevant context for the remainder of this dissertation, which includes an investigation of design rules for macromolecule delivery, development of a novel technique to detect intracellular trafficking, and quantification of the nuclear delivery of a high-impact biologic, the Cas9 ribonucleoprotein complex.

1.2 Assays to detect delivery

The ability to detect successful delivery (that is, delivery to a productive non-endosomal location) is critical for the establishment of effective delivery modalities. Though many techniques have been developed for this purpose, the use of non-quantitative assays can vastly overrepresent true delivery and has contributed to the

clinical failure of many delivery vehicles. For this chapter, we will focus on summarizing recent advances in techniques that establish absolute quantities of delivered material.

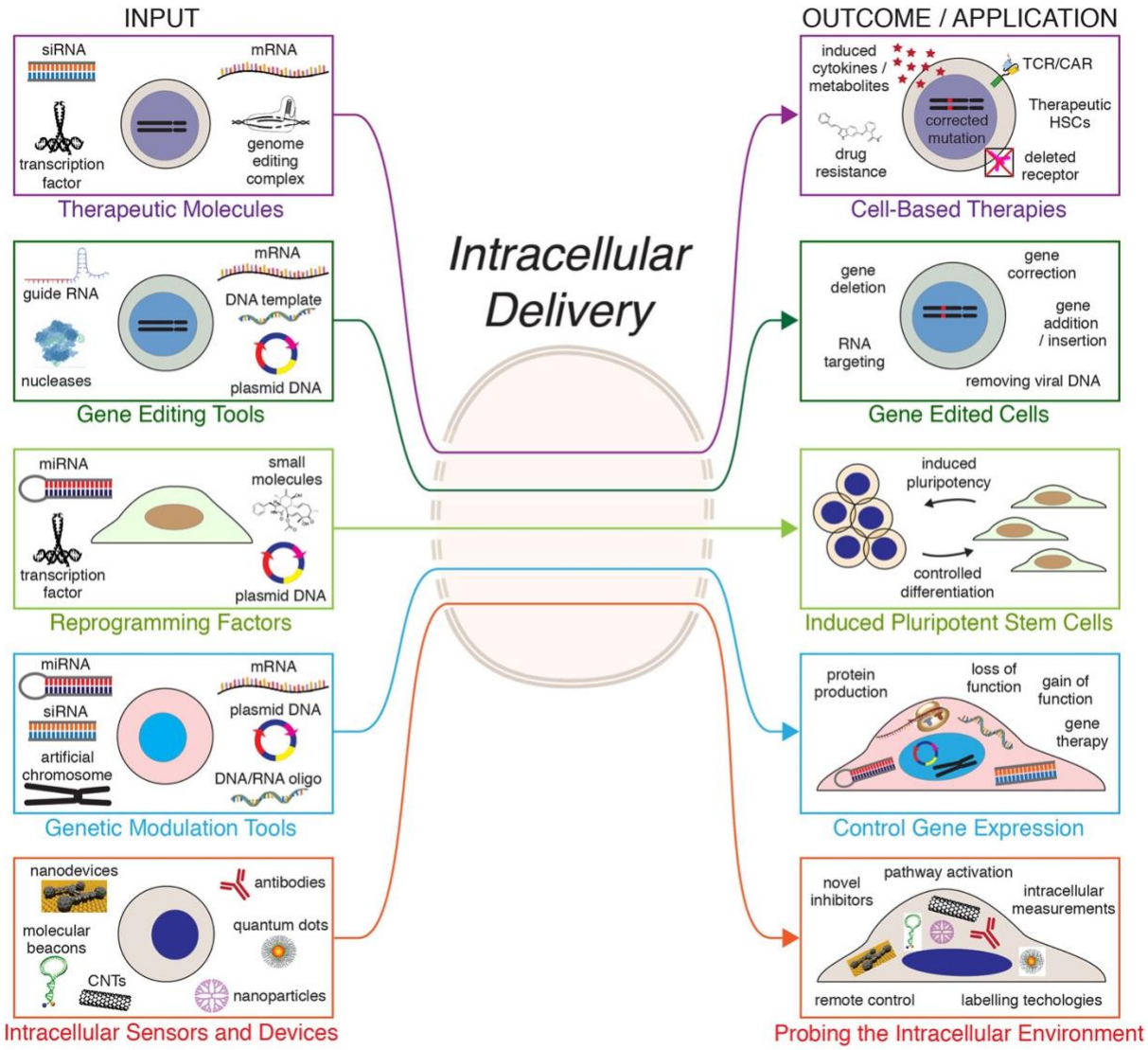

Figure 1.1. Motivations for the intracellular delivery of macromolecules. Examples of biologics with therapeutic impacts are shown on the left and grouped by broad functions. Horizontal lines denote potential outputs of each class of macromolecule, although these relationships are not mutually exclusive. Abbreviations: TCR = T cell receptor. CAR = chimeric antigen receptor. CNT = carbon nanotube. HSCs = hematopoietic stem cells. Reprinted with permission from Ref.[144] Copyright 2018, ACS Chemical Reviews.

1.2.1 Why quantification matters

A primary obstacle to the preclinical development of potentially deliverable macromolecular therapeutics is a lack of standardized assays to quantify successful delivery. At a minimum, a readout for delivery must (1) be performed in live cells, as most

fixing techniques disrupt plasma and endosomal membrane integrity and thus misrepresent genuine delivery,[11–13] and (2) distinguish endosomally sequestered material from that which reaches the desired cellular compartment, which is usually the cytosol or nucleus. A variety of techniques within this framework have been reported, though many are non- or semi-quantitative and therefore cannot be used for large-scale comparisons across multiple research groups or publications.

The most rigorous way to reliably and reproducibly assess the delivery of macromolecules is to directly measure the absolute number of molecules in a specific cellular location. Absolute quantification enables objective comparisons across molecules and cell lines and provides direct information on the relationship between the number of molecules present and the desired phenotypic outcome - for example, the number of siRNAs required to achieve a certain percent knockdown. Because the concentration of a cargo that must reach a specific location to exert therapeutic effect varies significantly based on its application, quantitative readouts provide invaluable information on the success of a delivery strategy.

1.2.2 Absolute methods to detect intracellular macromolecules

Several techniques that enable such direct quantification have been reported to assess the delivery of both protein and RNA biologics. Fluorescence correlation spectroscopy (FCS) is a single-molecule technique that has been applied to quantify the cytosolic and nuclear concentrations of a variety of protein- and peptide-based biomolecules.[14] Time-dependent fluctuations in fluorescence intensity are detected within a known sub-femtoliter volume generated by the laser beam and analyzed using an autocorrelation function. This function provides the number of molecules that diffused within the detection volume, and thus enables measurement of high-picomolar to low-micromolar concentrations of delivered material in discrete locations.[15,16] The laser of the microscope can be manually positioned to avoid endosomal puncta using a standard confocal microscopy image. When combined with flow cytometry, FCS provides information on both endosomal uptake and compartment-specific delivery in a single experiment. FCS has been applied to compare the relative cytosolic access of a variety of prototypical, designed, cyclic, and stapled cell-penetrating peptides.[17–19] Additionally, FCS has been used to extensively characterize the scope and mechanism of cytosolic trafficking for the cell-permeant miniature protein ZF5.3.[20,21] Most recently, this included the discovery that the highly efficient endosomal escape pathway undertaken by ZF5.3 demands unfolding of both ZF5.3 itself[22] and any covalently linked protein cargo.[23] Quantification by FCS is fairly low-throughput (~40-80 cells per experimental condition). Although multi-focus[24–26] and high-throughput[27] FCS techniques have been reported and even applied in live cells,[24,28] there remain significant challenges including automation of choosing cellular regions devoid of endosomes and developing instrumentation capable of measuring more than a few cells at once.

One method to improve the throughput is by calibration of fluorescence intensity from microscopy-derived images using photon counting and/or FCS. For instance, confocal imaging in photon counting mode provides fluorescent intensity values that can

be calibrated with known concentrations of fluorescent standards. This technique was applied to the delivery of locked nucleic acid antisense oligonucleotides (LNA-ASOs) into MCF-7 cells, enabling 1) quantification of both vesicular and nuclear concentrations of exogenously supplied LNA-ASOs and 2) correlation between the number of LNA-ASO molecules in the cytosol and knockdown of a model RNA (10^5 for >50% knockdown).[29] Similarly, FCS can be used to calibrate fluorescence intensity values in confocal microscopy images with defined concentrations.[30] This technique, integrated with observer-independent post-acquisition masking to capture only cytosolic signal, was applied to the measurement of individual endosomal release events for siRNAs delivered to HeLa cells. These data revealed that only ~1000 siRNAs must reach the cytosol to reach half-maximal knockdown of a model RNA after 10 hr. This experimental setup was highly sensitive (capable of measuring <1 nM) and compatible with automated imaging and analysis, enabling measurement of ~100-200 cells per condition.[31] This technique is also compatible with continuous measurements of delivery over time, a feat that can be challenging with live-cell FCS due to the high laser intensity and long timescales sometimes required.[15] Importantly, the calibrations required for these experiments must be performed carefully to ensure that they accurately represent the environment of the delivered material in live cells, where fluorescence intensity and diffusion can be significantly altered.[15]

The techniques described thus far require specialized instrumentation to directly capture low-abundance molecular events. One recent approach applied post-acquisition single-molecule analysis to images acquired from a relatively straightforward TIRF microscopy setup using the software ThunderSTORM. They showed that cytosolic delivery of functionalized quantum dots could be quantified using a multi-emitter algorithm that derives the absolute number of fluorescent particles in the cell.[32] Particle diffusion or, in principle, segmentation analysis can be applied to exclude signal derived from endosomes. In practice, however, photochemical events like “blinking” can lead to inaccurate absolute values derived from this method, which must be interpreted with caution.

It is important to note that although these fluorescence-based techniques report delivery with high sensitivity and accuracy, they require modification of the delivered material with a fluorophore and must be combined with careful biochemical and/or activity studies to ensure 1) the fluorophore does not affect delivery and 2) the delivered material is intact and functional. Examples of appropriate experiments include pairing quantitative methods with functional assays to assess the impact of the tag[21,31,33] and performing western blot,[20,21,23] LC-MS/MS,[21] or UPLC analysis[17] of cytosolic or nuclear extract to verify the delivered material is intact. This biochemistry must be performed carefully and with appropriate controls to ensure that the cytosolic and/or nuclear material is not contaminated with material from endosomes.[14]

Several non-fluorescence methods have been reported for absolute quantitative analysis of intracellular delivery. One report exploits the reactivity of SNAP-tag for the benzylguanine (BG) moiety by delivering biotin- and BG-modified macromolecules into cells expressing a cytosolic SNAP-Tag-mNeonGreen fusion protein.[34] Material that

reaches the cytosol will react with SNAP-tag, which can be subsequently isolated and quantified using the biotin moiety by ELISA to obtain the number of molecules that reached the cytosol. Unreacted SNAP-tag is quenched with excess cell-permeable BG before lysis to avoid false positive signal. This assay is analogous to a previously reported assay used to measure DARPin delivery, in which Avi-tagged macromolecules were delivered to cells expressing a cytoplasmic biotin ligase that recognized and biotinylated the Avi peptide. Cells were then lysed and quantification of biotinylated molecules was performed by western blot.[35] Analysis by ELISA is more quantitative and significantly higher throughput than by western blot, although one cannot filter out false positive signals from degraded material using ELISA alone. One must exercise caution when designing and interpreting results from either of these experiments to ensure that 1) differences in cytosolic access using these methods do not arise from inherent variability in reactivity between the delivered molecules and their cognate cytosolic partners and 2) the cytosolic protein remains in the cytosol and not secreted into extracellular space, as has been reported for some endosomal escape assays.[36] Additionally, these methods inherently measure the total amount of material that reaches the cytosol at any time (rather than an equilibrium value), which can misrepresent true delivery.

Approaches with minimal modification to the delivered material are ideal to assess trafficking of macromolecules in their native physicochemical states. Multiple mass spectrometry methods have been reported to detect label-free intracellular delivery of proteins,[37,38] though typically they report only on total internalization and cannot mask signal from material trapped in endosomes. Because the amount of total uptake does not necessarily correlate to the amount that reaches the cytosol,[18] these results can be misleading. Nanoscale secondary ion mass spectrometry (NanoSIMS) has been recently reported to map the subcellular distribution and report absolute numbers of isotopically labeled RNAs that were incubated with primary human hepatocytes.[39] Though highly quantitative, this method demands fixation of cells which may cause localization artifacts as described in **1.2.1**. Other mass spectrometry-based methods that have been reported require comparison to a standard curve to estimate intracellular concentrations and are thus discussed in the following section.

1.2.3 Assays that can be adapted for quantitation

The techniques described above represent, to our knowledge, the only direct strategies to absolutely quantify the number of molecules delivered to a discrete cellular location. Significant effort has been put into the optimization of higher-throughput assays for non- or semi-quantitatively detecting intracellular delivery, reviewed extensively elsewhere.[40,41] For this section, we will only focus on a subset of these assays which have been demonstrated in the literature to derive concentration values using a variety of assumptions.

Recently, the throughput and detection limits for FCS were increased for nuclear-targeted macromolecules by combining FCS with nuclear flow cytometry. Intact nuclei from treated cells can be stringently isolated following established protocols[21] and evaluated by flow cytometry for fluorescence intensity. These nuclear flow values have

been demonstrated to correlate linearly with intranuclear concentration values established by FCS (R^2 = 0.75)[21] and can thus approximate nuclear concentrations outside the optimal range of FCS. Critically, such experiments must be performed with careful controls to ensure nuclei remain intact and devoid of endosomal contamination in all cases.

Several label-free methods have been developed that can estimate intracellular concentrations of delivered biologics. Mass spectrometry of cytosolic extract, obtained by fractionation or microneedle extraction, has been applied to screen a range of linear and cyclic peptides for their permeability.[42,43] By incorporating internal standards, these approaches can estimate cytosolic concentrations, revealing that cyclosporin and its derivatives can reach cytosolic concentrations of up to ~6.8 μM. Currently, these methods are incompatible with isotopically labeled peptides, which would enable truly quantitative analyses.[43] For oligonucleotide delivery, sub-nanomolar concentrations of nucleic acids can be detected by hybridization with a peptide-nucleic acid (PNA) probe. Comparison of probe binding using capillary electrophoresis or other methods enables quantification by comparing to a calibration curve.[44,45] So far, these methods have only been applied to whole cell lysate (and thus capture all internalized molecules), but in principle they could be utilized with fractionated cytosol and/or nuclei.

A different strategy to assess delivery relies on cytosolic or nuclear tethering of a protein that can react with a delivered molecule only when that molecule escapes an endosome or otherwise reaches the correct compartment. This strategy requires the delivered molecule to be tagged with a recognition motif for the intracellular protein. A straightforward example is the recent application of the split luciferase endosomal escape quantification (SLEEQ) assay toward the large-scale comparison of cytosolic delivery for peptides, nanoparticles, and even tau aggregates in Parkinson's models.[36,46,47] The delivered molecule is decorated with a small peptide fragment (HiBiT) that complements with cytosolic luciferase (LgBiT) to produce a luminescent signal with up to 4 orders of magnitude better sensitivity than split fluorescent proteins (e.g. GFP).[36,48] Though powerful for widespread comparisons across many conditions, the signal is highly amplified and therefore provides little information on how much material has actually reached the cytosol or nucleus. Quantitation is possible with some adaptations, as demonstrated by a report that measures cytosolic concentrations of cell-permeable Ras inhibitors.[49] A standard curve was constructed by titrating known amounts of HiBiT into LgBiT-expressing cellular lysate, to which *in cellulo* luminescence values were compared. Additional nontreated wells in the same experiment were used to count the number of cells per well and estimate the average cellular volume, which were then used to derive intracellular concentrations.

Another common assay for intracellular delivery is the chloroalkane penetration assay, or CAPA, which has been used extensively in recent years to interrogate delivery of protein and RNA-based therapeutics,[33,50,51] lipid nanoparticles,[52] and macrocyclic peptides.[53,54] CAPA relies on reactivity of a chloroalkane- (ct)-modified molecule with cytosolic or nuclear HaloTag, followed by incubation with a ct-fluorophore to react with free HaloTag and produce a fluorescent signal inversely proportional to the degree of

delivery.[55] The delivered molecule must be functionalized with a chloroalkane moiety which, although smaller than the HiBiT peptide required for split luciferase complementation,[36] may still affect the trafficking of the molecule.[33] Because the signal comes from the proportion of HaloTag sites bound by the delivered material, the signal depends entirely on the expression level of cytosolic (or nuclear) HaloTag and provides no information on the actual amount of delivered material. Colleagues at Merck published an analogous assay called NanoClick, which exploits bioluminescence resonance energy transfer to improve the sensitivity of CAPA and reduce the degree of chemical modification even further to a simple azide.[56,57] A mechanism to derive absolute quantities from CAPA (and by extrapolation, NanoClick) data has been published that requires a Molecule "X" with 100% delivery efficiency. The CAPA value for this molecule is used to benchmark delivery of less efficient molecules and calculate estimated cytosolic concentrations.[55] It is critical to note that this method is dependent on the unlikely assumption that Molecule X is fully penetrant, and is therefore likely to overestimate intracellular concentrations.

These assays hold tremendous promise for large-scale analyses to improve biologic therapeutics including screening compound libraries, optimal delivery conditions, genetic determinants for trafficking, and more. These techniques also highlight several pitfalls shared by many published intracellular delivery readouts that can distort actual delivery efficiencies. They are prone to degradation artifacts from degraded fragments of the delivered material that can still react to produce positive signal.[33,55] Some assays capture delivered molecules immediately upon cytosolic or nuclear entry rather than measuring at equilibrium, and they rely on the assumption that all delivered molecules will react equally well with their desired binding partners in cells (or require extensive controls to correct for this). Thus, unless one can benchmark their data with absolute values determined by truly quantitative techniques, it is quite easy to mistake positive signal for genuine delivery.

1.2.4 Advantages and disadvantages of both: How to thoughtfully compromise

There are many techniques to detect intracellular delivery beyond those described here.[40,41] Many purport to quantify endosomal escape, though few report absolute concentrations of delivered material. The assays discussed in this chapter are either directly quantitative or enable quantitation with varying sets of assumptions. For the field of macromolecular delivery to progress, it is essential to pursue ground-truth data that can establish absolute delivery efficiencies across cell lines, delivery vehicles, treatment conditions, and more. Given the breadth of delivery vehicles reported each day by groups around the world, such information is increasingly necessary to establish which strategies are best suited for which applications.

As discussed in this chapter, there are a variety of established assays to truly quantify intracellular delivery. Quantitative fluorescence assays inform on quantity delivered but not function, while amplified and/or large-scale readouts report on intra-experimental comparisons but provide little information on the number of molecules that reach a particular location. To choose an appropriate assay, one must consider the initial

research question carefully. If the goal is to probe structure-activity relationships or compare relative delivery across many conditions, a high-throughput assay that sacrifices some direct quantitation may be most appropriate at the outset. It is essential that "hits" from such screens are validated with absolute quantification to benchmark the success of the delivery strategy. If, instead, a molecule is being evaluated for clinical applications or mechanisms of trafficking, it is most appropriate to directly quantify the amount that reaches the desired cellular location and, if appropriate, pair this information with a functional readout. It is particularly important to follow up functional assays with quantitation to determine whether function may be improved by enhancing delivery to the proper location or by modifying the structure of the delivered molecule itself. For mechanism studies, quantitative imaging techniques and FCS are particularly useful because they are able to capture single-cell dynamics (including identification of individual endosomal escape events in real time[31,58]), providing valuable mechanistic insights that are masked by aggregation of information in large-scale assays. In all cases, careful controls must be performed to account for the pitfalls presented by the assay used.

Beyond assays to simply detect delivery, there is also significant need for readouts to explore mechanisms used by exogenously delivered proteins and RNAs. Endosomes are small (100 – 1000 nm in diameter[59]) and thus require precise and high-resolution approaches to detect their contents.[23,31,58,60] They are also acidic, a property that can be exploited for analysis by pH-responsive probes.[61,62] A thorough discussion of assays to detect mechanisms is beyond the scope of this chapter; see **Chapter 3** for more detail.

1.3 Vehicles to enhance intracellular delivery

A variety of strategies have been reported to improve the cytosolic or nuclear delivery of hydrophilic biomolecules such as proteins and nucleic acids (Fig. 1.2). In all cases, these strategies must disrupt a hydrophobic lipid bilayer, either on the cell surface or within an endosome, to enable passage of the macromolecule. Here we discuss several classes of delivery vehicles that have successfully delivered proteins or RNAs, with a brief discussion of their hypothesized mechanisms.

1.3.1 Peptide-mediated delivery

Over three decades ago, it was discovered that certain trans-activating factors can reach the nucleus and function as gene regulatory agents when added to cells in culture. The early discovery that arginine residues enhance cell penetration[63,64] inspired an entire class of peptides called cell-penetrating peptides (CPPs) to promote delivery of macromolecules by either co-incubation or covalent attachment.[65] The guanidinium head groups of consecutive arginine residues can engage negatively charged sulfate, phosphate, and carboxylate moieties that are abundant in cell-surface proteoglycans and phospholipids. This has been suggested to promote internalization through a variety of mechanisms, including by induction of membrane curvature[66] and/or loosening of lipid packing.[65] Unfortunately, prototypical CPPs like Tat[67] and Arg8[63] have fallen short despite initial promise. Although Tat and Arg8 are endocytosed by cells, both on their own[17] and when conjugated to cargo,[18,21] quantitative analysis of cytosolic concentrations revealed

that the vast majority of material remains endosomally sequestered.[17,18] For Tat- and Arg8 material that reaches a productive intracellular location, multiple groups have reported significant degradation.[21,68] Even Arg-rich CPPs that have been re-engineered to enhance delivery,[69,70] including through dimerization or incorporation of unnatural amino acids, tend to suffer from low proteolytic stability or toxicity, limiting their clinical applications.[71,72]

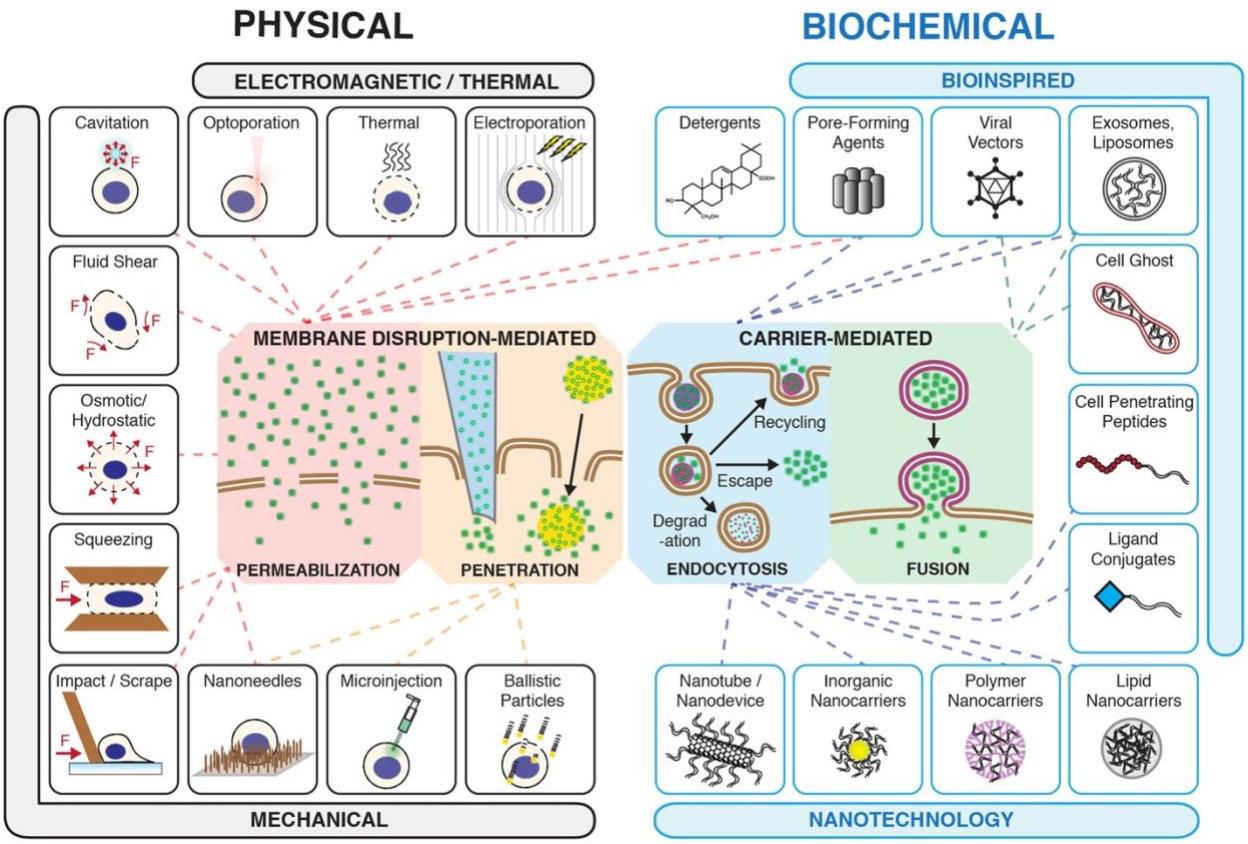

Figure 1.2. Overview of vehicles and methods to deliver macromolecules into cells. These can be differentiated into physical methods to disrupt cellular membranes (primarily used for *in vitro* and *ex vivo* applications) and biochemical methods that exploit natural or synthetic materials to enter cells via endogenous pathways. Reprinted with permission from Ref.[144] Copyright 2018, ACS Chemical Reviews.

Though many first-generation CPPs failed to meet expectations, they inspired significant engineering efforts that have yielded diverse peptides extending far beyond the prototypical Arg-rich scaffold.[61,62,73,74] Recent efforts to stabilize CPPs by cyclization,[75,76] exploit coacervate-based materials,[77–80], apply large-scale screening methods,[42,81,82], and develop machine learning pipelines to predict molecular rules that govern cytosolic exposure[83–85] hold promise for designing improved CPPs. Such approaches have yielded peptides capable of trafficking larger cargos to the interior of cells, including Cyto1a (shown to deliver a nuclear PMO)[42] and MGS4 (shown to deliver toxic cargos in a tumor-specific manner),[86] among others.[87] A parallel strategy for peptide-mediated delivery is by co-incubation of the cargo with peptides capable of disrupting

endosomal membranes. Understanding design rules for nontoxic endosomolytic agents, particularly using pH-dependent conformational changes, has yielded multiple peptides capable of delivering high-impact cargos to the interior of cells, including the Cas9 ribonuclear protein complex.[69,88–92] Beyond physically disrupting endosomal membranes, several mechanisms have been postulated for the endosomal escape of cell-penetrating peptides. One such hypothesis is the so-called proton sponge effect, in which pH-induced protonation of amino groups on cationic polymers results in a massive proton influx. This influx is suspected to produce osmotic swelling and membrane disruption, though its role in delivery has been disputed.[93,94] Alternative hypotheses include budding of vesicles induced by CPP-membrane interactions and escape through “leaky” endosomal fusion events, though rigorous experimental evidence is difficult to obtain for such transient and nanoscopic events.[94,95] Significant efforts have also been taken to understand design rules for intrinsic permeability of peptides on their own;[96–100] however valuable, these chemical insights are limited to short sequences and cannot typically be generalized for the trafficking of larger protein and oligonucleotide cargos.

1.3.2 Delivery by mini-proteins

Though promising, cyclic and stapled peptide-biologic conjugates often require complex synthetic strategies that limit their scalability. Genetically encodable mini proteins can be readily conjugated or co-incubated with therapeutic cargos and have been demonstrated to effectively traffic biomolecules to the cytosol or nucleus. Some function by (presumably or empirically) inducing endosomal rupture,[101–103] while others have been demonstrated to selectively cross endosomal membranes.[19] In particular, the Schepartz lab has extensively characterized a miniature protein called ZF5.3 that escapes endosomes, both on its own[17] and with a covalently attached cargo,[18] with unprecedented efficiency across multiple cell lines. This activity demands a defined array of five α-helical arginine residues referred to as a penta-Arg or 5/3 motif.[104] ZF5.3 has been demonstrated to deliver a range of proteins, including the urea cycle enzyme argininosuccinate synthetase,[20] the neurological protein MeCP2,[21] the Ras inhibitor NS1,[23] and a nanobody-based degrader.[105]

Several mechanistic studies of ZF5.3 endosomal escape have been reported, including endosomal damage assays that revealed its escape is selective and does not induce endosomal leakage.[19] A genome-wide RNAi screen identified the HOPS complex, an endosomal tethering complex, as a key requisite for ZF5.3 delivery to the cytosol and nucleus.[19] Notably, choice of cargo dramatically impacts delivery, and ZF5.3 has been demonstrated to deliver physiologically unfolded cargos most efficiently.[23] This finding, discussed in detail in **Chapter Two** and supported by recent evidence that ZF5.3 undergoes pH-dependent unfolding,[22] suggests that ZF5.3 selectively crosses endosomal membranes through pores generated during or after endosomal fusion events. Specifically, the transition of ZF5.3 to a random coil at pH 4.6 enables selective interactions with lipids enriched in late endosomal membranes and is required for efficient endosomal escape.[22] This thorough characterization of ZF5.3 mechanism is highly unusual in the CPP field and paves the way for its optimization and therapeutic use.

1.3.3 Delivery by synthetic or molecular machines

Beyond peptides, several strategies have emerged to encapsulate biotherapeutics within larger synthetic or naturally derived structures to enhance delivery. Lipid nanoparticles (vesicles composed of ionizable and cell-targeting lipids, cholesterol, and polyethylene glycol) have exploded as a delivery modality since their success toward the delivery of mRNA vaccines against SARS-CoV-2[106–108] and have since been used for delivery of other mRNAs,[109,110] cell- or organ-specific targeting,[111–113] and immune activation,[114] among many other applications.[115] Their mechanisms of action vary based on composition,[116,117] though most are endocytosed and undergo pH-dependent conformational changes to release their contents within the endosome.[58,94,118] The enclosed macromolecule must still escape the endosome after its release, which may be supported by LNP-driven membrane disruption;[116] however, these mechanisms are still largely unclear and generally quite inefficient.[119–121]

Self-assembling molecular machines such as virus-like particles (VLPs),[122–126] artificial virus-like particles (AVLPs),[127] and protein capsules[128] can 'infect' cells through natural processes but lack self-propagation. VLPs are typically internalized by cells through receptor-mediated endocytosis.[123] During their transit through the endocytic pathway, they undergo rapid pH-induced membrane fusion once a critical pH is reached to deposit their contents in the cytosol.[125,129] These modalities are highly versatile and can be reengineered to target specific cell types by swapping out receptor-targeting modules, broadening their *in vivo* applicability.[125,130] Analogously, nanomachines derived from inactivated toxins are emerging as a modality to target chemotoxic materials to cancer cells[131] and deliver protein-based molecules via introduction of pores in biological membranes, either at the cell surface or within the endosome.[132-134] A diverse range of toxins has been examined including anthrax,[135,136] diphtheria,[137–139] and botulinum neurotoxin,[133,139,140] all of which enter the cell via receptor-mediated endocytosis and exploit pH-dependent conformational changes to escape the endosome.[132]

1.3.4 Direct injection

The delivery strategies discussed thus far typically exploit the endocytic pathway to deliver the desired macromolecule. An alternative approach is to introduce pores directly in the plasma membrane of cells to facilitate cytosolic access. This method has been traditionally applied in the transfection of nucleic acids in cell culture via electroporation, which supplies an electrical pulse to form pores in the plasma membrane. Though applicable to nearly every cell type and well-established as an *in vitro* or *ex vivo* delivery technique, electroporation can induce substantial cell death, is not adaptable for cell-type specific targeting, and cannot readily be translated to *in vivo* settings.[4,141] Most alternative membrane disruption methods function primarily *in vitro*, including microfluidic-induced membrane deformations[142] and focused ultrasound (sonoporation),[143] among others.[144] Excitingly, recent advances to microneedle technology have enabled the *in vivo* application of physical membrane disruption. Self-orienting microneedle devices that are triggered by pre-compressed springs,[145] magnetic fields,[146] or natural intestinal peristaltic contractions[147] effectively deliver their contents across intestinal mucosal barriers in animal models. This is a major advancement towards improving the oral bioavailability of

macromolecular therapeutics and can be paired with additional delivery vehicles, such as nanoparticles, to enable cell-type specific targeting after mucosal penetration.

1.3.5 How to choose the best delivery vehicle

These examples provide only a sampling of the many delivery vehicles that have been published in recent years. In truth, it is impossible to directly compare their relative effectiveness, due to both a lack of quantitative readouts for absolute delivery (as discussed in **Section 1.2**) and the influence of the individual cargo on delivery. For most delivery strategies, the cargo undoubtedly alters the trafficking and resulting delivery efficiency, leading to wide variations in the ability of a given modality to deliver various cargos. It is useful, thus, to consider delivery strategies not by their universal efficiency, but rather by the optimal cargos they can traffic to the interior of cells.

For instance, the physicochemical properties of peptides will be significantly altered by the presence of a macromolecule cargo.[148] It has been established that proteins with low thermostabilities are delivered more efficiently by the mini-protein ZF5.3 than highly stable proteins,[23] and that a Tat derivative is more efficient at delivering low-molecular weight cargos than large ones.[149] It is also well-documented that multiple toxin-based molecular machines require the cargo to unfold.[132,133,150–152] Thus, for peptide- or toxin-based systems, it may be optimal to exploit cargos that are small or capable of physiologically unfolding to maximize delivery, such as intrinsically disordered or meta-stable proteins. It has furthermore been demonstrated that the delivery efficiency for toxins and nanoparticles is exceedingly low (<10% for commonly used toxins such as diphtheria, botulinum, and ricin,[132,133] and <4% for LNPs[120,153]); thus, cargos with catalytic activity whose cytosolic or nuclear levels can be quite low to achieve therapeutic impact are most optimal. As nanoparticles can induce significant immunogenicity,[116,154,155] their application in vaccine development may be particularly useful. Larger carriers like VLPs and protein capsules can incorporate larger molecular weight cargos, thus emphasizing their application for sizeable biologics like gene editors. Clearly a thorough understanding of CPP mechanisms, both alone and when conjugated to cargos, will be necessary to fully understand their therapeutic scope.

1.4 Notable macromolecules in preclinical and clinical development

As of 2023, there were 671 FDA-approved brand-name biologics on the market.[156] The vast majority reach extracellular, cell surface, or lysosomal targets, but cannot access interior compartments like the cytosol or nucleus. There are notable exceptions, however, particularly in the field of RNA therapeutics. Since 1998, 17 RNA biologics have been approved by the FDA, and over 200 are actively undergoing clinical trials.[157] Antisense oligonucleotides (ASOs) have achieved the most clinical success, comprising 10 of the 17 approved RNA therapeutics. All FDA-approved ASOs are administered as naked nucleic acids with backbone modifications to enhance stability.[157] siRNA therapeutics represent the next largest class, with four approved siRNAs in the clinic. The siRNA Onpattro® (patisiran), developed by Alnylam for hereditary transthyretin-mediated amyloidosis, was both the first siRNA and the first lipid nanoparticle (LNP) to receive FDA

approval.[158] Notably, the recent success of the Spikevax®/Comirnaty® mRNA vaccines for COVID-19 (developed by Moderna and Pfizer-BioNTech, respectively) established the large-scale safety and efficacy of LNP-based delivery strategies. LNPs and liposomes are now represented in nearly 60% of RNA-based clinical trials.[157] Although currently Spikevax® and Comirnaty® are the only FDA-approved mRNA therapeutics, over 50% of current RNA-targeted clinical trials are evaluating mRNAs.[157] An interesting class of new LNP-RNA drugs aim to deliver gene editing systems by co-encapsulating mRNA encoding Cas9 with guide RNA targeted to the gene of interest. Verve Therapeutics, for example, developed VERVE-101 and VERVE-102, two LNPs with variable formulations containing mRNA coding for an adenine base editor as well as guide RNA that turns off production of hepatic *PCSK9,* a gene involved in regulation of circulating cholesterol levels.[159] Given the prevalence of RNAs in clinical trials and their success in the clinic, we can likely expect a surge in FDA approvals over the coming decade.

Despite the success of RNAs, protein-based biologics with intracellular targets are significantly underrepresented in the clinic. Perhaps the most widely discussed protein therapeutic is the recently-FDA-approved CRISPR-Cas9 therapy, Casgevy®, for use in treating sickle cell disease and transfusion-dependent beta thalassemia. This treatment involves harvesting a patient's blood stem cells to edit *ex vivo* before re-transplanting them, which is highly specialized and costly. For more generalized CRISPR therapeutics, however, novel strategies to deliver gene editors will be of utmost importance. For instance, delivery of the Cas9 ribonucleoprotein complex using cell-penetrating peptides and virus-like particles has garnered significant attention. Delivering the intact protein has considerable benefits over more traditional vector-based strategies, including finer control over intracellular lifetime to limit off-target effects[160] and reduced immunogenicity.[8,161] Doudna and coworkers recently reported that the fusion of SpyCas9 to three copies of A22p, a CPP derived from human semaphorin-3a, led to a 3-fold improvement in editing of mouse-derived neural progenitor cells and in mouse striatum.[162] The Wilson lab reported that the co-incubation of the Cas9 RNP, Cas12a RNP, or an adenine base editor with an amphiphilic peptide dramatically enhanced editing in multiple primary human cell lines.[89,163] The Doudna and Liu labs also demonstrated that encapsulation of gene editors in virus-like particles conferred both cell-type specificity and high editing efficiency in mouse models.[122,123,125,126] These strategies are among several others being actively explored for delivery of intact RNPs, including targeted and systemic administration by LNPs and direct delivery via local injection.[3,164] Beyond CRISPR, there are many proteins with potential therapeutic applications that have been preclinically validated, including replacement of the neurological protein MeCP2[21] and delivery of highly specific binders like monobodies[165] and nanobodies,[105] among others.

1.5 Conclusions and Outlook

Next-generation protein- and RNA-based therapeutics will have monumental impacts on human health. While technological advancements in machine learning and high-throughput screening platforms have yielded highly specific and stable therapeutic candidates, their delivery to the interior of cells has remained a major obstacle. Attempts to improve cytosolic and nuclear delivery have been historically thwarted by a shortage

of assays that both accurately quantify delivery efficiency and establish whether the delivered material is intact and active. As highly quantitative techniques have emerged, a broader understanding of the relationship between the number of molecules in the cytosol or nucleus and a phenotypic outcome will be critical for the development of delivery strategies appropriate for a given macromolecule.

At the same time, a deeper appreciation of mechanisms for cellular entry and trafficking is essential for the clinical success of biologics. Proteins and RNAs exhibit diverse structures, geometries, sizes, charges, and other physicochemical properties that influence their trafficking into and within cells. Given the breadth of delivery modalities that have been reported, pairing a molecule of interest to the appropriate strategy demands an understanding of that strategy's delivery route and how it may be affected by the therapeutic molecule.

In this dissertation, we explore mechanisms and design rules of cytosolic protein delivery using a cell-permeant miniature protein, develop and apply novel tools to detect intracellular trafficking, and quantify the delivery of genome editing machinery. In all chapters, we emphasize the importance of quantitation when discussing subcellular protein localization. The results set forth in this body of work contribute both to the development of the mini protein ZF5.3 as a therapeutic modality and to the field of biologics delivery as a whole by providing a framework with which to characterize and quantify endosomal, cytosolic, and nuclear trafficking.

1.6 Acknowledgments

I am immensely grateful to Angel Vázquez Maldonado, Teresia Chen, and Dr. Dan Brauer for their contributions to the analysis of delivery vehicles and notable macromolecules in the clinic discussed in this chapter.

1.7 References

(1) Huff, A. L.; Jaffee, E. M.; Zaidi, N. Messenger RNA Vaccines for Cancer Immunotherapy: Progress Promotes Promise. *J. Clin. Invest.* **2022**, *132* (6). https://doi.org/10.1172/JCI156211.

(2) Jain, S.; Venkataraman, A.; Wechsler, M. E.; Peppas, N. A. Messenger RNA-Based Vaccines: Past, Present, and Future Directions in the Context of the COVID-19 Pandemic. *Adv. Drug Deliv. Rev.* **2021**, *179*, 114000. https://doi.org/10.1016/j.addr.2021.114000.

(3) Raguram, A.; Banskota, S.; Liu, D. R. Therapeutic in Vivo Delivery of Gene Editing Agents. *Cell* **2022**, *185* (15), 2806–2827. https://doi.org/10.1016/j.cell.2022.03.045.

(4) Sinclair, F.; Begum, A. A.; Dai, C. C.; Toth, I.; Moyle, P. M. Recent Advances in the Delivery and Applications of Nonviral CRISPR/Cas9 Gene Editing. *Drug Deliv. Transl. Res.* **2023**,*13* (5), 1500–1519. https://doi.org/10.1007/s13346-023-01320-z.

(5) Tang, Q.; Khvorova, A. RNAi-Based Drug Design: Considerations and Future Directions. *Nat. Rev. Drug Discov.* **2024**, *23* (5), 341–364. https://doi.org/10.1038/s41573-024-00912-9.

(6) Paunovska, K.; Loughrey, D.; Dahlman, J. E. Drug Delivery Systems for RNA Therapeutics. *Nat. Rev. Genet.* **2022**, *23* (5), 265–280. https://doi.org/10.1038/s41576-021-00439-4.

(7) de la Fuente, M.; Lombardero, L.; Gómez-González, A.; Solari, C.; Angulo-Barturen, I.; Acera, A.; Vecino, E.; Astigarraga, E.; Barreda-Gómez, G. Enzyme Therapy: Current Challenges and Future Perspectives. *Int. J. Mol. Sci.* **2021**, *22* (17), 9181. https://doi.org/10.3390/ijms22179181.

(8) Yang, T.; Braun, M.; Lembke, W.; McBlane, F.; Kamerud, J.; DeWall, S.; Tarcsa, E.; Fang, X.; Hofer, L.; Kavita, U.; Upreti, V. V.; Gupta, S.; Loo, L.; Johnson, A. J.; Chandode, R. K.; Stubenrauch, K.-G.; Vinzing, M.; Xia, C. Q.; Jawa, V. Immunogenicity Assessment of AAV-Based Gene Therapies: An IQ Consortium Industry White Paper. *Mol. Ther. Methods Clin. Dev.* **2022**, *26*, 471–494. https://doi.org/10.1016/j.omtm.2022.07.018.

(9) Urquhart, L. Top Companies and Drugs by Sales in 2022. *Nat. Rev. Drug Discov.* **2023**, *22* (4), 260–260. https://doi.org/10.1038/d41573-023-00039-3.

(10) Nguyen, A. W.; Maynard, J. A. Engineering Antibody-Based Therapeutics: Progress and Opportunities. In *Protein Engineering*; John Wiley & Sons, Ltd, 2021; pp 317–351. https://doi.org/10.1002/9783527815128.ch13.

(11) Cheng, R.; Zhang, F.; Li, M.; Wo, X.; Su, Y.-W.; Wang, W. Influence of Fixation and Permeabilization on the Mass Density of Single Cells: A Surface Plasmon Resonance Imaging Study. *Front. Chem.* **2019**, *7*, 588. https://doi.org/10.3389/fchem.2019.00588.

(12) Hobro, A. J.; Smith, N. I. An Evaluation of Fixation Methods: Spatial and Compositional Cellular Changes Observed by Raman Imaging. *Vib. Spectrosc.* **2017**, *91*, 31–45. https://doi.org/10.1016/j.vibspec.2016.10.012.

(13) Okada, S.; Fukai, Y.; Tanoue, Y.; Nasser, H.; Fukuda, T.; Ikeda, T.; Saitoh, H. Basic Structure and Cytocompatibility of Giant Membrane Vesicles Derived from

Paraformaldehyde-Exposed Human Cells. *J. Biochem. (Tokyo)* **2022**, *171* (3), 339–347. https://doi.org/10.1093/jb/mvab144.
(14) Knox, S. L.; Steinauer, A.; Alpha-Cobb, G.; Trexler, A.; Rhoades, E.; Schepartz, A. Chapter Twenty-One - Quantification of Protein Delivery in Live Cells Using Fluorescence Correlation Spectroscopy. In *Methods in Enzymology*; Chenoweth, D. M., Ed.; Chemical Tools for Imaging, Manipulating, and Tracking Biological Systems: Diverse Chemical, Optical and Bioorthogonal Methods; Academic Press, 2020; Vol. 641, pp 477–505. https://doi.org/10.1016/bs.mie.2020.05.007.
(15) Schwille, P. Fluorescence Correlation Spectroscopy and Its Potential for Intracellular Applications. *Cell Biochem. Biophys.* **2001**, *34* (3), 383–408. https://doi.org/10.1385/CBB:34:3:383.
(16) Weidemann, T. Application of Fluorescence Correlation Spectroscopy (FCS) to Measure the Dynamics of Fluorescent Proteins in Living Cells. In *Fluorescence Spectroscopy and Microscopy: Methods and Protocols*; Engelborghs, Y., Visser, A. J. W. G., Eds.; Humana Press: Totowa, NJ, 2014; pp 539–555. https://doi.org/10.1007/978-1-62703-649-8_24.
(17) LaRochelle, J. R.; Cobb, G. B.; Steinauer, A.; Rhoades, E.; Schepartz, A. Fluorescence Correlation Spectroscopy Reveals Highly Efficient Cytosolic Delivery of Certain Penta-Arg Proteins and Stapled Peptides. *J. Am. Chem. Soc.* **2015**, *137* (7), 2536–2541. https://doi.org/10.1021/ja510391n.
(18) Wissner, R. F.; Steinauer, A.; Knox, S. L.; Thompson, A. D.; Schepartz, A. Fluorescence Correlation Spectroscopy Reveals Efficient Cytosolic Delivery of Protein Cargo by Cell-Permeant Miniature Proteins. *ACS Cent. Sci.* **2018**, *4* (10), 1379–1393. https://doi.org/10.1021/acscentsci.8b00446.
(19) Steinauer, A.; LaRochelle, J. R.; Knox, S. L.; Wissner, R. F.; Berry, S.; Schepartz, A. HOPS-Dependent Endosomal Fusion Required for Efficient Cytosolic Delivery of Therapeutic Peptides and Small Proteins. *Proc. Natl. Acad. Sci.* **2019**, *116* (2), 512–521. https://doi.org/10.1073/pnas.1812044116.
(20) Knox, S. L.; Wissner, R.; Piszkiewicz, S.; Schepartz, A. Cytosolic Delivery of Argininosuccinate Synthetase Using a Cell-Permeant Miniature Protein. *ACS Cent. Sci.* **2021**, *7* (4), 641–649. https://doi.org/10.1021/acscentsci.0c01603.
(21) Zhang, X.; Cattoglio, C.; Zoltek, M.; Vetralla, C.; Mozumdar, D.; Schepartz, A. Dose-Dependent Nuclear Delivery and Transcriptional Repression with a Cell-Penetrant MeCP2. *ACS Cent. Sci.* **2023**, *9* (2), 277–288. https://doi.org/10.1021/acscentsci.2c01226.
(22) Giudice, J.; Brauer, D. D.; Zoltek, M.; Maldonado, A. L. V.; Kelly, M.; Schepartz, A. Requirements for Efficient Endosomal Escape by Designed Mini-Proteins. bioRxiv April 6, 2024, p 2024.04.05.588336. https://doi.org/10.1101/2024.04.05.588336.
(23) Zoltek, M.; Vázquez Maldonado, A. L.; Zhang, X.; Dadina, N.; Lesiak, L.; Schepartz, A. HOPS-Dependent Endosomal Escape Demands Protein Unfolding. *ACS Cent. Sci.* **2024**, *10* (4), 860–870. https://doi.org/10.1021/acscentsci.4c00016.
(24) Needleman, D. J.; Xu, Y.; Mitchison, T. J. Pin-Hole Array Correlation Imaging: Highly Parallel Fluorescence Correlation Spectroscopy. *Biophys. J.* **2009**, *96* (12), 5050–5059. https://doi.org/10.1016/j.bpj.2009.03.023.

(25) Oh, D.; Zidovska, A.; Xu, Y.; Needleman, D. J. Development of Time-Integrated Multipoint Moment Analysis for Spatially Resolved Fluctuation Spectroscopy with High Time Resolution. *Biophys. J.* **2011**, *101* (6), 1546–1554. https://doi.org/10.1016/j.bpj.2011.08.013.
(26) Otosu, T.; Ishii, K.; Tahara, T. Multifocus Fluorescence Correlation Spectroscopy with Spatially Separated Excitation Beams. *Bull. Chem. Soc. Jpn.* **2019**, *92* (9), 1495–1502. https://doi.org/10.1246/bcsj.20190109.
(27) Fu, X.; Song, Y.; Masud, A.; Nuti, K.; DeRouchey, J. E.; Richards, C. I. High-Throughput Fluorescence Correlation Spectroscopy Enables Analysis of Surface Components of Cell-Derived Vesicles. *Anal. Bioanal. Chem.* **2020**, *412* (11), 2589–2597. https://doi.org/10.1007/s00216-020-02485-z.
(28) Yu, L.; Lei, Y.; Ma, Y.; Liu, M.; Zheng, J.; Dan, D.; Gao, P. A Comprehensive Review of Fluorescence Correlation Spectroscopy. *Front. Phys.* **2021**, *9*. https://doi.org/10.3389/fphy.2021.644450.
(29) Buntz, A.; Killian, T.; Schmid, D.; Seul, H.; Brinkmann, U.; Ravn, J.; Lindholm, M.; Knoetgen, H.; Haucke, V.; Mundigl, O. Quantitative Fluorescence Imaging Determines the Absolute Number of Locked Nucleic Acid Oligonucleotides Needed for Suppression of Target Gene Expression. *Nucleic Acids Res.* **2019**, *47* (2), 953–969. https://doi.org/10.1093/nar/gky1158.
(30) Politi, A. Z.; Cai, Y.; Walther, N.; Hossain, M. J.; Koch, B.; Wachsmuth, M.; Ellenberg, J. Quantitative Mapping of Fluorescently Tagged Cellular Proteins Using FCS-Calibrated Four-Dimensional Imaging. *Nat. Protoc.* **2018**, *13* (6), 1445–1464. https://doi.org/10.1038/nprot.2018.040.
(31) Hedlund, H.; Du Rietz, H.; Johansson, J. M.; Eriksson, H. C.; Zedan, W.; Huang, L.; Wallin, J.; Wittrup, A. Single-Cell Quantification and Dose-Response of Cytosolic siRNA Delivery. *Nat. Commun.* **2023**, *14* (1), 1075. https://doi.org/10.1038/s41467-023-36752-1.
(32) Jing, H.; Pálmai, M.; Saed, B.; George, A.; Snee, P. T.; Hu, Y. S. Cytosolic Delivery of Membrane-Penetrating QDs into T Cell Lymphocytes: Implications in Immunotherapy and Drug Delivery. *Nanoscale* **2021**, *13* (10), 5519–5529. https://doi.org/10.1039/D0NR08362C.
(33) Deprey, K.; Batistatou, N.; Debets, M. F.; Godfrey, J.; VanderWall, K. B.; Miles, R. R.; Shehaj, L.; Guo, J.; Andreucci, A.; Kandasamy, P.; Lu, G.; Shimizu, M.; Vargeese, C.; Kritzer, J. A. Quantitative Measurement of Cytosolic and Nuclear Penetration of Oligonucleotide Therapeutics. *ACS Chem. Biol.* **2022**, *17* (2), 348–360. https://doi.org/10.1021/acschembio.1c00830.
(34) Lucchino, M.; Billet, A.; Bai, S.-K.; Dransart, E.; Hadjerci, J.; Schmidt, F.; Wunder, C.; Johannes, L. Absolute Quantification of Drug Vector Delivery to the Cytosol. *Angew. Chem. Int. Ed.* **2021**, *60* (27), 14824–14830. https://doi.org/10.1002/anie.202102332.
(35) Becker, L.; Singh Badwal, J.; Brandl, F.; Verdurmen, W. P. R.; Plückthun, A. Thermodynamic Stability Is a Strong Predictor for the Delivery of DARPins to the Cytosol via Anthrax Toxin. *Pharmaceutics* **2021**, *13* (8), 1285. https://doi.org/10.3390/pharmaceutics13081285.
(36) Teo, S. L. Y.; Rennick, J. J.; Yuen, D.; Al-Wassiti, H.; Johnston, A. P. R.; Pouton, C. W. Unravelling Cytosolic Delivery of Cell Penetrating Peptides with a

Quantitative Endosomal Escape Assay. *Nat. Commun.* **2021**, *12* (1), 3721. https://doi.org/10.1038/s41467-021-23997-x.

(37) Rakowska, P. D.; Lamarre, B.; Ryadnov, M. G. Probing Label-Free Intracellular Quantification of Free Peptide by MALDI-ToF Mass Spectrometry. *Methods* **2014**, *68* (2), 331–337. https://doi.org/10.1016/j.ymeth.2014.03.012.

(38) Makarov, A. A.; Jiang, Y.; Sondey, C.; Zhang, M.; Mansueto, M. S.; Pirrone, G. F.; Huang, C.; Biswas, K.; Duggal, R.; Al-Sayah, M. A.; Regalado, E. L.; Mangion, I. Rapid Label-Free Cell-Based Approach Membrane Permeability Assay Using MALDI-Hydrogen-Deuterium Exchange Mass Spectrometry for Peptides. *Anal. Chim. Acta* **2022**, *1225*, 340234. https://doi.org/10.1016/j.aca.2022.340234.

(39) Becquart, C.; Stulz, R.; Thomen, A.; Dost, M.; Najafinobar, N.; Dahlén, A.; Andersson, S.; Ewing, A. G.; Kurczy, M. E. Intracellular Absolute Quantification of Oligonucleotide Therapeutics by NanoSIMS. *Anal. Chem.* **2022**, *94* (29), 10549–10556. https://doi.org/10.1021/acs.analchem.2c02111.

(40) Batistatou, N.; Kritzer, J. A. Recent Advances in Methods for Quantifying the Cell Penetration of Macromolecules. *Curr. Opin. Chem. Biol.* **2024**, *81*, 102501. https://doi.org/10.1016/j.cbpa.2024.102501.

(41) Deprey, K.; Becker, L.; Kritzer, J.; Plückthun, A. Trapped! A Critical Evaluation of Methods for Measuring Total Cellular Uptake versus Cytosolic Localization. *Bioconjug. Chem.* **2019**, *30* (4), 1006–1027. https://doi.org/10.1021/acs.bioconjchem.9b00112.

(42) Schissel, C. K.; Farquhar, C. E.; Loas, A.; Malmberg, A. B.; Pentelute, B. L. In-Cell Penetration Selection–Mass Spectrometry Produces Noncanonical Peptides for Antisense Delivery. *ACS Chem. Biol.* **2023**, *18* (3), 615–628. https://doi.org/10.1021/acschembio.2c00920.

(43) Kawai, T.; Mihara, Y.; Morita, M.; Ohkubo, M.; Asami, T.; Watanabe, T. M. Quantitation of Cell Membrane Permeability of Cyclic Peptides by Single-Cell Cytoplasm Mass Spectrometry. *Anal. Chem.* **2021**, *93* (7), 3370–3377. https://doi.org/10.1021/acs.analchem.0c03901.

(44) Roehl, I.; Schuster, M.; Seiffert, S. Oligonucleotide Detection Method. US10711298B2, July 14, 2020. https://patents.google.com/patent/US10711298B2/en (accessed 2024-07-25).

(45) Hutanu, A.; Signori, C.; Moritz, B.; Gregoritza, M.; Rohde, A.; Schwarz, M. A. Using Peptide Nucleic Acid Hybridization Probes for Qualitative and Quantitative Analysis of Nucleic Acid Therapeutics by Capillary Electrophoresis. *Anal. Chem.* **2023**, *95* (11), 4914–4922. https://doi.org/10.1021/acs.analchem.2c04813.

(46) Beach, M. A.; Teo, S. L. Y.; Chen, M. Z.; Smith, S. A.; Pouton, C. W.; Johnston, A. P. R.; Such, G. K. Quantifying the Endosomal Escape of pH-Responsive Nanoparticles Using the Split Luciferase Endosomal Escape Quantification Assay. *ACS Appl. Mater. Interfaces* **2022**, *14* (3), 3653–3661. https://doi.org/10.1021/acsami.1c18359.

(47) Tuck, B. J.; Miller, L. V. C.; Katsinelos, T.; Smith, A. E.; Wilson, E. L.; Keeling, S.; Cheng, S.; Vaysburd, M. J.; Knox, C.; Tredgett, L.; Metzakopian, E.; James, L. C.; McEwan, W. A. Cholesterol Determines the Cytosolic Entry and Seeded Aggregation of Tau. *Cell Rep.* **2022**, *39* (5), 110776. https://doi.org/10.1016/j.celrep.2022.110776.

(48) Milech, N.; Longville, B. A.; Cunningham, P. T.; Scobie, M. N.; Bogdawa, H. M.; Winslow, S.; Anastasas, M.; Connor, T.; Ong, F.; Stone, S. R.; Kerfoot, M.; Heinrich, T.; Kroeger, K. M.; Tan, Y.-F.; Hoffmann, K.; Thomas, W. R.; Watt, P. M.; Hopkins, R. M. GFP-Complementation Assay to Detect Functional CPP and Protein Delivery into Living Cells. *Sci. Rep.* **2015**, *5* (1), 18329. https://doi.org/10.1038/srep18329.

(49) Nomura, T. K.; Heishima, K.; Sugito, N.; Sugawara, R.; Ueda, H.; Yukihiro, A.; Honda, R. Specific Inhibition of Oncogenic RAS Using Cell-Permeable RAS-Binding Domains. *Cell Chem. Biol.* **2021**, *28* (11), 1581-1589.e6. https://doi.org/10.1016/j.chembiol.2021.04.013.

(50) Batistatou, N.; Kritzer, J. A. Investigation of Sequence-Penetration Relationships of Antisense Oligonucleotides. *ChemBioChem* **2023**, *24* (9), e202300009. https://doi.org/10.1002/cbic.202300009.

(51) Batistatou, N.; Kritzer, J. A. Comparing Cell Penetration of Biotherapeutics across Human Cell Lines. *ACS Chem. Biol.* **2024**. https://doi.org/10.1021/acschembio.4c00211.

(52) Wang, J.; Zhang, S.; Li, Y.; Xu, Q.; Kritzer, J. A. Investigating the Cytosolic Delivery of Proteins by Lipid Nanoparticles Using the Chloroalkane Penetration Assay. *Biochemistry* **2024**, *63* (4), 512–522. https://doi.org/10.1021/acs.biochem.3c00614.

(53) Brown, H.; Chung, M.; Üffing, A.; Batistatou, N.; Tsang, T.; Doskocil, S.; Mao, W.; Willbold, D.; Bast, R. C. Jr.; Lu, Z.; Weiergräber, O. H.; Kritzer, J. A. Structure-Based Design of Stapled Peptides That Bind GABARAP and Inhibit Autophagy. *J. Am. Chem. Soc.* **2022**, *144* (32), 14687–14697. https://doi.org/10.1021/jacs.2c04699.

(54) Huh, S.; Batistatou, N.; Wang, J.; Saunders, G. J.; Kritzer, J. A.; Yudin, A. K. Cell Penetration of Oxadiazole-Containing Macrocycles. *RSC Chem. Biol.* **2024**, *5* (4), 328–334. https://doi.org/10.1039/D3CB00201B.

(55) Deprey, K.; Kritzer, J. A. Chapter Twelve - Quantitative Measurement of Cytosolic Penetration Using the Chloroalkane Penetration Assay. In *Methods in Enzymology*; Chenoweth, D. M., Ed.; Chemical Tools for Imaging, Manipulating, and Tracking Biological Systems: Diverse Chemical, Optical and Bioorthogonal Methods; Academic Press, 2020; Vol. 641, pp 277–309. https://doi.org/10.1016/bs.mie.2020.03.003.

(56) Peier, A.; Ge, L.; Boyer, N.; Frost, J.; Duggal, R.; Biswas, K.; Edmondson, S.; Hermes, J. D.; Yan, L.; Zimprich, C.; Sadruddin, A.; Kristal Kaan, H. Y.; Chandramohan, A.; Brown, C. J.; Thean, D.; Lee, X. E.; Yuen, T. Y.; Ferrer-Gago, F. J.; Johannes, C. W.; Lane, D. P.; Sherborne, B.; Corona, C.; Robers, M. B.; Sawyer, T. K.; Partridge, A. W. NanoClick: A High Throughput, Target-Agnostic Peptide Cell Permeability Assay. *ACS Chem. Biol.* **2021**, *16* (2), 293–309. https://doi.org/10.1021/acschembio.0c00804.

(57) Chandramohan, A.; Josien, H.; Yuen, T. Y.; Duggal, R.; Spiegelberg, D.; Yan, L.; Juang, Y.-C. A.; Ge, L.; Aronica, P. G.; Kaan, H. Y. K.; Lim, Y. H.; Peier, A.; Sherborne, B.; Hochman, J.; Lin, S.; Biswas, K.; Nestor, M.; Verma, C. S.; Lane, D. P.; Sawyer, T. K.; Garbaccio, R.; Henry, B.; Kannan, S.; Brown, C. J.; Johannes, C. W.; Partridge, A. W. Design-Rules for Stapled Peptides with in Vivo Activity and

Their Application to Mdm2/X Antagonists. *Nat. Commun.* **2024**, *15* (1), 489. https://doi.org/10.1038/s41467-023-43346-4.
(58) Johansson, J. M.; Rietz, H. D.; Hedlund, H.; Eriksson, H. C.; Blenke, E. O.; Pote, A.; Harun, S.; Nordenfelt, P.; Lindfors, L.; Wittrup, A. Cellular and Biophysical Barriers to Lipid Nanoparticle Mediated Delivery of RNA to the Cytosol. bioRxiv June 2, 2024, p 2024.05.31.596627. https://doi.org/10.1101/2024.05.31.596627.
(59) Huotari, J.; Helenius, A. Endosome Maturation. *EMBO J.* **2011**, *30* (17), 3481–3500. https://doi.org/10.1038/emboj.2011.286.
(60) Perrin, P.; Janssen, L.; Janssen, H.; van den Broek, B.; Voortman, L. M.; van Elsland, D.; Berlin, I.; Neefjes, J. Retrofusion of Intralumenal MVB Membranes Parallels Viral Infection and Coexists with Exosome Release. *Curr. Biol.* **2021**, *31* (17), 3884-3893.e4. https://doi.org/10.1016/j.cub.2021.06.022.
(61) Herling, M. R.; Dmochowski, I. J. Ratiometric, pH-Sensitive Probe for Monitoring siRNA Delivery. *J. Am. Chem. Soc.* **2023**, *145* (17), 9417–9422. https://doi.org/10.1021/jacs.3c01032.
(62) Salim, H.; Pei, D. Assessing the Cellular Uptake, Endosomal EscapeEndosomal Escape, and Cytosolic Entry Efficiencies of Cyclic PeptidesCyclic Peptides. In *Peptide Macrocycles: Methods and Protocols*; Coppock, M. B., Winton, A. J., Eds.; Methods in Molecular Biology; Springer US: New York, NY, 2022; pp 301–316. https://doi.org/10.1007/978-1-0716-1689-5_16.
(63) Futaki, S.; Suzuki, T.; Ohashi, W.; Yagami, T.; Tanaka, S.; Ueda, K.; Sugiura, Y. Arginine-Rich Peptides: AN ABUNDANT SOURCE OF MEMBRANE-PERMEABLE PEPTIDES HAVING POTENTIAL AS CARRIERS FOR INTRACELLULAR PROTEIN DELIVERY*. *J. Biol. Chem.* **2001**, *276* (8), 5836–5840. https://doi.org/10.1074/jbc.M007540200.
(64) LINDGREN, M. E.; HÄLLBRINK, M. M.; ELMQUIST, A. M.; LANGEL, Ü. Passage of Cell-Penetrating Peptides across a Human Epithelial Cell Layer in Vitro. *Biochem. J.* **2004**, *377* (1), 69–76. https://doi.org/10.1042/bj20030760.
(65) Futaki, S.; Nakase, I. Cell-Surface Interactions on Arginine-Rich Cell-Penetrating Peptides Allow for Multiplex Modes of Internalization. *Acc. Chem. Res.* **2017**, *50* (10), 2449–2456. https://doi.org/10.1021/acs.accounts.7b00221.
(66) Lamazière, A.; Wolf, C.; Lambert, O.; Chassaing, G.; Trugnan, G.; Ayala-Sanmartin, J. The Homeodomain Derived Peptide Penetratin Induces Curvature of Fluid Membrane Domains. *PLOS ONE* **2008**, *3* (4), e1938. https://doi.org/10.1371/journal.pone.0001938.
(67) Frankel, A. D.; Pabo, C. O. Cellular Uptake of the Tat Protein from Human Immunodeficiency Virus. *Cell* **1988**, *55* (6), 1189–1193. https://doi.org/10.1016/0092-8674(88)90263-2.
(68) Grunwald, J.; Rejtar, T.; Sawant, R.; Wang, Z.; Torchilin, V. P. TAT Peptide and Its Conjugates: Proteolytic Stability. *Bioconjug. Chem.* **2009**, *20* (8), 1531–1537. https://doi.org/10.1021/bc900081e.
(69) Erazo-Oliveras, A.; Najjar, K.; Dayani, L.; Wang, T.-Y.; Johnson, G. A.; Pellois, J.-P. Protein Delivery into Live Cells by Incubation with an Endosomolytic Agent. *Nat. Methods* **2014**, *11* (8), 861–867. https://doi.org/10.1038/nmeth.2998.
(70) Najjar, K.; Erazo-Oliveras, A.; Brock, D. J.; Wang, T.-Y.; Pellois, J.-P. An L- to d-Amino Acid Conversion in an Endosomolytic Analog of the Cell-Penetrating

Peptide TAT Influences Proteolytic Stability, Endocytic Uptake, and Endosomal Escape*. *J. Biol. Chem.* **2017**, *292* (3), 847–861. https://doi.org/10.1074/jbc.M116.759837.

(71) Szabó, I.; Yousef, M.; Soltész, D.; Bató, C.; Mező, G.; Bánóczi, Z. Redesigning of Cell-Penetrating Peptides to Improve Their Efficacy as a Drug Delivery System. *Pharmaceutics* **2022**, *14* (5), 907. https://doi.org/10.3390/pharmaceutics14050907.

(72) Lafarga, V.; Sirozh, O.; Díaz-López, I.; Galarreta, A.; Hisaoka, M.; Zarzuela, E.; Boskovic, J.; Jovanovic, B.; Fernandez-Leiro, R.; Muñoz, J.; Stoecklin, G.; Ventoso, I.; Fernandez-Capetillo, O. Widespread Displacement of DNA- and RNA-binding Factors Underlies Toxicity of Arginine-rich Cell-penetrating Peptides. *EMBO J.* **2021**, *40* (13), e103311. https://doi.org/10.15252/embj.2019103311.

(73) Porosk, L.; Gaidutšik, I.; Langel, Ü. Approaches for the Discovery of New Cell-Penetrating Peptides. *Expert Opin. Drug Discov.* **2021**, *16* (5), 553–565. https://doi.org/10.1080/17460441.2021.1851187.

(74) Kardani, K.; Bolhassani, A. Cppsite 2.0: An Available Database of Experimentally Validated Cell-Penetrating Peptides Predicting Their Secondary and Tertiary Structures. *J. Mol. Biol.* **2021**, *433* (11), 166703. https://doi.org/10.1016/j.jmb.2020.11.002.

(75) Buyanova, M.; Sahni, A.; Yang, R.; Sarkar, A.; Salim, H.; Pei, D. Discovery of a Cyclic Cell-Penetrating Peptide with Improved Endosomal Escape and Cytosolic Delivery Efficiency. *Mol. Pharm.* **2022**, *19* (5), 1378–1388. https://doi.org/10.1021/acs.molpharmaceut.1c00924.

(76) Panigrahi, B.; Singh, R. K.; Mishra, S.; Mandal, D. Cyclic Peptide-Based Nanostructures as Efficient siRNA Carriers. *Artif. Cells Nanomedicine Biotechnol.* **2018**, *46* (sup3), 763–773. https://doi.org/10.1080/21691401.2018.1511574.

(77) Iwata, T.; Hirose, H.; Sakamoto, K.; Hirai, Y.; Arafiles, J. V. V.; Akishiba, M.; Imanishi, M.; Futaki, S. Liquid Droplet Formation and Facile Cytosolic Translocation of IgG in the Presence of Attenuated Cationic Amphiphilic Lytic Peptides. *Angew. Chem. Int. Ed.* **2021**, *60* (36), 19804–19812. https://doi.org/10.1002/anie.202105527.

(78) Sun, Y.; Lau, S. Y.; Lim, Z. W.; Chang, S. C.; Ghadessy, F.; Partridge, A.; Miserez, A. Phase-Separating Peptides for Direct Cytosolic Delivery and Redox-Activated Release of Macromolecular Therapeutics. *Nat. Chem.* **2022**, *14* (3), 274–283. https://doi.org/10.1038/s41557-021-00854-4.

(79) Sun, Y.; Wu, X.; Li, J.; Radiom, M.; Mezzenga, R.; Verma, C. S.; Yu, J.; Miserez, A. Phase-Separating Peptide Coacervates with Programmable Material Properties for Universal Intracellular Delivery of Macromolecules. bioRxiv June 24, 2024, p 2024.06.20.599859. https://doi.org/10.1101/2024.06.20.599859.

(80) Gleason, J. M.; Klass, S. H.; Huang, P.; Ozawa, T.; Santos, R. A.; Fogarty, M. M.; Raleigh, D. R.; Berger, M. S.; Francis, M. B. Intrinsically Disordered Protein Micelles as Vehicles for Convection-Enhanced Drug Delivery to Glioblastoma Multiforme. *ACS Appl. Bio Mater.* **2022**, *5* (8), 3695–3702. https://doi.org/10.1021/acsabm.2c00215.

(81) Hoffmann, K.; Milech, N.; Juraja, S. M.; Cunningham, P. T.; Stone, S. R.; Francis, R. W.; Anastasas, M.; Hall, C. M.; Heinrich, T.; Bogdawa, H. M.; Winslow, S.;

Scobie, M. N.; Dewhurst, R. E.; Florez, L.; Ong, F.; Kerfoot, M.; Champain, D.; Adams, A. M.; Fletcher, S.; Viola, H. M.; Hool, L. C.; Connor, T.; Longville, B. A. C.; Tan, Y.-F.; Kroeger, K.; Morath, V.; Weiss, G. A.; Skerra, A.; Hopkins, R. M.; Watt, P. M. A Platform for Discovery of Functional Cell-Penetrating Peptides for Efficient Multi-Cargo Intracellular Delivery. *Sci. Rep.* **2018**, *8* (1), 12538. https://doi.org/10.1038/s41598-018-30790-2.

(82) Carney, R. P.; Thillier, Y.; Kiss, Z.; Sahabi, A.; Heleno Campos, J. C.; Knudson, A.; Liu, R.; Olivos, D.; Saunders, M.; Tian, L.; Lam, K. S. Combinatorial Library Screening with Liposomes for Discovery of Membrane Active Peptides. *ACS Comb. Sci.* **2017**, *19* (5), 299–307. https://doi.org/10.1021/acscombsci.6b00182.

(83) Schissel, C. K.; Mohapatra, S.; Wolfe, J. M.; Fadzen, C. M.; Bellovoda, K.; Wu, C.-L.; Wood, J. A.; Malmberg, A. B.; Loas, A.; Gómez-Bombarelli, R.; Pentelute, B. L. Deep Learning to Design Nuclear-Targeting Abiotic Miniproteins. *Nat. Chem.* **2021**, *13* (10), 992–1000. https://doi.org/10.1038/s41557-021-00766-3.

(84) López-Vidal, E. M.; Schissel, C. K.; Mohapatra, S.; Bellovoda, K.; Wu, C.-L.; Wood, J. A.; Malmberg, A. B.; Loas, A.; Gómez-Bombarelli, R.; Pentelute, B. L. Deep Learning Enables Discovery of a Short Nuclear Targeting Peptide for Efficient Delivery of Antisense Oligomers. *JACS Au* **2021**, *1* (11), 2009–2020. https://doi.org/10.1021/jacsau.1c00327.

(85) Kalafatovic, D.; Giralt, E. Cell-Penetrating Peptides: Design Strategies beyond Primary Structure and Amphipathicity. *Molecules* **2017**, *22* (11), 1929. https://doi.org/10.3390/molecules22111929.

(86) Allred, C. A.; Gormley, C.; Venugopal, I.; Li, S.; McGuire, M. J.; Brown, K. C. Tumor-Specific Intracellular Delivery: Peptide-Guided Transport of a Catalytic Toxin. *Commun. Biol.* **2023**, *6* (1), 1–11. https://doi.org/10.1038/s42003-022-04385-7.

(87) Kurrikoff, K.; Vunk, B.; Langel, Ü. Status Update in the Use of Cell-Penetrating Peptides for the Delivery of Macromolecular Therapeutics. *Expert Opin. Biol. Ther.* **2021**, *21* (3), 361–370. https://doi.org/10.1080/14712598.2021.1823368.

(88) Tamemoto, N.; Akishiba, M.; Sakamoto, K.; Kawano, K.; Noguchi, H.; Futaki, S. Rational Design Principles of Attenuated Cationic Lytic Peptides for Intracellular Delivery of Biomacromolecules. *Mol. Pharm.* **2020**, *17* (6), 2175–2185. https://doi.org/10.1021/acs.molpharmaceut.0c00312.

(89) Sahu, S. U.; Castro, M.; Muldoon, J. J.; Asija, K.; Wyman, S. K.; Krishnappa, N.; Eyquem, J.; Nguyen, D. N.; Wilson, R. C. Peptide-Enabled Ribonucleoprotein Delivery for CRISPR Engineering (PERC) in Primary Human Immune Cells and Hematopoietic Stem Cells. bioRxiv July 16, 2024, p 2024.07.14.603391. https://doi.org/10.1101/2024.07.14.603391.

(90) Li, J.; Tuma, J.; Han, H.; Kim, H.; Wilson, R. C.; Lee, H. Y.; Murthy, N. The Coiled-Coil Forming Peptide (KVSALKE)5 Is a Cell Penetrating Peptide That Enhances the Intracellular Delivery of Proteins. *Adv. Healthc. Mater.* **2022**, *11* (9), 2102118. https://doi.org/10.1002/adhm.202102118.

(91) Zhang, Z.; Baxter, A. E.; Ren, D.; Qin, K.; Chen, Z.; Collins, S. M.; Huang, H.; Komar, C. A.; Bailer, P. F.; Parker, J. B.; Blobel, G. A.; Kohli, R. M.; Wherry, E. J.; Berger, S. L.; Shi, J. Efficient Engineering of Human and Mouse Primary Cells

Using Peptide-Assisted Genome Editing. *Nat. Biotechnol.* **2024**, *42* (2), 305–315. https://doi.org/10.1038/s41587-023-01756-1.

(92) Wang, Z.; Zhang, J.; Wang, Y.; Zhou, J.; Jiao, X.; Han, M.; Zhang, X.; Hu, H.; Su, R.; Zhang, Y.; Qi, W. Overcoming Endosomal Escape Barriers in Gene Drug Delivery Using De Novo Designed pH-Responsive Peptides. *ACS Nano* **2024**. https://doi.org/10.1021/acsnano.4c02400.

(93) Behr, J.-P. The Proton Sponge: A Trick to Enter Cells the Viruses Did Not Exploit. *CHIMIA* **1997**, *51* (1–2), 34–34. https://doi.org/10.2533/chimia.1997.34.

(94) Pei, D.; Buyanova, M. Overcoming Endosomal Entrapment in Drug Delivery. *Bioconjug. Chem.* **2019**, *30* (2), 273–283. https://doi.org/10.1021/acs.bioconjchem.8b00778.

(95) Yang, S.-T.; Chernomordik, L.; Melikov, K. Fusion Between Intraluminal Vesicles of Late Endosomes as a Possible Mechanism of Endosomal Escape by Cell-Penetrating Peptides. *Biophys. J.* **2010**, *98* (3), 672a. https://doi.org/10.1016/j.bpj.2009.12.3692.

(96) Abrigo, N. A.; Dods, K. K.; Makovsky, C. A.; Lohan, S.; Mitra, K.; Newcomb, K. M.; Le, A.; Hartman, M. C. T. Development of a Cyclic, Cell Penetrating Peptide Compatible with In Vitro Selection Strategies. *ACS Chem. Biol.* **2023**, *18* (4), 746–755. https://doi.org/10.1021/acschembio.2c00680.

(97) Faris, J. H.; Adaligil, E.; Popovych, N.; Ono, S.; Takahashi, M.; Nguyen, H.; Plise, E.; Taechalertpaisarn, J.; Lee, H.-W.; Koehler, M. F. T.; Cunningham, C. N.; Lokey, R. S. Membrane Permeability in a Large Macrocyclic Peptide Driven by a Saddle-Shaped Conformation. *J. Am. Chem. Soc.* **2024**, *146* (7), 4582–4591. https://doi.org/10.1021/jacs.3c10949.

(98) Merz, M. L.; Habeshian, S.; Li, B.; David, J.-A. G. L.; Nielsen, A. L.; Ji, X.; Il Khwildy, K.; Duany Benitez, M. M.; Phothirath, P.; Heinis, C. De Novo Development of Small Cyclic Peptides That Are Orally Bioavailable. *Nat. Chem. Biol.* **2023**, 1–10. https://doi.org/10.1038/s41589-023-01496-y.

(99) Ramelot, T. A.; Palmer, J.; Montelione, G. T.; Bhardwaj, G. Cell-Permeable Chameleonic Peptides: Exploiting Conformational Dynamics in de Novo Cyclic Peptide Design. *Curr. Opin. Struct. Biol.* **2023**, *80*, 102603. https://doi.org/10.1016/j.sbi.2023.102603.

(100) Garcia Jimenez, D.; Poongavanam, V.; Kihlberg, J. Macrocycles in Drug Discovery—Learning from the Past for the Future. *J. Med. Chem.* **2023**, *66* (8), 5377–5396. https://doi.org/10.1021/acs.jmedchem.3c00134.

(101) Boyken, S. E.; Benhaim, M. A.; Busch, F.; Jia, M.; Bick, M. J.; Choi, H.; Klima, J. C.; Chen, Z.; Walkey, C.; Mileant, A.; Sahasrabuddhe, A.; Wei, K. Y.; Hodge, E. A.; Byron, S.; Quijano-Rubio, A.; Sankaran, B.; King, N. P.; Lippincott-Schwartz, J.; Wysocki, V. H.; Lee, K. K.; Baker, D. De Novo Design of Tunable, pH-Driven Conformational Changes. *Science* **2019**, *364* (6441), 658–664. https://doi.org/10.1126/science.aav7897.

(102) Goldbach, N.; Benna, I.; Wicky, B. I. M.; Croft, J. T.; Carter, L.; Bera, A. K.; Nguyen, H.; Kang, A.; Sankaran, B.; Yang, E. C.; Lee, K. K.; Baker, D. De Novo Design of Monomeric Helical Bundles for pH-Controlled Membrane Lysis. *Protein Sci.* **2023**, *32* (11), e4769. https://doi.org/10.1002/pro.4769.

(103) Torres, S. V.; Leung, P. J. Y.; Venkatesh, P.; Lutz, I. D.; Hink, F.; Huynh, H.-H.; Becker, J.; Yeh, A. H.-W.; Juergens, D.; Bennett, N. R.; Hoofnagle, A. N.; Huang, E.; MacCoss, M. J.; Expòsit, M.; Lee, G. R.; Bera, A. K.; Kang, A.; De La Cruz, J.; Levine, P. M.; Li, X.; Lamb, M.; Gerben, S. R.; Murray, A.; Heine, P.; Korkmaz, E. N.; Nivala, J.; Stewart, L.; Watson, J. L.; Rogers, J. M.; Baker, D. De Novo Design of High-Affinity Binders of Bioactive Helical Peptides. *Nature* **2023**, 1–3. https://doi.org/10.1038/s41586-023-06953-1.

(104) Appelbaum, J. S.; LaRochelle, J. R.; Smith, B. A.; Balkin, D. M.; Holub, J. M.; Schepartz, A. Arginine Topology Controls Escape of Minimally Cationic Proteins from Early Endosomes to the Cytoplasm. *Chem. Biol.* **2012**, *19* (7), 819–830. https://doi.org/10.1016/j.chembiol.2012.05.022.

(105) Shen, F.; Zheng, G.; Setegne, M.; Tenglin, K.; Izadi, M.; Xie, H.; Zhai, L.; Orkin, S. H.; Dassama, L. M. K. A Cell-Permeant Nanobody-Based Degrader That Induces Fetal Hemoglobin. *ACS Cent. Sci.* **2022**, *8* (12), 1695–1703. https://doi.org/10.1021/acscentsci.2c00998.

(106) Guerrini, G.; Magrì, D.; Gioria, S.; Medaglini, D.; Calzolai, L. Characterization of Nanoparticles-Based Vaccines for COVID-19. *Nat. Nanotechnol.* **2022**, *17* (6), 570–576. https://doi.org/10.1038/s41565-022-01129-w.

(107) Polack, F. P.; Thomas, S. J.; Kitchin, N.; Absalon, J.; Gurtman, A.; Lockhart, S.; Perez, J. L.; Pérez Marc, G.; Moreira, E. D.; Zerbini, C.; Bailey, R.; Swanson, K. A.; Roychoudhury, S.; Koury, K.; Li, P.; Kalina, W. V.; Cooper, D.; Frenck, R. W.; Hammitt, L. L.; Türeci, Ö.; Nell, H.; Schaefer, A.; Ünal, S.; Tresnan, D. B.; Mather, S.; Dormitzer, P. R.; Şahin, U.; Jansen, K. U.; Gruber, W. C. Safety and Efficacy of the BNT162b2 mRNA Covid-19 Vaccine. *N. Engl. J. Med.* **2020**, *383* (27), 2603–2615. https://doi.org/10.1056/NEJMoa2034577.

(108) Baden, L. R.; El Sahly, H. M.; Essink, B.; Kotloff, K.; Frey, S.; Novak, R.; Diemert, D.; Spector, S. A.; Rouphael, N.; Creech, C. B.; McGettigan, J.; Khetan, S.; Segall, N.; Solis, J.; Brosz, A.; Fierro, C.; Schwartz, H.; Neuzil, K.; Corey, L.; Gilbert, P.; Janes, H.; Follmann, D.; Marovich, M.; Mascola, J.; Polakowski, L.; Ledgerwood, J.; Graham, B. S.; Bennett, H.; Pajon, R.; Knightly, C.; Leav, B.; Deng, W.; Zhou, H.; Han, S.; Ivarsson, M.; Miller, J.; Zaks, T. Efficacy and Safety of the mRNA-1273 SARS-CoV-2 Vaccine. *N. Engl. J. Med.* **2021**, *384* (5), 403–416. https://doi.org/10.1056/NEJMoa2035389.

(109) Cui, L.; Pereira, S.; Sonzini, S.; Pelt, S. van; M. Romanelli, S.; Liang, L.; Ulkoski, D.; R. Krishnamurthy, V.; Brannigan, E.; Brankin, C.; S. Desai, A. Development of a High-Throughput Platform for Screening Lipid Nanoparticles for mRNA Delivery. *Nanoscale* **2022**, *14* (4), 1480–1491. https://doi.org/10.1039/D1NR06858J.

(110) Hou, X.; Zaks, T.; Langer, R.; Dong, Y. Lipid Nanoparticles for mRNA Delivery. *Nat. Rev. Mater.* **2021**, *6* (12), 1078–1094. https://doi.org/10.1038/s41578-021-00358-0.

(111) Wang, X.; Liu, S.; Sun, Y.; Yu, X.; Lee, S. M.; Cheng, Q.; Wei, T.; Gong, J.; Robinson, J.; Zhang, D.; Lian, X.; Basak, P.; Siegwart, D. J. Preparation of Selective Organ-Targeting (SORT) Lipid Nanoparticles (LNPs) Using Multiple Technical Methods for Tissue-Specific mRNA Delivery. *Nat. Protoc.* **2023**, *18* (1), 265–291. https://doi.org/10.1038/s41596-022-00755-x.

(112) Kim, M.; Jeong, M.; Hur, S.; Cho, Y.; Park, J.; Jung, H.; Seo, Y.; Woo, H. A.; Nam, K. T.; Lee, K.; Lee, H. Engineered Ionizable Lipid Nanoparticles for Targeted Delivery of RNA Therapeutics into Different Types of Cells in the Liver. *Sci. Adv.* **2021**, *7* (9), eabf4398. https://doi.org/10.1126/sciadv.abf4398.
(113) Dilliard, S. A.; Siegwart, D. J. Passive, Active and Endogenous Organ-Targeted Lipid and Polymer Nanoparticles for Delivery of Genetic Drugs. *Nat. Rev. Mater.* **2023**, *8* (4), 282–300. https://doi.org/10.1038/s41578-022-00529-7.
(114) Zhu, Y.; Ma, J.; Shen, R.; Lin, J.; Li, S.; Lu, X.; Stelzel, J. L.; Kong, J.; Cheng, L.; Vuong, I.; Yao, Z.-C.; Wei, C.; Korinetz, N. M.; Toh, W. H.; Choy, J.; Reynolds, R. A.; Shears, M. J.; Cho, W. J.; Livingston, N. K.; Howard, G. P.; Hu, Y.; Tzeng, S. Y.; Zack, D. J.; Green, J. J.; Zheng, L.; Doloff, J. C.; Schneck, J. P.; Reddy, S. K.; Murphy, S. C.; Mao, H.-Q. Screening for Lipid Nanoparticles That Modulate the Immune Activity of Helper T Cells towards Enhanced Antitumour Activity. *Nat. Biomed. Eng.* **2023**, 1–17. https://doi.org/10.1038/s41551-023-01131-0.
(115) Namiot, E. D.; Sokolov, A. V.; Chubarev, V. N.; Tarasov, V. V.; Schiöth, H. B. Nanoparticles in Clinical Trials: Analysis of Clinical Trials, FDA Approvals and Use for COVID-19 Vaccines. *Int. J. Mol. Sci.* **2023**, *24* (1), 787. https://doi.org/10.3390/ijms24010787.
(116) Hald Albertsen, C.; Kulkarni, J. A.; Witzigmann, D.; Lind, M.; Petersson, K.; Simonsen, J. B. The Role of Lipid Components in Lipid Nanoparticles for Vaccines and Gene Therapy. *Adv. Drug Deliv. Rev.* **2022**, *188*, 114416. https://doi.org/10.1016/j.addr.2022.114416.
(117) Witten, J.; Hu, Y.; Langer, R.; Anderson, D. G. Recent Advances in Nanoparticulate RNA Delivery Systems. *Proc. Natl. Acad. Sci.* **2024**, *121* (11), e2307798120. https://doi.org/10.1073/pnas.2307798120.
(118) Kazemian, P.; Yu, S.-Y.; Thomson, S. B.; Birkenshaw, A.; Leavitt, B. R.; Ross, C. J. D. Lipid-Nanoparticle-Based Delivery of CRISPR/Cas9 Genome-Editing Components. *Mol. Pharm.* **2022**, *19* (6), 1669–1686. https://doi.org/10.1021/acs.molpharmaceut.1c00916.
(119) Chatterjee, S.; Kon, E.; Sharma, P.; Peer, D. Endosomal Escape: A Bottleneck for LNP-Mediated Therapeutics. *Proc. Natl. Acad. Sci.* **2024**, *121* (11), e2307800120. https://doi.org/10.1073/pnas.2307800120.
(120) Gilleron, J.; Querbes, W.; Zeigerer, A.; Borodovsky, A.; Marsico, G.; Schubert, U.; Manygoats, K.; Seifert, S.; Andree, C.; Stöter, M.; Epstein-Barash, H.; Zhang, L.; Koteliansky, V.; Fitzgerald, K.; Fava, E.; Bickle, M.; Kalaidzidis, Y.; Akinc, A.; Maier, M.; Zerial, M. Image-Based Analysis of Lipid Nanoparticle–Mediated siRNA Delivery, Intracellular Trafficking and Endosomal Escape. *Nat. Biotechnol.* **2013**, *31* (7), 638–646. https://doi.org/10.1038/nbt.2612.
(121) Zhao, Y.; Wang, Z. M.; Song, D.; Chen, M.; Xu, Q. Rational Design of Lipid Nanoparticles: Overcoming Physiological Barriers for Selective Intracellular mRNA Delivery. *Curr. Opin. Chem. Biol.* **2024**, *81*, 102499. https://doi.org/10.1016/j.cbpa.2024.102499.
(122) An, M.; Raguram, A.; Du, S. W.; Banskota, S.; Davis, J. R.; Newby, G. A.; Chen, P. Z.; Palczewski, K.; Liu, D. R. Engineered Virus-like Particles for Transient Delivery of Prime Editor Ribonucleoprotein Complexes in Vivo. *Nat. Biotechnol.* **2024**, 1–12. https://doi.org/10.1038/s41587-023-02078-y.

(123) Banskota, S.; Raguram, A.; Suh, S.; Du, S. W.; Davis, J. R.; Choi, E. H.; Wang, X.; Nielsen, S. C.; Newby, G. A.; Randolph, P. B.; Osborn, M. J.; Musunuru, K.; Palczewski, K.; Liu, D. R. Engineered Virus-like Particles for Efficient in Vivo Delivery of Therapeutic Proteins. *Cell* **2022**, *185* (2), 250-265.e16. https://doi.org/10.1016/j.cell.2021.12.021.

(124) Segel, M.; Lash, B.; Song, J.; Ladha, A.; Liu, C. C.; Jin, X.; Mekhedov, S. L.; Macrae, R. K.; Koonin, E. V.; Zhang, F. Mammalian Retrovirus-like Protein PEG10 Packages Its Own mRNA and Can Be Pseudotyped for mRNA Delivery. *Science* **2021**, *373* (6557), 882–889. https://doi.org/10.1126/science.abg6155.

(125) Hamilton, J. R.; Chen, E.; Perez, B. S.; Sandoval Espinoza, C. R.; Kang, M. H.; Trinidad, M.; Ngo, W.; Doudna, J. A. In Vivo Human T Cell Engineering with Enveloped Delivery Vehicles. *Nat. Biotechnol.* **2024**, 1–9. https://doi.org/10.1038/s41587-023-02085-z.

(126) Hamilton, J. R.; Tsuchida, C. A.; Nguyen, D. N.; Shy, B. R.; McGarrigle, E. R.; Sandoval Espinoza, C. R.; Carr, D.; Blaeschke, F.; Marson, A.; Doudna, J. A. Targeted Delivery of CRISPR-Cas9 and Transgenes Enables Complex Immune Cell Engineering. *Cell Rep.* **2021**, *35* (9), 109207. https://doi.org/10.1016/j.celrep.2021.109207.

(127) Moreno-Gutierrez, D. S.; del Toro-Ríos, X.; Martinez-Sulvaran, N. J.; Perez-Altamirano, M. B.; Hernandez-Garcia, A. Programming the Cellular Uptake of Protein-Based Viromimetic Nanoparticles for Enhanced Delivery. *Biomacromolecules* **2023**, *24* (4), 1563–1573. https://doi.org/10.1021/acs.biomac.2c01295.

(128) Takahashi, K.; Nishiyama, T.; Umezawa, N.; Inoue, Y.; Akiba, I.; Dewa, T.; Ikeda, A.; Mizuno, T. Delivery of External Proteins into the Cytoplasm Using Protein Capsules Modified with IgG on the Surface, Created from the Amphiphilic Two Helix-Bundle Protein OLE-ZIP. *Chem. Commun.* **2024**, *60* (8), 968–971. https://doi.org/10.1039/D3CC05347D.

(129) Sun, X.; Roth, S. L.; Bialecki, M. A.; Whittaker, G. R. Internalization and Fusion Mechanism of Vesicular Stomatitis Virus and Related Rhabdoviruses. *Future Virol.* **2010**, *5* (1), 85–96. https://doi.org/10.2217/FVL.09.72.

(130) Buchholz, C. J.; Friedel, T.; Büning, H. Surface-Engineered Viral Vectors for Selective and Cell Type-Specific Gene Delivery. *Trends Biotechnol.* **2015**, *33* (12), 777–790. https://doi.org/10.1016/j.tibtech.2015.09.008.

(131) Lu, Z.; Truex, N. L.; Melo, M. B.; Cheng, Y.; Li, N.; Irvine, D. J.; Pentelute, B. L. IgG-Engineered Protective Antigen for Cytosolic Delivery of Proteins into Cancer Cells. *ACS Cent. Sci.* **2021**, *7* (2), 365–378. https://doi.org/10.1021/acscentsci.0c01670.

(132) Ruschig, M.; Marschall, A. L. J. Targeting the Inside of Cells with Biologicals: Toxin Routes in a Therapeutic Context. *BioDrugs* **2023**, *37* (2), 181–203. https://doi.org/10.1007/s40259-023-00580-y.

(133) Roh, H.; Dorner, B. G.; Ting, A. Y. Cell-Type-Specific Intracellular Protein Delivery with Inactivated Botulinum Neurotoxin. *J. Am. Chem. Soc.* **2023**, *145* (18), 10220–10226. https://doi.org/10.1021/jacs.3c01145.

(134) Piot, N.; van der Goot, F. G.; Sergeeva, O. A. Harnessing the Membrane Translocation Properties of AB Toxins for Therapeutic Applications. *Toxins* **2021**, *13* (1), 36. https://doi.org/10.3390/toxins13010036.
(135) Becker, L.; Plückthun, A. DARPins Bind Their Cytosolic Targets after Having Been Translocated through the Protective Antigen Pore of Anthrax Toxin. *Sci. Rep.* **2023**, *13* (1), 8048. https://doi.org/10.1038/s41598-023-34647-1.
(136) Loftis, A. R.; Santos, M. S.; Truex, N. L.; Biancucci, M.; Satchell, K. J. F.; Pentelute, B. L. Anthrax Protective Antigen Retargeted with Single-Chain Variable Fragments Delivers Enzymes to Pancreatic Cancer Cells. *Chembiochem Eur. J. Chem. Biol.* **2020**, *21* (19), 2772–2776. https://doi.org/10.1002/cbic.202000201.
(137) Madshus, I. H.; Olsnes, S.; Stenmark, H. Membrane Translocation of Diphtheria Toxin Carrying Passenger Protein Domains. *Infect. Immun.* **1992**, *60* (8), 3296–3302.
(138) Auger, A.; Park, M.; Nitschke, F.; Minassian, L. M.; Beilhartz, G. L.; Minassian, B. A.; Melnyk, R. A. Efficient Delivery of Structurally Diverse Protein Cargo into Mammalian Cells by a Bacterial Toxin. *Mol. Pharm.* **2015**, *12* (8), 2962–2971. https://doi.org/10.1021/acs.molpharmaceut.5b00233.
(139) Tian, S.; Liu, Y.; Appleton, E.; Wang, H.; Church, G. M.; Dong, M. Targeted Intracellular Delivery of Cas13 and Cas9 Nucleases Using Bacterial Toxin-Based Platforms. *Cell Rep.* **2022**, *38* (10), 110476. https://doi.org/10.1016/j.celrep.2022.110476.
(140) Park, S. G.; Lee, H. B.; Kang, S. Development of Plug-and-Deliverable Intracellular Protein Delivery Platforms Based on Botulinum Neurotoxin. *Int. J. Biol. Macromol.* **2024**, *261*, 129622. https://doi.org/10.1016/j.ijbiomac.2024.129622.
(141) Chan, A.; Tsourkas, A. Intracellular Protein Delivery: Approaches, Challenges, and Clinical Applications. *BME Front. 5*, 0035. https://doi.org/10.34133/bmef.0035.
(142) Sharei, A.; Zoldan, J.; Adamo, A.; Sim, W. Y.; Cho, N.; Jackson, E.; Mao, S.; Schneider, S.; Han, M.-J.; Lytton-Jean, A.; Basto, P. A.; Jhunjhunwala, S.; Lee, J.; Heller, D. A.; Kang, J. W.; Hartoularos, G. C.; Kim, K.-S.; Anderson, D. G.; Langer, R.; Jensen, K. F. A Vector-Free Microfluidic Platform for Intracellular Delivery. *Proc. Natl. Acad. Sci.* **2013**, *110* (6), 2082–2087. https://doi.org/10.1073/pnas.1218705110.
(143) Togtema, M.; Pichardo, S.; Jackson, R.; Lambert, P. F.; Curiel, L.; Zehbe, I. Sonoporation Delivery of Monoclonal Antibodies against Human Papillomavirus 16 E6 Restores P53 Expression in Transformed Cervical Keratinocytes. *PLOS ONE* **2012**, *7* (11), e50730. https://doi.org/10.1371/journal.pone.0050730.
(144) Stewart, M. P.; Langer, R.; Jensen, K. F. Intracellular Delivery by Membrane Disruption: Mechanisms, Strategies, and Concepts. *Chem. Rev.* **2018**, *118* (16), 7409–7531. https://doi.org/10.1021/acs.chemrev.7b00678.
(145) Abramson, A.; Caffarel-Salvador, E.; Khang, M.; Dellal, D.; Silverstein, D.; Gao, Y.; Frederiksen, M. R.; Vegge, A.; Hubálek, F.; Water, J. J.; Friderichsen, A. V.; Fels, J.; Kirk, R. K.; Cleveland, C.; Collins, J.; Tamang, S.; Hayward, A.; Landh, T.; Buckley, S. T.; Roxhed, N.; Rahbek, U.; Langer, R.; Traverso, G. An Ingestible Self-Orienting System for Oral Delivery of Macromolecules. *Science* **2019**, *363* (6427), 611–615. https://doi.org/10.1126/science.aau2277.

(146) Zhang, X.; Chen, G.; Fu, X.; Wang, Y.; Zhao, Y. Magneto-Responsive Microneedle Robots for Intestinal Macromolecule Delivery. *Adv. Mater.* **2021**, *33* (44), 2104932. https://doi.org/10.1002/adma.202104932.
(147) Gao, X.; Li, J.; Li, J.; Zhang, M.; Xu, J. Pain-Free Oral Delivery of Biologic Drugs Using Intestinal Peristalsis–Actuated Microneedle Robots. *Sci. Adv.* **2024**, *10* (1), eadj7067. https://doi.org/10.1126/sciadv.adj7067.
(148) Hymel, H. C.; Rahnama, A.; Sanchez, O. M.; Liu, D.; Gauthier, T. J.; Melvin, A. T. How Cargo Identity Alters the Uptake of Cell-Penetrating Peptide (CPP)/Cargo Complexes: A Study on the Effect of Net Cargo Charge and Length. *Cells* **2022**, *11* (7), 1195. https://doi.org/10.3390/cells11071195.
(149) Diaz, J.; Pietsch, M.; Davila, M.; Jaimes, G.; Hudson, A.; Pellois, J.-P. Elucidating the Impact of Payload Conjugation on the Cell-Penetrating Efficiency of the Endosomal Escape Peptide dfTAT: Implications for Future Designs for CPP-Based Delivery Systems. *Bioconjug. Chem.* **2023**, *34* (10), 1861–1872. https://doi.org/10.1021/acs.bioconjchem.3c00369.
(150) Beaumelle, B.; Taupiac, M.-P.; Lord, J. M.; Roberts, L. M. Ricin A Chain Can Transport Unfolded Dihydrofolate Reductase into the Cytosol*. *J. Biol. Chem.* **1997**, *272* (35), 22097–22102. https://doi.org/10.1074/jbc.272.35.22097.
(151) Haug, G.; Wilde, C.; Leemhuis, J.; Meyer, D. K.; Aktories, K.; Barth, H. Cellular Uptake of Clostridium Botulinum C2 Toxin: Membrane Translocation of a Fusion Toxin Requires Unfolding of Its Dihydrofolate Reductase Domain. *Biochemistry* **2003**, *42* (51), 15284–15291. https://doi.org/10.1021/bi0354278.
(152) Klingenberg, O.; Olsnes, S. Ability of Methotrexate to Inhibit Translocation to the Cytosol of Dihydrofolate Reductase Fused to Diphtheria Toxin. *Biochem. J.* **1996**, *313* (Pt 2), 647–653.
(153) Wittrup, A.; Ai, A.; Liu, X.; Hamar, P.; Trifonova, R.; Charisse, K.; Manoharan, M.; Kirchhausen, T.; Lieberman, J. Visualizing Lipid-Formulated siRNA Release from Endosomes and Target Gene Knockdown. *Nat. Biotechnol.* **2015**, *33* (8), 870–876. https://doi.org/10.1038/nbt.3298.
(154) Lee, Y.; Jeong, M.; Park, J.; Jung, H.; Lee, H. Immunogenicity of Lipid Nanoparticles and Its Impact on the Efficacy of mRNA Vaccines and Therapeutics. *Exp. Mol. Med.* **2023**, *55* (10), 2085–2096. https://doi.org/10.1038/s12276-023-01086-x.
(155) Chen, S. P.; Blakney, A. K. Immune Response to the Components of Lipid Nanoparticles for Ribonucleic Acid Therapeutics. *Curr. Opin. Biotechnol.* **2024**, *85*, 103049. https://doi.org/10.1016/j.copbio.2023.103049.
(156) FDA at a Glance - From the Office of the Commissioner April 2023.
(157) Curreri, A.; Sankholkar, D.; Mitragotri, S.; Zhao, Z. RNA Therapeutics in the Clinic. *Bioeng. Transl. Med.* **2023**, *8* (1), e10374. https://doi.org/10.1002/btm2.10374.
(158) Thi, T. T. H.; Suys, E. J. A.; Lee, J. S.; Nguyen, D. H.; Park, K. D.; Truong, N. P. Lipid-Based Nanoparticles in the Clinic and Clinical Trials: From Cancer Nanomedicine to COVID-19 Vaccines. *Vaccines* **2021**, *9* (4), 359. https://doi.org/10.3390/vaccines9040359.
(159) Vafai, S. B.; Gladding, P. A.; Scott, R.; Kerr, J.; Taubel, J.; Cegla, J.; Barbir, M.; Humphries, S. E.; Karsten, V.; Jensen, C. L.; Falzone, R.; Lister, T.; Stolz, L. E.;

Khera, A. V.; Kathiresan, S.; Bellinger, A. M. Safety and Pharmacodynamic Effects of VERVE-10.
(160) Jang, H.-K.; Jo, D. H.; Lee, S.-N.; Cho, C. S.; Jeong, Y. K.; Jung, Y.; Yu, J.; Kim, J. H.; Woo, J.-S.; Bae, S. High-Purity Production and Precise Editing of DNA Base Editing Ribonucleoproteins. *Sci. Adv.* **2021**, *7* (35), eabg2661. https://doi.org/10.1126/sciadv.abg2661.
(161) Bulcha, J. T.; Wang, Y.; Ma, H.; Tai, P. W. L.; Gao, G. Viral Vector Platforms within the Gene Therapy Landscape. *Signal Transduct. Target. Ther.* **2021**, *6* (1), 1–24. https://doi.org/10.1038/s41392-021-00487-6.
(162) Chen, K.; Stahl, E. C.; Kang, M. H.; Xu, B.; Allen, R.; Trinidad, M.; Doudna, J. A. Engineering Self-Deliverable Ribonucleoproteins for Genome Editing in the Brain. *Nat. Commun.* **2024**, *15* (1), 1727. https://doi.org/10.1038/s41467-024-45998-2.
(163) Foss, D. V.; Muldoon, J. J.; Nguyen, D. N.; Carr, D.; Sahu, S. U.; Hunsinger, J. M.; Wyman, S. K.; Krishnappa, N.; Mendonsa, R.; Schanzer, E. V.; Shy, B. R.; Vykunta, V. S.; Allain, V.; Li, Z.; Marson, A.; Eyquem, J.; Wilson, R. C. Peptide-Mediated Delivery of CRISPR Enzymes for the Efficient Editing of Primary Human Lymphocytes. *Nat. Biomed. Eng.* **2023**, *7* (5), 647–660. https://doi.org/10.1038/s41551-023-01032-2.
(164) Tsuchida, C. A.; Wasko, K. M.; Hamilton, J. R.; Doudna, J. A. Targeted Nonviral Delivery of Genome Editors in Vivo. *Proc. Natl. Acad. Sci.* **2024**, *121* (11), e2307796121. https://doi.org/10.1073/pnas.2307796121.
(165) Zoltek, M.; Vázquez Maldonado, A. L.; Zhang, X.; Dadina, N.; Lesiak, L.; Schepartz, A. HOPS-Dependent Endosomal Escape Demands Protein Unfolding. *ACS Cent. Sci.* **2024**. https://doi.org/10.1021/acscentsci.4c00016.

CHAPTER TWO

HOPS-Dependent Endosomal Escape Demands Protein Unfolding

Reproduced in part with permission from

Zoltek, M. *et al.* **HOPS-Dependent Endosomal Escape Demands Protein Unfolding**. *ACS Cent. Sci.* **10**, 860–870 (2024). Copyright 2024 American Chemical Society.

and adapted with permission from all co-authors.

2.1 Abstract

The inefficient translocation of proteins across biological membranes limits their application as therapeutic compounds and research tools. In many cases, translocation involves two steps: uptake into the endocytic pathway and endosomal escape. Certain charged or amphiphilic molecules promote protein uptake, but few enable efficient endosomal escape. One exception is ZF5.3, a mini-protein that exploits natural endosomal machinery to translocate across endosomal membranes. Although certain ZF5.3-protein conjugates are delivered efficiently into the cytosol or nucleus, overall delivery efficiency varies widely for different cargos with no obvious design rules. Here we show that delivery depends on the ability of a protein cargo to unfold using fluorescence correlation spectroscopy, a single-molecule technique that precisely measures intra-cytosolic protein concentration. We show that regardless of size and pI, low-T_m cargos of ZF5.3 (including intrinsically disordered domains) bias its endosomal escape toward a high-efficiency pathway that requires the homotypic fusion and protein sorting (HOPS) complex. Small protein domains are delivered with moderate efficiency through the same HOPS portal even if the T_m is high. These findings imply a novel pathway out of endosomes that is exploited by ZF5.3 and provide clear guidance for the selection or design of optimally deliverable therapeutic cargo.

2.2 Introduction

Protein- and nucleic acid-derived biologics are a rapidly expanding sector of modern drug development. When compared to small molecules, biologics can improve target specificity, inhibit or activate recalcitrant targets, replace missing or malfunctioning enzymes, and deliver gene editing or protein-editing machineries.[1] Direct protein delivery is simpler than lipid nanoparticle or viral vector delivery strategies[2] and provides fine-tuned control over dosage and intracellular lifetime. Despite this potential, there is not a single approved protein therapeutic that operates in the cytosol or nucleus. The problem is endosomal escape. Decades of research dedicated to improving endosomal escape of proteins delivered via the endosomal pathway has yielded many molecules that stimulate endocytic uptake, but almost none that escape endosomes and avoid a degradative fate.

One molecule that has shown significant promise with regard to endosomal escape is ZF5.3, a 27-aa mini-protein that exploits the HOPS complex, a natural and ubiquitous component of the endosomal maturation machinery,[3–6] to efficiently guide certain proteins into the cytosol and nucleus.[6–9] A conjugate of ZF5.3 and the transcription factor MeCP2 (implicated in Rett Syndrome) reaches the nucleus of mammalian cells with an efficiency of >80% (defined as nuclear concentration divided by treatment concentration) while retaining its native binding partners and function.[6] The delivery of ZF5.3-MeCP2 is substantially more efficient than other ZF5.3-protein conjugates[7,8] and, to our knowledge, any other reported nucleic acid or protein biologic that escapes the endocytic pathway. Precisely which attributes of ZF5.3-MeCP2 enabled such efficient endosomal escape, and whether these attributes could be generalized, however, remained unclear.

Endosomal escape of a biologic inherently requires the energetically unfavorable translocation of a hydrophilic molecule across a hydrophobic membrane. Nature overcomes the challenges of protein translocation through two distinct mechanisms: one that requires unfolding of the protein being transported (e.g. via Sec-translocases[10,11] or mitochondrial import pathways[12–14]), and one that accommodates the globular fold of the protein in transit (e.g. during peroxisome entry[15] or unconventional protein secretion[16,17]). Regardless of the cellular machinery required, given that the structure of MeCP2 is up to 60% disordered,[6,18] we hypothesized that intrinsic disorder could favor endosomal escape through a pathway that demands protein unfolding.

Here we test this hypothesis and discover that the ability to unfold is a key determinant in how well ZF5.3 guides a protein into the cytosol. Proteins that are intrinsically disordered or unfold at physiological temperatures are delivered into the cytosol by ZF5.3 with high efficiency and in a HOPS-dependent manner. We also discovered that proteins with greater stability can be delivered with modest efficiency and in a HOPS-dependent manner if the domain is sufficiently compact. Super-resolution microscopy images of endolysosomes in ZF5.3-treated cells provide evidence for distinct condensed sub-populations that associate with the limiting membrane. Our data support a model in which intrinsically disordered proteins or those that unfold readily are privileged with respect to efficient endosomal escape via a HOPS-dependent portal. We anticipate that these design rules will constitute a useful filter in the further development of direct protein delivery strategies and provide new insights into how proteins, natural or designed, circumnavigate biological membranes.

2.3 Results

2.3.1 ZF5.3-DHFR as a model to study role of protein unfolding

To establish whether unfolding plays a role in ZF5.3-mediated endosomal escape, we built on classic work of Eilers & Schatz, who almost forty years ago utilized the ligand-dependent stability of dihydrofolate reductase (DHFR) to study protein import into mitochondria.[12] The thermal stability of DHFR (T_m) increases by approximately 15°C upon the binding of ligands such as methotrexate (MTX) or trimethoprim.[12] Indeed, the effect of MTX or trimethoprim on protein import and export established a role for protein unfolding during chaperone-mediated lysosomal import mediated by heat shock family molecular chaperones,[19,20] protein translocation across the *E. coli* plasma membrane mediated by the Sec-translocase,[10,11] endoplasmic reticulum retrotranslocation,[21] and cytosolic delivery of toxins such as ricin and diphtheria.[22–24]

We purified samples of DHFR and ZF5.3-DHFR from *E. coli* and confirmed their identities using SDS-PAGE and LC/MS, respectively (Fig. S2.1a-c). The presence of ZF5.3 at the N-terminus of DHFR has little or no effect on overall protein secondary structure or catalytic activity (Fig. S2.1d,e). With these materials in hand, we established baseline values for the cytosolic delivery of DHFR and ZF5.3-DHFR using rhodamine-tagged variants ($DHFR^{Rho}$ and ZF5.3-$DHFR^{Rho}$) prepared using sortase, as described previously (Fig. S2.1a-c).[6–8] We incubated human osteosarcoma (Saos-2) cells with 0.1

- 1 µM DHFR^{Rho} or ZF5.3-DHFR^{Rho} for 1 h, washed and trypsin-treated the cells to remove surface-bound material, and visualized the cells using confocal microscopy, flow cytometry (FC), and fluorescence correlation spectroscopy (FCS) (Fig. 2.1 and Fig. S2.2,2.3). Confocal microscopy and FC revealed that cells treated with ZF5.3-DHFR^{Rho} showed substantially higher total intracellular fluorescence than those treated with DHFR^{Rho} at all treatment concentrations and time points. The overall uptake of DHFR^{Rho} and ZF5.3-DHFR^{Rho} revealed by confocal microscopy (Fig. 2.1a, Fig. S2.2) and FC (Fig. 2.1b) was dose-dependent; the total uptake of ZF5.3-DHFR^{Rho} was significantly higher than that of DHFR^{Rho}, especially at treatment concentrations of 0.5 µM (15.5-fold increase) and 1 µM (30.6-fold increase). These increases in total uptake due to fusion to ZF5.3 are in line with values measured for other ZF5.3-protein conjugates.[7,8] No increase in uptake was observed when cells were treated with a 1:1 mixture of ZF5.3 and DHFR^{Rho} (Fig. 2.1b), confirming that a covalent linkage is required for enhanced delivery.[8]

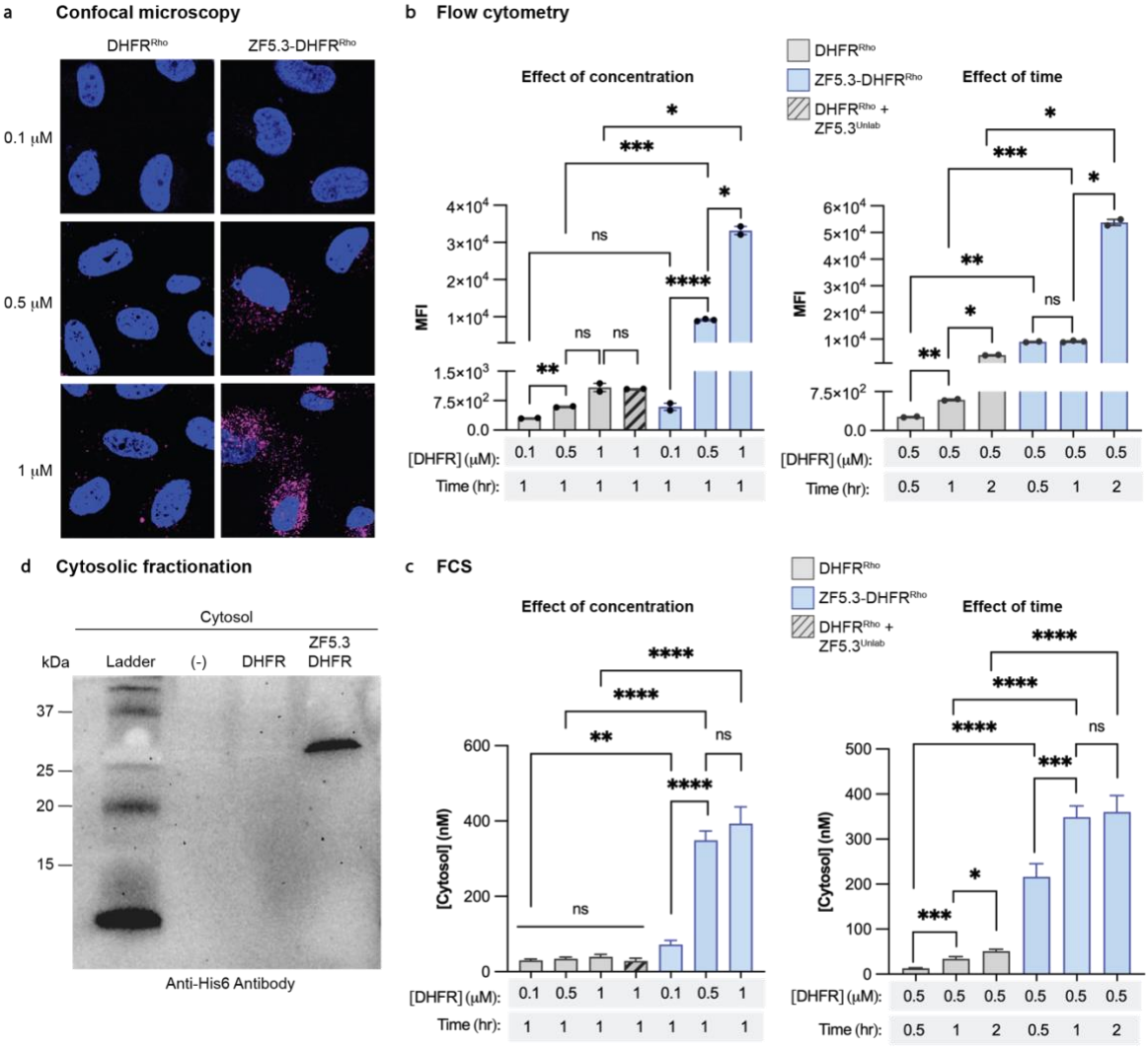

Figure 2.1. DHFR reaches the cytosol efficiently when covalently fused to ZF5.3. (A) 2-D confocal microscopy images of Saos-2 cells incubated with the indicated concentration of DHFR^{Rho} or ZF5.3-DHFR^{Rho} as described in Methods. Scale bar = 10 µm. Plots showing **(B)** flow cytometry analysis of total cellular uptake or **(C)** FCS analysis of cytosolic concentration of DHFR^{Rho}, ZF5.3-DHFR^{Rho}, or a 1:1 mixture

of ZF5.3 and DHFR^{Rho} after the indicated treatment concentration and incubation time; see Methods for detailed procedure. Flow cytometry values are provided as Median Fluorescence Intensity (MFI) for the lissamine rhodamine B channel, n = 20000 in total per condition containing at least 2 biological replicates each (mean ± SEM). FCS values provided in nM, n>20 for each FCS condition with two biological replicates each (mean ± SEM). Statistical significance comparing the given concentrations was assessed using the Brown-Forsythe and Welch one-way analysis of variance (ANOVA) followed by an unpaired t-test with Welch's correction. ****p ≤ 0.0001, ***p ≤ 0.001, **p ≤ 0.01, *p ≤ 0.05. **(D)** Western blot analysis of fractionated cytosol from Saos-2 cells treated with either DMEM media alone (-), DHFR, or ZF5.3-DHFR at 0.5 µM for 1 h. The presence of DHFR or ZF5.3-DHFR was assessed using an anti-His6 antibody. The gel results shown are representative of two biological replicates.

Although endocytic uptake is the first step along the pathway to the cytosol, the key determinant of delivery efficiency is endosomal escape – the fractional concentration of intact protein that reaches the cytosol. Two challenges have thwarted attempts to improve cytosolic delivery. The first is the absence of tools to accurately quantify delivery efficiency, and the second is the difficulty in establishing whether the delivered material is intact (or not) and thus capable of function. We used live cell FCS[25] to establish delivery efficiency[26] by quantifying the concentration of DHFR^{Rho} and ZF5.3-DHFR^{Rho} that reached the cytosol of Saos-2 cells. Unlike flow cytometry, FCS provides both the concentration and the diffusion time of a fluorescent molecule within a subcellular compartment, such as the cytosol or nucleus.[26–29] The former value provides an accurate measure of delivery efficiency, while the latter, when combined with careful biochemistry, establishes whether the fluorescent material is intact.[26,30]

2.3.2 ZF5.3-DHFR^{Rho} traffics efficiently into the Saos-2 cytosol

Examination of treated Saos-2 cells using FCS revealed substantial differences in the efficiencies with which DHFR^{Rho} and ZF5.3-DHFR^{Rho} reached the cytosol. Cells treated with DHFR^{Rho} showed little trafficking of this material to the cytosol at any concentration studied (Fig. 2.1c and Fig. S2.3). At the highest treatment concentration (1 µM) the measured cytosolic concentration of DHFR^{Rho} was 39 nM, a delivery efficiency of only 3.9%. By contrast, ZF5.3-DHFR^{Rho} reached the cytosol efficiently and in a dose-dependent manner, establishing average concentrations of 72, 350, and 393 nM when cells were treated with 0.1, 0.5, and 1 µM ZF5.3-DHFR^{Rho}, respectively, for 1 h (Fig. 2.1c). These values correspond to delivery efficiencies between 39 and 72%, up to 10-fold higher than those measured for DHFR^{Rho}. Notably, at a fixed treatment concentration of 0.5 µM ZF5.3-DHFR^{Rho}, additional incubation time (up to 2 hr) improves total uptake but does not substantially increase the fraction that reaches the cytosol (Fig. 2.1b,c). These data suggest that ZF5.3-DHFR^{Rho} follows a saturable pathway to escape from endosomes, and that endosomal escape (as opposed to an earlier endocytic event) kinetically limits delivery to the cytosol. When stringently isolated from the cytosol of treated cells, ZF5.3-DHFR was recovered fully intact with no evidence of either degradation or endosomal contamination (Fig. 2.1d and Fig. S2.4). Co-administration of ZF5.3 did not improve the cytosolic delivery of DHFR^{Rho}, confirming that efficient delivery demands a covalent linkage to ZF5.3[8] (Fig 2.1c). Thus, the presence of ZF5.3 at the N-terminus of DHFR^{Rho} improved delivery to the cytosol by up to 10-fold. The cytosolic delivery of ZF5.3-DHFR^{Rho} is more efficient than nearly all other proteins delivered by

ZF5.3 previously,[7,8] and though it is not intrinsically disordered, the translocation efficiency of ZF5.3-DHFR^{Rho} into the cytosol mirrors that of ZF5.3-MeCP2.[6]

2.3.3 Delivery of DHFR by ZF5.3 is inhibited by equimolar MTX

Next, to interrogate the role of protein folding in cytosolic delivery mediated by ZF5.3, we determined the impact of the DHFR-selective inhibitor methotrexate (MTX, Fig. 2.2a) on the cytosolic delivery efficiencies of DHFR^{Rho} and ZF5.3-DHFR^{Rho}. MTX binds DHFR with sub-nanomolar affinity ($K_D \approx 10^{-10}$ M)[31] and potently inhibits enzyme activity[32] (Fig. S2.1e). Temperature-dependent circular dichroism (CD) spectroscopy established that the apparent thermal stabilities ($*T_m$) of DHFR and ZF5.3-DHFR increased by approximately 15 degrees in the presence of 1 equivalent MTX. For DHFR, the $*T_m$ measured in the absence of MTX was 44.5°C, in line with previous measurements,[33] and increased by 16.6 °C in the presence of 1 equivalent MTX. For ZF5.3-DHFR, the $*T_m$ in the absence of MTX was 32.7°C and the corresponding increase was 17.3°C (Fig. 2.2b).

Samples of DHFR^{Rho} and ZF5.3-DHFR^{Rho} at concentrations from 0.1 - 1 µM were pre-incubated with 1 equivalent MTX for 30 minutes, added to Saos-2 cells, and incubated for 1 h as described previously. Under all conditions, the presence of 1 equivalent MTX substantially decreased the fraction of ZF5.3-DHFR^{Rho} that reached the cytosol (Fig. 2.2c). The effect of MTX was inversely related to ZF5.3-DHFR^{Rho} concentration, with reductions of 70.4%, 50.4%, and 42.8% at incubation concentrations of 0.1, 0.5, and 1 µM, respectively (Fig. 2.2c). Notably, MTX also decreased the concentration of DHFR^{Rho} that reached the cytosol by comparable amounts, but had no effect on the cytosolic delivery of ZF5.3-SNAP^{Rho}, an unrelated protein (Fig. 2.2d).

To evaluate the extent to which MTX affected cytosolic delivery by inhibiting overall uptake of ZF5.3-DHFR^{Rho}, we also evaluated treated cells using flow cytometry (Fig. 2.2e). These results indicate that MTX has different effects on the overall uptake of DHFR^{Rho} and ZF5.3-DHFR^{Rho}. Although one equivalent of MTX substantially decreased the overall uptake of DHFR^{Rho} by between 55 and 75% at all treatment concentrations, there was little or no effect of MTX on the overall uptake of ZF5.3-DHFR^{Rho} at treatment concentrations of 0.5 and 1 µM. MTX had no effect on the overall uptake of the unrelated protein ZF5.3-SNAP^{Rho} (Fig. 2.2e). The observation that MTX has a substantial effect on delivery of ZF5.3-DHFR^{Rho} to the cytosol but little or no effect on overall uptake implies that unfolding plays a significant role in one or more of the steps that guides ZF5.3-DHFR^{Rho} out of the endocytic pathway and into the cytosol. For this reason, the relatively low thermostability (T_m = 32.7°C) of ZF5.3-DHFR likely contributes to its highly efficient endosomal escape. These data also suggest that endosomal uptake and escape of DHFR^{Rho} and ZF5.3-DHFR^{Rho} proceed using fundamentally different molecular machinery or pathways, but only the pathway accessed by ZF5.3-DHFR results in efficient cytosolic delivery.

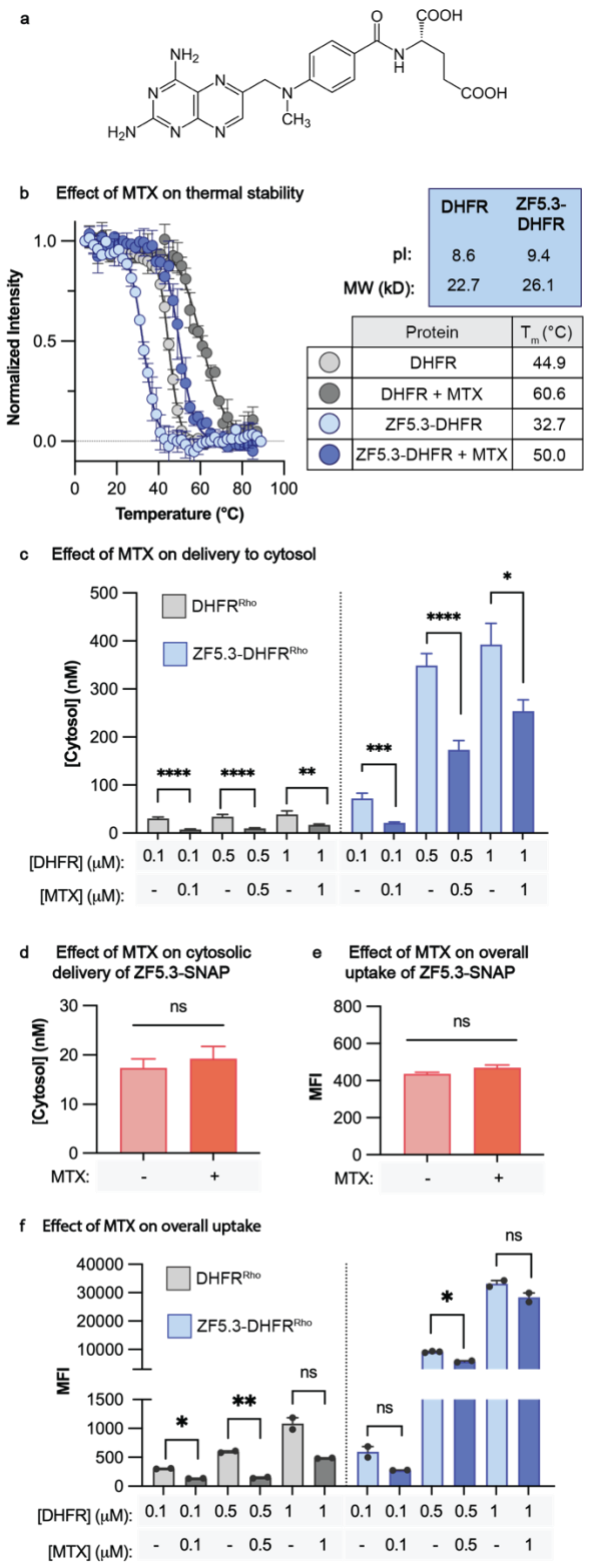

Figure 2.2. Delivery of DHFR by ZF5.3 is inhibited by equimolar MTX. (A) Chemical structure of methotrexate (MTX). **(B)** Plots illustrating the temperature- dependent loss in circular dichroism (CD) signal at 210 nm for DHFR and ZF5.3-DHFR (20 μM protein in 25 mM Tris, 150 mM KCl, 1 mM TCEP, pH 7.2) in the presence or absence of 1 equivalent MTX. For each melt, the temperature was increased in 2° increments between 5 and 90°C and the ellipticity at 210 nm was fitted using a Boltzmann sigmoidal nonlinear regression. The melts were irreversible and therefore we report the midpoint value of these fitted curves as apparent T_m values (*T_m). The data shown include two biological replicates. **(C-F),** Plots illustrating the effect of MTX on the cytosolic delivery **(C-D)** and overall uptake **(E-F)** of DHFR^{Rho}, ZF5.3-DHFR^{Rho}, or ZF5.3- SNAP^{Rho}. In all cases, the proteins were pre-incubated with 1 equivalent MTX for 30 minutes before treatment at 0.5 μM for 1 h (DHFR^{Rho} and ZF5.3- DHFR^{Rho}) or 1 μM for 30 min (ZF5.3-SNAP^{Rho}). Cells were then trypsinized and analyzed by flow cytometry or FCS as described in Methods. Flow cytometry values are provided as Median Fluorescence Intensity for the lissamine rhodamine B channel (MFI), n = 20000 per condition in total with at least 2 biological replicates each (mean ± SEM). FCS values provided in nM, n>20 for each FCS condition comprising two biological replicates each (mean ± SEM). Statistical significance comparing the given concentrations was assessed using the Brown- Forsythe and Welch one-way analysis of variance (ANOVA) followed by an unpaired t-test with Welch's correction. ****p ≤ 0.0001, ***p ≤ 0.001, **p ≤ 0.01, *p ≤ 0.05.

2.3.4 Attempts to generate alternative ZF5.3-DHFR materials

Although one equivalent MTX inhibits the fraction of ZF5.3-DHFR^{Rho} that reaches the cytosol (Fig. 2.2c), the inhibition is partial, not complete. We reasoned that this finding might be due to the loss of MTX from ZF5.3-DHFR^{Rho} before the complex reaches the late endosomal compartment from which escape occurs, especially as the compartments become progressively more acidic. In addition, the presence of MTX alters the total amount of DHFR material endocytosed by the cell to varying degrees (Fig. 2.2f). For these reasons, we sought to generate alternative variants of DHFR displaying intrinsically different melting temperatures to directly evaluate the role of unfolding during

endosomal escape without the use of a small molecule. We focused on two strategies to stabilize the DHFR protein: cyclization and active site mutation.

Backbone cyclization of DHFR via cyanocysteine ligation has been previously demonstrated to enhance its thermal stability.[34] Although this method was highly efficient, we desired a method that would tolerate an accessible cysteine for downstream fluorophore-maleimide conjugation. We turned to split intein-mediated cyclization, a widely used technique to both conjugate and cyclize peptides and proteins.[35,36] In this strategy, split intein sequences at the N- and C-terminal ends of the protein self-associate to form a functioning intein. Through two catalytic cysteine residues, the intein spontaneously self-excises and joins the amino acid sequences on either side, leaving a single cysteine residue as a scar that would be available for functionalization (Fig. S2.5a,b). Though naturally occurring inteins often have strict requirements for extein sequences,[37] engineering efforts have identified multiple promiscuous intein sequences with greater tolerance for adjacent residues.[38]

To generate cyclized untagged and ZF5.3-tagged DHFR, we designed a construct containing all the necessary residues for efficient splicing using the Cfa_{GEP} promiscuous split intein.[38] The construct included the following: the N-terminal portion of the split intein, a CFN sequence required for splicing that contains one catalytic cysteine, a GSG linker, the murine DHFR (or ZF5.3-DHFR) sequence with a C6S mutation to ensure there is only one cysteine in the final protein, a His6 tag, a second GSG linker, an AEY sequence required for splicing, and the C-terminal portion of the split intein which contains the second catalytic cysteine (Fig. S2.5a). We expressed the untagged and ZF5.3-tagged plasmids in *E. coli* and purified with Talon resin, as described for the linear variants. Cyclized DHFR(C6S) (cDHFR) is detected by a clear reduction in molecular weight from the linear version by ~15 kD. For both cDHFR(C6S) and ZF5.3-cDHFR(C6S), the predominant purified protein was cyclized; if needed, size exclusion chromatography was performed to remove excess linear product (Fig. S2.5c).

Next, the apparent thermal stabilities of the cyclized proteins were measured using temperature-dependent CD. Surprisingly, both cDHFR(C6S) and ZF5.3-cDHFR(C6S) exhibited comparable or lower thermal stabilities than their linear counterparts (Fig. S2.5e). The $*T_m$ was reduced by 7.5ºC for cDHFR(C6S) and raised by only 1.5ºC for ZF5.3-cDHFR(C6S); in contrast, cyanocysteine-mediated cyclization resulted in a ~7.5ºC increase in T_m for wildtype DHFR.[34] We reasoned that the C6S mutation in the murine DHFR sequence may destabilize the protein. Although a single cysteine residue is desirable for maleimide bioconjugation, the C6 position was previously shown to be nonreactive with maleimides (data not shown); thus, we generated cDHFR with the native cysteine present using the same procedure described above (Fig. S2.5d). Unfortunately, although the $*T_m$ of cDHFR (38.9ºC) was slightly higher than cDHFR(C6S) (36.9ºC), it was still lower than linear DHFR (44.5 ºC; Fig. S2.5e). Thus, we turned to another strategy to intrinsically stabilize the DHFR protein.

It was previously reported that a methotrexate-resistant variant of DHFR generated by mutation of Leu22 to Arg (L22R) exhibited greater thermal stability than the

wildtype protein.[39] We generated L22R mutants for both DHFR and ZF5.3-DHFR and purified them using Talon resin, as described for the wildtype variants (Fig. S2.6a,b). Temperature-dependent CD was then used to establish the $*T_m$ for each protein in the presence and absence of MTX. Without MTX, DHFR(L22R) was 2.5ºC more thermostable than DHFR, and ZF5.3-DHFR(L22R) was 5.9ºC more thermostable than ZF5.3-DHFR (Fig. S2.6c). The MTX-resistant variants were stabilized slightly in the presence of MTX (by 6.2ºC for DHFR(L22R) and by 3.1ºC for ZF5.3-DHFR(L22R)), indicating a low level of MTX binding is retained even with the active site mutation (Fig. S2.6c). Overall, although the L22R mutation did not dramatically alter the thermostability of the proteins, we reasoned that these variants could still yield useful insights into ZF5.3-mediated delivery. We attempted to prepare rhodamine-labeled variants using sortase, as described for the wildtype DHFR proteins (Fig. S2.6d). Although DHFR(L22R) was labeled with >90% efficiency, the procedure to fluorescently label ZF5.3-DHFR(L22R) was too inefficient to achieve sufficient labeling for FCS. This inefficiency stemmed from both a lower reactivity with sortase compared to DHFR(L22R) (Fig. S2.6d) and significant sample loss during concentration due to interactions with spin concentrator membranes. We thus chose to move forward with an alternative protein system to establish the role of protein unfolding during ZF5.3 delivery, described below.

2.3.5 Unfolding of cargo is a general requirement for high-efficiency delivery

To more directly evaluate the role of unfolding in endosomal escape, we turned to three known SNAP-tag variants that differ by only a few amino acid substitutions but nonetheless show distinctly different thermal stabilities.[40–43] These variants, all intermediates generated along the directed evolution pathway between human O^6-alkylguanine-DNA alkyltransferase and commercially available SNAP-tag, display thermal stabilities between 35 - 51 °C but with nearly indistinguishable molecular weights and isoelectric points of 8.7 ± 0.1 (Fig. 2.3a and Fig. S2.7a).[40] Each SNAP-tag variant was conjugated to the C-terminus of ZF5.3 and tagged with rhodamine upon reaction with benzylguanine-modified lissamine rhodamine B (BG-Rho) (Fig. S2.7b,c). Temperature-dependent CD studies confirmed the previously reported thermal stabilities; once again, the presence of ZF5.3 had a modest destabilizing effect on the $*T_m$ but little or no effect on overall secondary structure (Fig. 2.3b and Fig. S2.7d)**.**

Saos-2 cells were treated with each $SNAP^{Rho}$ variant (1 μM) for 0.5 - 2 h and evaluated using confocal microscopy, flow cytometry, and FCS as described previously (Fig. 2.3c,d and Fig. S2.8 and S2.9). The most stable variant (ZF5.3-$SNAP^{Rho}$, $*T_m$ = 51°C) showed minimal uptake (Fig. 2.3c) and poor trafficking to the cytosol (Fig. 2.3d) regardless of incubation time, in line with results described previously for a closely related variant.[7] The less thermostable proteins, ZF5.3-GE-AGT^{Rho} ($*T_m$ = 35°C) and ZF5.3-$AGT54^{Rho}$ ($*T_m$ = 46°C), were taken up with higher efficiency but not equally when evaluated by flow cytometry, with uptake increasing after longer incubation times (Fig. 2.3c). Given the roughly equal surface charges of SNAP, AGT54, and GE-AGT, it is interesting to note that decreased thermal stability seems to improve overall ZF5.3-mediated cellular uptake.

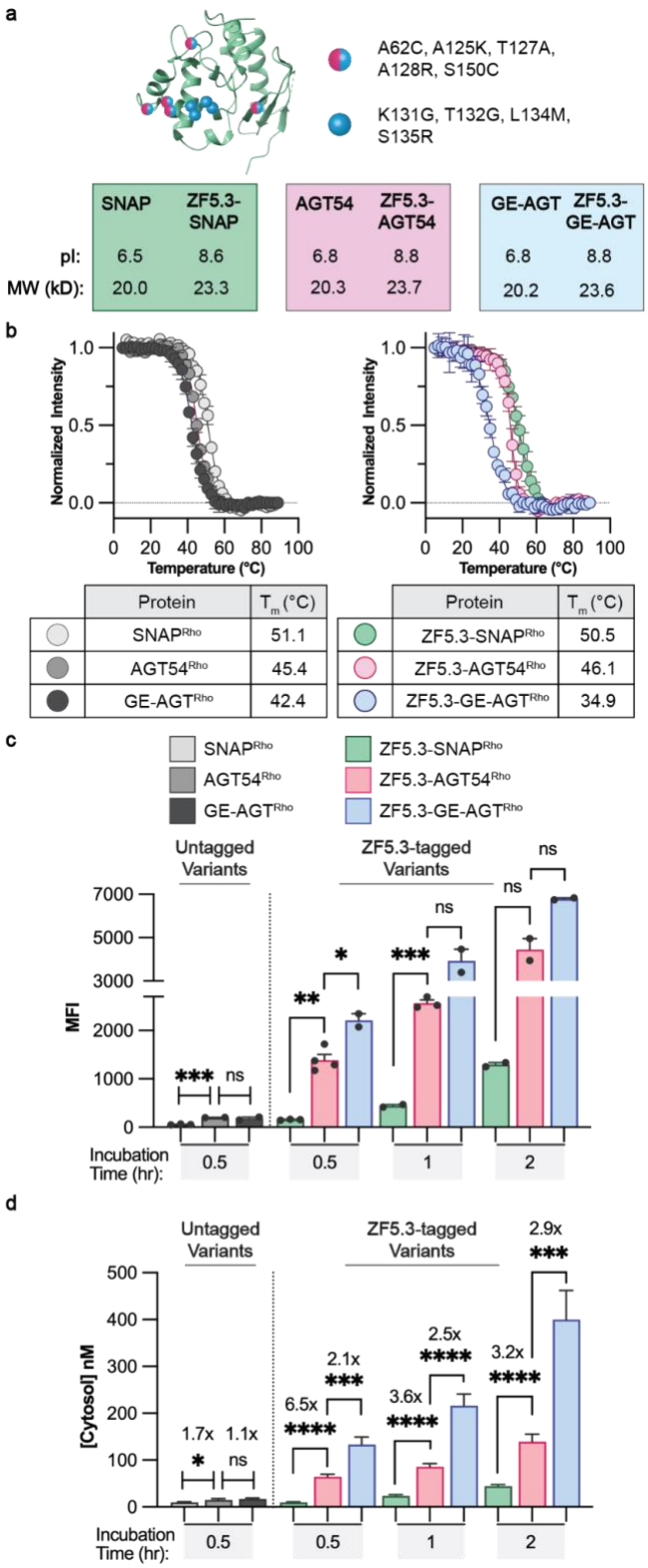

Figure 2.3. Destabilization of SNAP-tag enhances intracellular delivery only when conjugated to ZF5.3. (A) Structure of previously published SNAP-tag (PDB: 6Y8P) with destabilizing mutations marked by magenta and blue circles (for residues found in both AGT54 and GE-AGT) or blue circles (for residues found only in GE-AGT). Isoelectric point (pI) and molecular weight (in kilo-daltons, kD) are increased with the addition of ZF5.3 but remain highly similar among all variants. **(B)** Plots illustrating the temperature dependence of the 222 nm CD signal of GE-AGT^{Rho}, AGT54^{Rho}, and SNAP^{Rho} alongside the corresponding ZF5.3 conjugates. Each protein at 20 µM was measured in 20 mM Tris, 150 mM NaCl, pH 7.5. For each melt, the temperature was increased in 2° increments between 5 and 90°C and the ellipticity at 222 nm was fitted using a Boltzmann sigmoidal nonlinear regression to obtain *T_m values. The data shown include two biological replicates. **(C-D)** Total cellular uptake (top) and cytosolic concentration (bottom) of the untagged or ZF5.3-tagged SNAP^{Rho} variants were analyzed by flow cytometry and FCS. Saos-2 cells were incubated with 1 µM of the given protein for 30 min, 1 h, or 2 h before the cellular workup and measurements were performed as described previously. Flow cytometry values are provided as Median Fluorescence Intensity for the lissamine rhodamine B channel, n = 20000 per condition in total with two biological replicates each (mean ± SEM). FCS values are provided in nM, n>20 for each FCS condition with two biological replicates each (mean ± SEM). Statistical significance was assessed using the Brown-Forsythe and Welch one-way analysis of variance (ANOVA) followed by an unpaired t-test with Welch's correction. ****p ≤ 0.0001, ***p ≤ 0.001, **p ≤ 0.01, *p ≤ 0.05.

Notably, the three ZF5.3-SNAP^{Rho} variants trafficked to the cytosol with different efficiencies, and in a manner that correlated directly with *T_m (Fig. 2.3d and Fig. S2.8). At all incubation times, ZF5.3-GE-AGT^{Rho}, with the lowest *T_m (35°C), reached the cytosol between 2.1 - 2.9 -fold more efficiently than mid-*T_m ZF5.3-AGT54^{Rho}, which in turn reached the cytosol 3.2 - 6.5-fold more efficiently than high-*T_m ZF5.3-

SNAP^{Rho}. At its maximum, the least thermostable variant ZF5.3-GE-AGT^{Rho} reached a concentration of 400 nM in the cytosol, corresponding to a 40% delivery efficiency; under equal conditions, ZF5.3-AGT54^{Rho} reached 139.2 nM, and ZF5.3-SNAP^{Rho} only reached 44.2 nM. It is notable that ZF5.3-GE-AGT^{Rho} and ZF5.3-DHFR^{Rho} show comparable thermal stabilities (*T_m values of 35°C and 33°C, respectively) but ZF5.3-DHFR^{Rho} reaches the cytosol significantly more efficiently under comparable incubation conditions; this likely relates to the relatively higher total uptake of ZF5.3-DHFR^{Rho} (Fig. 2.1b,c). On their own, the series of SNAP variants lacking ZF5.3 reached the cytosol at virtually undetectable levels (cytosolic concentrations between 9 and 16.8 nM after a 30 min incubation) with minimal differences among the three (Fig. 2.3c,d), indicating that the relationship between thermostability and delivery is unique to a ZF5.3-driven pathway.

2.3.6 ZF5.3-mediated delivery of a small but stable mini-protein

Membrane translocation machines that transit unfolded protein domains sometimes tolerate secondary structures or even folded proteins if they are small and compact.[17,44,45] Moreover, proteins with high isoelectric points (pIs), and therefore excess cationic surface charge, can engage negatively charged phospholipids for enhanced cellular uptake.[46,47] Small stable protein domains, whether natural, evolved, or designed, are desirable research tools and are increasingly represented in clinical trials.[48] Indeed, ZF5.3 was recently shown to facilitate cytosolic delivery of a nanobody-derived Bio-Protac that catalytically induces degradation of Bcl-11 and upregulates fetal hemoglobin production, although the delivery efficiency was not evaluated.[9] To more quantitatively evaluate whether small, stable proteins could be delivered effectively by ZF5.3, we turned to synthetic mini-proteins derived from the fibronectin type III domain called monobodies. Monobodies can be engineered to display exceptionally high affinity for difficult-to-inhibit proteins,[49,50] are 20-25% more compact than nanobodies,[50] and are not themselves cell permeant.[51,52] In particular, we focused on NS1 (Fig. 2.4a), a small (12 kD), cationic (pI = 9.2 when conjugated to ZF5.3) monobody that binds HRAS and KRAS with high affinity (K_D values of 15 nM and 65 nM, respectively), and inhibits KRAS-driven tumor growth when expressed in vivo.[52]

NS1 and NS1-ZF5.3 were expressed and purified, labeled at the C-terminus with rhodamine via a thiol-Michael addition reaction (Fig. S2.10a,b), and characterized by LC/MS and CD (Fig. S2.10c,d). Comparison of the wavelength spectra for NS1 and NS1-ZF5.3 suggests the addition of ZF5.3 does not significantly perturb the secondary structure of NS1. As expected, both NS1 and NS1-ZF5.3 are highly thermostable (Fig. 2.4a; *T_m = 73.2°C for NS1 and 72.6°C for NS1-ZF5.3). To evaluate delivery, Saos-2 cells were treated with 1 - 2 µM NS1^{Rho} and NS1-ZF5.3^{Rho} for 1 h, washed and trypsinized, and analyzed by flow cytometry and FCS (Fig. 2.4b). Both the total uptake of NS1-ZF5.3^{Rho} and its ability to reach the cytosol were substantially higher than that of NS1^{Rho} (Fig. 2.4b). The total uptake of NS1 was improved by 63 - 117-fold upon conjugation to ZF5.3, whereas delivery to the cytosol was improved by 7-12-fold. NS1-ZF5.3^{Rho} reached a maximal cytosolic concentration of 122.9 nM and 268.3 nM with a starting incubation concentration of 1 and 2 µM, respectively, yielding a delivery efficiency of 12.3-13.4%. Under equivalent conditions, this cytosolic concentration is roughly equal to that of the

mid-stable SNAP variant ZF5.3-AGT54^{Rho} (Fig. 2.3d), which has a much lower *T_m (46°), but also a less cationic pI (8.8) and a larger molecular weight (23.6 kDa). Given that the total uptake is significantly higher for NS1-ZF5.3 than ZF5.3-AGT54, these results suggest that a cationic surface charge and compact fold can result in modest cytosolic delivery, but the specific step(s) at which ZF5.3 conjugates escape the endocytic pathway is most efficient for easily unfoldable proteins.

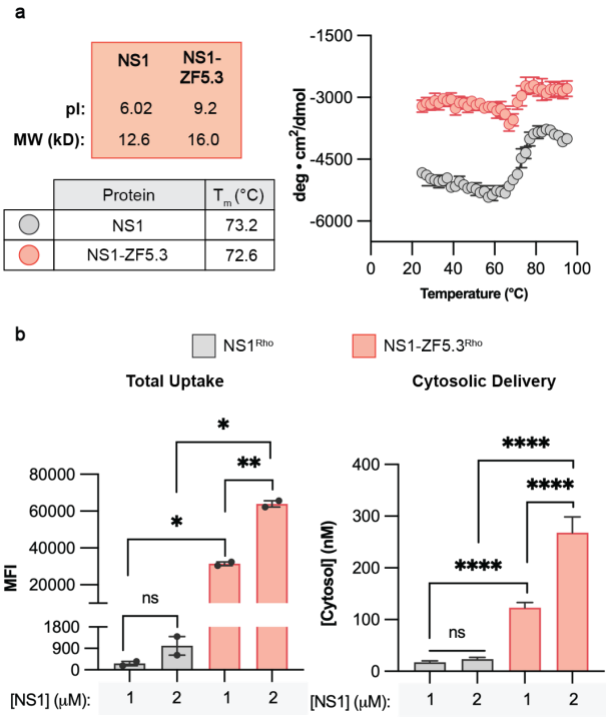

Figure 2.4. ZF5.3 can deliver the Ras-targeting monobody NS1 to the cytosol of cells. (A) Predicted isoelectric point (pI), molecular weight (kD), and experimentally determined *T_m (°C) of the Ras-targeting monobody NS1, with or without ZF5.3. The temperature-dependent CD signal at 218 nm was measured in 2° increments between 25 and 90°C and the ellipticity was fitted using a Boltzmann sigmoidal nonlinear regression to obtain *T_m values. Each protein was measured in a buffer containing 20 mM Tris, 150 mM KCl, 0.5 mM TCEP pH 7.5. The observation that molar ellipticity decreases with temperature until ~65°C for both NS1 and NS1-ZF5.3 has been documented for fibronectin-like domains[53,54] and may be due to a partial loss in structure at low temperatures. **(B)** Total cellular uptake (left) and cytosolic concentration (right) of NS1^{Rho} or NS1-ZF5.3^{Rho} were analyzed by flow cytometry and FCS. Saos-2 cells were incubated with 1 or 2 μM of the given protein for 1 h before the cellular workup and measurements as described previously. Flow cytometry values are provided as Median Fluorescence Intensity for the Lissamine rhodamine B channel, n = 20000 total per condition with two biological replicates each (mean ± SEM). FCS values are provided in nM, n>25 for each FCS condition with two biological replicates each (mean ± SEM). Statistical significance was assessed using the Brown-Forsythe and Welch one-way analysis of variance (ANOVA) followed by an unpaired t-test with Welch's correction. ****p ≤ 0.0001, ***p ≤ 0.001, **p ≤ 0.01, *p ≤ 0.05.

2.3.7 HOPS provides a portal for delivery of easily unfolded proteins

Given the evidence that efficient ZF5.3-mediated membrane translocation demands protein unfolding, we next asked whether this delivery pathway makes use of endosomal machinery. We were specifically interested in the role of the HOPS and CORVET complexes, two essential hexameric tethering complexes involved in endosomal maturation events.[55,56] HOPS coordinates with SNARE proteins and a Rab GTPase to drive late endosome-lysosome fusion, while CORVET performs an analogous role for early endosomal fusion (Fig. 2.5a).[57–59] Previous work revealed that efficient endosomal escape of ZF5.3, both alone and when fused to the intrinsically disordered cargo MeCP2, requires HOPS but not CORVET, suggesting an escape portal is generated during or after endo/lysosomal fusion.[5,6] Whether this dependency extended to all ZF5.3 cargoes or only those that easily unfold remained unclear.

We began by investigating the HOPS dependence of ZF5.3-mediated delivery of DHFR in the presence and absence of MTX. Saos-2 cells were transfected with siRNAs targeting either an essential HOPS subunit (VPS39) or the analogous CORVET subunit (TGF-BRAP1), as well as a non-targeting siRNA (RISC-free) as a negative control. All knockdowns were verified using qPCR (Fig. S2.11). We then treated cells with 500 nM $DHFR^{Rho}$ or ZF5.3-$DHFR^{Rho}$ for 1 h and analyzed each sample by flow cytometry and FCS (Fig. 2.5b). Although depletion of VPS39 had only a modest effect on the total uptake of either $DHFR^{Rho}$ or ZF5.3-$DHFR^{Rho}$, it substantially (51%) decreased the efficiency with which ZF5.3-$DHFR^{Rho}$ trafficked to the cytosol relative to the RISC-free control (Fig. 2.5b). Interestingly, knockdown of TGF-BRAP1 slightly increased the fraction of ZF5.3-$DHFR^{Rho}$ that reached the cytosol (Fig. 2.5b), a pattern also observed for $ZF5.3^{Rho}$ alone[5] but not for ZF5.3-MeCP2.[6] Notably, VPS39 knockdown had no effect on the cytosolic delivery of ZF5.3-$DHFR^{Rho}$ in the presence of one equivalent MTX, nor any effect on delivery of $DHFR^{Rho}$. These results demonstrate that ZF5.3-DHFR, like ZF5.3 alone and ZF5.3-MeCP2, makes use of late endosome tethering and/or fusion events to reach the cytosol. The lack of HOPS dependence for ZF5.3-$DHFR^{Rho}$ in the presence of MTX, as well as $DHFR^{Rho}$ (+/- MTX), suggests that certain proteins escape endosomes inefficiently through one or more pathways, but that attachment of ZF5.3 to a protein that easily unfolds biases endosomal escape toward a highly efficient, HOPS-dependent route.

To establish whether the link between HOPS and protein unfolding applied to other proteins, we examined the effect of HOPS- and CORVET-specific siRNA depletions on the uptake and cytosolic trafficking of SNAP-tag variants (Fig. 2.5c). As observed for $DHFR^{Rho}$ and ZF5.3-$DHFR^{Rho}$, depletion of VPS39 had no statistically significant effect on the uptake of any SNAP variant. Depletion of VPS39 also had no effect on the cytosolic delivery of the high-*T_m and mid-*T_m SNAP variants (ZF5.3-$SNAP^{Rho}$ and ZF5.3-$AGT54^{Rho}$) - in all cases the concentration established in the cytosol was relatively low (44 - 56 nM for ZF5.3-$SNAP^{Rho}$ and 107 - 130 nM for ZF5.3-$AGT54^{Rho}$). Depletion of VPS39 did, however, significantly decrease the cytosolic trafficking of the low-*T_m SNAP variant (ZF5.3-GE-AGT^{Rho}), by 51.4%. Knockdown of TGF-BRAP1 had no effect on delivery of the high- and mid-*T_m variants and a mild but statistically significant decrease (25.5%) in delivery of the low-*T_m variant. The untagged $SNAP^{Rho}$ variants reached extremely low cytosolic concentrations under all conditions tested and were too low to reliably quantify. For consistency, we also evaluated the effect of VPS39 and TGF-BRAP1 knockdown on NS1-$ZF5.3^{Rho}$ delivery (Fig. 2.5c). Depletion of both VPS39 and TGF-BRAP1 had minimal effect on total uptake and a modest and statistically significant (36% and 37%, respectively) reduction in cytosolic concentration of NS1-$ZF5.3^{Rho}$. The variable effect of TGF-BRAP1 knockdown on delivery of ZF5.3-$DHFR^{Rho}$, ZF5.3-GE-AGT^{Rho}, and NS1-$ZF5.3^{Rho}$ likely indicates some complexity in how the endosomal maturation machinery is utilized.[60] Together, these data suggest that ZF5.3 conjugates with easily unfolded cargos exploit a high-efficiency, HOPS-dependent pathway that can be partially adopted by cargos with high thermal stabilities provided the folded state is sufficiently compact and cationic. Even in this case, however, the delivery efficiency is markedly lower than that of a protein which can unfold under physiological conditions.

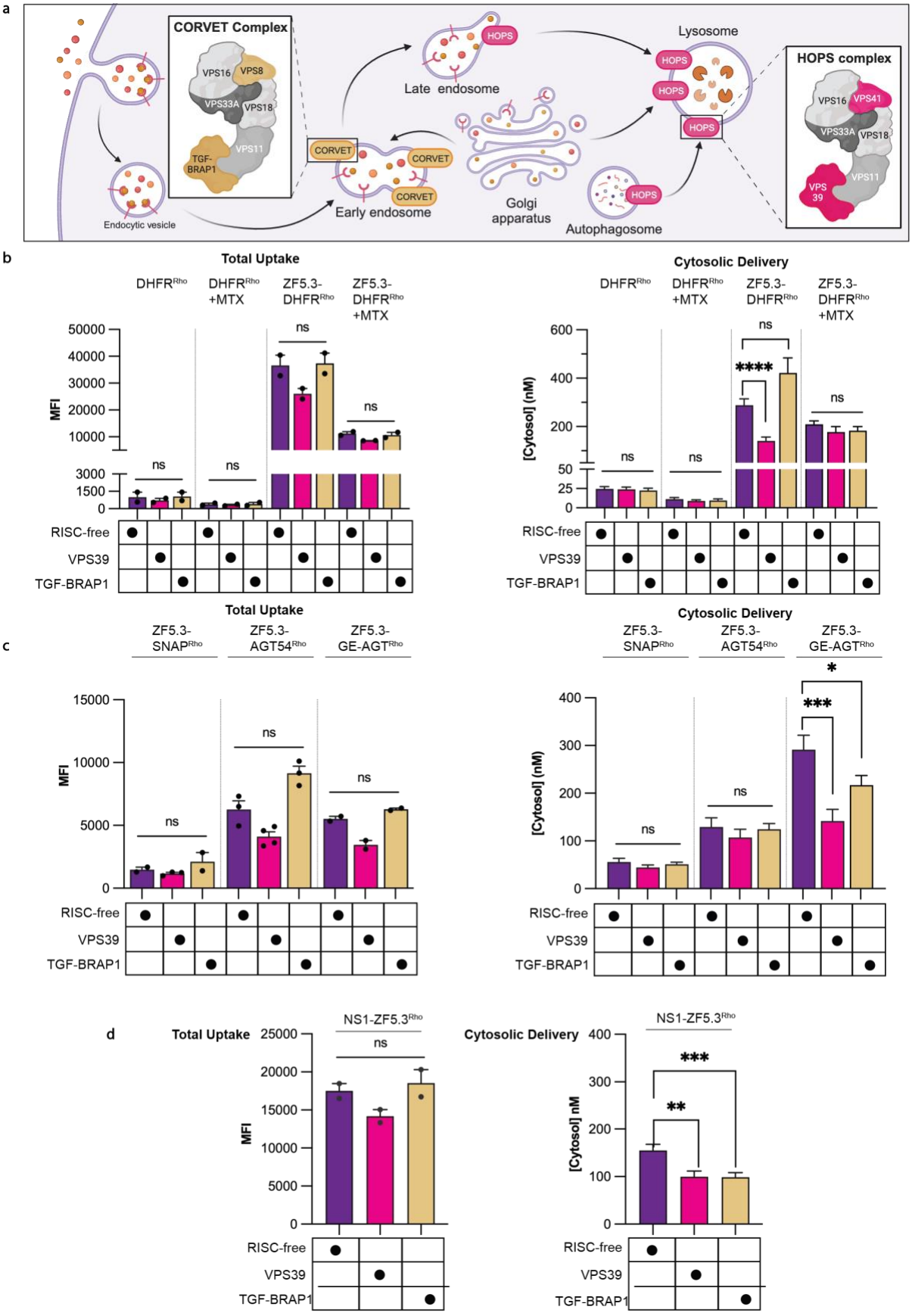
a
CORVET Complex
VPS16
VPS8
VPS33A
VPS18
VPS11
TGF-BRAP1
Endocytic vesicle
CORVET
Early endosome
Late endosome
HOPS
Golgi apparatus
Autophagosome
Lysosome
HOPS complex
VPS41
VPS39
b
Total Uptake
Cytosolic Delivery
DHFR^Rho
DHFR^Rho +MTX
ZF5.3-DHFR^Rho
ZF5.3-DHFR^Rho +MTX
MFI
[Cytosol] (nM)
ns
****
RISC-free
VPS39
TGF-BRAP1
c
ZF5.3-SNAP^Rho
ZF5.3-AGT54^Rho
ZF5.3-GE-AGT^Rho
***
*
d
NS1-ZF5.3^Rho
[Cytosol] nM
**

Figure 2.5. Easily unfolded proteins require HOPS and ZF5.3 to reach the cytosol efficiently. (A) Knockdowns were performed for the VPS39 subunit of the HOPS complex or the TGF-BRAP1 subunit of the CORVET complex. Both complexes participate in membrane tethering for either Rab5+ early endosomes and maturing endosomes (CORVET) or Rab7+ and Lamp1+ late endosomes and lysosomes (HOPS). Schematic adapted from "Role of HOPS in Lysosome Formation", by BioRender.com (2023). **(B-D)** Plots illustrating the effects of VPS39 and TGF-BRAP1 knockdowns on total uptake (flow cytometry, Median Fluorescence Intensity) and cytosolic access (FCS, nM) for DHFR proteins (**B**), SNAP-tag variants (**C**), and NS1-ZF5.3 (**D**) relative to a RISC-free negative control. Two biological replicates were performed for each experiment, n = 20000 per condition in total for flow cytometry and n>15 per condition for FCS. Error bars represent the SEM. ****P < 0.0001, ***P < 0.001, **P < 0.01, *P < 0.05, not significant (ns) for P > 0.05 from one-way ANOVA with unpaired t-test with Welch's correction.

2.3.8 STED microscopy reveals membrane-associated subcompartments within endolysosomes

But how does HOPS, which catalyzes homotypic and heterotypic membrane fusion from the cytosol, communicate with material within the endosomal lumen? Two lines of evidence suggest that endosomal escape involves more than the establishment of a membrane defect during vesicle fusion. First, efficient endosomal escape demands a covalent link between ZF5.3 and the delivered cargo.[8] Second, ZF5.3 does not promote endosomal escape of other endosomally sequestered material.[5] Although both ZF5.3[5] and ZF5.3-DHFR localize primarily within the lumen of Lamp1+ endolysosomes when evaluated using confocal microscopy (Fig. S2.12a), TauSTED microscopy of ZF5.3-DHFR^{Rho} treated cells (Fig. S2.12b) revealed fluorescent populations that resemble intraluminal vesicles (ILVs, Fig. S10c). ILVs are a critical component of multivesicular bodies, and it is possible that HOPS-catalyzed fusion events enable ZF5.3 and ZF5.3-DHFR to interact with ILVs in a manner that facilitates endosomal release. Notably, at super-resolution the fluorescent sub-populations all appear near endolysosomal membranes (Fig. S2.12c), suggestive of membrane interactions that facilitate endosomal release along a concentration gradient into the cytosol. Precisely how luminal ZF5.3-DHFR communicates with HOPS to ultimately cross the endosomal membrane, and whether this mechanism proceeds through an ILV-related pathway, is an area of active investigation.

2.4 Conclusions and Discussion

Here we describe design rules for efficient endosomal escape of cargo proteins conjugated to the cell-permeant miniature protein ZF5.3. We find that the efficiency of ZF5.3-mediated protein delivery to the cytosol is highest when the protein cargo readily unfolds under physiological conditions. Similar findings that low thermodynamic stability enhances intracellular delivery have been reported for toxin-mediated delivery of DARPins[61] and even cytosolic penetration of antisense oligonucleotides,[62] suggesting that the relationship between folding and endosomal escape may apply broadly to the passage of therapeutic macromolecules across cellular membranes.

Other groups have demonstrated that additional biophysical features, such as surface charge (measured by isoelectric point, pI) and molecular weight (MW), influence

intracellular protein delivery.[46,47,63] Our results strongly suggest that thermal stability is the most significant predictor of efficient endosomal escape, especially through a HOPS-dependent portal. This point is highlighted first by the observation that two ZF5.3-protein conjugates with equal thermal stabilities but very different molecular weights, ZF5.3-AS (200 kD) and ZF5.3-AGT54 (24 kD), are delivered with equal efficiencies (defined as the concentration established in the cytosol divided by the treatment concentration, Fig. 2.6). Conversely, two ZF5.3-protein conjugates with equal molecular weights but different thermal stabilities, ZF5.3-SNAP (T_m = 50°C) and ZF5.3-GE-AGT (T_m = 35°C), are not delivered equally; the low-T_m protein is delivered efficiently (40%) whereas the high-T_m protein is not (11%) (Fig. 2.6).

a

	Protein	[Deliv.]/ [Treat.]	MW	pI	T_m (pH 7)
	APEX-2[7]	1.7%	31.7	6.8	Unknown
	SNAP	5.5 -11.7%	23.3	8.6	50
	AS[8]	3.5 -12%	200	8.8	46.7
	NS1	12.3-13.4%	16.0	9.2	70
	AGT54	6.4-13.9%	24.3	8.8	46
	GE-AGT	13.3-40%	24.3	8.8	35
	ZF5.3[4,5]	25 -70.1%	3	11.4	Unknown
	DHFR	43.3-72.4%	26.1	9.4	32.7
	MeCP2[6]	18.1-84.4%	31.9	10.9	Disord.

b

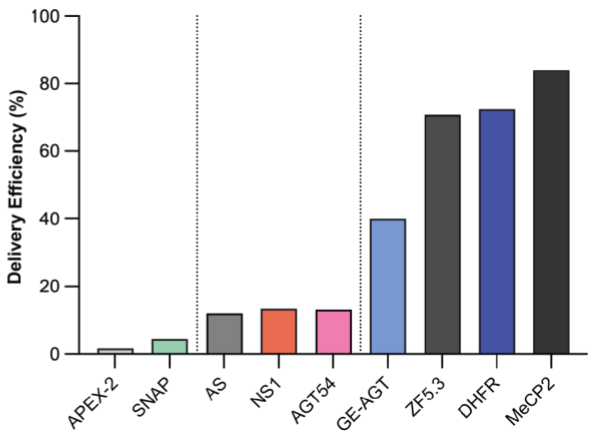

Figure 2.6. Efficient delivery of covalent ZF5.3 conjugates correlates directly with melting temperature. (A) Biophysical parameters and delivery efficiency for ZF5.3 alone (dark gray) or when conjugated to protein cargos. Delivery efficiency is defined as the concentration that reaches the cytosol (or nucleus, for MeCP2) divided by the treatment concentration; range is reported for all conditions tested. Molecular weight (MW) is defined in kilodaltons, pI is the isoelectric point, and T_m is the melting temperature, determined experimentally when conjugated to ZF5.3. **(B)** Graphical representation of the maximal delivery efficiency for ZF5.3-tagged cargos listed in (a). Proteins with high T_m that are larger than 20 kD are delivered with the lowest efficiency. Proteins with a T_m ~46, or a high T_m but small molecular weight, are delivered with mid-range efficiency. Only proteins with a T_m <35°C or that are intrinsically disordered are delivered with the highest efficiency.

We find that a low MW and high cationic charge can partially compensate for an unfavorably high T_m to improve cytosolic localization, as observed for NS1-ZF5.3; however, these attributes are insufficient to drive efficient delivery to the levels seen with intrinsically disordered or low-T_m cargo proteins. A close examination of our studies using NS1-ZF5.3 reveal two key patterns that further suggest delivery depends more on thermal stability than size or surface charge (Fig. 2.6). First, although the cytosolic concentrations established by NS1-ZF5.3 (T_m = 73°C) and ZF5.3-AGT54 (T_m = 46°C) are similar, the overall uptake as measured by flow cytometry is different. The uptake of NS1-ZF5.3 is high, presumably because it possesses a higher pI, whereas the uptake of ZF5.3-AGT54 is relatively low. Thus, although NS1-ZF5.3 and ZF5.3-AGT54 reach the cytosol equivalently, the degree of endosomal escape is much higher for the low-T_m ZF5.3-AGT54. Secondly, when comparing NS1-ZF5.3 (T_m = 73°C) with ZF5.3-DHFR (T_m =

32°C), the total amount of endocytosed protein is nearly equal (indeed, the pI of both proteins are almost identical), but the fraction of ZF5.3-DHFR that reaches the cytosol is >3-fold higher. These comparisons suggest that cationic charge may stimulate overall uptake, but the efficiency of endosomal escape is highest for low-T_m proteins regardless of size or charge, at least when conjugated to ZF5.3.

There are dozens of annotated proteins with T_m values comparable to those chosen in this study[64] and hundreds of proteins containing >40% intrinsic disorder.[65] Protein engineering efforts to introduce pH- or temperature-dependent destabilizing mutations into otherwise ideal therapeutic candidates to improve ZF5.3-mediated delivery, such as NS1, may be a viable strategy to enhance delivery efficiency. The observation that ZF5.3-mediated endosomal escape is most efficient when conjugated to low-T_m proteins, and that this pathway demands communication between luminal ZF5.3 and cytosol-facing HOPS, suggests the existence of a selective portal through which membrane transport occurs. In nearly all cases, nature mediates such transport via a proteinaceous channel embedded within the membrane, such as the recently reported perforin-2 channel in dendritic cells.[66] Whether ZF5.3 accomplishes its escape via lipid interactions or makes use of a yet-undetected protein channel remains under active investigation. Regardless, the results of this study provide clear biophysical guidelines to promote endosomal escape of ZF5.3-tagged cargos and can be applied to the development and expansion of novel protein therapies.

2.5 Supplementary Figures 1-12

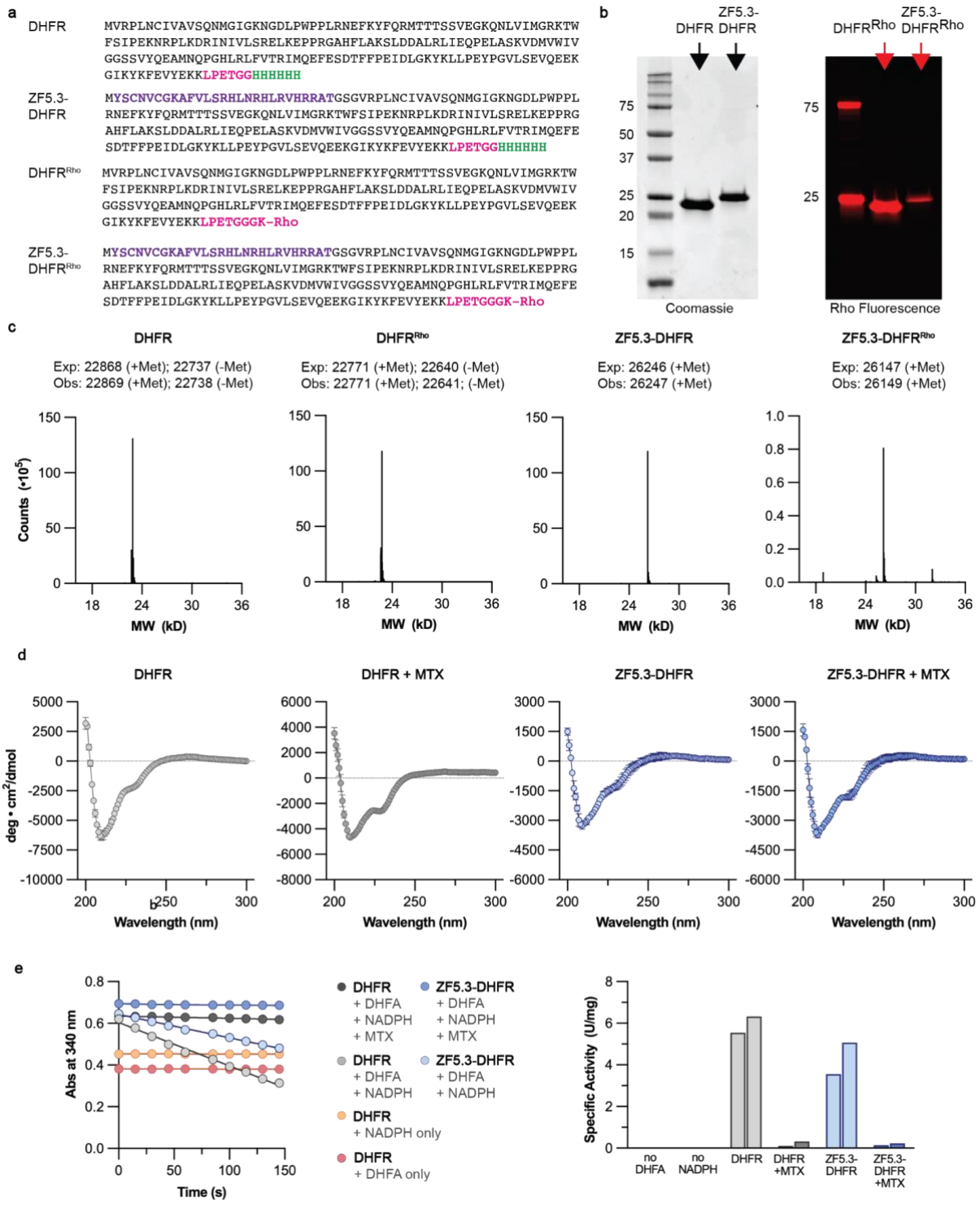

Figure S2.1. Purification and characterization of DHFR, ZF5.3-DHFR, and rhodamine-tagged variants. (A) DHFR proteins used in this study comprised the complete sequence of murine DHFR with or without a ZF5.3 module (purple, 27 aa) appended to the N-terminus. All proteins also contained a His6 tag for affinity purification (green) and a C-terminal LPETGG sortase recognition motif (magenta) to enable

subsequent labeling with rhodamine, as described previously[6–8] and in Methods; see also **Table 2.6.13**. **(B)** SDS-PAGE analysis of purified DHFR, ZF5.3-DHFR, $DHFR^{Rho}$ and ZF5.3-$DHFR^{Rho}$, with proteins visualized either using Coomassie stain or fluorescence imaging. Labeling efficiency ranged between 9 and 88%. **(C)** LC/MS analysis of all DHFR proteins confirms the correct identity of each. For DHFR and $DHFR^{Rho}$, prominent peaks were observed for the protein +/- the N-terminal methionine residue. **(D)** Wavelength-dependent circular dichroism (CD) analysis of DHFR and ZF5.3-DHFR (20 µM) at room temperature in a buffer composed of 25 mM Tris, 150 mM KCl, pH 7.2 and in the presence and absence of 1 equivalent methotrexate (MTX). Spectra were collected between 200 and 300 nm at 1 nm intervals with an averaging time of 5 seconds. Data shown are from at least two biological replicates and are represented as mean ± SEM. **(E)** All purified DHFR proteins retain catalytic activity. DHFR catalyzes the reduction of dihydrofolate (DHFA) to tetrahydrofolate (THFA) using NADPH as an electron donor. Plot on left illustrates the time-dependent loss in NADPH absorbance at 340 nm of solutions containing the indicated components. Conversion of DHFA to THFA occurs only when all reaction components are present; activity is abolished when (1) MTX is present (dark gray and dark blue), (2) DHFA is missing (orange), or (3) NADPH is missing (pink). Absorbance plot on left is representative of two activity assays performed on separate batches of protein. Plot on right shows the specific activity calculated in units per mg of protein for the same six conditions. Each bar represents activity from a separate batch of purified protein. One unit will convert 1.0 µmol of DHFA to THFA in 1 minute at pH 7.5 at room temperature.

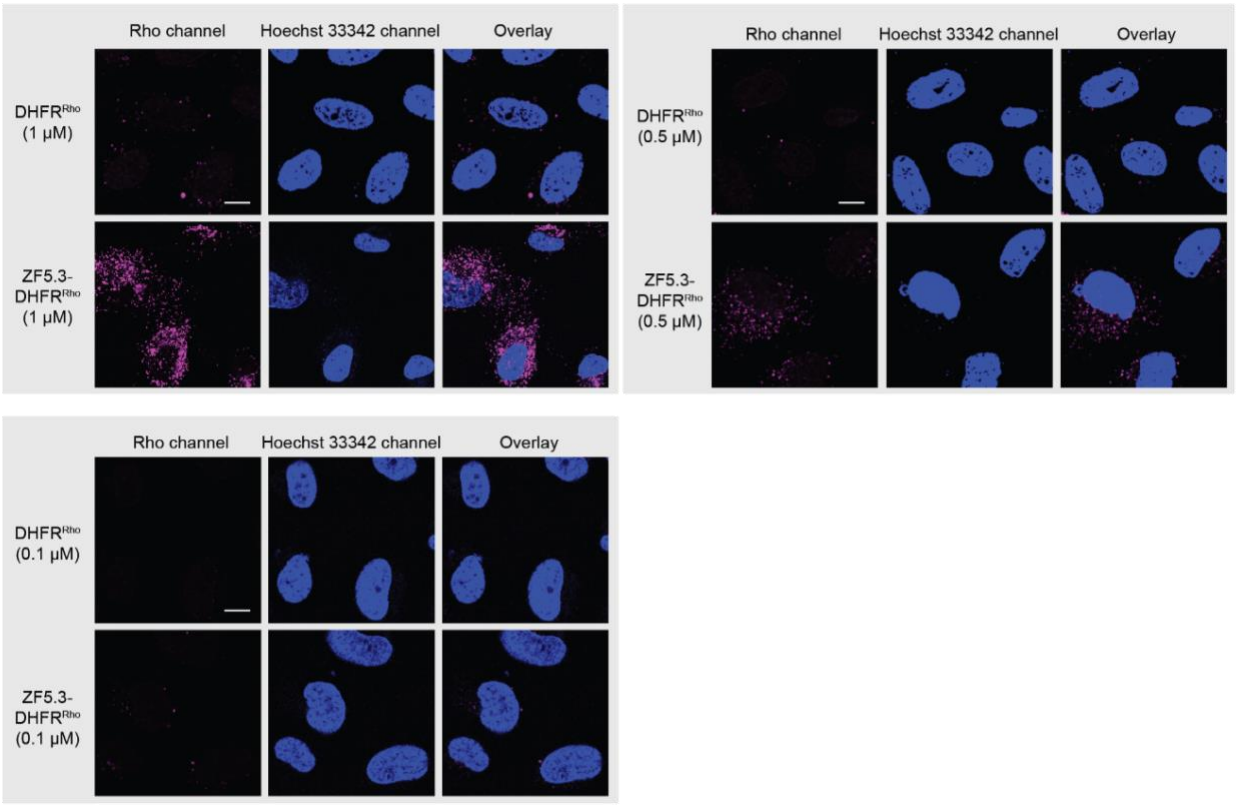

Figure S2.2. 2D confocal microscopy images depicting total intracellular fluorescence of Saos-2 cells treated with DHFR^{Rho} and ZF5.3-DHFR^{Rho}. Saos-2 cells were incubated with the given concentration of DHFR^{Rho} or ZF5.3-DHFR^{Rho} for 1 h, followed by three DPBS washes and trypsinization to remove exogenous protein. Cells were then replated in a fibronectin-coated 8-well microscopy dish and visualized using confocal microscopy. Nuclear fluorescence was detected by adding 300 nM Hoechst 33342 for the final 5 minutes of the protein incubation period. The results shown are representative of at least two biological replicates. Scale bar = 10 μm.

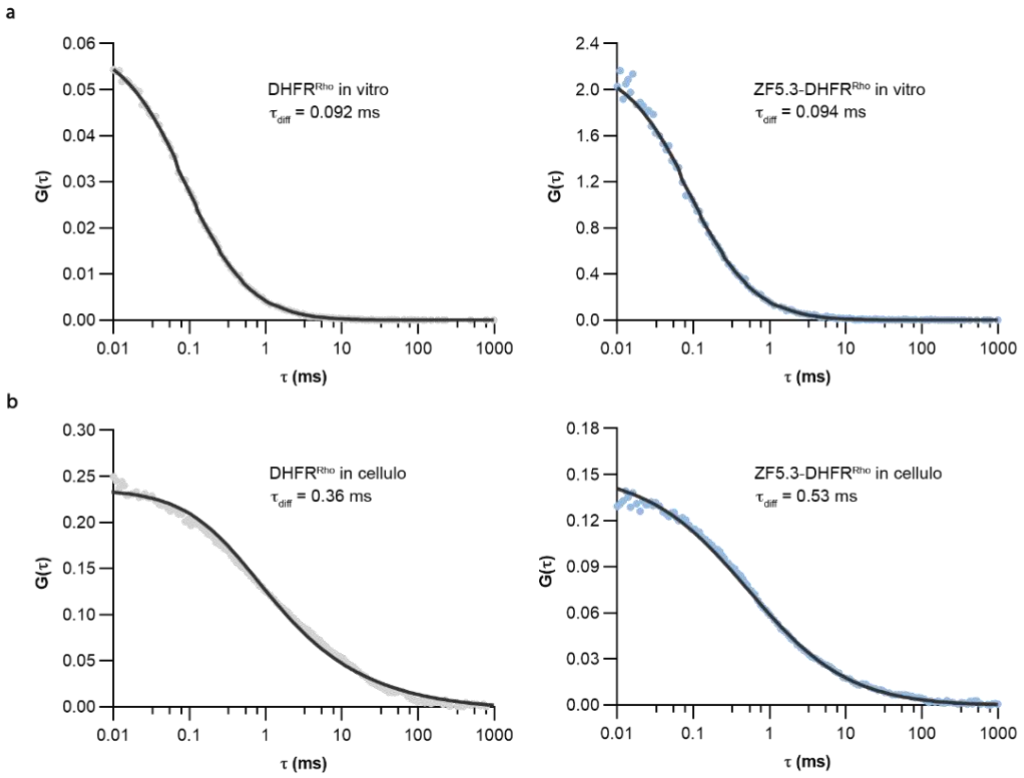

Figure S2.3. Autocorrelation traces generated during FCS analysis of DHFR^{Rho} and ZF5.3-DHFR^{Rho} *in vitro* and in Saos-2 cells. (A) Autocorrelation traces generated for *in vitro* samples of 100-500 nM DHFR^{Rho} and ZF5.3-DHFR^{Rho} in DMEM cell media are shown. All traces were fitted to a 3D diffusion model (solid dark curve) to obtain *in vitro* diffusion times (t_{diff}) as described in Methods. **(B)** Representative autocorrelation traces of Saos-2 cells treated with 500 nM DHFR^{Rho} and ZF5.3-DHFR^{Rho} for 1 h. Traces were fitted using a 3D anomalous diffusion model as previously described[3] to obtain *in cellula* diffusion times. *In cellula* diffusion times are longer than those *in vitro* due to increased viscosity and impaired diffusion in the cytosol.

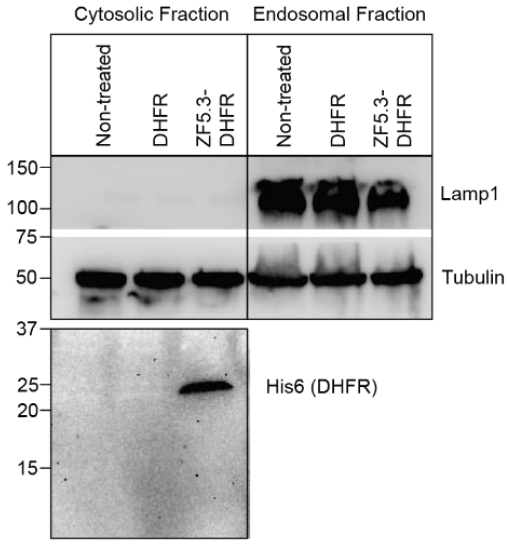

Figure S2.4. Cytosolic fractionation of cells treated with DHFR and ZF5.3-DHFR. Western blot analysis was performed for cytosolic or endosomal fractions isolated from Saos-2 cells treated with clear McCoy's media alone (non-treated) or 1 μM DHFR or ZF5.3-DHFR for 1 hour. After treatment, cells were lysed and the cytosol was isolated by ultracentrifugation at 350 kg for 1 h; see Methods for detailed cytosolic fractionation procedure. Western blot was performed with antibodies against endocytic (Lamp1) and cytosolic (tubulin) markers for both the endosomal and cytosolic fractions. Gel results are representative of two biological replicates.

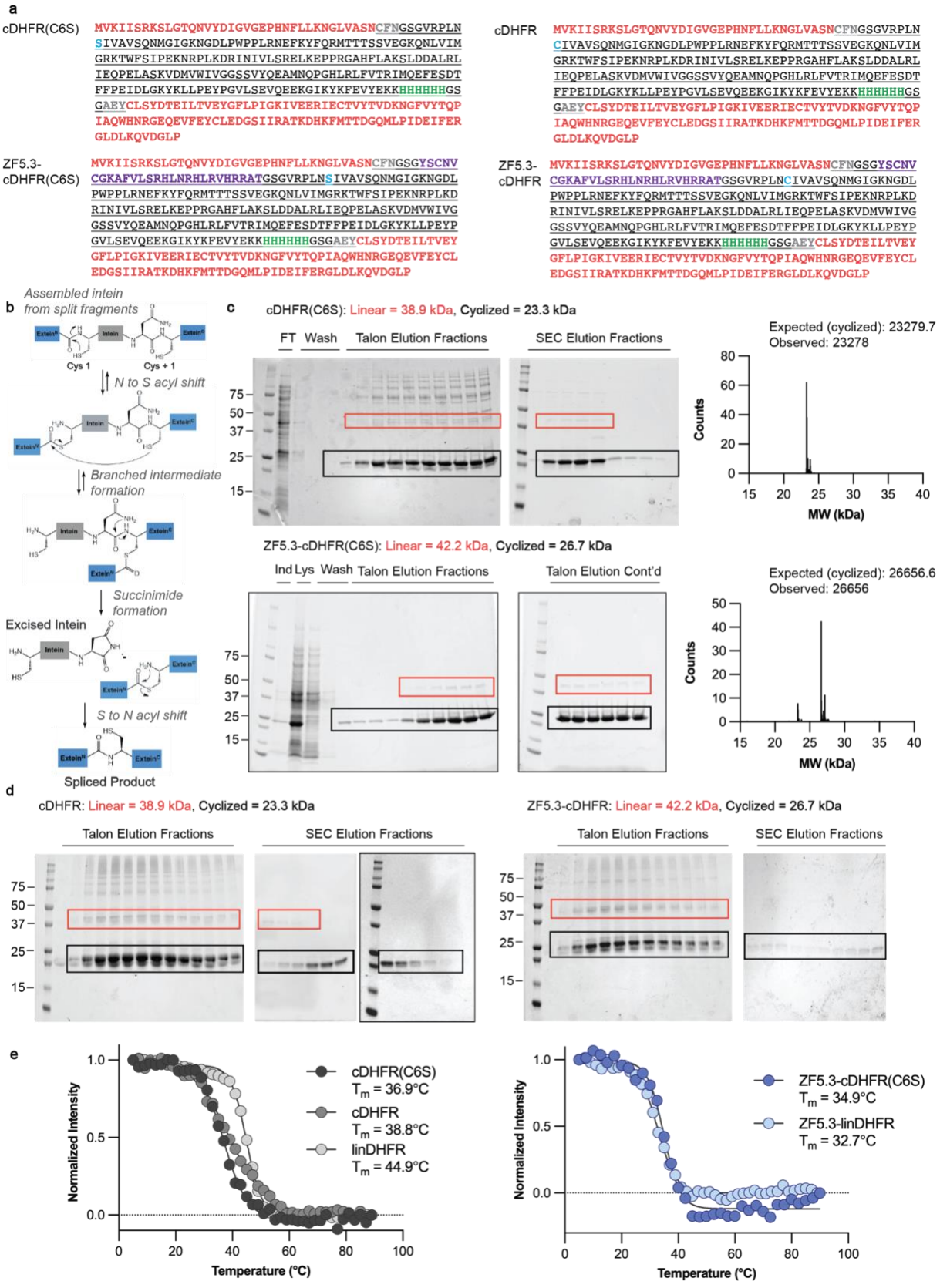
a
cDHFR(C6S) MVKIISRKSLGTQNVYDIGVGEPHNFLLKNGLVASNCFNGSGVRPLN SIVAVSQNMGIGKNGDLPWPPLRNEFKYFQRMTTTSSVEGKQNLVIM GRKTWFSIPEKNRPLKDRINIVLSRELKEPPRGAHFLAKSLDDALRL IEQPELASKVDMVWIVGGSSVYQEAMNQPGHLRLFVTRIMQEFESDT FFPEIDLGKYKLLPEYPGVLSEVQEEKGIKYKFEVYEKKHHHHHHGS GAEYCLSYDTEILTVEYGFLPIGKIVEERIECTVYTVDKNGFVYTQP IAQWHNRGEQEVFEYCLEDGSIIRATKDHKFMTTDGQMLPIDEIFER GLDLKQVDGLP
cDHFR MVKIISRKSLGTQNVYDIGVGEPHNFLLKNGLVASNCFNGSGVRPLN CIVAVSQNMGIGKNGDLPWPPLRNEFKYFQRMTTTSSVEGKQNLVIM GRKTWFSIPEKNRPLKDRINIVLSRELKEPPRGAHFLAKSLDDALRL IEQPELASKVDMVWIVGGSSVYQEAMNQPGHLRLFVTRIMQEFESDT FFPEIDLGKYKLLPEYPGVLSEVQEEKGIKYKFEVYEKKHHHHHHGS GAEYCLSYDTEILTVEYGFLPIGKIVEERIECTVYTVDKNGFVYTQP IAQWHNRGEQEVFEYCLEDGSIIRATKDHKFMTTDGQMLPIDEIFER GLDLKQVDGLP
ZF5.3-cDHFR(C6S) MVKIISRKSLGTQNVYDIGVGEPHNFLLKNGLVASNCFNGSGYSCNV CGKAFVLSRHLNRHLRVHRRATGSGVRPLNSIVAVSQNMGIGKNGDL PWPPLRNEFKYFQRMTTTSSVEGKQNLVIMGRKTWFSIPEKNRPLKD RINIVLSRELKEPPRGAHFLAKSLDDALRLIEQPELASKVDMVWIVG GSSVYQEAMNQPGHLRLFVTRIMQEFESDTFFPEIDLGKYKLLPEYP GVLSEVQEEKGIKYKFEVYEKKHHHHHGSGAEYCLSYDTEILTVEY GFLPIGKIVEERIECTVYTVDKNGFVYTQPIAQWHNRGEQEVFEYCL EDGSIIRATKDHKFMTTDGQMLPIDEIFERGLDLKQVDGLP
ZF5.3-cDHFR MVKIISRKSLGTQNVYDIGVGEPHNFLLKNGLVASNCFNGSGYSCNV CGKAFVLSRHLNRHLRVHRRATGSGVRPLNCIVAVSQNMGIGKNGDL PWPPLRNEFKYFQRMTTTSSVEGKQNLVIMGRKTWFSIPEKNRPLKD RINIVLSRELKEPPRGAHFLAKSLDDALRLIEQPELASKVDMVWIVG GSSVYQEAMNQPGHLRLFVTRIMQEFESDTFFPEIDLGKYKLLPEYP GVLSEVQEEKGIKYKFEVYEKKHHHHHGSGAEYCLSYDTEILTVEY GFLPIGKIVEERIECTVYTVDKNGFVYTQPIAQWHNRGEQEVFEYCL EDGSIIRATKDHKFMTTDGQMLPIDEIFERGLDLKQVDGLP
b
Assembled intein from split fragments
Cys 1
Cys + 1
N to S acyl shift
Branched intermediate formation
Succinimide formation
Excised Intein
S to N acyl shift
Spliced Product
c
cDHFR(C6S): Linear = 38.9 kDa, Cyclized = 23.3 kDa
FT Wash Talon Elution Fractions
SEC Elution Fractions
Expected (cyclized): 23279.7
Observed: 23278
Counts
MW (kDa)
ZF5.3-cDHFR(C6S): Linear = 42.2 kDa, Cyclized = 26.7 kDa
Ind Lys Wash Talon Elution Fractions
Talon Elution Cont'd
Expected (cyclized): 26656.6
Observed: 26656
d
cDHFR: Linear = 38.9 kDa, Cyclized = 23.3 kDa
Talon Elution Fractions
SEC Elution Fractions
ZF5.3-cDHFR: Linear = 42.2 kDa, Cyclized = 26.7 kDa
e
Normalized Intensity
Temperature (°C)
cDHFR(C6S) Tm = 36.9°C
cDHFR Tm = 38.8°C
linDHFR Tm = 44.9°C
ZF5.3-cDHFR(C6S) Tm = 34.9°C
ZF5.3-linDHFR Tm = 32.7°C

Figure S2.5. Purification and characterization of cyclized DHFR variants via SDS-PAGE, LC/MS, and circular dichroism. (A) The sequences chosen for this study were adapted from the literature[38] and included an N-terminal Cfa_{GEP} split intein (coral), a CFN extein sequence required for efficient splicing (gray), a GSG linker, the ZF5.3 sequence if included (purple) followed by another GSG linker, the murine DHFR sequence with or without a C6S mutation (blue), a C-terminal His6 tag for affinity purification (green), a GSG linker, an AEY extein sequence required for efficient splicing (gray), and the C-terminal portion of the Cfa_{GEP} split intein (coral). The final cyclized protein sequence (containing an accessible Cys from the CFN extein sequence for fluorophore labeling) is underlined. **(B)** Chemical mechanism for intein-mediated protein splicing. Figure adapted from permission from Ref.[38] **(C)** SDS-PAGE gels (visualized via Coomassie stain) and LC/MS traces for the purification of cDHFR (C6S) and ZF5.3-cDHFR (C6S). cDHFR(C6S) was purified by Talon resin followed by size exclusion chromatography (SEC), whereas ZF5.3-cDHFR (C6S) was purified only with Talon resin. Black boxes are used to designate the cyclized protein, and orange boxes are used to denote the linear protein. FT = Talon resin flowthrough; Ind = induced culture; Lys = clarified lysate. **(D)** SDS-PAGE gels (visualized via Coomassie stain) showing the purification of cDHFR and ZF5.3-cDHFR without the C6S mutation. Both proteins were purified by Talon resin followed by SEC. Black boxes designate cyclized protein, and orange boxes show linear protein. **(E)** Temperature- dependent CD analysis of cyclized vs non-cyclized DHFR proteins. CD was performed in a buffer composed of 20 mM Tris, 150 mM KCl pH 7.5. Measurements were recorded between 5-90ºC in 2ºC increments at 210 nm. Data shown are from between one and two biological replicates and are represented as mean ± SEM. Non-ZF5.3-tagged variants are shown on the left (gray tones) and ZF5.3-tagged DHFR variants are shown on the right (blue tones). LinDHFR corresponds to the original DHFR and ZF5.3-DHFR temperature melt data depicted in Fig. 2.2b.

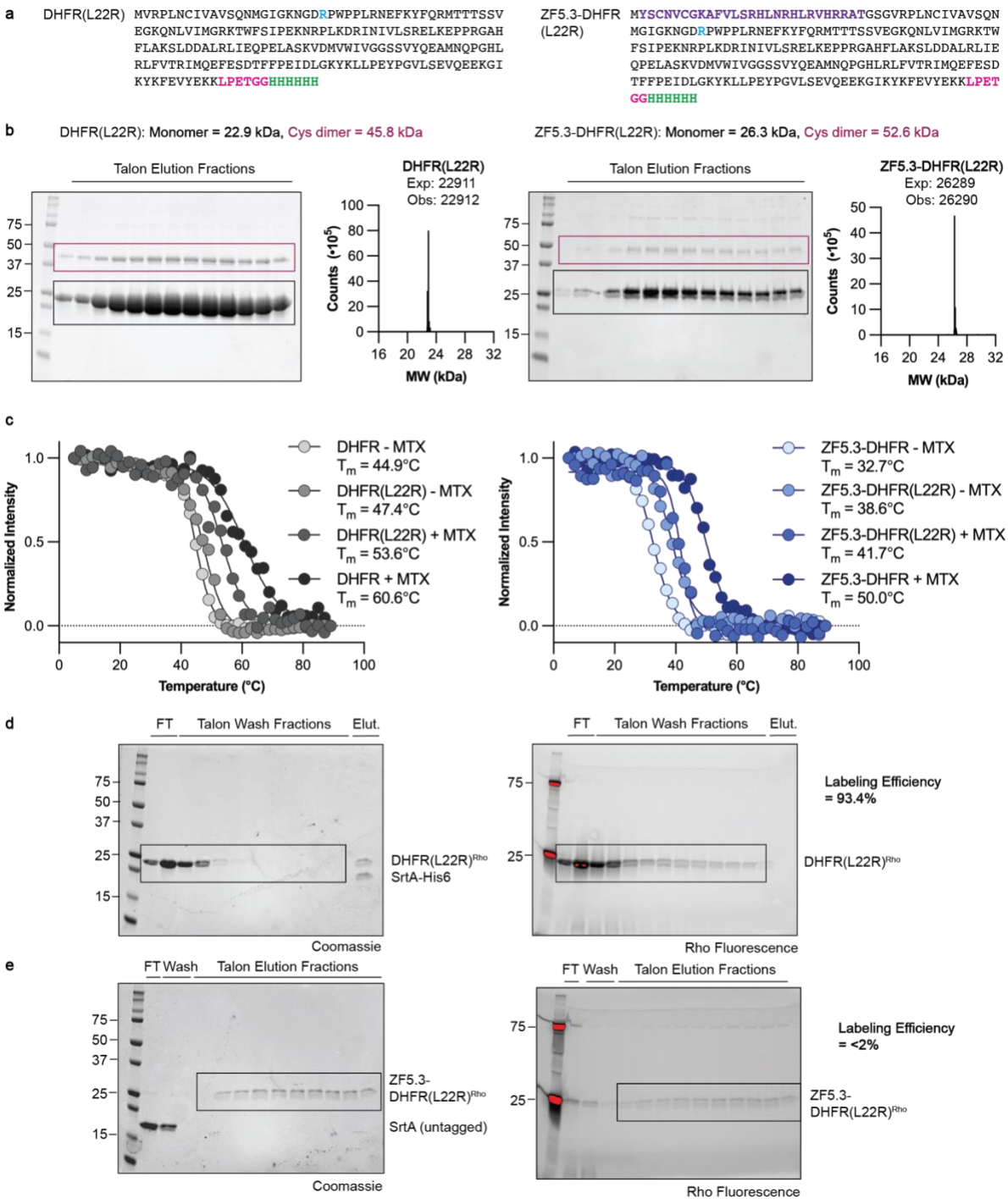

Figure S2.6. Purification and characterization of MTX-resistant DHFR variants via SDS-PAGE, LC/MS, and circular dichroism. (A) The sequences chosen for this study comprised the complete sequence of murine DHFR with a L22R mutation to confer methotrexate (MTX) resistance[39] (blue), with or without a ZF5.3 module (purple), appended to the N-terminus. All proteins also contained a His6 tag (green) for affinity purification and a C-terminal LPETGG sortase recognition motif (magenta) for subsequent rhodamine labeling. **(B)** SDS-PAGE gels (visualized via Coomassie stain) and LC/MS traces for the purification of DHFR(L22R) and ZF5.3-DHFR(L22R). Black boxes denote protein at the correct molecular

weight. Purple boxes denote a likely dimer formed by cysteine oxidation; higher molecular weight band disappeared upon incubation with reducing agent (data not shown). **(C)** Temperature- dependent CD analysis of wildtype and L22R DHFR and ZF5.3-DHFR proteins in the presence and absence of MTX. CD was performed in a buffer composed of 20 mM Tris, 150 mM KCl pH 7.5. Measurements were recorded between 5-90ºC in 2ºC increments at 210 nm. Data shown are from between one and two biological replicates and are represented as mean ± SEM. **(D)** and **(E)** SDS-PAGE gels visualized by Coomassie stain (left) or rhodamine fluorescence (right) showing the sortase-mediated fluorescent labeling of **(D)** DHFR(L22R) or **(E)** ZF5.3-DHFR(L22R); see Methods for more details. FT = Talon flowthrough, Elut = Talon elution. Black box denotes rho-labeled protein pooled for analysis. Labeling efficiency is calculated as the concentration of rhodamine-labeled protein (determined by absorbance at 570 nm) divided by the concentration of total protein.

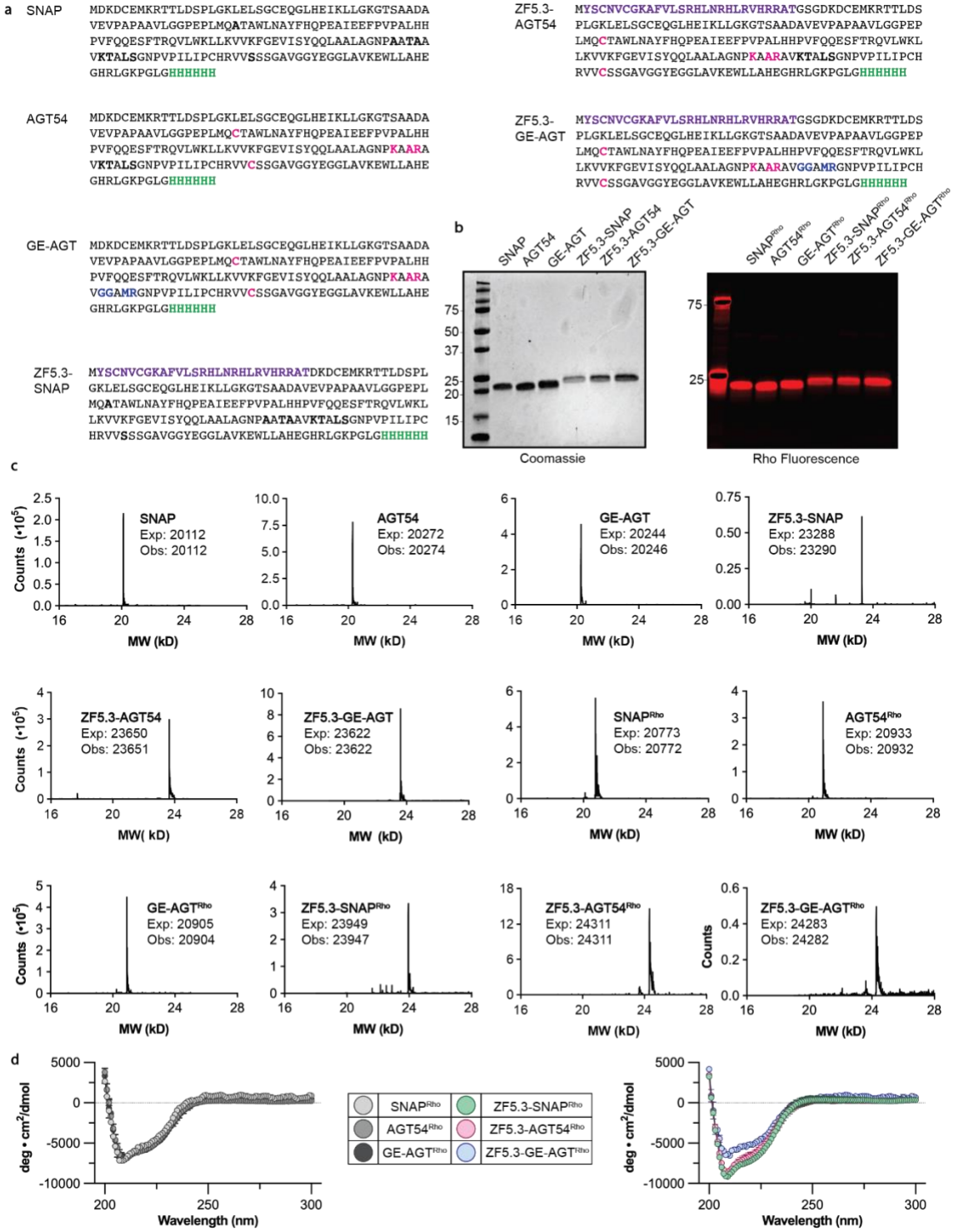

Figure S2.7. Purification and characterization of SNAP variants via SDS-PAGE, LC/MS, and circular dichroism. (A) The SNAP sequences chosen for this study were adapted from the literature[40] and modified with an N-terminal ZF5.3 moiety (purple) and a C-terminal His6 tag for affinity purification (green). Mutations introduced to AGT54 and GE-AGT to decrease thermostability are shown in magenta; mutations introduced only to GE-AGT are shown in blue; see also **Table 2.6.13**. All proteins were reacted with a lissamine rhodamine B dye derivatized with benzylguanine to enable fluorescent labeling, as previously described.[7]

(B) SDS-PAGE analysis of all purified variants with or without an attached rhodamine dye were visualized using Coomassie stain (for unlabeled proteins) or fluorescence imaging (for rhodamine-modified proteins). **(C)** LC/MS analysis confirmed the identity of all unlabeled and rhodamine-labeled proteins. Additional peaks for some samples with successive +98 Da molecular weights are observed due to sulfate adducts formed during ammonium sulfate precipitation. **(D)** Wavelength- dependent CD analysis of rho-labeled SNAP and ZF5.3-SNAP variants (20 µM) at room temperature in a buffer composed of 20 mM Tris, 150 mM NaCl pH 7.5. Measurements were recorded between 200 and 300 nm in 1 nm intervals with an averaging time of 5 seconds. Data shown are from at least two biological replicates and are represented as mean ± SEM.

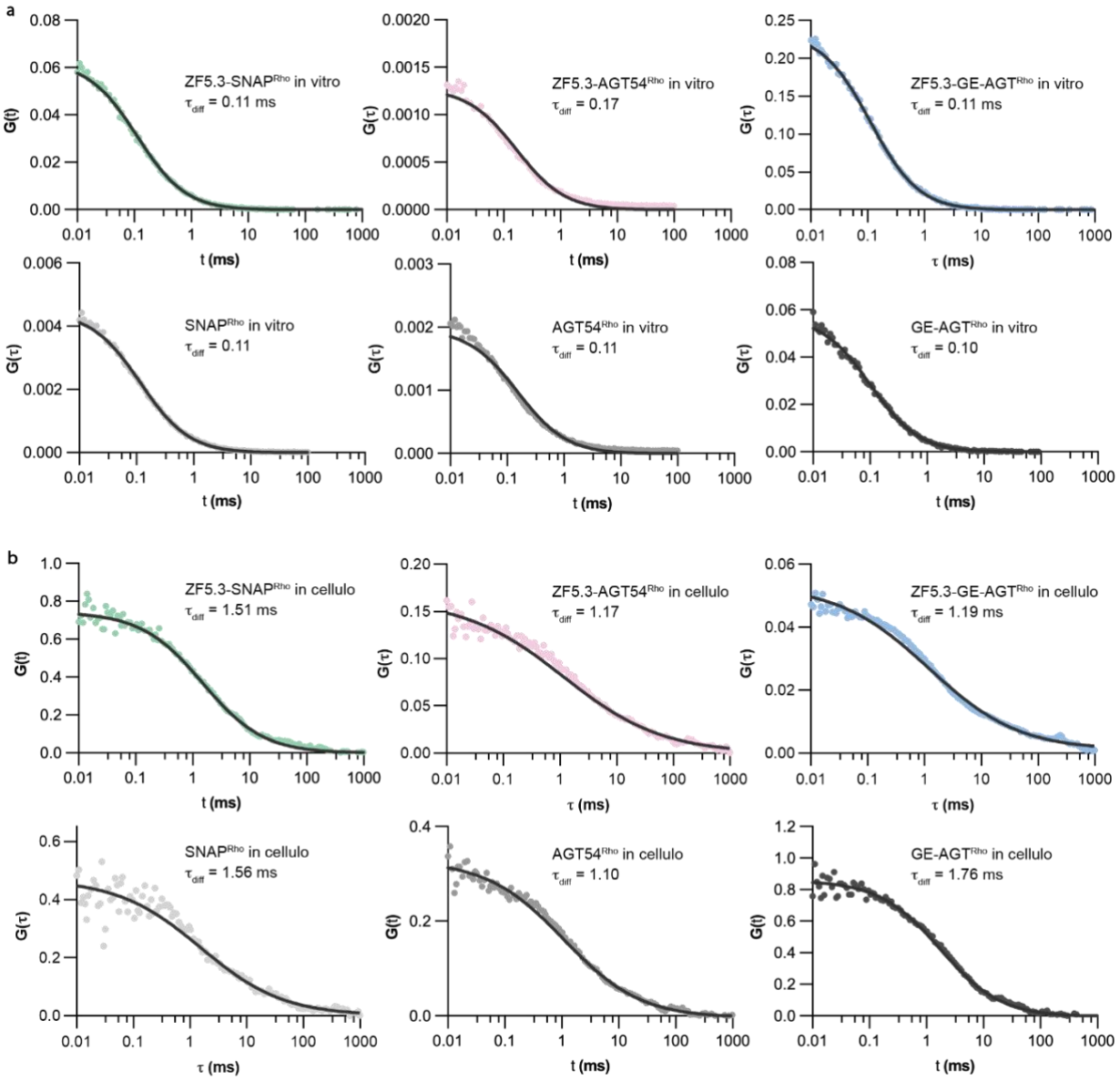

Figure S2.8. *In vitro* and *in cellula* autocorrelation traces for all SNAP^{Rho} variants. (A) *In vitro* autocorrelation traces for 50-150 nM SNAP^{Rho}, AGT54^{Rho}, GE-AGT^{Rho}, ZF5.3-SNAP^{Rho}, ZF5.3-AGT54^{Rho}, and ZF5.3-GE-AGT^{Rho} were collected in DMEM. All traces were fitted to a 3D diffusion model (solid dark curve) to obtain in vitro diffusion times (t_{diff}) as described in Methods. **(B)** Representative *in cellula* autocorrelation traces for Saos-2 cells treated with 1 µM of SNAP^{Rho}, AGT54^{Rho}, GE-AGT^{Rho}, ZF5.3-SNAP^{Rho}, ZF5.3-AGT54^{Rho}, or ZF5.3-GE-AGT^{Rho} for 0.5 - 2 h. Autocorrelation traces were fitted using a 3D anomalous diffusion model as described in Methods to obtain *in cellula* diffusion times. *In cellula* diffusion times are longer than those *in vitro* due to increased viscosity and impaired diffusion in the cytosol.

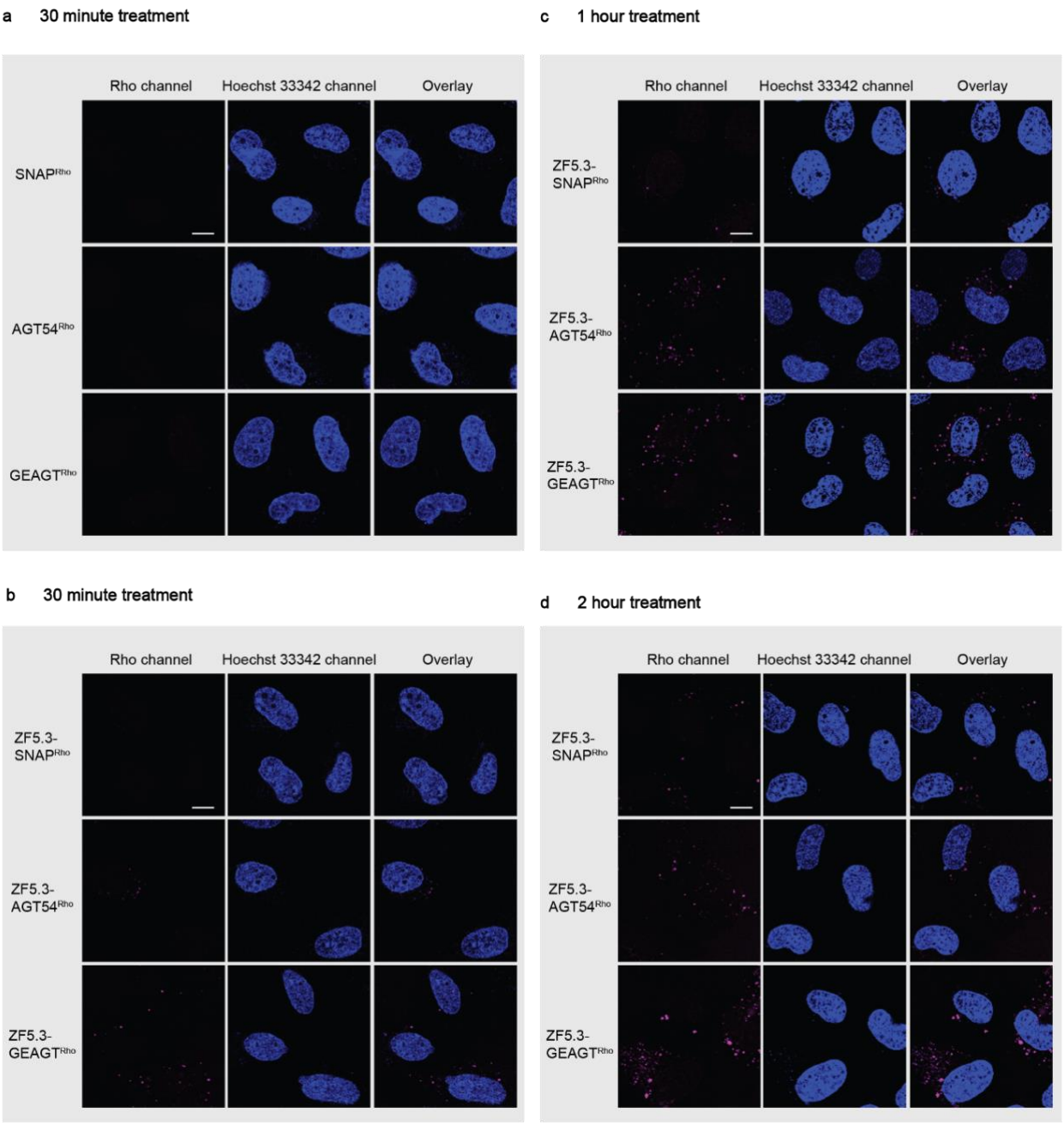

Figure S2.9. 2D confocal microscopy images depicting total intracellular fluorescence of cells treated with SNAP and ZF5.3-SNAP variants. Saos-2 cells were incubated with 1 µM of SNAP^{Rho}, AGT54^{Rho}, or GE-AGT^{Rho} for 30 min **(A)** or 1 µM of ZF5.3-SNAP^{Rho}, ZF5.3-AGT54^{Rho}, or ZF5.3-GE-AGT^{Rho} for 30 min **(B)**, 1 h **(C)**, or 2 h **(D)**, followed by three DPBS washes and trypsinization. Cells were then replated in a fibronectin-coated 8-well microscopy dish and visualized using confocal microscopy. Nuclei were detected by adding 300 nM Hoechst 33342 for the final 5 minutes of the incubation period. The results shown are representative of 2+ biological replicates. Scale bar = 10 µm.

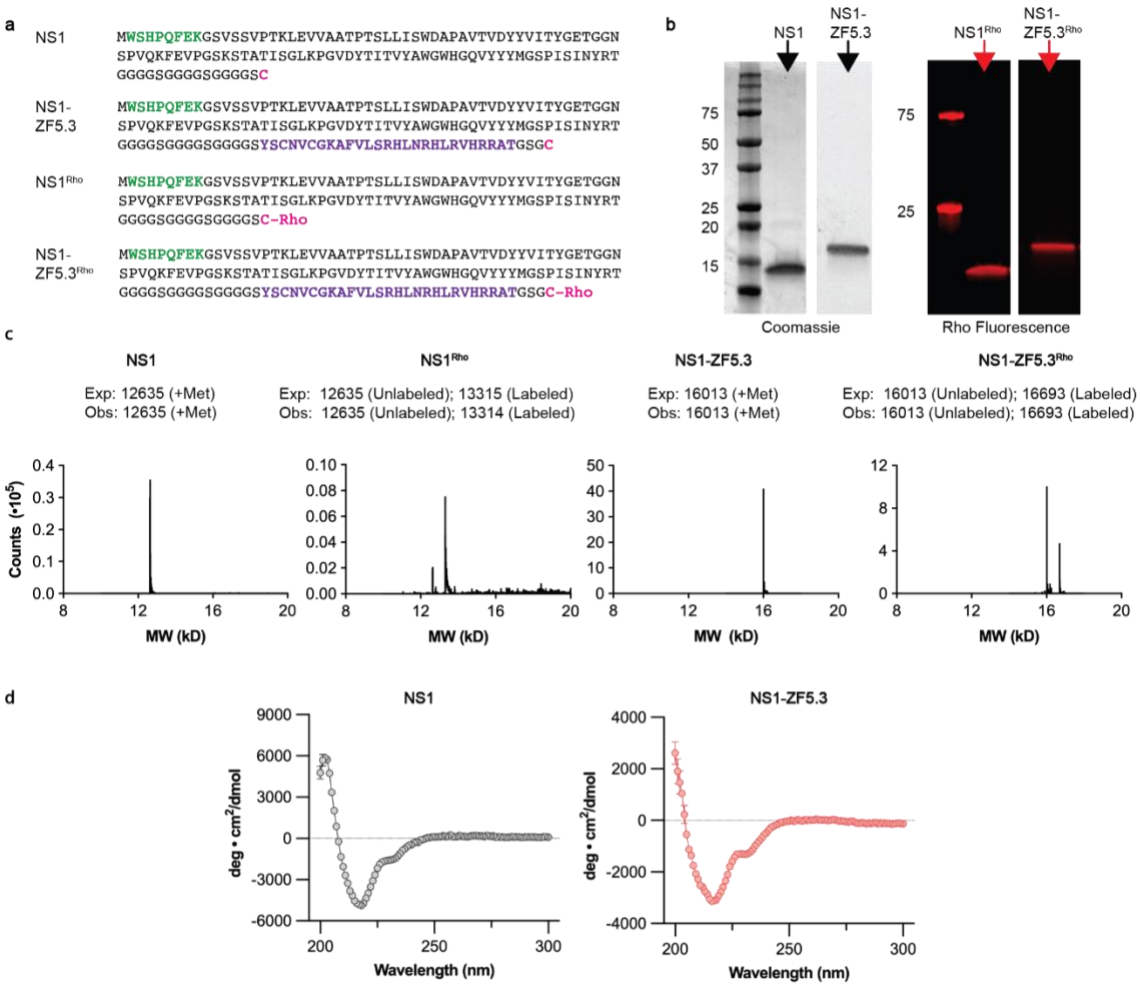

Figure S2.10: **Purification and characterization of NS1, NS1-ZF5.3, and rhodamine-tagged variants.** **(A)** NS1 proteins chosen for this work included the full-length published NS1 sequence[52] with or without ZF5.3 (purple, 27 aa). All proteins contained an N-terminal Strep-tag for affinity purification (green) and a C-terminal cysteine separated with a flexible linker for conjugation to a maleimide-linked rhodamine dye (magenta); see also **Table 2.6.13**. ZF5.3 was appended to the C-terminus of NS1 due to multiple unsuccessful purification attempts with ZF5.3 placed at the N-terminus. **(B)** SDS-PAGE analysis of purified NS1, NS1-ZF5.3, NS1^{Rho} and NS1-ZF5.3^{Rho}, with proteins visualized either using Coomassie stain (for unlabeled proteins) or fluorescence imaging (for rhodamine-labeled proteins). Labeling efficiency ranged between 20.9 and 50.0%. **(C)** LC/MS analysis confirmed the identity of NS1, NS1-ZF5.3, NS1^{Rho}, and NS1-ZF5.3^{Rho}. For NS1^{Rho} and NS1-ZF5.3^{Rho}, prominent peaks were observed for both the unlabeled and rhodamine-labeled species. **(D)** Wavelength-dependent CD spectra reveal no significant differences between the secondary structures of NS1 and NS1-ZF5.3. NS1 and NS1-ZF5.3 were measured at 18 µM in 20 mM Tris, 150 mM KCl, 0.5 mM TCEP pH 7.5. Measurements were recorded between 200 and 300 nm in 1 nm intervals with an averaging time of 5 seconds. Data shown are from two biological replicates and are represented as mean ± SEM.

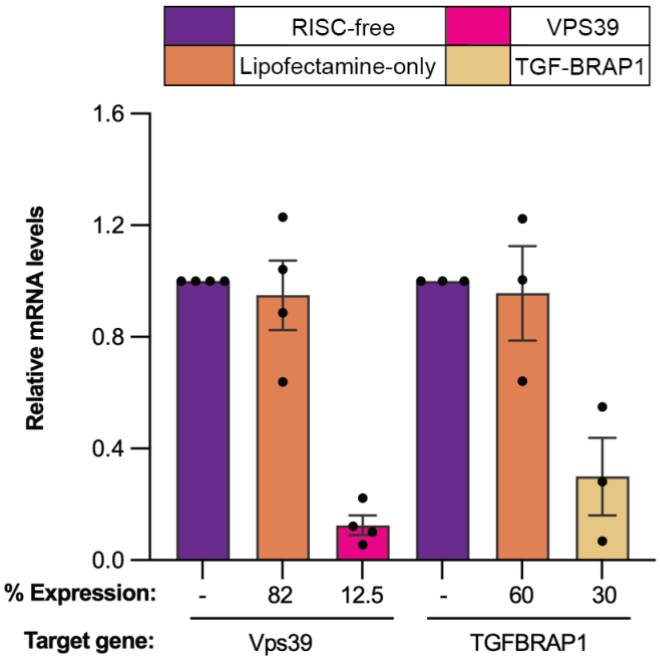

Figure S2.11. qPCR analysis of siRNA knockdowns. The gene expression level of VPS39 (HOPS complex subunit) and TGF-BRAP1 (CORVET complex subunit) was determined using RT-qPCR and compared to RISC-free and lipofectamine-only negative controls. Data are represented as mean ± SEM with three biological replicates.

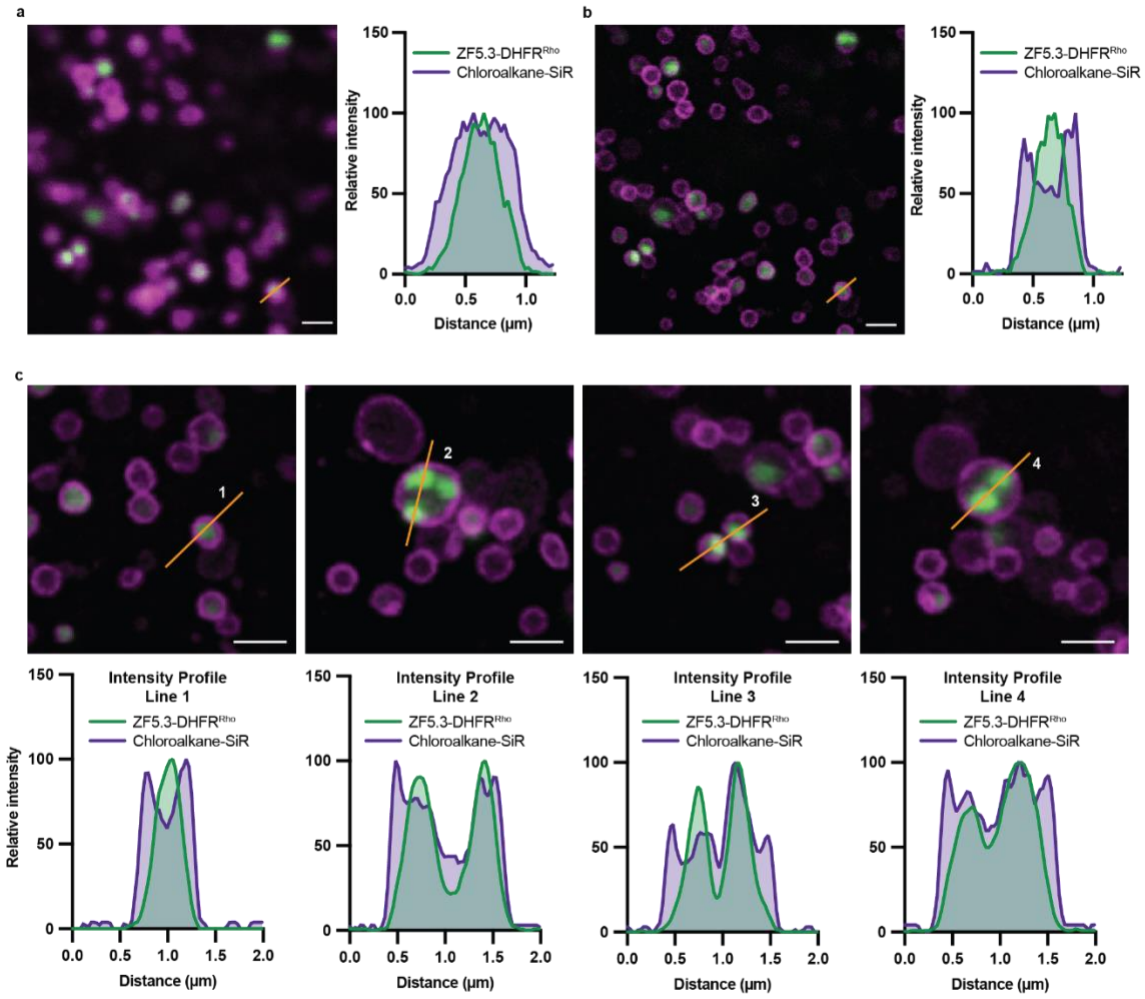

Figure S2.12. ZF5.3-DHFR^{Rho} localizes to the lumen of Lamp1+ vesicles. Saos-2 cells expressing a Lamp1-HaloTag construct tagged with chloroalkane-SiR were incubated with 0.5 µM ZF5.3-DHFR^{Rho} for 1 hour. Cells were then washed 3x with DPBS, trypsinized to remove exogenously bound protein, and replated in a fibronectin-coated 4-well microscopy dish. **(A)** Representative live-cell confocal microscopy images of Saos-2 cells. **(B)** TauSTED images depicting lumenal ZF5.3-DHFR^{Rho} within Lamp1+ vesicles. Representative fluorescence intensity line profile shows the relative position of emission from ZF5.3-DHFR^{Rho} (green) and Lamp1-HaloTag-SiR (purple), and demonstrates the superior resolution provided by TauSTED. **(C)** TauSTED images depicting sublocalization of ZF5.3-DHFRRho within Lamp1+ vesicles labelled with chloroalkane-SiR. Intensity profiles of lines in each images are graphed below to depict localization of signal from each channel. Scale bar = 1 µm.

2.6 Materials & Methods

2.6.1 Materials

Cell culture/Microscopy: SsoFast™ EvaGreen® Supermix (#1725200, BioRad); McCoy's 5A Medium without phenol red (#SH30270, Cytiva); all siRNAs (Dharmacon, **Table 2.6.13**); RT-qPCR primers (IDT, **Table 2.6.13**); 4-well #1.5H glass bottom coverslip (#80427, Ibidi); Lipofectamine RNAiMAX transfection reagent (#13778150, Invitrogen); Fibronectin bovine plasma (#F1141), Omni 0.5mL Tubes w/ 1.4mm Ceramic Beads (#19626) (Millipore Sigma); FuGENE HD transfection reagent (Promega, #E2311); Gibco™ Dulbecco's modified eagle medium (DMEM) without phenol red, high glucose, with 25 mM HEPES (#21063), Gibco™ GlutaMAX™ Supplement, 200 mM (#35050061), Gibco™ Sodium Pyruvate, 100 mM (#11360070), Gibco™ TrypLE Express Enzyme (1x) with (#12605010) and without (#12604013) phenol red, McCoy's 5a Medium (#16600082), Nunc™ Lab-Tek™ 8-well Chambered Coverglass (#155411) (Thermofisher Scientific); Saos-2 cell stock (UC Berkeley Cell Culture Facility).

Cell lines & plasmids: CMV-LAMP1-HaloTag plasmid (#164209, Addgene); *E. coli* BL21(DE3) competent cells (#230132) and *E. coli* BL21-CodonPlus(DE3)-RP cells (#230255) (Agilent); all synthetic gBlocks (IDT, **Table 2.6.13**); pet-32a(+) vector (Millipore Sigma, #69015).

Chemicals: O6-(4-Aminomethyl-benzyl)guanine (#12560, AAT Bioquest); Isopropyl β-D-thiogalactopyranoside (#367-93-1, American Bio); Ammonium Chloride (#A9434), Biotin (#B4501), Calcium Chloride (#C5670), Fmoc-Gly-OH (#47627), Fmoc-Lys(Mtt)-OH (#852065), Glucose (#G5767), Lissamine Rhodamine B Sulfonyl Chloride (#86186), M9 Minimal Salts 5x (#M6030), Magnesium Sulfate (#M2643), N,N-Diisopropylethylamine (#387649), Potassium Chloride (#P3911), Sodium Chloride (#S9888) (Millipore Sigma); Lissamine Rhodamine B C2 Maleimide (Tenova, #T01196); 1M Tris-HCl buffer pH 7.5 (#15567027), Ammonium Sulfate (#011566), Glycerol (#J61059), Imidazole (#A10221), Invitrogen Alexa Fluor™ 594 hydrazide (#A10438), Rhodamine Red™ C2 Maleimide (#R6029), Thiamine Hydrochloride (#148990100), Tris (2-Carboxyethyl) Phosphine Hydrochloride (#50-153-2844) (Thermofisher Scientific).

Molecular biology reagents: α-Tubulin Rabbit antibody (#2125S), Anti-rabbit IgG, HRP-linked Antibody (#7074S), His-tag Rabbit antibody (#2365S), Lamp1 XP® Rabbit antibody (#9091S) (Cell Signaling Technology); HiTrap® SP HP 5-mL column (#17115101), StrepTrap® HP 5-mL column (#28907547), PD-10 desalting columns (#17085101) (Cytiva); 3 kDa MWCO Amicon® Ultra-15 Centrifugal Filter Unit (#UFC90003), 10 kDa MWCO Amicon® Ultra-15 Centrifugal Filter Unit (#UFC9010), Benzonase® Nuclease HC (#71205), cOmplete, Mini EDTA-free protease inhibitor cocktail (#4693159001), ZipTips with 0.6 µL C4 resin (#ZTC04S008), 0.22 µm hydrophilic PVDF membrane filter (#SLGVR33RS, Millipore Sigma); NEBuilder® HiFi DNA Assembly Master Mix (#E2621L), Q5® High-Fidelity 2X Master Mix (#M0492S) (New England Biolabs); TALON® metal affinity resin (Takara, #635504); Pierce™ 660 nm Protein Assay Reagent

(#22660), Pierce™ BCA Protein Assay Kit (#23227), Pierce™ Universal Nuclease for Cell Lysis (#88700) (Thermofisher Scientific).

2.6.2 Plasmid construction

All gBlocks were codon-optimized for expression in E. coli B strain and ordered from Integrated DNA Technologies (IDT). The gBlocks for DHFR proteins encoded the DNA sequence for murine DHFR with or without an N-terminal ZF5.3 separated from the DHFR sequence with a glycine-serine-glycine (GSG) linker. MTX-resistant variants had a L22R substitution.[39] Wildtype and MTX-resistant sequences included a C-terminal LPETGG motif for sortase conjugation[6–8] followed by a His6 tag for affinity purification (Fig. S2.1a and S2.6a). The gBlocks for cyclized DHFR and ZF5.3-DHFR (cDHFR and ZF5.3-cDHFR) were designed with an N- and C-terminal split intein[38] separated from the extein equence with a GSG linker on either side, with or without a C6S mutation (Fig. S2.5a). gBlocks encoding AGT54 and GE-AGT[40] were designed with or without ZF5.3 at the N-terminus separated by a GSG linker and included a C-terminal His6 tag. The plasmids for SNAP-tag and ZF5.3-SNAP-tag were reported in a previous publication.[7] For NS1,[52] initial attempts to purify a variant with ZF5.3 at the N-terminus were unsuccessful and could not be optimized. gBlocks encoding the sequence for NS1 with or without a C-terminal ZF5.3 separated by a $(GGGGS)_3$ linker were designed with an N-terminal Strep tag for affinity purification and a C-terminal cysteine residue for fluorophore conjugation. All gBlocks were inserted into a pET-32a(+) backbone vector (Sigma) linearized with **Primers 1** and **2** using Gibson assembly. The identities of all plasmids were confirmed by Sanger and whole plasmid sequencing. Relevant DNA and protein sequences are listed in **Table 2.6.13**.

2.6.3 Protein expression and purification

The expression and purification protocols for all proteins used in this study are detailed below. For all expression steps, the cultures were grown in an incubator at the specified temperature with shaking at 200 rpm. The compositions of all buffers described in this section are listed in **Table 2.6.14**. Expression and purification of SNAP-tag proteins was performed in collaboration with Dr. Xizi Zhang. Expression and purification of NS1 proteins were performed by Angel Vázquez Maldonado.

<u>Expression and purification of DHFR proteins</u>

The plasmids encoding DHFR, DHFR(L22R), cDHFR(C6S), cDHFR, ZF5.3-DHFR, ZF5.3-DHFR(L22R), ZF5.3-cDHFR(C6S), and ZF5.3-cDHFR were transformed into E. coli BL21(DE3) competent cells and selected on an ampicillin (amp) LB agar plate. For each protein, one colony was used to inoculate a 20 mL overnight starter culture of

LB media supplemented with 100 µg/mL amp and incubated at 37°C. The next morning, the starter culture was added to 1 L of LB with 100 mg/L amp and incubated at 37°C until the optical density (OD_{600}) reached 0.6-0.8. Protein expression was induced with 1 mM IPTG and the cultures were transferred to 20°C for 20 h. All steps from this point forward were performed at 4°C. To harvest the cells, cultures were spun at 4300 g for 40 min and resuspended in 20 mL of ice-cold Lysis Buffer 1 supplemented with 1 cOmplete, mini EDTA-free protease inhibitor cocktail tablet and 1 µL of Pierce Universal Nuclease for Cell Lysis. Cells were lysed by sonication for 7 min total, pulsing for 30 s and recovering for 30 s for 7 cycles. The lysate was cleared by centrifugation at 18,000 rpm for 35 min and transferred to a 50 mL conical tube containing 2 mL of TALON® metal affinity resin pre-equilibrated with Wash Buffer 2. The lysate was incubated with the resin for 40 min with gentle rotation. After incubation, the mixture was transferred to a gravity column and the flowthrough was allowed to drain. The resin was washed twice with 20 mL of Wash Buffer 1 and twice with 20 mL of Wash Buffer 2. The protein was then eluted with 14 mL of Elution Buffer 1 and collected in 1 mL fractions. All fractions were run on an SDS-PAGE gel, and fractions containing pure protein were pooled and dialyzed overnight at 4°C into 1 L of Storage Buffer 1, supplemented with 100 µM $ZnCl_2$ for ZF5.3-DHFR. If needed for cyclized DHFR proteins, dialyzed protein was concentrated to ~1 mL and applied to a HiLoad Superdex 75 pg preparative size exclusion chromatography column equilibrated with Storage Buffer 1 to remove linear DHFR. All proteins were quantified using a Pierce™ BCA Protein Assay kit and, if needed, concentrated to >1 mg/mL using an Amicon 10 kDA MWCO spin concentrator. The identities of final purified proteins were confirmed using liquid chromatography-mass spectrometry (Agilent Infinity II LC/6530 Accurate- Mass Q-TOF LC/MS) and stored at -80° until use.

Expression and purification of sortase enzymes

Two variants of the hepta-mutant Staphylococcus aureus Sortase A (SrtA7m)[67] were used for conjugation of a rhodamine dye to the C-terminus of DHFR proteins: one encoding S35 StrepTagII-SrtA7m-His6 (for generation of $DHFR^{Rho}$), and one encoding His6-SUMO-SrtA7m (for generation of ZF5.3-$DHFR^{Rho}$). Purification of both sortase enzymes was performed as previously described[7] with minor modifications. Both plasmids were transformed into E. coli BL21(DE3) competent cells and selected on a 50 µg/mL kanamycin (kan) LB agar plate (for S35 StrepTagII-SrtA7m-His6) or a 100 µg/mL amp LB agar plate (His6-SUMO-SrtA7m). A 5 mL starter culture inoculated with 1 colony was prepared for each with the appropriate antibiotic and grown at 37°C for 3.5 h. The starter culture was diluted into 1 L of LB with antibiotic and grown to OD_{600} = 0.6 - 0.8, followed by induction with 0.5 mM IPTG. The culture was then transferred to 30°C for 18-24 h. All steps from this point forward were performed at 4°C. Cells were harvested by centrifugation at 4300 g for 40 min, resuspended in 20 mL Lysis Buffer 1, and lysed by

sonication for 3 min (30 s on/30 s off pulses). The lysate was cleared by centrifugation at 10,000 rpm for 40 min and transferred to a 50 mL Falcon tube containing 2 mL of TALON® metal affinity resin pre-equilibrated with Wash Buffer 1. The resin was incubated with cleared lysate for 1 h with gentle rotation and added to a gravity column. The flowthrough was collected and the column was washed 3 times with 20 mL of Wash Buffer 1. The protein was then eluted in 13 mL of Elution Buffer 1, collected in 1 mL fractions, and run on an SDS-PAGE gel. Fractions containing pure protein were pooled and dialyzed overnight into Storage Buffer 1. The next day, the protein was quantified using a Pierce™ BCA Protein Assay kit.

For His6-SUMO-SrtA7m, the His6-SUMO was then cleaved by incubation with His6-SUMO protease (purified as previously described[68]) at a 4:1 molar ratio of His6-SUMO-SrtA7m to SUMO protease at room temperature for 2 hr. The cleaved SrtA7m protein was purified from the reaction mixture by incubation with TALON® metal affinity resin for 1 h at 4°C followed by collection of the column flowthrough and 10 1-mL wash fractions. The fractions were analyzed by SDS-PAGE, and those containing cleaved SrtA7m protein were pooled and dialyzed into fresh Storage Buffer 1 overnight at 4°C. Protein concentration was determined using a Pierce™ BCA Protein Assay kit. If needed, proteins were concentrated to >3 mg/mL with an Amicon 3 kDa MWCO spin concentrator and stored at -80°C until use.

Expression and purification of SNAP-tag proteins

Expression/Purification of SNAP-tag, AGT54, and GE-AGT:

The plasmids encoding SNAP-tag, AGT54, and GE-AGT were transformed into E. coli BL21(DE3) competent cells and selected on an amp/LB agar plate. For each protein, one colony was used to inoculate a 20 mL overnight starter culture of LB media supplemented with 100 µg/mL amp grown at 37°C. The next morning, the starter cultures were added to 1 L of LB per protein with 100 mg/L amp at 37°C until OD_{600} = 0.6 - 0.8. Protein expression was induced with 1 mM IPTG, and the cultures were transferred to 18°C for 18 - 22 h. All steps from this point forward were performed at 4°C. The cells were harvested by centrifugation at 4300 g for 40 min and pellets were resuspended in 20 mL Lysis Buffer 2 supplemented with 1 cOmplete, mini EDTA-free protease inhibitor cocktail tablet per pellet. The cells were lysed using an EmulsiFlex-C3 homogenizer, and the lysate was cleared by centrifugation at 18,000 rpm for 35 min at 4°C. The cleared lysate was incubated with 2 mL of TALON® metal affinity resin for 1 h at 4°C with gentle rotation. The mixture was then added to a gravity column and the flowthrough was collected. The column was washed twice with High-Salt Buffer and twice with Low-Salt Buffer. The protein was then eluted with 10 mL Elution Buffer 2 and analyzed by SDS-PAGE.

Fractions containing pure protein were pooled and dialyzed into Storage Buffer 2 overnight at 4°C. We observed that protein concentration using standard Amicon spin concentrators resulted in significant sample loss, so the proteins were concentrated using a 65% w/v ammonium sulfate precipitation.[69] Ammonium sulfate was added to the protein solution in a 15 mL conical tube, vortexed until fully dissolved, and incubated with rotation at 4°C for 10 min. The solution was then centrifuged at 4300 g for 10 min to sediment the precipitated protein in the pellet. The protein was resuspended in Storage Buffer 2. Protein concentration was determined using the Beer-Lambert law $A = \varepsilon bC$ where A = absorbance at 280 nm measured on a NanoDrop spectrophotometer (ND-1000), ε = the extinction coefficient for the protein, b = the optical path length in cm, and C = the protein concentration in M. To confirm the identity of all proteins, ~5 µg of each was desalted using ZipTip$_{C4}$® pipette tips (EMD Millipore) and analyzed by LC/MS. Purified proteins were stored at -80°C until use.

Expression of ZF5.3-SNAP-tag:

The expression of ZF5.3-SNAP was modified slightly from previous protocols to enable expression in minimal media in order to prevent formation of a +80 Da oxidative modification.[7] The plasmid encoding ZF5.3-SNAP was transformed into E. coli BL21(DE3) competent cells and selected on an amp/LB agar plate. One colony was used to inoculate a 5 mL starter culture in LB supplemented with 100 µg/mL amp, which was grown for 6 h at 37°C. The starter culture was then transferred to 500 mL minimal M9 media supplemented with 1 g/L NH_4Cl, 4 g/L glucose, 2 mM $MgSO_4$, 0.1 mM $CaCl_2$, 100 mg/L amp, and 1 mM thiamine and grown with shaking overnight at 37°C. The next morning, 50 mL of overnight culture was transferred to 1 L of minimal M9 media with the same supplements described above plus a dash of biotin. The culture was grown with shaking at 37°C until OD_{600} = 0.6, followed by induction with 1 mM IPTG. The culture was then transferred to 18°C and grown for 18 - 22 h.

Expression of ZF5.3-AGT54:

The expression of ZF5.3-AGT54 followed the same protocol as the untagged variants. The plasmid encoding ZF5.3-AGT54 was transformed into E. coli BL21(DE3) competent cells and selected on an amp/LB agar plate. One colony was used to inoculate a 20-mL overnight starter culture of LB media supplemented with 100 µg/mL amp. The next morning, the starter culture was added to 1 L of LB with 100 mg/L amp and incubated at 37°C until OD_{600} = 0.6 - 0.8. Protein expression was induced with 1 mM IPTG, and the cultures were transferred to 18°C for 18 - 22 h.

Expression of ZF5.3-GE-AGT:

The expression of ZF5.3-GE-AGT was optimized further to improve yield. The plasmid encoding ZF5.3-GE-AGT was transformed into E. coli BL21-CodonPlus(DE3)-RP cells and selected on a double antibiotic LB agar plate containing 100 µg/mL amp and 25 µg/mL chloramphenicol (Cm). One colony was used to inoculate a 20 mL overnight starter culture of LB media supplemented with 100 µg/mL amp and 25 g/mL Cm, which was grown at 37°C. The starter culture was added to 1 L of LB with the appropriate antibiotics and grown to OD_{600} = 0.8. ZF5.3-GE-AGT expression was induced with 0.5 mM IPTG and transferred to 18°C for 6 h.

Purification of ZF5.3-SNAP, ZF5.3-AGT54, and ZF5.3-GE-AGT:

After expression, all three proteins were purified using the same protocol. All steps were carried out at 4°C. Cells were harvested by centrifugation at 4300 g for 40 min, and pellets were resuspended in 20 mL Lysis Buffer 2 supplemented with 1 cOmplete, mini EDTA-free protease inhibitor cocktail tablet per pellet. The cells were lysed using an EmulsiFlex-C3 homogenizer, and the lysate was cleared by centrifugation at 18,000 rpm for 35 min at 4°C. The cleared lysate was passed through a 0.22 µm membrane filter and the protein of interest was isolated using a two-step purification. First, the filtered lysate was applied to a 5 mL HiTrap® SP HP cation exchange column (Cytiva) and eluted using a linear gradient from 0.15 - 1 M NaCl over 10 column volumes (CV). Protein-containing fractions were analyzed by SDS-PAGE, and those containing the desired protein were pooled and further purified using TALON® metal affinity resin as described for SNAP-tag, AGT54, and GE-AGT above. We observed that the ZF5.3-tagged variants were not stable for overnight dialysis, and instead they were concentrated using a 65% w/v ammonium sulfate precipitation directly after elution from the resin. The precipitated protein was resuspended in Storage Buffer 2 and quantified using absorbance at 280 nm as described above. To confirm the identity of all proteins, ~5 µg of each was desalted using ZipTip$_{C4}$® pipette tips and analyzed by LC/MS. Purified proteins were stored at -80°C until use.

<u>Expression and purification of NS1 proteins</u>

The plasmid encoding NS1 or NS1-ZF5.3 was transformed into E. coli BL21(DE3) competent cells and selected on an amp/LB agar plate. One colony was used to inoculate a 5 mL starter culture of LB media supplemented with 100 µg/mL amp, which was grown at 37°C overnight. The next day, the starter culture was added to 1 L of LB with 100 mg/L amp and incubated with shaking at 37°C until the OD_{600} reached 0.6-0.7. Expression was induced with 0.5 mM IPTG and, for NS1-ZF5.3 only, $ZnCl_2$ was added to the LB at a final concentration of 100 µM. The cultures were transferred to 18°C for 14-16 h.

All steps from this point forward were performed at 4°C. The cells were harvested by centrifugation at 4300 g for 30 min and resuspended in 10 mL ice-cold Lysis Buffer 3 supplemented with 1 µL of Benzonase® Nuclease and 1 cOmplete, mini EDTA-free protease inhibitor cocktail tablet. Cells were lysed by sonicating for 30 s and recovering for 30 s for 7 cycles. The lysate was cleared by centrifugation at 16,000 rpm for 35 min, filtered with a 0.22 µm membrane, and subjected to a one-step (for NS1) or two-step (for NS1-ZF5.3) purification. For NS1, the filtered lysate was applied to a 5 mL StrepTrap® HP Streptactin Sepharose affinity column (Cytiva) and eluted with a linear gradient from 0 - 2.5 mM desthiobiotin over 10 CV. Fractions containing pure protein were assessed using SDS-PAGE. For NS1-ZF5.3, the filtered lysate was first applied to a 5 mL HiTrap® SP HP cation exchange column (Cytiva) and eluted using a linear gradient from 0.05 - 2 M NaCl over 10 CV. Protein-containing fractions were analyzed by SDS-PAGE. We observed significant nucleic acid contamination for some fractions (monitored using a NanoDrop spectrophotometer) and only chose fractions with a 260/280 nm ratio < 0.6 for the next purification step. These fractions were then applied to a 5 mL StrepTrap® HP Streptactin Sepharose affinity column (Cytiva) and eluted with a linear gradient from 0 - 2.5 mM desthiobiotin over 10 CV. The NS1 and NS1-ZF5.3 proteins were not stable for overnight dialysis and were therefore either immediately labeled with rhodamine (see Rhodamine Labeling of NS1 Proteins below) or buffer-exchanged into Storage Buffer 3 using a PD-10 desalting column. Protein concentration was determined using absorbance at 280 nm as described above. LC/MS was used to confirm the identity of all proteins, which were then stored at -80°C until use.

2.6.4 Fluorescent labeling of proteins

Sortase-mediated rhodamine labeling of DHFR proteins

Wildtype and MTX-resistant DHFR^{Rho} ZF5.3-DHFR^{Rho} were generated by reaction with a GGGK^{Rho} peptide and either the StrepTagII-SrtA7m-His6 enzyme (for DHFR^{Rho}) or the His6-SUMO-SrtA7m enzyme with the His6 tag cleaved (for ZF5.3-DHFR^{Rho}). The different enzymes were chosen for their ability to be separated from the reaction mixture, as described below. The GGGK^{Rho} peptide was synthesized as previously described.[8] For labeling, DHFR and ZF5.3-DHFR were diluted to 35 µM in a 1.5 mL solution containing 75 µM of the appropriate SrtA7m enzyme and 200 µM GGGK^{Rho} in 20 mM Tris, 150 mM KCl, 1 mM TCEP pH 7.5. The reaction was incubated with gentle rotation for 4 h at 4°C.

After 4 h, DHFR^{Rho} was separated from the reaction mixture by incubating with 1 mL TALON® resin for 1 h at 4°C and applying the solution to a gravity column. The gravity

column was washed with 10 mL of Wash Buffer 2. Because the His6 tag is C-terminal to the LPETGG motif on DHFR, successful reaction with sortase should result in loss of the His6 tag and therefore $DHFR^{Rho}$ is collected in the column washes and flowthrough. Fractions containing fluorescent DHFR were analyzed by SDS-PAGE using a fluorescence imager, pooled, and desalted into Storage Buffer 1 using a disposable PD-10 desalting column (Cytiva) to remove excess $GGGK^{Rho}$. The final rhodamine-labeled protein was concentrated using a 10 kDA MWCO Amicon spin concentrator.

To separate ZF5.3-$DHFR^{Rho}$ from the other reaction components, the reaction mixture was incubated with 1 mL TALON® resin for 1 h at 4°C and applied to a gravity column. In this case, although successful reaction with sortase will still result in loss of the His6 tag, ZF5.3-DHFR binds the TALON® resin due to nonspecific interactions between ZF5.3 and the resin. The resin was washed with 10 mL Wash Buffer 2 to remove excess $GGGK^{Rho}$ and SrtA7m. ZF5.3-$DHFR^{Rho}$ was eluted with 15 mL Elution Buffer 1 and dialyzed overnight at 4°C into Storage Buffer 1 + 100 µM $ZnCl_2$. After dialysis, the protein was concentrated using a 10 kDA MWCO Amicon spin concentrator.

For $DHFR^{Rho}$ and ZF5.3-$DHFR^{Rho}$, the identities of the purified proteins were confirmed using LC/MS. Protein concentrations were calculated using the Pierce™ 660 nm Protein Assay. The concentrations of rhodamine-labeled proteins were determined by calculating the rhodamine concentration in each sample using the Beer-Lambert law $A = \varepsilon bC$ where A = the absorbance at 570 nm on a NanoDrop spectrophotometer, ε = the extinction coefficient of lissamine rhodamine B in water (112000 M^{-1} cm^{-1}), b = the path length in cm, and C = the concentration in M. The labeling efficiency was calculated by dividing the rhodamine concentration by the concentration of total protein. All proteins were stored at -80°C until use.

Rhodamine labeling of SNAP-tag proteins

All SNAP proteins were tagged with rhodamine using a self-labeling reaction between the SNAP-tag variant and a rhodamine dye functionalized with a benzylguanine moiety (BG-Rho). BG-rho was synthesized as previously described.[7] BG-amine (3 mg, 11 µmol) was dissolved in 500 µL anhydrous DMSO and added to 3 equivalents of lissamine rhodamine B sulfonyl chloride (33 µmol) and 6 equivalents of N,N-Diisopropylethylamine (66 µmol). The reaction was stirred under nitrogen at room temperature overnight. The next day, BG-Rho was purified with a reverse-phase preparative HPLC (Waters Prep 150 System) using a C18 column (CSH C18 19 x 150 mm OBD Column 5 µm), and fractions with the desired product were identified using LC/MS. These fractions were pooled, lyophilized, and resuspended in DMSO for labeling

experiments. The concentration of BG-rho was determined using absorbance at 570 nm as described above.

$SNAP^{Rho}$, $AGT54^{Rho}$, and GE-AGT^{Rho} were generated by incubating a 40 µM solution of each respective protein with 80 µM BG-Rho in SNAP Labeling Reaction Buffer overnight with rotation at 4°C. ZF5.3-$SNAP^{Rho}$, ZF5.3-$AGT54^{Rho}$, and ZF5.3-GE-AGT^{Rho} were generated by incubating a 20 µM solution of each respective protein with 40 µM BG-Rho in SNAP Labeling Reaction Buffer for 24 h at 4°C with rotation. Reaction progress in all cases was monitored by LC/MS until completion. Excess BG-Rho was removed from the reactions using a PD-10 desalting column and the rhodamine-labeled proteins were concentrated using a 65% w/v ammonium sulfate precipitation as described above. The $SNAP^{Rho}$, $AGT54^{Rho}$, and GE-AGT^{Rho} protein pellets were resuspended in Storage Buffer 2, while the ZF5.3-$SNAP^{Rho}$, ZF5.3-$AGT54^{Rho}$, and ZF5.3-GE-AGT^{Rho} pellets were resuspended in Storage Buffer 2 + 100 µM $ZnCl_2$. The rhodamine-labeled protein concentrations were determined using absorbance at 570 nm as described above, with the extinction coefficient (ε) for lissamine rhodamine B measured in salty storage buffer (64417 M^{-1} cm^{-1}). All proteins were stored at -80°C until use.

Rhodamine labeling of NS1 proteins

Fractions containing pure NS1 or NS1-ZF5.3 from the Strep affinity purification were pooled and immediately incubated with 5 equiv of lissamine rhodamine B-maleimide (Tenova) in the buffer with which they were eluted off the column. The solution was incubated with rotation at RT for 1 h. To remove excess dye, the protein was desalted using a PD-10 column and eluted into Storage Buffer 3. The rhodamine-labeled protein concentrations were determined by absorbance at 570 nm. Concentration of total protein was determined using absorbance at 280 nm. Labeling efficiencies were determined by dividing the concentration of rhodamine-labeled protein by the concentration of total protein and ranged between 22-53%. LC/MS was used to confirm the identity of all proteins, which were then stored at -80°C until use.

2.6.5 Circular dichroism

Circular dichroism (CD) measurements were performed and analyzed using existing protocols.[70] All spectra were recorded using either an AVIV Biomedical, Inc. (Lakewood, NJ) Circular Dichroism Spectrometer Model 410 or a JASCO J-1500 Circular Dichroism Spectropolarimeter. In all cases, spectra were recorded using a 0.1 cm pathlength quartz cuvette (Starna). Wavelength-dependent CD spectra were collected between 300 and 200 nm in 1 nm intervals with an averaging time of 5 sec and normalized to a baseline buffer-only spectrum. Temperature-dependent CD spectra were collected

between 5 and 90°C measuring every 2° with an equilibration time of 120 s at each temperature step. The wavelength used for the temperature melt for each protein was chosen based on the wavelength spectra and set to 210 nm for DHFR proteins, 222 nm for SNAP-tag proteins, and 218 nm for NS1 proteins. For wildtype, MTX-resistant, and cyclized DHFR and ZF5.3-DHFR, all spectra were collected at 20 µM protein concentration in 25 mM Tris, 150 mM KCl, 1 mM TCEP pH 7.5 (+25 µM $ZnCl_2$ for ZF5.3-DHFR only). For measurements with methotrexate (MTX), DHFR or ZF5.3-DHFR was pre-incubated with one equiv of MTX for 30 min prior to measurements. For $SNAP^{Rho}$, $AGT54^{Rho}$, $GE\text{-}AGT^{Rho}$, $ZF5.3\text{-}SNAP^{Rho}$, $ZF5.3\text{-}AGT54^{Rho}$, and $ZF5.3\text{-}GE\text{-}AGT^{Rho}$, all spectra were collected at 12 - 20 µM protein concentration in 25 mM Tris, 150 mM NaCl, 1 mM TCEP pH 7.5 (+25 µM $ZnCl_2$ for ZF5.3 variants). For NS1 and NS1-ZF5.3, the spectra were collected at 18 µM in a buffer composed of 20 mM Tris, 150 mM KCl, 0.5 mM TCEP pH 7.5. Raw ellipticity values were converted to mean residue ellipticity using eq (1):

$$\theta = \frac{m^\circ \bullet MRW}{l \cdot C} \qquad (1)$$

where θ = mean residue ellipticity in deg • cm^2 • $dmol^{-1}$, m° = raw ellipticity in millidegrees, MRW = mean residue weight (calculated as the molecular weight divided by the number of backbone amide bonds), l = path length of the cuvette in millimeters, and C = concentration of the protein in mg mL^{-1}. For temperature melts, normalized intensity was calculated by normalizing all ellipticity values to the value at 5°C.

2.6.6 DHFR activity assay:

The catalytic activities of purified DHFR and ZF5.3-DHFR were assessed using a commercially available Dihydrofolate Reductase Assay kit (Sigma). The assay monitors the NADPH-dependent reduction of dihydrofolate (DHFA) to tetrahydrofolate (THFA) by measuring the loss in absorbance at 340 nm over time using a UV/Vis spectrometer (Cary 60 UV-Vis, Agilent Technologies). Purified DHFR or ZF5.3-DHFR was added to a final concentration of 50 nM in a 1 mL solution of 1x activity assay buffer provided in the kit. The solution was transferred to a 1 cm quartz cuvette, followed by addition of 6.6 µL of 10 mM NADPH. The cuvette was inverted to mix the reaction components. In quick succession, 5 µL of 10 mM DHFA was added, the mixture was inverted again, and the reaction progress was monitored by absorbance at 340 nm. Absorbance readings were taken every 15 s for 150 s. For measurements in the presence of MTX, MTX was added to a final concentration of 100 nM and incubated with the protein for 5 min before addition of NADPH and DHFA.

Specific activity (in units per mg) of each enzyme was calculated using eq (2):

$$Units/mg = \frac{(\triangle OD/min(sample) - \triangle OD/min(blank)) \cdot d}{12.3 \cdot V \cdot mg/mL} \quad (2)$$

where ΔOD/min(sample) = the slope of the 340 nm absorbance curve for the sample, ΔOD/min(blank) = the slope of the 340 nm absorbance curve for a buffer blank, d = dilution factor of the enzyme sample, 12.3 = the extinction coefficient (mM^{-1} cm^{-1}) for the DHFR reaction at 340 nm, V = the volume of enzyme used in the reaction, and mg/mL = concentration of the DHFR protein in mg mL^{-1}.

2.6.7 Cell culture

Saos-2 cell stocks were purchased from the UC Berkeley Cell Culture Facility. Saos-2 cells were cultured in McCoy's 5A medium with phenol red containing 15% fetal bovine serum (FBS), penicillin and streptomycin (P/S, 100 units/mL and 100 µg/mL, respectively), 1 mM sodium pyruvate, and 2 mM GlutaMax.

2.6.8 Intracellular delivery experiments

Cellular workup for delivery experiments

All fluorescence-based intracellular delivery experiments (confocal microscopy, flow cytometry, and fluorescence correlation spectroscopy) followed previously published protocols.[26] The day prior to experiments, $0.2 \cdot 10^6$ Saos-2 cells were plated in a 6-well dish in McCoy's 5A medium +15% FBS, without phenol red or P/S. The following day, cells were incubated with a 0.5 mL (SNAP proteins) or 1 mL (DHFR proteins and NS1 proteins) solution of rhodamine-labeled protein diluted to the appropriate concentration (0.1 - 2 µM) in clear McCoy's 5A medium without FBS or P/S. During the incubation, a fibronectin solution diluted into DPBS (0.1 mg/mL) was added to the appropriate number of wells of an 8-well microscopy dish. In a separate well of the same dish, 200 µL of a 100 nM solution of AlexaFluor 594 hydrazide dye in water was added for FCS analysis to calculate the microscope focal volume. The dish was incubated at 37°C, 5% CO_2 for the duration of the cell incubation and work-up. During the last 5 min of the cell incubation (0.5 - 2 h total length), Hoechst 33342 nuclear dye was added to each well of the 6-well dish at a final concentration of 300 nM. After the incubation was over, the protein-containing solution was removed and the cells were washed three times with 2 mL of DPBS per wash. To remove exogenously bound protein, cells were trypsinized with 500 µL trypsin (no phenol red). The trypsin reaction was quenched with 1 mL clear McCoy's 5A medium + 15% FBS and each well was thoroughly washed with another 1 mL of the same media. The cells were pelleted in a 15 mL Falcon tube and washed one time with 1 mL of clear DMEM + Hepes. During this centrifugation step, the microscopy dish was

removed from the incubator and fibronectin-containing wells were washed three times with 200 uL DPBS per wash. The DPBS was left in each well until cells were ready to add. The pelleted cells were then resuspended in 600 µL DMEM + Hepes. Of this, 300 µL was added to each fibronectin-coated well of the microscopy dish for confocal microscopy and FCS analysis, and transferred to 37°C, 5% CO_2 to allow the cells to adhere flatly. The remaining 300 µL of cells were pelleted, resuspended in 200 µL DPBS, and transferred to a 1.5-mL Eppendorf tube for flow cytometry.

Flow Cytometry

For each sample processed as described above, 10,000 cells were analyzed using flow cytometry. Forward scatter and side scatter gating parameters were established to select only whole cells using the same settings as reported previously.[6,8] For all experiments, >75% of cells were included in the gated population. The fluorescence intensities for Hoechst 33342 (excited using the violet laser at 405 nm, detected emission of 440 ± 50 nm) and lissamine rhodamine B (excited using the yellow laser at 561 nm, detected emission of 586 ± 16 nm) channels were monitored using an Attune NxT Focusing Flow Cytometer. The median fluorescence intensity (MFI) for the lissamine rhodamine B channel was reported for the gated population of cells, corrected for the rhodamine labeling efficiency of each protein when appropriate. Each flow cytometry experiment was performed with a minimum of two biological replicates (**Table 2.6.15**).

Confocal microscopy and fluorescence correlation spectroscopy (FCS)

The procedures used for confocal microscopy and FCS have been generally described previously.[6,26] Experiments were performed with a STELLARIS 8 microscope (Leica Microsystems) with a Leica DMi8 CS scanhead, a HC Plan-Apo 100/1.4NA STED white oil immersion objective (used for STED imaging), a HC Plan-Apo 63x/1.4NA water immersion objective (used for FCS measurements), a pulsed white-light laser (440 nm-790 nm; 440 nm: > 1.1 mW; 488 nm: > 1.6 mW; 560 nm: > 2.0 mW; 630 nm: > 2.6 mW; 790 nm: > 3.5 mW, 78 MHz), and a pulsed 775 nm STED laser. All confocal imaging was performed using HyD S or HyD X detectors in analog mode, while FCS measurements were carried out using only a Hybrid HyD X detector. All microscopy experiments were performed at 37°C (monitored using Oko-Touch) and 5% CO_2 in a blacked out cage enclosure from Okolab. Before the start of each experiment, the correction collar of the objective was adjusted by maximizing the counts per molecule for the AlexaFluor 594 hydrazide dye standard; minor fluctuations in the correction collar are expected based on the variable thickness of the glass-bottom microscopy dishes (LabTek™). Lissamine rhodamine B was excited at 561 nm with a fluorescence filter of 570 - 660 nm, and the pinhole S5 of the laser was set to 1 AU. Before beginning *in cellula* experiments, ten five-

second autocorrelation traces were obtained using the well containing 100 nM AlexaFluor 594 hydrazide dye standard to calculate the focal volume of the microscope; see below. For *in cellula* data procurement, a confocal microscopy image of the cells was used to position the crosshairs of the microscope laser in the cytosol of cells within the frame. Areas with punctate fluorescence indicative of endosomally entrapped protein were avoided. All FCS measurements consisted of ten five-second traces. A minimum of 35 cells per condition were measured for each biological replicate, and a minimum of two biological replicates were collected for each condition. Expected diffusion times (τ_{diff}) for rhodamine-labeled DHFR, SNAP, and NS1 proteins were obtained by measuring *in vitro* autocorrelation traces for 50-200 nM solutions of each protein in DMEM media (25 mM Hepes, no phenol red) at 37°C.

Analysis of FCS data

Autocorrelation traces obtained from FCS measurements were analyzed using a custom MATLAB script.[6,7,26,68] To extract quantitative information from *in cellula* data, the effective confocal volume of the microscope must be known. This value was determined using eqs 3-5 by and the *in vitro* autocorrelation traces for the AlexaFluor 594 hydrazide standard measured at the start of each experiment, which has a known diffusion coefficient in water.[5] These traces were fitted to a 3D diffusion equation (eq 3):

$$G(\tau) = \frac{1}{N} \cdot \frac{1}{(1+\frac{\tau}{\tau diff})\sqrt{1+(s^2\frac{\tau}{\tau diff})}} \qquad (3)$$

where N = the average number of molecules detected in the focal volume (V_{eff}), τ_{diff} = the average diffusion time that a molecule requires to cross V_{eff}, and s = the structure factor (the ratio of the radial to axial dimensions of the focal volume). The structure factor was measured to be 0.17 using the autocorrelation function of AlexaFluor 594 in water at 25°C and fixed for all subsequent analysis. V_{eff} can be extracted from these data by inserting the τ_{diff} value derived from eq (3) to calculate ω_1 in eq (4):

$$\omega_1 = \sqrt{4 \cdot D \cdot \tau_{diff}} \qquad (4)$$

where ω_1 = the lateral extension of the confocal volume and D = the known diffusion coefficient of AlexaFluor 594 in water at 37°C (5.20×10^{-6} cm^2 s^{-1}). V_{eff} can then be directly calculated from eq (5):

$$V_{eff} = \pi^{\frac{3}{2}} \cdot (\omega_1)^3 \cdot \frac{1}{s} \qquad (5)$$

The average V_{eff} for all experiments ranged from 0.25-0.4 fL.

Autocorrelation traces derived from *in cellula* measurements were fitted using a 3D anomalous diffusion equation (eq 6):

$$G(\tau) = \frac{1}{N} \cdot \frac{1}{(1+\frac{\tau}{\tau diff})^{\alpha} \sqrt{1+s^2 \frac{\tau}{\tau_{diff}}^{\alpha}}} + G(\infty) \qquad (6)$$

where N = the average number of molecules in the focal volume, τ_{diff} = the average diffusion time that a molecule requires to cross V_{eff}, α = the anomalous diffusion coefficient, and s = the structure factor (0.17). Parameters resulting from the fitting (including diffusion time, anomalous diffusion coefficient, and counts per molecule) were filtered as reported previously,[4] and only fitted curves that passed this filtering and displayed Chi-squared values under 40 (for DHFR proteins) or 100 (for SNAP and NS1 proteins) were selected for further analysis. Expected τ_{diff} values for *in cellula* samples were predicted from autocorrelation traces for *in vitro* protein samples in DMEM that were fitted using eq (3). Only curves that displayed *in cellula* τ_{diff} values within 2-15-fold of the *in vitro* value were selected. Shorter diffusion times can indicate degradation, while longer diffusion times may reflect aggregated material with abnormal diffusion dynamics. The concentration (C) of protein in the cytosol was then calculated using the value of N derived above in eq (7):

$$C = \frac{N}{N_A \cdot V_{eff}} \qquad (7)$$

where N_A = Avogadro's number (6.023×10^{23} mol^{-1}). When relevant, the concentration values were adjusted for fluorophore labeling efficiency. At least 15 concentration values from curves that pass all filters were used for each FCS condition (**Table 2.6.15**).

2.6.9 Cytosolic fractionation

The day before the experiment, 5.0×10^6 Saos-2 cells were plated in a 100 mm dish in McCoy's 5A medium + 15% FBS (no phenol red, no P/S). The following morning, the cells were washed three times with DPBS and the media was replaced with 10 mL of McCoy's 5A media (no FBS, no phenol red, no P/S) containing a 1 µM solution of DHFR or ZF5.3-DHFR. The cells were incubated at 37°C, 5% CO_2 for 1 hour. After incubation, the cells were washed three times with DPBS and lifted from the dish with trypsin. The trypsin reaction was quenched with 15 mL of McCoy's 5A media + 15% FBS (no phenol red, no P/S) and the cells were transferred to a 50 mL conical tube. The dish was washed with an additional 5 mL of the same media. The cells were pelleted by centrifugation at 200 g for 3 min and washed by resuspension with 3 mL of DPBS. After centrifugation, the

cells were washed by resuspending in 1 mL of precooled buffered isotonic sucrose (290 mM sucrose, 10 mM imidazole pH 7.0, 1 mM DTT, and 1 cOmplete protease inhibitor tablet) and pelleted again. The cells were then resuspended in 100 µL of the isotonic sucrose buffer and transferred to 0.5 mL tubes with 1.4 mm ceramic beads (Omni International). A Bead Ruptor was used to lyse the cells for 10 sec at speed 1. Homogenized cells were then transferred to polycarbonate ultracentrifuge tubes and balanced within 1 mg. The cytosolic fraction was separated from the membrane fraction by centrifugation at 350 kg for 1 h at 4°C (Beckman Coulter, TLA-100 rotor). The supernatant (cytosol) was immediately removed and transferred to a 1.5 mL Eppendorf tube. The pellet (containing endosomes) was resuspended in 60 µL of 8 M urea and boiled at 95°C for 5 min to fully dissolve the pellet. Samples for Western blot analysis were prepared by mixing 20 µL of cytosolic or endosomal membrane fractions with 5 µL of 5x SDS gel loading dye and boiling at 95°C for 5 min. Western blot analysis was performed using primary antibodies against His-tag (CST #2365), tubulin (CST #2125), and Lamp1 (CST #9091) and a secondary HRP-linked anti-Rabbit IgG antibody (CST #7074).

2.6.10 siRNA knockdown studies

siRNA transfections

Knockdowns for VPS39 and TGF-BRAP1 were evaluated using the siRNAs listed in **Table 2.6.13** and were performed as described previously.[5] Four days before delivery, 0.085×10^6 Saos-2 cells were plated in a 6-well dish in McCoy's 5A media +15% FBS (no phenol red, no P/S). The next day, cells were transfected with the siRNA of interest at a final concentration of 100 nM using Lipofectamine RNAi/MAX transfection agent in McCoy's 5A media + 15% FBS (no phenol red, no P/S) and incubated for 4 h at 37°C, 5% CO_2. Cells were then washed three times with DPBS and incubated for 72 h at 37°C, 5% CO_2 in McCoy's 5A media + 15% FBS (2 mL/well, no phenol red, no P/S) before delivery experiments.

RT-qPCR analysis of siRNA knockdowns

All RT-qPCR data was obtained by Dr. Xizi Zhang. RT-qPCR was used to confirm siRNA-mediated knockdown of the desired genes after 72 h.[26] cDNA extracted from Saos-2 cells was amplified with gene-specific primers (150 nM, **Table 2.6.13**) using SsoFast EvaGreen Supermix (Bio-Rad) on a Bio-Rad CFX96 real-time PCR detection system. Three biological replicates were performed for each knockdown, and each sample was run in triplicate. Each RT-qPCR analysis included the gene that was knocked

down, GAPDH as a reference gene, and negative controls lacking either reverse transcriptase or template cDNA.

2.6.11 Analysis of ZF5.3-DHFR^{Rho} localization in Lamp1+ vesicles using confocal microscopy and STED

All STED experiments were performed with and analyzed by Neville Dadina. Two days prior to experiments, 0.05 × 10^6 Saos-2 cells were plated in a 4-well glass-bottom µslide microscopy dish (Ibidi) in McCoy's 5A media + 15% FBS (no phenol red, no P/S). The next day, cells were transfected with a plasmid encoding Lamp1-HaloTag (Addgene) using FuGENE HD transfection reagent (Promega) according to the manufacturer's protocol. After 6 h, the cells were washed 2 times with DPBS and incubated overnight in McCoy's 5A media + 15% FBS (no phenol red, no P/S) at 37°C, 5% CO_2. On the day of the experiment, cells were incubated with a chloroalkane-modified silicon rhodamine dye (SiR-CA)[71] for 1 h at a final concentration of 2 µM in OptiMEM (700 µL final volume). After this incubation, the cells were washed twice with DPBS and the media was replaced with McCoy's 5A media (no FBS, no phenol red, no P/S) containing 0.5 µM ZF5.3-DHFR^{Rho} for 1 hr. The cells were then washed three times with DPBS, trypsinized to remove exogenous protein, and replated in a fibronectin-coated 4-well glass-bottom µslide microscopy dish in DMEM (+Hepes). The sample was then imaged on a Leica Stellaris 8 STED-capable confocal microscope with a HC PL APO CS2 100x/1.4 NA Oil Leica STED-White objective. Beam path settings: ZF5.3DHFR^{Rho} (Excited at 573 nm with 0.5% laser power, HyD X detector window: 579 nm - 636 nm), SiR-CA (excited at 652 nm with 20% laser power, HyD X detector window: 662 nm - 750 nm); depletion at 775 nm at 30% laser power. Detectors were in photon counting mode and were set up to acquire signal simultaneously. Pinhole was set to 1 AU at 580 nm emission. Scanhead settings: Format: 1024 x 1024; pixel size: 28 nm pixel size; pixel dwell time: 3.8375 **µ**s. TauSTED parameters were adjusted in post-processing. Images were processed using FIJI software package. Images were cropped and a smoothening filter was applied before plotting line profiles

2.6.12 Statistics

All statistical tests were performed using GraphPad Prism 9 software and are detailed in the appropriate figure legends. Flow cytometry and FCS data were analyzed using Brown-Forsythe and Welch ANOVA statistical tests followed by unpaired t-tests with Welch's correction.

2.6.13 Relevant Sequences

Protein Sequences	
DHFR	VRPLNCIVAVSQNMGIGKNGDLPWPPLRNEFKYFQRMTTTS SVEGKQNLVIMGRKTWFSIPEKNRPLKDRINIVLSRELKEPPR GAHFLAKSLDDALRLIEQPELASKVDMVWIVGGSSVYQEAM NQPGHLRLFVTRIMQEFESDTFFPEIDLGKYKLLPEYPGVLSE VQEEKGIKYKFEVYEKKLPETGGHHHHHH
ZF5.3-DHFR	YSCNVCGKAFVLSRHLNRHLRVHRRATGSGVRPLNCIVAVS QNMGIGKNGDLPWPPLRNEFKYFQRMTTTSSVEGKQNLVIM GRKTWFSIPEKNRPLKDRINIVLSRELKEPPRGAHFLAKSLDD ALRLIEQPELASKVDMVWIVGGSSVYQEAMNQPGHLRLFVT RIMQEFESDTFFPEIDLGKYKLLPEYPGVLSEVQEEKGIKYKF EVYEKKLPETGGHHHHHH
DHFR(L22R)	VRPLNCIVAVSQNMGIGKNGDRPWPPLRNEFKYFQRMTTTS SVEGKQNLVIMGRKTWFSIPEKNRPLKDRINIVLSRELKEPPR GAHFLAKSLDDALRLIEQPELASKVDMVWIVGGSSVYQEAM NQPGHLRLFVTRIMQEFESDTFFPEIDLGKYKLLPEYPGVLSE VQEEKGIKYKFEVYEKKLPETGGHHHHHH
ZF5.3-DHFR(L22R)	YSCNVCGKAFVLSRHLNRHLRVHRRATGSGVRPLNCIVAVS QNMGIGKNGDRPWPPLRNEFKYFQRMTTTSSVEGKQNLVI MGRKTWFSIPEKNRPLKDRINIVLSRELKEPPRGAHFLAKSL DDALRLIEQPELASKVDMVWIVGGSSVYQEAMNQPGHLRLF VTRIMQEFESDTFFPEIDLGKYKLLPEYPGVLSEVQEEKGIKY KFEVYEKKLPETGGHHHHHH
cDHFR(C6S)	VKIISRKSLGTQNVYDIGVGEPHNFLLKNGLVASNCFNGSGV RPLNSIVAVSQNMGIGKNGDLPWPPLRNEFKYFQRMTTTSS VEGKQNLVIMGRKTWFSIPEKNRPLKDRINIVLSRELKEPPRG AHFLAKSLDDALRLIEQPELASKVDMVWIVGGSSVYQEAMN QPGHLRLFVTRIMQEFESDTFFPEIDLGKYKLLPEYPGVLSEV QEEKGIKYKFEVYEKKHHHHHHGSGAEYCLSYDTEILTVEYG FLPIGKIVEERIECTVYTVDKNGFVYTQPIAQWHNRGEQEVF EYCLEDGSIIRATKDHKFMTTDGQMLPIDEIFERGLDLKQVDG LP
ZF5.3-cDHFR(C6S)	VKIISRKSLGTQNVYDIGVGEPHNFLLKNGLVASNCFNGSGY SCNVCGKAFVLSRHLNRHLRVHRRATGSGVRPLNSIVAVSQ NMGIGKNGDLPWPPLRNEFKYFQRMTTTSSVEGKQNLVIMG RKTWFSIPEKNRPLKDRINIVLSRELKEPPRGAHFLAKSLDDA LRLIEQPELASKVDMVWIVGGSSVYQEAMNQPGHLRLFVTRI MQEFESDTFFPEIDLGKYKLLPEYPGVLSEVQEEKGIKYKFE

	VYEKKHHHHHHGSGAEYCLSYDTEILTVEYGFLPIGKIVEERI ECTVYTVDKNGFVYTQPIAQWHNRGEQEVFEYCLEDGSIIRA TKDHKFMTTDGQMLPIDEIFERGLDLKQVDGLP
cDHFR	VKIISRKSLGTQNVYDIGVGEPHNFLLKNGLVASNCFNGSGV RPLNCIVAVSQNMGIGKNGDLPWPPLRNEFKYFQRMTTTSS VEGKQNLVIMGRKTWFSIPEKNRPLKDRINIVLSRELKEPPRG AHFLAKSLDDALRLIEQPELASKVDMVWIVGGSSVYQEAMN QPGHLRLFVTRIMQEFESDTFFPEIDLGKYKLLPEYPGVLSEV QEEKGIKYKFEVYEKKHHHHHHGSGAEYCLSYDTEILTVEYG FLPIGKIVEERIECTVYTVDKNGFVYTQPIAQWHNRGEQEVF EYCLEDGSIIRATKDHKFMTTDGQMLPIDEIFERGLDLKQVDG LP
ZF5.3-cDHFR	VKIISRKSLGTQNVYDIGVGEPHNFLLKNGLVASNCFNGSGY SCNVCGKAFVLSRHLNRHLRVHRRATGSGVRPLNCIVAVSQ NMGIGKNGDLPWPPLRNEFKYFQRMTTTSSVEGKQNLVIMG RKTWFSIPEKNRPLKDRINIVLSRELKEPPRGAHFLAKSLDDA LRLIEQPELASKVDMVWIVGGSSVYQEAMNQPGHLRLFVTRI MQEFESDTFFPEIDLGKYKLLPEYPGVLSEVQEEKGIKYKFE VYEKKHHHHHHGSGAEYCLSYDTEILTVEYGFLPIGKIVEERI ECTVYTVDKNGFVYTQPIAQWHNRGEQEVFEYCLEDGSIIRA TKDHKFMTTDGQMLPIDEIFERGLDLKQVDGLP
SNAP-tag	DKDCEMKRTTLDSPLGKLELSGCEQGLHEIKLLGKGTSAADA VEVPAPAAVLGGPEPLMQATAWLNAYFHQPEAIEEFPVPAL HHPVFQQESFTRQVLWKLLKVVKFGEVISYQQLAALAGNPA ATAAVKTALSGNPVPILIPCHRVVSSSGAVGGYEGGLAVKEW LLAHEGHRLGKPGLGHHHHHH
ZF5.3-SNAP-tag	YSCNVCGKAFVLSRHLNRHLRVHRRATDKDCEMKRTTLDSP LGKLELSGCEQGLHEIKLLGKGTSAADAVEVPAPAAVLGGPE PLMQATAWLNAYFHQPEAIEEFPVPALHHPVFQQESFTRQV LWKLLKVVKFGEVISYQQLAALAGNPAATAAVKTALSGNPVP ILIPCHRVVSSSGAVGGYEGGLAVKEWLLAHEGHRLGKPGL GHHHHHH
AGT54	DKDCEMKRTTLDSPLGKLELSGCEQGLHEIKLLGKGTSAADA VEVPAPAAVLGGPEPLMQCTAWLNAYFHQPEAIEEFPVPAL HHPVFQQESFTRQVLWKLLKVVKFGEVISYQQLAALAGNPK AARAVKTALSGNPVPILIPCHRVVCSSGAVGGYEGGLAVKE WLLAHEGHRLGKPGLGHHHHHH
ZF5.3-AGT54	YSCNVCGKAFVLSRHLNRHLRVHRRATGSGDKDCEMKRTT LDSPLGKLELSGCEQGLHEIKLLGKGTSAADAVEVPAPAAVL GGPEPLMQCTAWLNAYFHQPEAIEEFPVPALHHPVFQQESF TRQVLWKLLKVVKFGEVISYQQLAALAGNPKAARAVKTALSG

	NPVPILIPCHRVVCSSGAVGGYEGGLAVKEWLLAHEGHRLG KPGLGHHHHHH
GE-AGT	DKDCEMKRTTLDSPLGKLELSGCEQGLHEIKLLGKGTSAADA VEVPAPAAVLGGPEPLMQCTAWLNAYFHQPEAIEEFPVPAL HHPVFQQESFTRQVLWKLLKVVKFGEVISYQQLAALAGNPK AARAVGGAMRGNPVPILIPCHRVVCSSGAVGGYEGGLAVKE WLLAHEGHRLGKPGLGHHHHHH
ZF5.3-GE-AGT	YSCNVCGKAFVLSRHLNRHLRVHRRATGSGDKDCEMKRTT LDSPLGKLELSGCEQGLHEIKLLGKGTSAADAVEVPAPAAVL GGPEPLMQCTAWLNAYFHQPEAIEEFPVPALHHPVFQQESF TRQVLWKLLKVVKFGEVISYQQLAALAGNPKAARAVGGAMR GNPVPILIPCHRVVCSSGAVGGYEGGLAVKEWLLAHEGHRL GKPGLGHHHHHH
NS1	WSHPQFEKGSVSSVPTKLEVVAATPTSLLISWDAPAVTVDYY VITYGETGGNSPVQKFEVPGSKSTATISGLKPGVDYTITVYA WGWHGQVYYYMGSPISINYRTGGGGSGGGGSGGGGSC
NS1-ZF5.3	WSHPQFEKGSVSSVPTKLEVVAATPTSLLISWDAPAVTVDYY VITYGETGGNSPVQKFEVPGSKSTATISGLKPGVDYTITVYA WGWHGQVYYYMGSPISINYRTGGGGSGGGGSGGGGSYSC NVCGKAFVLSRHLNRHLRVHRRATGSGC
StrepTagII-SrtA7m-His6	WSHPQFEKQAKPQIPKDKSKVAGYIEIPDADIKEPVYPGPAT REQLNRGVSFAKENQSLDDQNISIAGHTFIDRPNYQFTNLKA AKKGSMVYFKVGNETRKYKMTSIRNVKPTAVEVLDEQKGKD KQLTLITCDDYNEETGVWETRKIFVATEVKLEHHHHHH
His6-SUMO-SrtA7m	GSSHHHHHHGSGLVPRGSASMSDSEVNQEAKPEVKPEVKP ETHINLKVSDGSSEIFFKIKKTTPLRRLMEAFAKRQGKEMDSL RFLYDGIRIQADQTPEDLDMEDNDIIEAHREQIGGMQAKPQIP KDKSKVAGYIEIPDADIKEPVYPGPATREQLNRGVSFAKENQ SLDDQNISIAGHTFIDRPNYQFTNLKAAKKGSMVYFKVGNET RKYKMTSIRNVKPTAVEVLDEQKGKDKQLTLITCDDYNEETG VWETRKIFVATEVKLE
Primers	
Primer 1 (to linearize pet-32a(+) vector)	ATGTATATCTCCTTCTTAAAGTTAAACAAAATTATT

Primer 2 (to linearize pet-32a(+) vector)	TAACAAAGCCCGAAAGGAAG
siRNA used for RNAi	
RISC-free	siGENOME RISC-Free Control siRNA: D-001220-01 (Dharmacon)
KIF11	siGENOME human SMARTpool siRNA KIF11: D-001220-01 (Dharmacon)
VPS39	siGENOME human SMARTpool siRNA VPS39: M-014052-01 (Dharmacon)
TGF-BRAP1	siGENOME human SMARTpool siRNA TGFBRAP1: M-006903-01 (Dharmacon)
Primers for RT-qPCR	
GAPDH	PrimeTime qPCR primers Hs.PT.39a.22214836 (IDT)
VPS39 - Forward	AGGGTCTGGCTATTCCTTATCT
VPS39 - Reverse	CCTTGCACCTTCTCACAGTATAG
TGF-BRAP1 - Forward	CTGACCACTCAGTACATCATCC
TGF-BRAP1 - Reverse	CTCCTGTCTCCCTATCCTCTT

2.6.14 Protein Purification Buffers

Buffer name	Relevant Protein(s)	Composition
Lysis Buffer 1	DHFR proteins, S35 StrepTagII-SrtA7m-His6, His6-SUMO-SrtA7m	25 mM Tris, 400 mM KCl, 5 mM TCEP, 5% glycerol, pH 7.5
Wash Buffer 1	DHFR proteins, S35 StrepTagII-SrtA7m-His6, His6-SUMO-SrtA7m	25 mM Tris, 400 mM KCl, 15 mM imidazole, 5 mM TCEP, 5% glycerol, pH 7.5

Wash Buffer 2	DHFR proteins, S35 StrepTagII-SrtA7m-His6, His6-SUMO-SrtA7m	25 mM Tris, 400 mM KCl, 5 mM imidazole, 5 mM TCEP, 5% glycerol, pH 7.5
Elution Buffer 1	DHFR proteins, S35 StrepTagII-SrtA7m-His6, His6-SUMO-SrtA7m	25 mM Tris, 300 mM KCl, 250 mM imidazole, 15% glycerol, pH 7.5
Storage Buffer 1	DHFR proteins, S35 StrepTagII-SrtA7m-His6, His6-SUMO-SrtA7m	25 mM Tris, 150 mM KCl, 1 mM TCEP, 15% glycerol, pH 7.5
Lysis Buffer 2	All SNAP variants	20 mM Tris, 150 mM NaCl, 10% glycerol, pH 8.0
High-Salt Buffer	All SNAP variants	20 mM Tris, 1M NaCl, 30 mM imidazole, 10% glycerol, pH 8.0
Low-Salt Buffer	All SNAP variants	20 mM Tris, 150 mM NaCl, 10% glycerol, pH 8.0
Elution Buffer 2	All SNAP variants	20 mM Tris, 150 mM NaCl, 250 mM imidazole, 10% glycerol, pH 8.0
Storage Buffer 2	All SNAP variants	20 mM Tris, 150 mM NaCl, 5 mM TCEP, 15% glycerol, pH 8.0
SNAP Labeling Reaction Buffer	All SNAP variants	20 mM Tris, 150 mM NaCl, 10% glycerol pH 7.5
Lysis Buffer 3	NS1 proteins	50 mM Hepes, 50 mM NaCl, 10% Glycerol, 1 mM TCEP, 3 mM $MgCl_2$, pH 7.5
Storage Buffer 3	NS1 proteins	50 mM Hepes, 150 mM NaCl, 10% Glycerol, 1 mM TCEP, pH 7.5

2.6.15 Summary Values for Intracellular Delivery Experiments

For flow cytometry (FC) experiments, *n* refers to the number of biological replicates. For each biological replicate, 10,000 cells were measured. The “FC Mean” corresponds to the average Median Fluorescence Intensity recorded across all biological

replicates. For fluorescence correlation spectroscopy (FCS), *n* refers to the number of individual cell measurements that passed all final filtering criteria (see Methods for more details) across all biological replicates. The number of biological replicates for FCS experiments is the same as that shown for the corresponding flow cytometry experiment. The “FCS Mean” corresponds to the average cytosolic concentration measured for that condition.

Condition	Fig	*n* - FC	FC Mean	FC SEM	*n* - FCS	FCS Mean	FCS SEM
$DHFR^{Rho}$ - 1 µM, 1h	1	2	1085	102.9	20	39.27	7.184
$DHFR^{Rho}$ - 0.5 µM, 1h	1	2	591.9	13.72	27	34.28	4.810
$DHFR^{Rho}$ - 0.1 µM, 1h	1	2	304.7	7.280	35	30.38	3.483
ZF5.3-$DHFR^{Rho}$ - 1 µM, 1h	1	2	33209	1073	35	392.8	44.14
ZF5.3-$DHFR^{Rho}$ - 0.5 µM, 1h	1	3	9146	168.8	63	348.9	24.66
ZF5.3-$DHFR^{Rho}$ - 0.1 µM, 1h	1	2	594.1	92.30	24	72.40	10.94
$DHFR^{Rho}$ + $ZF5.3^{Unlab}$, 1 µM, 1h	1	2	1048	4.9	21	28.42	7.518
$DHFR^{Rho}$ - 0.5 µM, 30min	1	2	263.9	8.475	46	12.65	1.166
$DHFR^{Rho}$ - 0.5 µM, 2h	1	2	4067	97.75	47	51.01	4.308
ZF5.3-$DHFR^{Rho}$ - 0.5 µM, 30min	1	2	8997	116.6	34	216.7	28.83
ZF5.3-$DHFR^{Rho}$ - 0.5 µM, 2h	1	2	53813	1099	51	360.3	36.27
$DHFR^{Rho}$ - 1 µM, 1h + MTX	2	2	485.9	4.520	38	17.01	2.052
$DHFR^{Rho}$ - 0.5 µM, 1h + MTX	2	2	148.0	10.78	29	10.18	0.8816
$DHFR^{Rho}$ - 0.1 µM, 1h + MTX	2	2	135.6	1.130	27	7.828	1.006
ZF5.3-$DHFR^{Rho}$ - 1 µM, 1h + MTX	2	2	28322	1548	36	254.2	23.09
ZF5.3-$DHFR^{Rho}$ - 0.5 µM, 1h + MTX	2	2	5764	303.9	35	173.2	19.65

ZF5.3-DHFR^{Rho} - 0.1 µM, 1h + MTX	2	2	275.6	2.600	32	21.42	1.652
ZF5.3-SNAP^{Rho} + MTX - 1 µM, 30min	2	2	470.5	13.50	17	19.46	2.473
SNAP^{Rho} - 1 µM, 30min	3	3	57.33	5.840	16	8.975	1.342
AGT54^{Rho} - 1 µM, 30min	3	2	199.5	1.500	20	15.34	2.672
GE-AGT^{Rho} - 1 µM, 30min	3	2	183.0	30.00	24	16.80	2.309
ZF5.3-SNAP^{Rho} - 1 µM, 30min	3	3	156.0	6.110	26	9.862	1.345
ZF5.3-SNAP^{Rho} - 1 µM, 1h	3	2	444.5	25.50	33	23.73	2.805
ZF5.3-SNAP^{Rho} - 1 µM, 2h	3	2	1297	43.00	48	44.24	3.493
ZF5.3-AGT54^{Rho} - 1 µM, 30min	3	4	1391	117.4	26	64.33	5.2777
ZF5.3-AGT54^{Rho} - 1 µM, 1h	3	3	2567	65.29	37	85.89	6.815
ZF5.3-AGT54^{Rho} - 1 µM, 2h	3	2	4435	505.0	28	139.2	16.12
ZF5.3-GE-AGT^{Rho} - 1 µM, 30min	3	2	2213	134.5	41	133.3	16.01
ZF5.3-GE-AGT^{Rho} - 1 µM, 1h	3	2	3927	533.5	20	216.2	24.53
ZF5.3-GE-AGT^{Rho} - 1 µM, 2h	3	2	6795	42.00	28	399.9	62.42
NS1^{Rho} - 1 µM, 1h	4	2	266.9	89.48	28	17.32	2.760
NS1^{Rho} - 2 µM, 1h	4	2	1009	388.2	45	23.68	3.281
NS1-ZF5.3^{Rho} - 1 µM, 1h	4	2	31450	985.5	43	122.9	10.31
NS1-ZF5.3^{Rho} - 2 µM, 1h	4	2	63974	1735	32	268.3	30.16
DHFR^{Rho} - RISC-free siRNA	5	2	1005	4341.1	23	24.56	2.947
DHFR^{Rho} - VPS39 siRNA	5	2	7072.7	171.9	21	24.02	2.823
DHFR^{Rho} - TGF-BRAP1 siRNA	5	2	1061	362.7	35	22.60	2.886
DHFR^{Rho} + MTX - RISC-free siRNA	5	2	393.8	86.45	30	11.04	1.932

DHFR^{Rho} + MTX - VPS39 siRNA	5	2	322.1	70.06	20	8.993	1.472
DHFR^{Rho} + MTX - TGF-BRAP1 siRNA	5	2	407.9	128.8	36	9.480	2.000
ZF5.3-DHFR^{Rho} - RISC-free siRNA	5	2	36604	3815	51	288.2	26.50
ZF5.3-DHFR^{Rho} - VPS39 siRNA	5	2	26052	1954	26	140.3	15.96
ZF5.3-DHFR^{Rho} - TGF-BRAP1 siRNA	5	2	36336	3836	41	422.2	61.72
ZF5.3-DHFR^{Rho} + MTX - RISC-free siRNA	5	2	11222	688.2	40	209.0	14.38
ZF5.3-DHFR^{Rho} + MTX - VPS39 siRNA	5	2	8580	11.10	25	177.8	22.16
ZF5.3-DHFR^{Rho} + MTX - TGF-BRAP1 siRNA	5	2	10689	1010	38	183.5	16.11
ZF5.3-SNAP^{Rho} - RISC-free siRNA	5	2	1484	195.5	20	55.83	7.835
ZF5.3-SNAP^{Rho} - VPS39 siRNA	5	3	1174	92.93	20	44.20	5.406
ZF5.3-SNAP^{Rho} - TGF-BRAP1 siRNA	5	2	2118	724.0	30	51.02	4.440
ZF5.3-AGT54^{Rho} - RISC-free siRNA	5	3	6258	693.6	45	129.5	18.84
ZF5.3-AGT54^{Rho} - VPS39 siRNA	5	4	4113	371.3	15	107.3	17.15
ZF5.3-AGT54^{Rho} - TGF-BRAP1 siRNA	5	3	9150	561.9	28	124.3	11.99
ZF5.3-GE-AGT^{Rho} - RISC-free siRNA	5	2	5530	194.0	44	291.6	30.06
ZF5.3-GE-AGT^{Rho} - VPS39 siRNA	5	2	3456	348.0	28	141.6	24.40
ZF5.3-GE-AGT^{Rho} - TGF-	5	2	6284	83.50	42	217.1	129.5

BRAP1 siRNA							
NS1-ZF5.3^{Rho} - RISC-free siRNA	5	2	17505	978.5	49	155.0	12.98
NS1-ZF5.3^{Rho} - VPS39 siRNA	5	2	14193	863.0	25	99.46	12.22
NS1-ZF5.3^{Rho} - TGF-BRAP1 siRNA	5d	2	18519	1778	37	98.68	9.467

2.7 Acknowledgments

I am extremely appreciative to all the people who contributed to this project, including Dr. Xizi Zhang for her experimental and intellectual contributions to analysis of SNAP-tag delivery, Angel Vázquez Maldonado for preparing and delivering the NS1 proteins, Neville Dadina for his help with super-resolution imaging, Lauren Lesiak for providing the SiR-chloroalkane ligand for STED imaging, and Miriam Hood and Prof. Susan Marqusee for answering many CD-related questions over the years.

2.8 References

(1) Leader, B.; Baca, Q. J.; Golan, D. E. Protein Therapeutics: A Summary and Pharmacological Classification. *Nat. Rev. Drug Discov.* **2008**, *7* (1), 21–39. https://doi.org/10.1038/nrd2399.

(2) Hald Albertsen, C.; Kulkarni, J. A.; Witzigmann, D.; Lind, M.; Petersson, K.; Simonsen, J. B. The Role of Lipid Components in Lipid Nanoparticles for Vaccines and Gene Therapy. *Adv. Drug Deliv. Rev.* **2022**, *188*, 114416. https://doi.org/10.1016/j.addr.2022.114416.

(3) Appelbaum, J. S.; LaRochelle, J. R.; Smith, B. A.; Balkin, D. M.; Holub, J. M.; Schepartz, A. Arginine Topology Controls Escape of Minimally Cationic Proteins from Early Endosomes to the Cytoplasm. *Chem. Biol.* **2012**, *19* (7), 819–830. https://doi.org/10.1016/j.chembiol.2012.05.022.

(4) LaRochelle, J. R.; Cobb, G. B.; Steinauer, A.; Rhoades, E.; Schepartz, A. Fluorescence Correlation Spectroscopy Reveals Highly Efficient Cytosolic Delivery of Certain Penta-Arg Proteins and Stapled Peptides. *J. Am. Chem. Soc.* **2015**, *137* (7), 2536–2541. https://doi.org/10.1021/ja510391n.

(5) Steinauer, A.; LaRochelle, J. R.; Knox, S. L.; Wissner, R. F.; Berry, S.; Schepartz, A. HOPS-Dependent Endosomal Fusion Required for Efficient Cytosolic Delivery of Therapeutic Peptides and Small Proteins. *Proc. Natl. Acad. Sci.* **2019**, *116* (2), 512–521. https://doi.org/10.1073/pnas.1812044116.

(6) Zhang, X.; Cattoglio, C.; Zoltek, M.; Vetralla, C.; Mozumdar, D.; Schepartz, A. Dose-Dependent Nuclear Delivery and Transcriptional Repression with a Cell-Penetrant MeCP2. *ACS Cent. Sci.* **2023**, *9* (2), 277–288. https://doi.org/10.1021/acscentsci.2c01226.

(7) Wissner, R. F.; Steinauer, A.; Knox, S. L.; Thompson, A. D.; Schepartz, A. Fluorescence Correlation Spectroscopy Reveals Efficient Cytosolic Delivery of Protein Cargo by Cell-Permeant Miniature Proteins. *ACS Cent. Sci.* **2018**, *4* (10), 1379–1393. https://doi.org/10.1021/acscentsci.8b00446.

(8) Knox, S. L.; Wissner, R.; Piszkiewicz, S.; Schepartz, A. Cytosolic Delivery of Argininosuccinate Synthetase Using a Cell-Permeant Miniature Protein. *ACS Cent. Sci.* **2021**, *7* (4), 641–649. https://doi.org/10.1021/acscentsci.0c01603.

(9) Shen, F.; Zheng, G.; Setegne, M.; Tenglin, K.; Izadi, M.; Xie, H.; Zhai, L.; Orkin, S. H.; Dassama, L. M. K. A Cell-Permeant Nanobody-Based Degrader That Induces Fetal Hemoglobin. *ACS Cent. Sci.* **2022**, *8* (12), 1695–1703. https://doi.org/10.1021/acscentsci.2c00998.

(10) Arkowitz, R. A.; Joly, J. C.; Wickner, W. Translocation Can Drive the Unfolding of a Preprotein Domain. *EMBO J.* **1993**, *12* (1), 243–253.

(11) Lycklama a Nijeholt, J. A.; Driessen, A. J. M. The Bacterial Sec-Translocase: Structure and Mechanism. *Philos. Trans. R. Soc. B Biol. Sci.* **2012**, *367* (1592), 1016–1028. https://doi.org/10.1098/rstb.2011.0201.

(12) Eilers, M.; Schatz, G. Binding of a Specific Ligand Inhibits Import of a Purified Precursor Protein into Mitochondria. *Nature* **1986**, *322* (6076), 228–232. https://doi.org/10.1038/322228a0.

(13) Wienhues, U.; Becker, K.; Schleyer, M.; Guiard, B.; Tropschug, M.; Horwich, A. L.; Pfanner, N.; Neupert, W. Protein Folding Causes an Arrest of Preprotein

Translocation into Mitochondria in Vivo. *J. Cell Biol.* **1991**, *115* (6), 1601–1609. https://doi.org/10.1083/jcb.115.6.1601.
(14) Vestweber, D.; Brunner, J.; Baker, A.; Schatz, G. A 42K Outer-Membrane Protein Is a Component of the Yeast Mitochondrial Protein Import Site. *Nature* **1989**, *341* (6239), 205–209. https://doi.org/10.1038/341205a0.
(15) Kim, P. K.; Hettema, E. H. Multiple Pathways for Protein Transport to Peroxisomes. *J. Mol. Biol.* **2015**, *427* (6, Part A), 1176–1190. https://doi.org/10.1016/j.jmb.2015.02.005.
(16) Rabouille, C.; Malhotra, V.; Nickel, W. Diversity in Unconventional Protein Secretion. *J. Cell Sci.* **2012**, *125* (22), 5251–5255. https://doi.org/10.1242/jcs.103630.
(17) Pei, D.; Dalbey, R. E. Membrane Translocation of Folded Proteins. *J. Biol. Chem.* **2022**, *298* (7), 102107. https://doi.org/10.1016/j.jbc.2022.102107.
(18) Chávez-García, C.; Hénin, J.; Karttunen, M. Multiscale Computational Study of the Conformation of the Full-Length Intrinsically Disordered Protein MeCP2. *J. Chem. Inf. Model.* **2022**, *62* (4), 958–970. https://doi.org/10.1021/acs.jcim.1c01354.
(19) Salvador, N.; Aguado, C.; Horst, M.; Knecht, E. Import of a Cytosolic Protein into Lysosomes by Chaperone-Mediated Autophagy Depends on Its Folding State*. *J. Biol. Chem.* **2000**, *275* (35), 27447–27456. https://doi.org/10.1016/S0021-9258(19)61529-2.
(20) Agarraberes, F. A.; Dice, J. F. A Molecular Chaperone Complex at the Lysosomal Membrane Is Required for Protein Translocation. *J. Cell Sci.* **2001**, *114* (13), 2491–2499. https://doi.org/10.1242/jcs.114.13.2491.
(21) Shi, J.; Hu, X.; Guo, Y.; Wang, L.; Ji, J.; Li, J.; Zhang, Z.-R. A Technique for Delineating the Unfolding Requirements for Substrate Entry into Retrotranslocons during Endoplasmic Reticulum–Associated Degradation. *J. Biol. Chem.* **2019**, *294* (52), 20084–20096. https://doi.org/10.1074/jbc.RA119.010019.
(22) Beaumelle, B.; Taupiac, M.-P.; Lord, J. M.; Roberts, L. M. Ricin A Chain Can Transport Unfolded Dihydrofolate Reductase into the Cytosol*. *J. Biol. Chem.* **1997**, *272* (35), 22097–22102. https://doi.org/10.1074/jbc.272.35.22097.
(23) Klingenberg, O.; Olsnes, S. Ability of Methotrexate to Inhibit Translocation to the Cytosol of Dihydrofolate Reductase Fused to Diphtheria Toxin. *Biochem. J.* **1996**, *313* (Pt 2), 647–653.
(24) Haug, G.; Wilde, C.; Leemhuis, J.; Meyer, D. K.; Aktories, K.; Barth, H. Cellular Uptake of Clostridium Botulinum C2 Toxin: Membrane Translocation of a Fusion Toxin Requires Unfolding of Its Dihydrofolate Reductase Domain. *Biochemistry* **2003**, *42* (51), 15284–15291. https://doi.org/10.1021/bi0354278.
(25) Kim, S. A.; Heinze, K. G.; Schwille, P. Fluorescence Correlation Spectroscopy in Living Cells. *Nat. Methods* **2007**, *4* (11), 963–973. https://doi.org/10.1038/nmeth1104.
(26) Knox, S. L.; Steinauer, A.; Alpha-Cobb, G.; Trexler, A.; Rhoades, E.; Schepartz, A. Chapter Twenty-One - Quantification of Protein Delivery in Live Cells Using Fluorescence Correlation Spectroscopy. In *Methods in Enzymology*; Chenoweth, D. M., Ed.; Chemical Tools for Imaging, Manipulating, and Tracking Biological Systems: Diverse Chemical, Optical and Bioorthogonal Methods; Academic Press, 2020; Vol. 641, pp 477–505. https://doi.org/10.1016/bs.mie.2020.05.007.

(27) Schwille, P. Fluorescence Correlation Spectroscopy and Its Potential for Intracellular Applications. *Cell Biochem. Biophys.* **2001**, *34* (3), 383–408. https://doi.org/10.1385/CBB:34:3:383.
(28) Magde, D.; Elson, E.; Webb, W. W. Thermodynamic Fluctuations in a Reacting System—Measurement by Fluorescence Correlation Spectroscopy. *Phys. Rev. Lett.* **1972**, *29* (11), 705–708. https://doi.org/10.1103/PhysRevLett.29.705.
(29) Schwille, P.; Haustein, E. Fluorescence Correlation Spectroscopy.
(30) Elson, E. L. Fluorescence Correlation Spectroscopy: Past, Present, Future. *Biophys. J.* **2011**, *101* (12), 2855–2870. https://doi.org/10.1016/j.bpj.2011.11.012.
(31) Waltham, M. C.; Holland, J. W.; Nixon, P. F.; Winzor, D. J. Thermodynamic Characterization of the Interactions of Methotrexate with Dihydrofolate Reductase by Quantitative Affinity Chromatography. *Biochem. Pharmacol.* **1988**, *37* (3), 541–545. https://doi.org/10.1016/0006-2952(88)90226-2.
(32) Werkheiser, W. C. Specific Binding of 4-Amino Folic Acid Analogues by Folic Acid Reductase. *J. Biol. Chem.* **1961**, *236* (3), 888–893. https://doi.org/10.1016/S0021-9258(18)64324-8.
(33) Swanwick, R. S.; Daines, A. M.; Tey, L.-H.; Flitsch, S. L.; Allemann, R. K. Increased Thermal Stability of Site-Selectively Glycosylated Dihydrofolate Reductase. *ChemBioChem* **2005**, *6* (8), 1338–1340. https://doi.org/10.1002/cbic.200500103.
(34) Takahashi, K.; Nishiyama, T.; Umezawa, N.; Inoue, Y.; Akiba, I.; Dewa, T.; Ikeda, A.; Mizuno, T. Delivery of External Proteins into the Cytoplasm Using Protein Capsules Modified with IgG on the Surface, Created from the Amphiphilic Two Helix-Bundle Protein OLE-ZIP. *Chem. Commun.* **2024**, *60* (8), 968–971. https://doi.org/10.1039/D3CC05347D.
(35) Shah, N. H.; Eryilmaz, E.; Cowburn, D.; Muir, T. W. Naturally Split Inteins Assemble through a “Capture and Collapse” Mechanism. *J. Am. Chem. Soc.* **2013**, *135* (49), 18673–18681. https://doi.org/10.1021/ja4104364.
(36) Stevens, A. J.; Brown, Z. Z.; Shah, N. H.; Sekar, G.; Cowburn, D.; Muir, T. W. Design of a Split Intein with Exceptional Protein Splicing Activity. *J. Am. Chem. Soc.* **2016**, *138* (7), 2162–2165. https://doi.org/10.1021/jacs.5b13528.
(37) Shah, N. H.; Muir, T. W. Inteins: Nature’s Gift to Protein Chemists. *Chem. Sci. R. Soc. Chem. 2010* **2014**, *5* (1), 446–461. https://doi.org/10.1039/C3SC52951G.
(38) Stevens, A. J.; Sekar, G.; Shah, N. H.; Mostafavi, A. Z.; Cowburn, D.; Muir, T. W. A Promiscuous Split Intein with Expanded Protein Engineering Applications. *Proc. Natl. Acad. Sci.* **2017**, *114* (32), 8538–8543. https://doi.org/10.1073/pnas.1701083114.
(39) Thillet, J.; Absil, J.; Stone, S. R.; Pictet, R. Site-Directed Mutagenesis of Mouse Dihydrofolate Reductase. Mutants with Increased Resistance to Methotrexate and Trimethoprim. *J. Biol. Chem.* **1988**, *263* (25), 12500–12508. https://doi.org/10.1016/S0021-9258(18)37783-4.
(40) Mollwitz, B.; Brunk, E.; Schmitt, S.; Pojer, F.; Bannwarth, M.; Schiltz, M.; Rothlisberger, U.; Johnsson, K. Directed Evolution of the Suicide Protein O6-Alkylguanine-DNA Alkyltransferase for Increased Reactivity Results in an Alkylated Protein with Exceptional Stability. *Biochemistry* **2012**, *51* (5), 986–994. https://doi.org/10.1021/bi2016537.

(41) Juillerat, A.; Gronemeyer, T.; Keppler, A.; Gendreizig, S.; Pick, H.; Vogel, H.; Johnsson, K. Directed Evolution of O6-Alkylguanine-DNA Alkyltransferase for Efficient Labeling of Fusion Proteins with Small Molecules In Vivo. *Chem. Biol.* **2003**, *10* (4), 313–317. https://doi.org/10.1016/S1074-5521(03)00068-1.

(42) Juillerat, A.; Heinis, C.; Sielaff, I.; Barnikow, J.; Jaccard, H.; Kunz, B.; Terskikh, A.; Johnsson, K. Engineering Substrate Specificity of O6-Alkylguanine-DNA Alkyltransferase for Specific Protein Labeling in Living Cells. *ChemBioChem* **2005**, *6* (7), 1263–1269. https://doi.org/10.1002/cbic.200400431.

(43) Gronemeyer, T.; Chidley, C.; Juillerat, A.; Heinis, C.; Johnsson, K. Directed Evolution of O6-Alkylguanine-DNA Alkyltransferase for Applications in Protein Labeling. *Protein Eng. Des. Sel.* **2006**, *19* (7), 309–316. https://doi.org/10.1093/protein/gzl014.

(44) Craig, E. A. Hsp70 at the Membrane: Driving Protein Translocation. *BMC Biol.* **2018**, *16* (1), 11. https://doi.org/10.1186/s12915-017-0474-3.

(45) Madshus, I. H.; Olsnes, S.; Stenmark, H. Membrane Translocation of Diphtheria Toxin Carrying Passenger Protein Domains. *Infect. Immun.* **1992**, *60* (8), 3296–3302.

(46) Thompson, D. B.; Villaseñor, R.; Dorr, B. M.; Zerial, M.; Liu, D. R. Cellular Uptake Mechanisms and Endosomal Trafficking of Supercharged Proteins. *Chem. Biol.* **2012**, *19* (7), 831–843. https://doi.org/10.1016/j.chembiol.2012.06.014.

(47) Madani, F.; Lindberg, S.; Langel, Ü.; Futaki, S.; Gräslund, A. Mechanisms of Cellular Uptake of Cell-Penetrating Peptides. *J. Biophys.* **2011**, *2011*, 414729. https://doi.org/10.1155/2011/414729.

(48) Jin, B.; Odongo, S.; Radwanska, M.; Magez, S. Nanobodies: A Review of Generation, Diagnostics and Therapeutics. *Int. J. Mol. Sci.* **2023**, *24* (6), 5994. https://doi.org/10.3390/ijms24065994.

(49) Koide, A.; Bailey, C. W.; Huang, X.; Koide, S. The Fibronectin Type III Domain as a Scaffold for Novel Binding proteins11Edited by J. Wells. *J. Mol. Biol.* **1998**, *284* (4), 1141–1151. https://doi.org/10.1006/jmbi.1998.2238.

(50) Carrasco-López, C.; Zhao, E. M.; Gil, A. A.; Alam, N.; Toettcher, J. E.; Avalos, J. L. Development of Light-Responsive Protein Binding in the Monobody Non-Immunoglobulin Scaffold. *Nat. Commun.* **2020**, *11* (1), 4045. https://doi.org/10.1038/s41467-020-17837-7.

(51) Sha, F.; Salzman, G.; Gupta, A.; Koide, S. Monobodies and Other Synthetic Binding Proteins for Expanding Protein Science. *Protein Sci.* **2017**, *26* (5), 910–924. https://doi.org/10.1002/pro.3148.

(52) Spencer-Smith, R.; Koide, A.; Zhou, Y.; Eguchi, R. R.; Sha, F.; Gajwani, P.; Santana, D.; Gupta, A.; Jacobs, M.; Herrero-Garcia, E.; Cobbert, J.; Lavoie, H.; Smith, M.; Rajakulendran, T.; Dowdell, E.; Okur, M. N.; Dementieva, I.; Sicheri, F.; Therrien, M.; Hancock, J. F.; Ikura, M.; Koide, S.; O'Bryan, J. P. Inhibition of RAS Function through Targeting an Allosteric Regulatory Site. *Nat. Chem. Biol.* **2017**, *13* (1), 62–68. https://doi.org/10.1038/nchembio.2231.

(53) Litvinovich, S. V.; Brew, S. A.; Aota, S.; Akiyama, S. K.; Haudenschild, C.; Ingham, K. C. Formation of Amyloid-like Fibrils by Self-Association of a Partially Unfolded Fibronectin Type III module11Edited by R. Huber. *J. Mol. Biol.* **1998**, *280* (2), 245–258. https://doi.org/10.1006/jmbi.1998.1863.

(54) Kruziki, M. A.; Bhatnagar, S.; Woldring, D. R.; Duong, V. T.; Hackel, B. J. A 45-Amino-Acid Scaffold Mined from the PDB for High-Affinity Ligand Engineering. *Chem. Biol.* **2015**, *22* (7), 946–956. https://doi.org/10.1016/j.chembiol.2015.06.012.
(55) Messler, S.; Kropp, S.; Episkopou, V.; Felici, A.; Würthner, J.; Lemke, R.; Jerabek-Willemsen, M.; Willecke, R.; Scheu, S.; Pfeffer, K.; Wurthner, J. U. The TGF-β Signaling Modulators TRAP1/TGFBRAP1 and VPS39/Vam6/TLP Are Essential for Early Embryonic Development. *Immunobiology* **2011**, *216* (3), 343–350. https://doi.org/10.1016/j.imbio.2010.07.006.
(56) Luo, H.; Lin, Y.; Liu, T.; Lai, F.-L.; Zhang, C.-T.; Gao, F.; Zhang, R. DEG 15, an Update of the Database of Essential Genes That Includes Built-in Analysis Tools. *Nucleic Acids Res.* **2021**, *49* (D1), D677–D686. https://doi.org/10.1093/nar/gkaa917.
(57) Song, H.; Orr, A. S.; Lee, M.; Harner, M. E.; Wickner, W. T. HOPS Recognizes Each SNARE, Assembling Ternary Trans-Complexes for Rapid Fusion upon Engagement with the 4th SNARE. *eLife* **2020**, *9*, e53559. https://doi.org/10.7554/eLife.53559.
(58) van der Kant, R.; Jonker, C. T. H.; Wijdeven, R. H.; Bakker, J.; Janssen, L.; Klumperman, J.; Neefjes, J. Characterization of the Mammalian CORVET and HOPS Complexes and Their Modular Restructuring for Endosome Specificity*. *J. Biol. Chem.* **2015**, *290* (51), 30280–30290. https://doi.org/10.1074/jbc.M115.688440.
(59) Shvarev, D.; Schoppe, J.; König, C.; Perz, A.; Füllbrunn, N.; Kiontke, S.; Langemeyer, L.; Januliene, D.; Schnelle, K.; Kümmel, D.; Fröhlich, F.; Moeller, A.; Ungermann, C. Structure of the HOPS Tethering Complex, a Lysosomal Membrane Fusion Machinery. *eLife* **2022**, *11*, e80901. https://doi.org/10.7554/eLife.80901.
(60) Sőth, Á.; Molnár, M.; Lőrincz, P.; Simon-Vecsei, Z.; Juhász, G. CORVET-Specific Subunit Levels Determine the Balance between HOPS/CORVET Endosomal Tethering Complexes. *Sci. Rep.* **2024**, *14* (1), 10146. https://doi.org/10.1038/s41598-024-59775-0.
(61) Becker, L.; Singh Badwal, J.; Brandl, F.; Verdurmen, W. P. R.; Plückthun, A. Thermodynamic Stability Is a Strong Predictor for the Delivery of DARPins to the Cytosol via Anthrax Toxin. *Pharmaceutics* **2021**, *13* (8), 1285. https://doi.org/10.3390/pharmaceutics13081285.
(62) Batistatou, N.; Kritzer, J. A. Investigation of Sequence-Penetration Relationships of Antisense Oligonucleotides. *ChemBioChem* **2023**, *24* (9), e202300009. https://doi.org/10.1002/cbic.202300009.
(63) Diaz, J.; Pietsch, M.; Davila, M.; Jaimes, G.; Hudson, A.; Pellois, J.-P. Elucidating the Impact of Payload Conjugation on the Cell-Penetrating Efficiency of the Endosomal Escape Peptide dfTAT: Implications for Future Designs for CPP-Based Delivery Systems. *Bioconjug. Chem.* **2023**, *34* (10), 1861–1872. https://doi.org/10.1021/acs.bioconjchem.3c00369.
(64) Nikam, R.; Kulandaisamy, A.; Harini, K.; Sharma, D.; Gromiha, M. M. ProThermDB: Thermodynamic Database for Proteins and Mutants Revisited after

15 Years. *Nucleic Acids Res.* **2021**, *49* (D1), D420–D424. https://doi.org/10.1093/nar/gkaa1035.

(65) Quaglia, F.; Mészáros, B.; Salladini, E.; Hatos, A.; Pancsa, R.; Chemes, L. B.; Pajkos, M.; Lazar, T.; Peña-Díaz, S.; Santos, J.; Ács, V.; Farahi, N.; Fichó, E.; Aspromonte, M. C.; Bassot, C.; Chasapi, A.; Davey, N. E.; Davidović, R.; Dobson, L.; Elofsson, A.; Erdős, G.; Gaudet, P.; Giglio, M.; Glavina, J.; Iserte, J.; Iglesias, V.; Kálmán, Z.; Lambrughi, M.; Leonardi, E.; Longhi, S.; Macedo-Ribeiro, S.; Maiani, E.; Marchetti, J.; Marino-Buslje, C.; Mészáros, A.; Monzon, A. M.; Minervini, G.; Nadendla, S.; Nilsson, J. F.; Novotný, M.; Ouzounis, C. A.; Palopoli, N.; Papaleo, E.; Pereira, P. J. B.; Pozzati, G.; Promponas, V. J.; Pujols, J.; Rocha, A. C. S.; Salas, M.; Sawicki, L. R.; Schad, E.; Shenoy, A.; Szaniszló, T.; Tsirigos, K. D.; Veljkovic, N.; Parisi, G.; Ventura, S.; Dosztányi, Z.; Tompa, P.; Tosatto, S. C. E.; Piovesan, D. DisProt in 2022: Improved Quality and Accessibility of Protein Intrinsic Disorder Annotation. *Nucleic Acids Res.* **2022**, *50* (D1), D480–D487. https://doi.org/10.1093/nar/gkab1082.

(66) Rodríguez-Silvestre, P.; Laub, M.; Krawczyk, P. A.; Davies, A. K.; Schessner, J. P.; Parveen, R.; Tuck, B. J.; McEwan, W. A.; Borner, G. H. H.; Kozik, P. Perforin-2 Is a Pore-Forming Effector of Endocytic Escape in Cross-Presenting Dendritic Cells. *Science* **2023**, *380* (6651), 1258–1265. https://doi.org/10.1126/science.adg8802.

(67) Wu, Q.; Ploegh, H. L.; Truttmann, M. C. Hepta-Mutant Staphylococcus Aureus Sortase A (SrtA7m) as a Tool for in Vivo Protein Labeling in Caenorhabditis Elegans. *ACS Chem. Biol.* **2017**, *12* (3), 664–673. https://doi.org/10.1021/acschembio.6b00998.

(68) Knox, S. L.; Wissner, R.; Piszkiewicz, S.; Schepartz, A. Cytosolic Delivery of Argininosuccinate Synthetase Using a Cell-Permeant Miniature Protein. *ACS Cent. Sci.* **2021**, *7* (4), 641–649. https://doi.org/10.1021/acscentsci.0c01603.

(69) Wingfield, P. T. Protein Precipitation Using Ammonium Sulfate. *Curr. Protoc. Protein Sci. Editor. Board John E Coligan Al* **2001**, *APPENDIX 3*, Appendix-3F. https://doi.org/10.1002/0471140864.psa03fs13.

(70) Greenfield, N. J. Using Circular Dichroism Spectra to Estimate Protein Secondary Structure. *Nat. Protoc.* **2006**, *1* (6), 2876–2890. https://doi.org/10.1038/nprot.2006.202.

(71) Zheng, S.; Dadina, N.; Mozumdar, D.; Lesiak, L.; Martinez, K. N.; Miller, E. W.; Schepartz, A. Long-Term Super-Resolution Inner Mitochondrial Membrane Imaging with a Lipid Probe. *Nat. Chem. Biol.* **2023**, 1–10. https://doi.org/10.1038/s41589-023-01450-y.

CHAPTER THREE

Exploiting pH Sensitivity and Fluorescence Lifetime to Monitor and Quantify Intracellular Trafficking of ZF5.3

3.1 Abstract

Intracellular trafficking pathways of exogenously delivered biomolecules are of enormous interest for the optimization of novel delivery strategies. Most macromolecules enter the cell by endocytosis, where they become trapped in membrane-bound endosomes. The ability of a macromolecule to interact with and ultimately escape from endocytic vesicles is a key property for successful delivery. However, there are few strategies to comprehensively track the vesicular properties of endocytosed material. A hallmark of endosomes is their low pH, a property often exploited by macromolecular delivery vehicles. The increasing acidity of the endocytic pathway presents an opportunity to develop pH-responsive tools to explore both trafficking and delivery of biotherapeutics. Here, we use chemical and cell biology tools to track the pH microenvironment experienced by the model peptide ZF5.3 during its intracellular delivery pathway. We discuss attempts to design a ratiometric fluorescent intensity-based assay to monitor endosomal escape, which was refined by introducing the measurement of fluorescence lifetime. Using fluorescence lifetime imaging microscopy (FLIM) in live cells, we demonstrated that ZF5.3 experiences diverse microenvironments within the endocytic pathway that correspond to vesicular pH. We further integrated FLIM analysis into fluorescence correlation spectroscopy (FCS) to enrich measurements of cytosolic concentration by filtering out fluorescent signal derived from acidic vesicles. Such lifetime analysis provides a complete snapshot of ZF5.3 localization in the endocytic pathway with a single experiment and paves the way to systematically evaluate the relationship between pH and biomolecule delivery.

3.2 Introduction

The delivery of proteins and nucleic acids to the cell cytosol or nucleus is a major obstacle for modern drug development. Cellular entry of biotherapeutics occurs primarily via endocytosis, a blanket term for a variety of internalization pathways that converge on the formation of the early endosome. The specific route of entry varies by cell type, dosage, modality, and even cargo and can include clathrin-mediated endocytosis, fast endophilin-mediated endocytosis, clathrin-independent endocytosis, micropinocytosis, and phagocytosis.[1,2] The endocytic pathway provides spatially restricted compartments that are biochemically distinct from the cell cytosol and enable the cell to selectively sort and degrade extracellular stimuli. For macromolecular delivery, however, endosomes present a barrier to reaching the cytosol or nucleus by trapping material in membrane-bound vesicles.

Endosomes are distinguishable from one another by two key traits: membrane composition and luminal pH. Early endosomal membranes contain cholesterol, phosphatidylserine (PS), and phosphatidylinositol 3-phosphate (PI(3)P), whereas late endosomes are enriched with the anionic lipid bis(monoacylglycerol)phosphate (BMP), particularly in intraluminal vesicles.[3] The lipid composition of a vesicle determines its membrane protein landscape, enabling the use of canonical markers like Rab proteins to identify these vesicles within a cell.[3–5]

The second identifying attribute of an endosome is its luminal pH.[6] The proton concentration within an endocytic vesicle is tightly regulated through the concerted activity of proton influx and efflux pumps and counter-ion transporters.[7] Vacuolar ATPase (V-ATPase) is the predominant route for proton influx and consists of two subunits, one responsible for catalysis and the other for anchoring to the membrane. The degree of association between the two subunits controls proton pump activity and is a primary determinant of intravesicular pH.[8,9] Lipid composition has been suggested as a mechanism to control the ratio of assembled (and therefore active) V-ATPase, allowing the pH of distinct vesicles to be differentially maintained.[10] The activity of V-ATPase is also regulated by anion transporters that counteract the buildup of positive charge, further contributing to endosomal pH homeostasis.[9] Together, these mechanisms establish a pH of ~6.1-6.8 in early endosomes, ~5.0 – 6.0 in late endosomes, and ~4.5 – 5.0 in lysosomes.[6,7,11] This endosomal proton concentration and resulting membrane potential have numerous biological implications, including clearance of neurodegenerative aggregates,[7,12,13] cytosolic entry of pathogens like viruses,[14] and proliferation and prognosis of many cancers,[15] among many others.

In the context of biotherapeutic delivery, endosomal pH plays a critical role. Toxin-mediated delivery systems such as anthrax, botulinum, or diphtheria undergo a pH-dependent conformational change to generate pores in endosomal membranes.[16] Synthetic modalities like nanoparticles are often engineered to swell or disrupt membranes at low pH to facilitate delivery of their contents.[17,18] Mini proteins and peptides for therapeutic delivery have been designed or demonstrated to exploit pH-induced structural changes for membrane lysis or selective escape.[19–22] While these different molecular agents take advantage of endosomal pH for their activity, many questions remain about the trafficking pathways they exploit in live cells.

For instance, one proposed mechanism for endosomal escape by such non-viral carriers is the proton sponge effect, in which pH-induced protonation of amino groups on cationic polymers results in a massive proton influx. This influx is suspected to produce osmotic swelling and membrane disruption.[23] Conflicting reports have both supported and disputed this theory, leaving many questions over the precise effect of pH on delivery pathways.[24–26] In some cases, macromolecule delivery induces cytotoxicity by causing defects in endosomal acidification, potentially by arresting endosomal maturation.[27] How and why this process affects both cellular health and the efficiency of delivery is unclear. Significant questions also remain on where exogenously delivered macromolecules localize within the endocytic pathway, and from which compartment(s) escape actually occurs.[19,28–30]

The increasingly low pH of the endocytic pathway presents an opportunity to develop pH-responsive tools to explore both trafficking and delivery of biotherapeutics. Such tools can be used in conjunction with or even in place of traditional methods, like colocalization with known endosomal markers, to gain insights into how macromolecules interact with and impact endocytic vesicles. The conjugation of pH-sensitive fluorophores to study intracellular biologic delivery has been reported by others to measure cytosolic localization by a pH-dependent change in brightness[31,32] or track endosomal escape

using ratiometric multi-fluorophore probes.[33,34] While useful, these existing tools rely only on relative changes in fluorescence intensity that are susceptible to background fluorescence, spectral overlap, and changes in concentration, and typically provide only "on" or "off" signals. Ratiometric probes can be more quantitative, but they may be subject to differential photobleaching and require modification of the delivered material with multiple dyes that can significantly impact the molecule's physicochemical properties. There remains a need for quantitative tools that capture the biological processes associated with intracellular delivery and trafficking with high sensitivity and minimal perturbation.

In this chapter, we use chemical and cell biology tools to study the pH microenvironment experienced by the model peptide ZF5.3 during its intracellular delivery pathway. We first attempted to design an assay that would enable ratiometric measurements of endosomal escape with a single fluorophore that exhibited a pH-dependent shift in emission. Unfortunately, the conjugation of this dye to ZF5.3 altered its photophysical properties and reduced its pH-dependent spectral separation. To circumvent these problems, we turned instead to an alternative fluorophore property known as fluorescence lifetime to study ZF5.3 trafficking. Fluorescence lifetime is the length of time for which a fluorophore remains in the excited state, and is affected significantly by both fluorophore structure and local environment. Using fluorescence lifetime imaging microscopy (FLIM) in live cells, we demonstrated that ZF5.3 experiences diverse microenvironments within the endocytic pathway that correspond to vesicular pH. FLIM revealed clear changes in the pH of ZF5.3-containing vesicles with both siRNA and small molecule manipulation, establishing this tool as a mechanism to track the pH of vesicles containing exogenously delivered biomolecules. We further integrated FLIM analysis into fluorescence correlation spectroscopy (FCS) to refine measurements of cytosolic concentration by filtering out lifetimes derived from acidic vesicles. We envision these fluorescence lifetime measurements will provide insights into mechanisms used by ZF5.3 to traffic cargos, including how pH both informs and is impacted by various delivery pathways, and create a framework for studying how other delivery agents integrate with the endosomal pathway.

3.3 Results

3.3.1 Attempts to design a high-throughput, ratiometric readout for endosomal escape

To develop a fluorescence tool that would report on both endosomally sequestered and cytosolic material with a single dye, we required a fluorophore with two key properties: a pKa around pH ~6.5 (the pH of an early endosome), and a pH-dependent shift (but not decrease) in emission as a result of protonation. Many dyes have been reported for the study of acidic vesicles and intracellular delivery,[35] including fluorescein and its derivatives,[31,33,36,37] pHrodo red and green,[27,38] Oregon green,[39] and LysoSensor, among others.[32,40–42] Notably, while these pH indicators have excellent dynamic range within the pH range of endocytic vesicles, they function predominantly by an increase or decrease in brightness at a single emission wavelength as a result of protonation and therefore are

not suitable for quantifying the ratio of endosomal to cytosolic signal. One LysoSensor variant (DND-160) exhibits a significantly blue-shifted emission spectrum with increasing pH,[35] but its pKa is too low (~4.5) for the purposes of this study. We turned instead to the seminaphthorhodafluor (SNARF) family of dyes, known for their high photostability and well-established shifts in emission with pH. Though the most common SNARF indicator, Carboxy-SNARF-1, has too high a pKa to reliably detect endosomal escape (pKa ~ 7.5), a fluorinated derivative called Carboxy-SNARF-4F (C-SNARF-4F) was developed with similar spectral properties but a lower pKa (~6.5). C-SNARF-4F has been thoroughly spectrally characterized and even demonstrated to be compatible with fluorescence correlation spectroscopy,[43] and thus was chosen to develop further for this study.

To generate a C-SNARF-4F-labeled ZF5.3 molecule (hereby referred to as SNARF-ZF5.3), we synthesized a version of the C-SNARF-4F dye with a bioconjugation handle. The commercially available C-SNARF-4F 5-(and-6)-carboxylic acid was modified with a dibenzocyclooctyne (DBCO) click chemistry handle at the 5' or 6' positions (Fig. S3.1a). To confirm that the addition of a DBCO group did not alter the pH sensitivity, we spectroscopically characterized SNARF-4F-DBCO at a variety of physiologically relevant pHs. Both the absorbance (Fig. S3.2a) and intensity (Fig. 3.1a) spectra reveal clearly discernible pH-dependent shifts as expected. When excited at either 514 nm or 550 nm, C-SNARF-4F-DBCO exhibits a pH-dependent change in the fluorescence intensity ratio between 633 nm and 586 nm. Fluorescence intensity reaches a peak at 586 nm when pH < 7.0, while the intensity peaks at 633 nm when pH > 7.0; intensity at both wavelengths is roughly equal when pH = 7.0. This shift is within an ideal range for studying cytosolic versus endosomal fluorescence, where cytosolic pH is expected between 7.0-7.4[35] and endosomal pH is expected between 4.5 – 6.5.[6]

We next conjugated C-SNARF-4F-DBCO to ZF5.3 using click chemistry. ZF5.3 was synthesized with an N-terminal azide as described previously[19] and incubated with 5 equivalents of SNARF-DBCO in DMSO at room temperature. Once the reaction reached completion, SNARF-ZF5.3 was purified and reconstituted in zinc-containing buffer to fold into the proper zinc finger structure (Fig. S3.1b,c). Unfortunately, the absorbance (Fig. S3.2b) and intensity (Fig. 3.1b) profiles revealed significant changes from the fluorophore alone. While there was still a pH-dependent shift in intensity, the emission peaks were closer together (589 nm for pH <7.0 and 623 nm for pH >7.0) and there was significant spectral overlap, regardless of excitation wavelength. The addition of a PEG2 or PEG4 linker between SNARF-4F and the DBCO moiety did not notably improve spectral separation (Fig. 3.1c,d) and led to decreased peptide solubility.

The reason for insufficient spectral separation of C-SNARF-4F when conjugated to ZF5.3 is unclear. It is known that ZF5.3 undergoes a pH-dependent conformational change with a pKa ~ 4.6,[19] which may contribute to the overlap. This assay could possibly be optimized with further fluorophore and/or peptide engineering, such as by using a different bioconjugation strategy, adjusting the terminus of ZF5.3 to which the fluorophore is conjugated, or introducing a longer peptide or polymer linker. However, given that ratiometric measurements would be impossible with the current spectral overlap, we turned to an alternative technique to use SNARF-ZF5.3 for a pH readout.

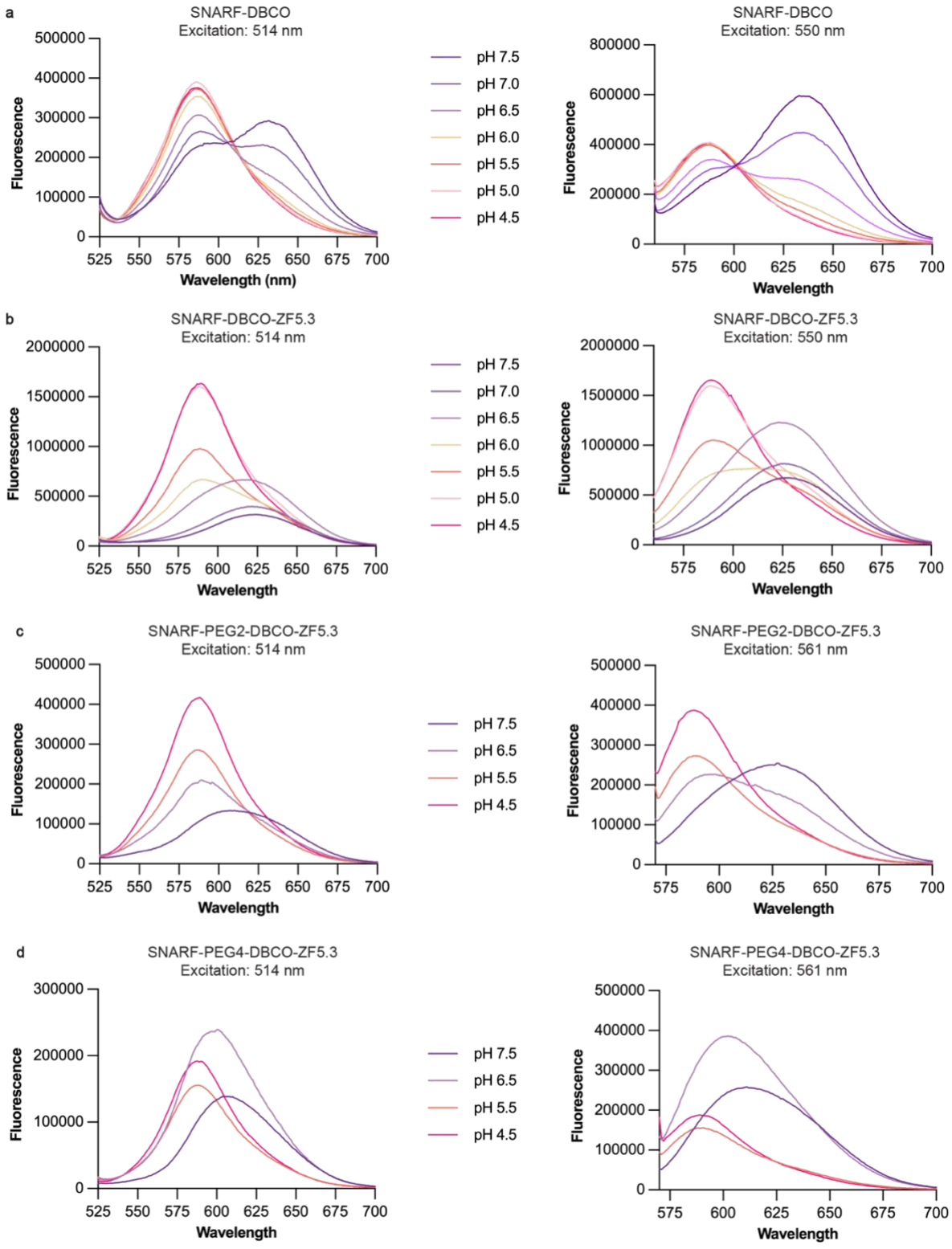

Figure 3.1. Conjugation of ZF5.3 to SNARF-4F reduces pH responsiveness of SNARF-4F. (A) – **(D)** Fluorescence intensity spectra of **(A)** SNARF-DBCO alone, (B) SNARF-ZF5.3, (C) SNARF-PEG2-ZF5.3, or (D) SNARF-PEG4-ZF5.3 when excited at 514 nm (left) or 550 nm (right). Spectra were collected from

525 – 700 nm when excited at 514 nm and from 560 – 700 when excited at 550 nm. All spectra were measured at 10 μM (SNARF-DBCO) or 4 μM (ZF5.3 variants) in 20 mM Tris, 150 mM KCl at pH 4.5 – 7.5.

3.3.2 Fluorescence lifetime distinguishes the pH of SNARF-ZF5.3 *in vitro*

Although fluorescence intensity is by far the most common method to distinguish spectrally separated fluorescent signal, another key property can be exploited to resolve signal from multiplexed fluorophores: fluorescence lifetime. After photon absorption, all fluorophores undergo a combination of radiative and nonradiative decay pathways from the excited state. The resulting decay has a characteristic time constant, known as the fluorescence lifetime, that is dependent on the rate of each decay pathway. Because the rate and route of decay is linked to a highly unstable excited state, the lifetime is highly susceptible to the photophysical properties and microenvironment of the fluorophore being studied.[44] Fluorescence lifetimes are affected by numerous environmental factors, such as temperature, ionic concentration, viscosity, polarity and pH, but are largely independent of fluorophore concentration, excitation wavelength, and photobleaching. Importantly, a fluorophore's lifetime is an absolute value, thus eliminating the need for ratiometric measurements as described above. Lifetime values for fluorescent species typically range from femtoseconds to nanoseconds.[44] Fluorescence lifetimes have been applied to study vesicle trafficking and pH regulation in a variety of cell types, though not in the context of in intracellular delivery.[45–48] We reasoned that, while SNARF-ZF5.3 did not have clearly separated pH-dependent changes in fluorescence intensity, the lifetimes of SNARF-ZF5.3 may be resolvable as a function of pH.

To measure the lifetime of SNARF-ZF5.3, we performed fluorescence lifetime imaging microscopy (FLIM) using time-correlated single photon counting (TCSPC). In TCSPC, a pulsed excitation source is applied to a sample, and the time between excitation and photon arrival time is quantified for each pulse (Fig. 3.2a). By tuning the laser intensity so <1 photon is detected per pulse, the distribution of "start-stop" times can be fit to an exponential decay curve. The amplitude of this curve represents the total number of photons detected at time *t*, and the time constant, τ, is the mean fluorescence lifetime (Fig. 3.2a). For multiexponential decays, the final mean τ can be calculated as an intensity-weighted or amplitude-weighted average where the lifetime of each component is weighted by its relative contribution to total fluorescence or exponential decay amplitude, respectively. Alternatively, fluorescence lifetime can be calculated from the same TCSPC data without fitting the exponential decay by applying a phasor plot analysis. In a phasor plot, the time-domain fluorescence decay data from each pixel in an image are Fourier transformed into polar coordinates and mapped onto a unit circle to differentiate fluorescent species based on their distinct lifetime characteristics (Fig. 3.2b). Fluorescence lifetimes with multiple components reside within the universal circle, while single-exponential lifetimes are plotted directly on the circle itself.[45]

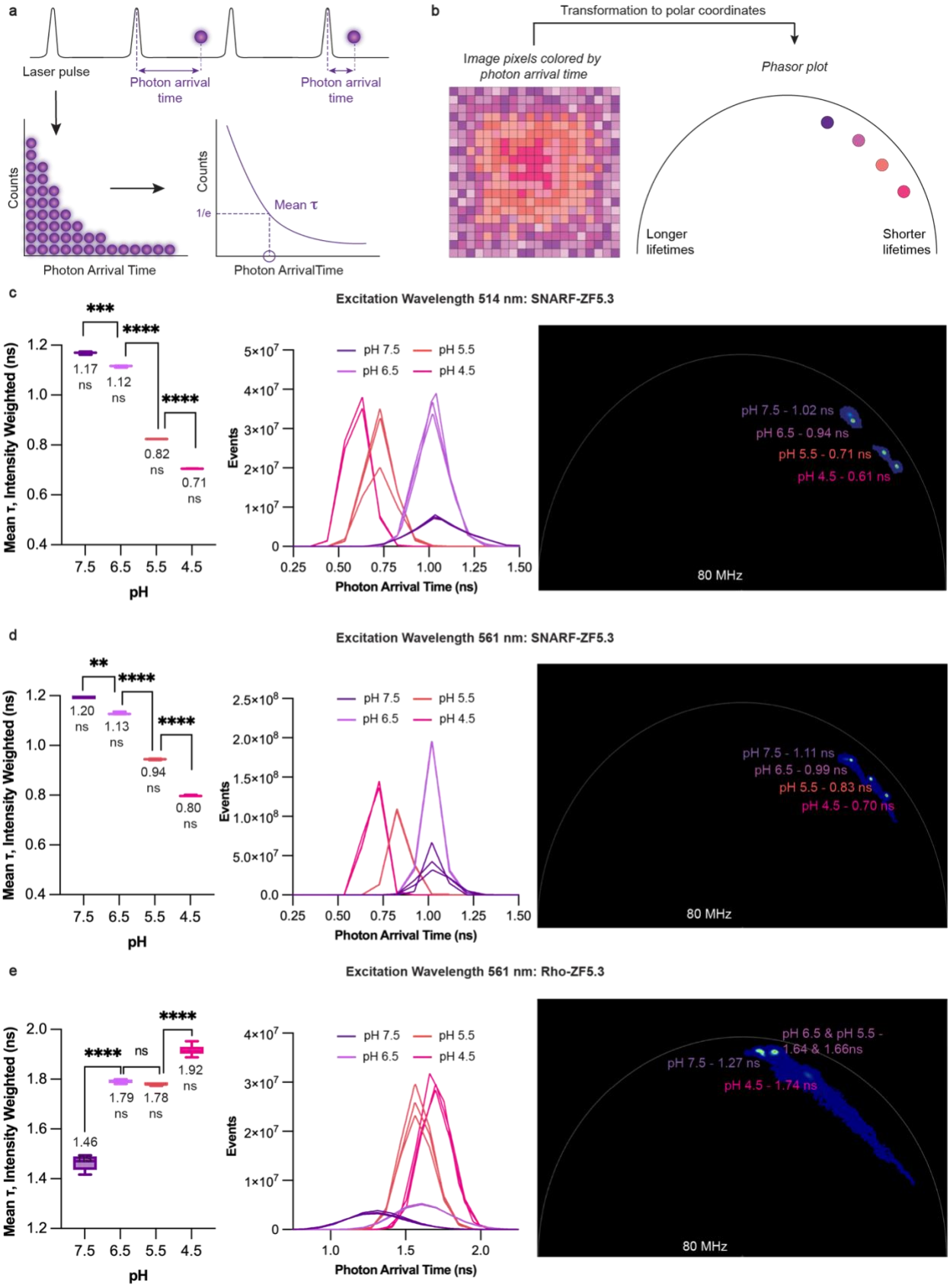
a
Laser pulse
Photon arrival time
Photon arrival time
Counts
Photon Arrival Time
Counts
Mean τ
1/e
Photon ArrivalTime
b
Transformation to polar coordinates
Image pixels colored by photon arrival time
Phasor plot
Longer lifetimes
Shorter lifetimes
c
Excitation Wavelength 514 nm: SNARF-ZF5.3
Mean τ, Intensity Weighted (ns)
pH
1.17 ns
1.12 ns
0.82 ns
0.71 ns
Events
Photon Arrival Time (ns)
pH 7.5
pH 6.5
pH 5.5
pH 4.5
pH 7.5 - 1.02 ns
pH 6.5 - 0.94 ns
pH 5.5 - 0.71 ns
pH 4.5 - 0.61 ns
80 MHz
d
Excitation Wavelength 561 nm: SNARF-ZF5.3
1.20 ns
1.13 ns
0.94 ns
0.80 ns
pH 7.5 - 1.11 ns
pH 6.5 - 0.99 ns
pH 5.5 - 0.83 ns
pH 4.5 - 0.70 ns
80 MHz
e
Excitation Wavelength 561 nm: Rho-ZF5.3
1.46
1.79 ns
1.78 ns
1.92 ns
pH 6.5 & pH 5.5 - 1.64 & 1.66ns
pH 7.5 - 1.27 ns
pH 4.5 - 1.74 ns
80 MHz

Figure 3.2. SNARF-ZF5.3 and Rho-ZF5.3 exhibit pH-dependent changes in fluorescence lifetime *in vitro*. (A) Fluorescence lifetime measurements were obtained using a pulsed excitation source to measure the delay between excitation and detection of individual photons (photon arrival time). The distribution of photon arrival times can be fit to an exponential decay from which the fluorescence lifetime can be derived. For single exponential decays, the lifetime is simply the characteristic time constant of the decay (as shown); for more complex systems, a multiexponential model must be used. **(B)** Phasor analysis is a "fit-free" approach to calculate fluorescence lifetimes. A phasor plot is constructed by the Fourier transformation of the photon arrival time histogram that is obtained for each pixel of a fluorescence lifetime image. Each pixel thus corresponds to one point in the phasor plot. Pixels with similar arrival times will cluster in the phasor plot, and their distance from the universal circle is determined by their respective number of exponential components. If the decay is fit by a single component, the phasor point will lie directly on the universal circle; a multiexponential decay will reside within the circle.[45] **(C)** – **(E)** *In vitro* fluorescence lifetime values calculated by fitting the obtained exponential decay (left), Fast FLIM analysis of *in vitro* samples (center), and phasor analysis (right) for SNARF-ZF5.3 and Rho-ZF5.3. Triexponential decays were fitted using LasX (Leica Microsystems) software (see Methods for more detail) and lifetime values are presented by weighting the individual components by their relative contributions to intensity. SNARF-ZF5.3 was excited at either 514 nm **(C)** or 561 nm **(D)** at 4 μM in 20 mM Tris, 150 mM KCl pH 4.5 – 7.5. Rho-ZF5.3 was excited at 561 nm **(E)** under identical conditions.

We used TCSPC to measure the *in vitro* fluorescent lifetimes of SNARF-ZF5.3 in buffer between pH 4.5 and 7.5. Notably, we observed statistically significant changes in fluorescence lifetime with each pH step. When calculated from an intensity-weighted, three-component exponential decay function, the lifetime (τ) of SNARF-ZF5.3 decreased from 1.17 ns to 0.71 ns as the pH was lowered from 7.5 to 4.5 (Fig. 3.2c, left). The Fast FLIM histogram, which records the number of events detected for different average photon arrival times per pixel within a sample, presents distinguishable peaks at each pH (Fig. 3.2c, middle). A phasor plot representation of the lifetimes of pH 4.5, 5.5, 6.5, and 7.5 solutions of SNARF-ZF5.3 also revealed clearly resolvable clusters with similar changes in lifetime to those calculated via multiexponential decay (Fig. 3.2c, right). These changes in lifetime were fairly consistent across multiple excitation wavelengths (Fig. 3.2d) and highly reproducible among replicates. As a comparison, we performed the same lifetime analyses for Rho-ZF5.3, a molecule used for previous studies of ZF5.3 delivery.[19] Rho-ZF5.3 is generated by reaction of azido-ZF5.3 with sulforhodamine B-DBCO (Fig. S3.1b,d), which is not expected to show pH-dependent changes in absorbance or fluorescence intensity.[46] Interestingly, Rho-ZF5.3 exhibits a significant change in lifetime between pH 7.5 and 6.5 ($\Delta\tau$ > 0.33 ns for all fitting methods), with relatively smaller changes between pH 6.5 and 4.5 that vary by fitting method (Fig. 3.2e). These lifetime changes for both SNARF-ZF5.3 and Rho-ZF5.3 are in line with previously reported values used in live cell imaging.[47]

Excitingly, the fluorescence lifetime profiles of both SNARF-ZF5.3 and Rho-ZF5.3 are appropriate to detect changes within the pH range of the endocytic pathway.[48] These findings open the door to exploit pH-dependent changes in lifetime to study both endosomal trafficking (pH 4.5 – 6.5)[48] and cytosolic delivery (pH 7.0 – 7.4).[35] SNARF-ZF5.3 exhibits the largest range in lifetime between pH 6.5 and 5.5 ($\Delta\tau$ = 0.19 ns) and pH 5.5 and 4.5 ($\Delta\tau$ = 0.14 ns), and is optimal for monitoring endosomal vesicle trafficking; conversely, Rho-ZF5.3 can reliably distinguish pH 7.5 from pH $\leq$ 6.5 ($\Delta\tau$ > 0.33 ns) and thus can report on cytosolic versus endosomal material. For the remainder of the chapter,

we will focus on two applications of fluorescence lifetime to monitor ZF5.3 delivery: tracking the pH microenvironment experienced by ZF5.3 in the endocytic pathway, and refining fluorescence correlation spectroscopy measurements by incorporating lifetime analyses.

3.3.3 FLIM reveals distinct subpopulations of ZF5.3-containing vesicles in live cells

Traditional methods to monitor trafficking of exogenously supplied peptides and proteins rely on colocalization with overexpressed GFP-tagged endosomal markers, such as Rab5, Rab7, or Lamp1. Though useful, each marker typically requires a separate time-intensive experiment, and the membrane protein redundancy among vesicles convolutes data interpretation. Given that endosomal maturation is characterized by an increasingly acidic luminal pH, FLIM can provide a snapshot of ZF5.3 localization within the endocytic pathway in a single experiment. Because SNARF-ZF5.3 displayed greater lifetime variability between pH 4.5 – 6.5 than Rho-ZF5.3 (Fig. 3.2c-e), we used SNARF-ZF5.3 for the following experiments.

To test if SNARF-ZF5.3 can report on vesicular pH differences in live cells, we incubated human osteosarcoma (Saos-2) cells with 2 µM SNARF-ZF5.3 for 1 h, washed and trypsin-treated the cells to remove surface-bound material, and visualized the cells using FLIM (Fig. 3.3a). Fast FLIM analysis of cell images, performed by displaying the average photon arrival time for each pixel without any curve fitting, revealed a wide range in arrival times for SNARF-ZF5.3-treated cells (Fig. 3.3a,b), represented by a pseudo-colored gradient from red (longer lifetimes) to blue (shorter lifetimes) (Fig. 3.3a,b). Intracellular vesicles with different lifetimes were occasionally observed in close contact with one another, and, in some cases, multiple lifetimes appeared present within single vesicles. Phasor analysis displayed a similarly broad range in detected lifetimes, ranging from ~0.16 ns to ~1.3 ns (Fig. 3.3a); this range is much larger than that detected *in vitro* (0.70 ns – 1.01 ns), likely as a result of the changes in viscosity, ionic strength, and/or interacting partners within the cellular milieu compared to buffer.

To confirm that the observed distribution in lifetimes is related to the vesicular pH, we performed FLIM in the presence of two pH-altering small molecules: Bafilomycin A1, an inhibitor of the vacuolar-type H(+)-ATPase that prevents endosomal acidification, and 4-aminopyridine (4-AP), a TMEM175 binder that inhibits proton efflux from endo/lysosomes, thus decreasing the pH of the endocytic pathway. We incubated Saos-2 cells with 2 µM SNARF-ZF5.3 for 1 h, washed and trypsinized, replated on a fibronectin-coated microscopy dish, and supplemented the media with either 250 nM Bafilomycin A1 for 20 min or 100 µM 4-AP for 10 min before FLIMaging. As expected, Fast FLIM and phasor analysis both reveal changes in the fluorescent lifetimes of SNARF-ZF5.3 with small molecule treatment. Bafilomycin A1 treatment depleted shorter lifetimes (presumably corresponding to low pH) from the phasor analysis and yielded Fast FLIM images that were fairly uniform in color and biased toward longer lifetimes (Fig. 3.3a,b). The presence of 4-AP produced the opposite effect, shifting the phasor and Fast FLIM analyses toward predominantly shorter lifetimes. (Fig. 3.3c). Thus, SNARF-ZF5.3 fluorescence lifetime

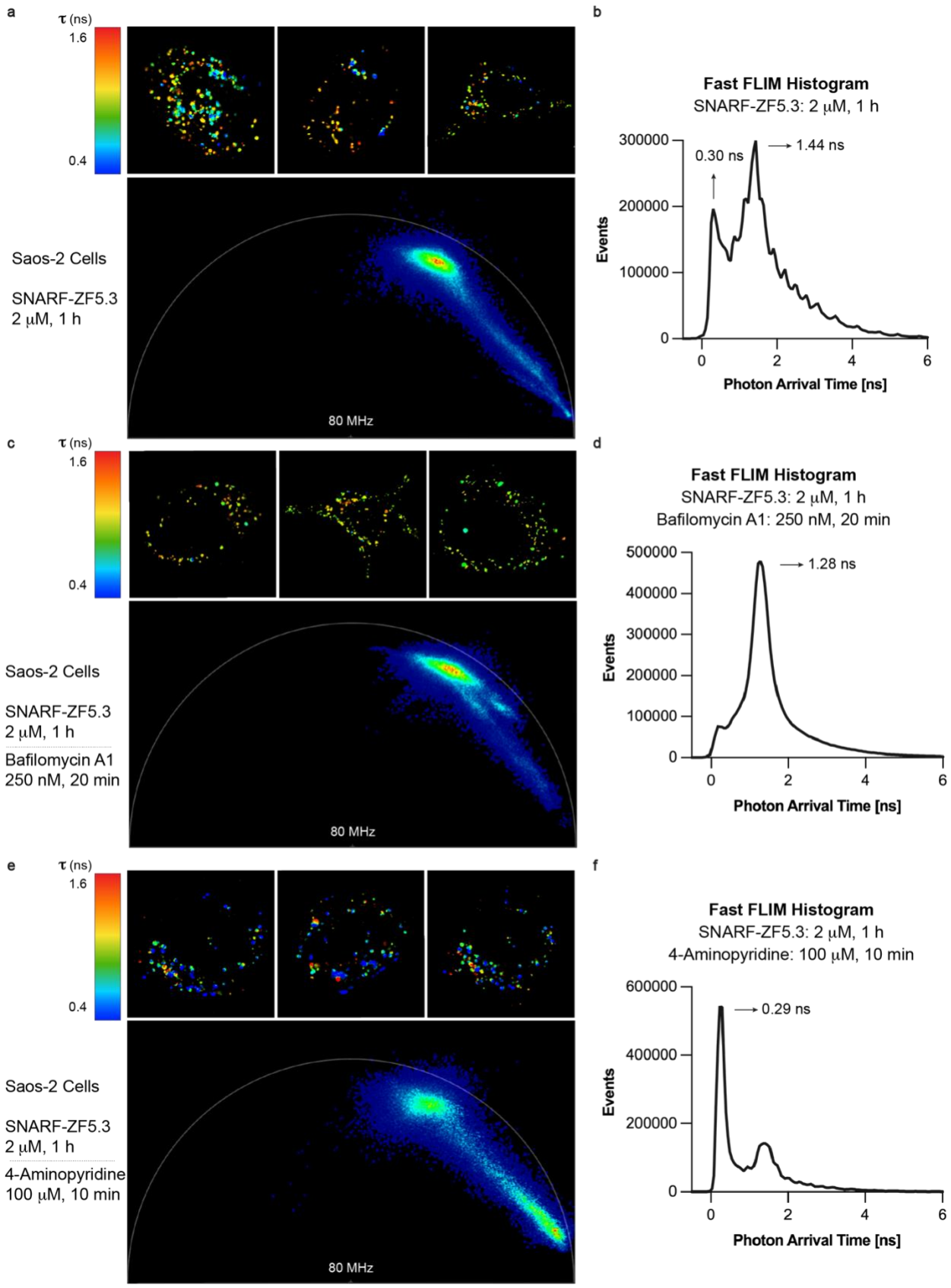
a
τ (ns)
1.6
0.4
Saos-2 Cells
SNARF-ZF5.3
2 μM, 1 h
80 MHz
b
Fast FLIM Histogram
SNARF-ZF5.3: 2 μM, 1 h
0.30 ns
1.44 ns
Events
Photon Arrival Time [ns]
c
τ (ns)
1.6
0.4
Saos-2 Cells
SNARF-ZF5.3
2 μM, 1 h
Bafilomycin A1
250 nM, 20 min
80 MHz
d
Fast FLIM Histogram
SNARF-ZF5.3: 2 μM, 1 h
Bafilomycin A1: 250 nM, 20 min
1.28 ns
Events
Photon Arrival Time [ns]
e
τ (ns)
1.6
0.4
Saos-2 Cells
SNARF-ZF5.3
2 μM, 1 h
4-Aminopyridine
100 μM, 10 min
80 MHz
f
Fast FLIM Histogram
SNARF-ZF5.3: 2 μM, 1 h
4-Aminopyridine: 100 μM, 10 min
0.29 ns
Events
Photon Arrival Time [ns]

Figure 3.3. The local microenvironment of SNARF-ZF5.3 in cells can be monitored using fluorescence lifetime imaging (FLIM). (A) Representative Fast FLIM images pseudocolored by photon arrival time and overlaid phasor plot for Saos-2 cell treated with 2 μM SNARF-ZF5.3 for 1 h. **(B)** Representative Fast FLIM histogram analysis of average photon arrival times for SNARF-ZF5.3-treated cells. Fast FLIM data represent the distribution of average photon arrival times calculated for each pixel in an image. A diverse range of average arrival times is observed for all cells. **(C)** Representative Fast FLIM images, phasor plot, and **(D)** Fast FLIM histogram for cells treated with 2 μM SNARF-ZF5.3 for 1 h followed by incubation with the V-ATPase inhibitor Bafilomycin A1 to inhibit endo/lysosomal acidification. Observed average arrival times are more uniform, corresponding to higher average pH. **(E)** Representative Fast FLIM images, phasor plot, and **(F)** Fast FLIM histogram for cells treated with 2 μM SNARF-ZF5.3 for 1 h followed by incubation with the TMEM 175 inhibitor 4-aminopyridine to increase endo/lysosomal acidification. Observed aveage arrival times are highly uniform, corresponding to lower average pH.

reports on endo/lysosomal pH in live cells and can be applied toward the study of endocytic trafficking of exogenously delivered peptides.

We have previously reported that delivery of ZF5.3 to the cytosol, both alone and when conjugated to physiologically unfolded protein cargos, requires the HOPS complex.[28,49,50] HOPS is a hexameric complex that promotes fusion of late endosomes and lysosomes by catalyzing ATP-dependent membrane tethering.[51] The mechanism by which HOPS depletion inhibits ZF5.3 endosomal escape has thus far remained unclear. A recent report identified that knockout of HOPS subunits results in significant dysregulation of endosomal compartments, including an aberrant increase in luminal pH.[52] We also recently published an NMR structural characterization of ZF5.3 that revealed a role for acid-induced unfolding in efficient ZF5.3 endosomal escape.[19] Given these findings, we hypothesized that knockdown of the HOPS complex may disrupt endosome acidification, thus preventing ZF5.3 from sufficiently unfolding. FLIM is a powerful tool to explore this question, as the pH microenvironment of SNARF-ZF5.3 can be directly monitored in the presence and absence of HOPS. We transfected Saos-2 cells with siRNAs targeting either an essential HOPS subunit (VPS39) or a non-targeting siRNA (RISC-free). We then treated cells with 2 μM SNARF-ZF5.3 for 1 h and analyzed each sample by Fast FLIM and phasor plot. As expected, the RISC-free control displayed a wide range of long and short lifetimes, similar to non-transfected cells (Fig. S3.3a). Interestingly, depletion of VPS39 appeared to increase the proportion of short lifetimes (Fig. S3.3b, more blue vesicles). As short lifetimes are indicative of lower pH, these data suggest that knockdown of HOPS actually decreases the endo/lysosomal pH, in disagreement with the previous report.[52] These results require follow-up to relate these pH changes to other endosomal machinery and investigate their role in ZF5.3 endosomal escape. Importantly, the lifetime analyses presented here are useful for establishing relative changes in the pH distribution of live cells, but they cannot assign specific pH values. To quantitatively describe the precise pH experienced by ZF5.3 in the endocytic pathway, we next sought to calibrate lifetimes to pH using an *in cellula* pH calibration.

3.3.4 Attempts to calibrate SNARF-ZF5.3 fluorescence lifetimes *in cellula* to specific pH values

The FLIM analyses described above provide useful insights into the fluorescence lifetimes experienced by SNARF-ZF5.3 in live cells. However, the distribution of lifetimes *in cellula* is significantly larger than what was observed in buffer. The *in vitro* data suggests that lifetime increases with increasing pH, but observed lifetimes in cells cannot be assigned a discrete pH without proper calibration.

Calibration of pH in live cells is traditionally performed using ionophores like nigericin and monensin, lipid-soluble small molecules that bind and shuttle ions across cellular membranes.[53] These ionophores bind cations and facilitate the exchange of K+ or Na+ for H+, resulting in equalization of K+/Na+ and H+ concentration gradients.[54] By incubating cells in buffer at the desired pH in the presence of ionophores, the intracellular and extracellular pHs should become equilibrated, including within vesicles.[53] We began by testing ionophore concentrations to identify conditions under which intracellular pH becomes uniform. We incubated Saos-2 cells with 3 μM SNARF-ZF5.3 (to ensure sufficient brightness) for 1 h, washed and trypsin-treated, and replated in a fibronectin-coated microscopy dish in DMEM. Ten minutes before imaging, the media was directly replaced with high-K+ imaging buffer at pH 7.5 containing 10 – 20 μM nigericin and 2 μM monensin (Fig. S3.4a,b). Compared to cells treated with SNARF-ZF5.3 alone (Fig. 3.3a), the distribution of Fast FLIM photon arrival times became significantly narrower in the presence of ionophores (Fig. S3.4a,b). Both 10 and 20 μM nigericin conditions yielded a single peak in the Fast FLIM histogram around ~1 ns (Fig. S3.4a,b). Since the pH within the endocytic pathway is not expected to be higher than 7.5, we might expect this to represent the longest lifetime observed in cells. Interestingly, this value matched the Fast FLIM value for SNARF-ZF5.3 at pH 7.5 calculated *in vitro* (1.02 ns, Fig. 3.2d, center), but was shorter than the longest Fast FLIM value identified *in cellula* (1.44 ns, Fig. 3.3b). We reasoned this could be a result of treating with a higher SNARF-ZF5.3 concentration in cells, as dye self-interactions can reduce observed lifetime.[44] Regardless, given that the lifetime distribution with 10 μM nigericin / 2 μM monensin appeared fairly uniform, we moved forward with these conditions to calibrate SNARF-ZF5.3 lifetime with pH 4.5 – 7.5 *in cellula* under the original treatment conditions.

We incubated Saos-2 cells with 2 μM SNARF-ZF5.3 for 1 h, washed and trypsin-treated, and replated in a fibronectin-coated microscopy dish in DMEM. Ten minutes before imaging, the media was directly replaced with high-K+ imaging buffer at pH 4.5, 5.5, 6.5, or 7.5 containing 10 μM nigericin and 2 μM monensin (Fig. 3.4). Fast FLIM analysis revealed definitive changes in the distribution of photon arrival times in all conditions. At pH 7.5 and 6.5, we observed minimal cell death during imaging and obtained fairly uniform Fast FLIM histograms with well-defined peaks indicating an average photon arrival time of 1.21 for pH 7. and 1.18 ns for pH 6.5 (Fig. 3.4a,b). Unfortunately, incubation with imaging buffers at pH 5.5 and 4.5 resulted in significantly more cell death, including an apparent mass leakage of vesicular contents throughout the cell within 5 min (Fig. S3.5). The few live cell images that were obtained showed highly

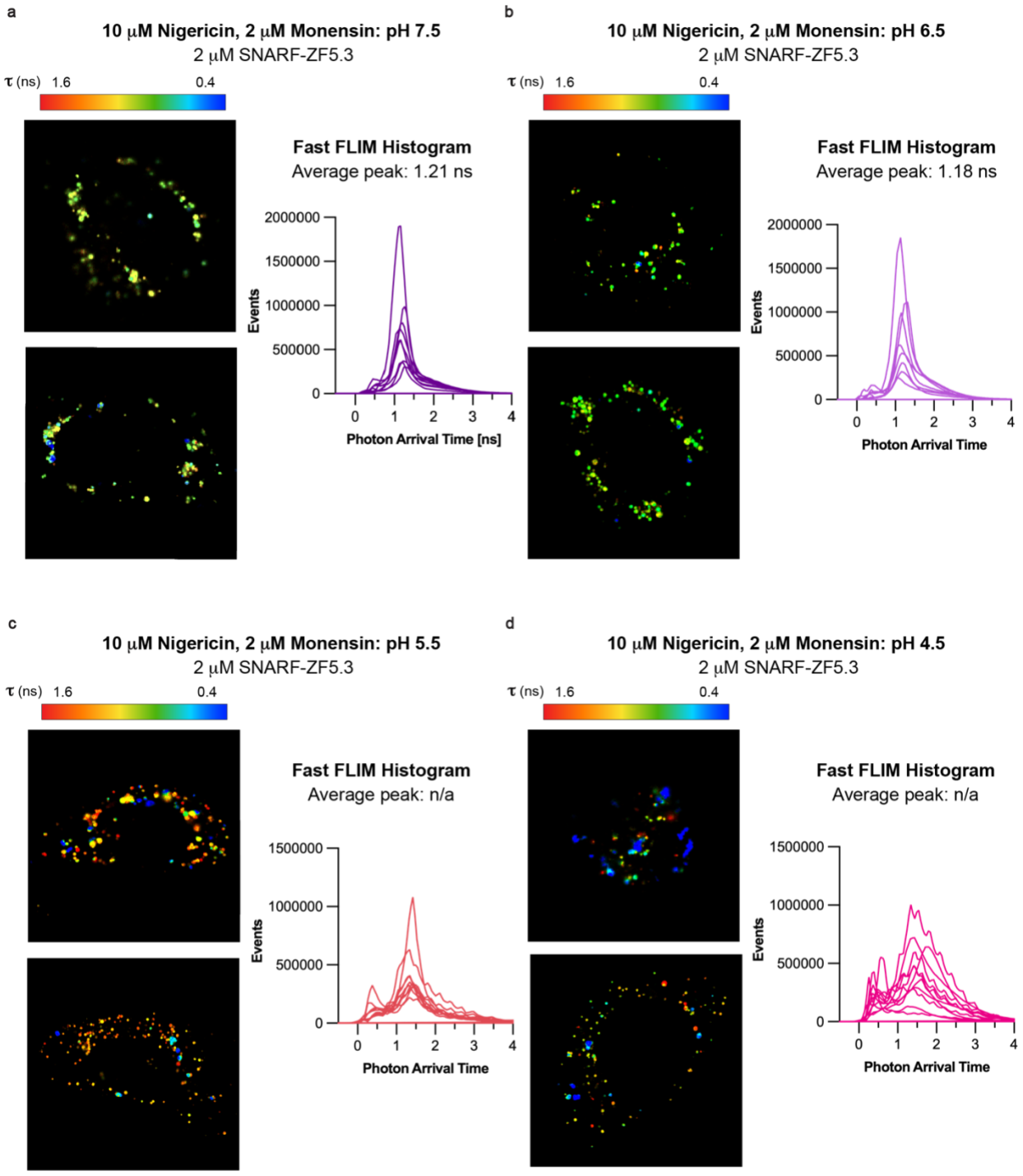

Figure 3.4. Ionophores are insufficient to calibrate intracellular pH with fluorescence lifetime at acidic pH values. (A) – **(D)** Representative Fast FLIM images pseudocolored by photon arrival time (left) and overlaid Fast FLIM histograms from 10-15 cells per condition (right) for cells at (A) pH 7.5, (B) pH 6.5, (C) pH 5.5, or (D) pH 4.5. For all conditions, Saos-2 cells were treated with 2 μM SNARF-ZF5.3 for 1 h. After the incubation and workup, cells were incubated with high K+ buffer at the designated pH for 10 min (pH 7.5 and 6.5) or 5 min (pH 5.5 and 4.5) before imaging.

variable intracellular lifetimes (Fig. 3.4c,d) that could not be reliably assigned to a pH value. Attempts to calibrate using a commercially available intracellular pH calibration kit (CAT#P35379), which uses nigericin and valinomycin ionophores, yielded similarly variable lifetime values (Fig. S3.6).

Equalization of pH in living cells disrupts membrane potentials that are critical for cellular fitness. In addition, low intracellular pH can activate endogenous nucleases, proteases, and other pro-apoptotic proteins that trigger cell death pathways.[55] Although ionophores have been utilized for pH calibration in live cells,[53,56] it is possible the SNARF-ZF5.3 treatment and/or replating procedure renders cells particularly susceptible to such drastic pH changes. Because ZF5.3 is expected to interact with endosomal lipids,[19] it is also possible that membrane changes resulting from the disruption in voltage may affect the observed lifetimes. Several strategies to troubleshoot these data are available, including altering the concentration and ratio of nigericin/monensin, performing calibration experiments in cellular extract or fractionated cytosol, and testing different cell lines. In any case, it will be essential to carry out pH calibration experiments with a positive control (e.g. a pHrodo or BCECF dye) that has a well-characterized pH dependence to confirm that the observed variability in SNARF-ZF5.3 *in cellula* lifetime during pH calibration experiments (e.g. Fig. 3.4c,d) is due to non-equalized intracellular pH, and not instead affected by other convoluting factors (e.g. ionic strength or viscosity).

3.3.5 Integrating fluorescence lifetime measurements into FCS data collection

Beyond the pH calibration experiments, we explored a second application of fluorescence lifetime detection in assessing ZF5.3 delivery: fluorescence lifetime imaging coupled with fluorescence correlation spectroscopy (FLIM-FCS). Fluorescence correlation spectroscopy (FCS) is a highly quantitative, single-molecule technique that quantifies the precise number of dye-labeled molecules that diffuse through a focal volume generated by the microscope laser.[57,58] By placing the laser in a discrete cellular location (e.g. the cytosol) and measuring the focal volume, a cytosolic concentration of fluorescent material can be calculated from the resulting autocorrelation function (ACF).[59] FCS has been used extensively to quantify the delivery of peptides and proteins and is more thoroughly discussed in **Chapter 1**.[19,28,49,50,59–62] Critically, the laser must be positioned to avoid endosomal puncta and ensure signal is coming exclusively from cytosolic fluorescence. This assumption is generally valid, as endosomes are significantly brighter than their surroundings and are typically filtered out by an abnormal spike in fluorescence intensity during an active measurement.[59] However, our current FCS practices cannot exclude the possibility that an out-of-focus or dim endosome (e.g. an endosome with only a small amount of fluorescent material) may contribute some signal to the otherwise “cytosolic” measurement. Fluorescence lifetime is a powerful strategy to overcome this pitfall.

In a typical FCS measurement, fluctuations in fluorescence intensity over time are detected and fit to an ACF. The amplitude of the ACF is determined by the number of molecules in the focal volume, while the inflection point reports on the diffusion time of the detected particles.[63] The sensitivity of these data can be enhanced by the concurrent

measurement of photon arrival time for each detected photon within the focal volume.[64] This produces a fluorescence decay curve for each ACF that can provide the fluorescence lifetime(s) of the diffusing species. Such information would be able to discriminate fluorescent signal originating from an undesired acidic compartment and provide an additional filter to refine cytosolic FCS measurements (Fig. 3.5a).

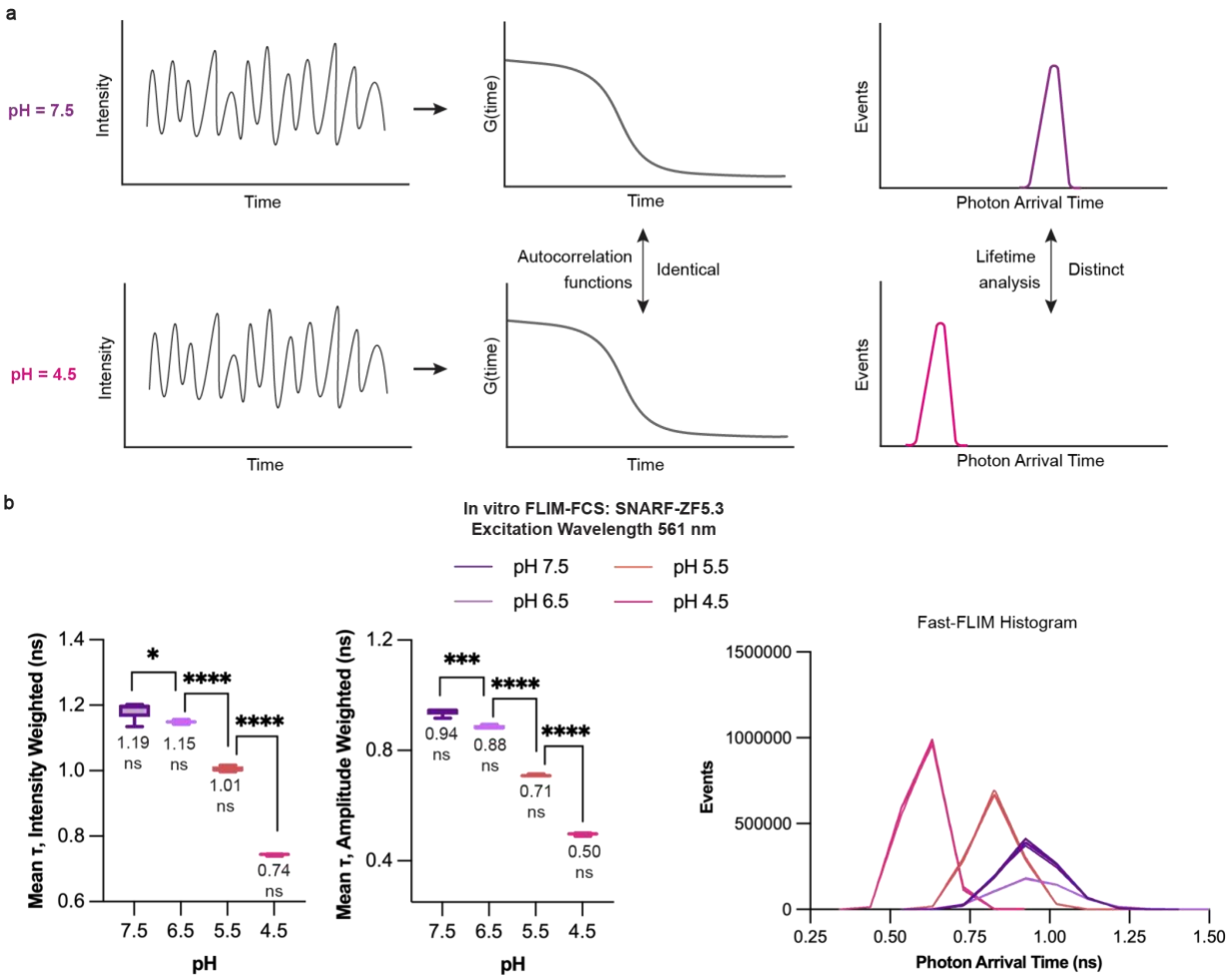

Figure 3.5. SNARF-ZF5.3 exhibits pH-dependent changes in fluorescence lifetime when measured by FLIM-FCS *in vitro*. (A) During a FLIM-FCS experiment, fluctuations in fluorescence intensity in the microscope confocal volume are measured over a discrete period of time. These fluctuations are fit to autocorrelation functions, which provide the number of molecules that diffused in the focal volume during the measurement period. The lifetime components that contribute fluorescence to the autocorrelation functions are then calculated by fitting the observed photon arrival times to an exponential decay. Although autocorrelation functions for SNARF-ZF5.3 will appear the same at pH 4.5 and pH 7.5, the lifetimes should be distinguishable. (B) *In vitro* fluorescence lifetime values for SNARF-ZF5.3 calculated by fitting the exponential decay obtained from FCS measurements at 4 μM in 20 mM Tris, 150 mM KCl pH 4.5 – 7.5. Triexponential decays were fitted using LasX (Leica Microsystems) software (see Methods for more detail) and lifetime values are presented by weighting the individual components by intensity or by amplitude. The corresponding Fast FLIM histograms at each pH are displayed on the right. For each pH, five points were measured with ten 5-second autocorrelation traces obtained per point.

Both SNARF-ZF5.3 and Rho-ZF5.3 exhibited suitable fluorescence lifetime shifts for this application when measured using FLIM alone (Fig. 3.2c-e). Although a thorough characterization of the potential for FLIM-FCS with Rho-ZF5.3 is warranted, it is beyond the scope of the present work. To ensure the observed changes in lifetime are recapitulated when performing FLIM-FCS, we measured the *in vitro* lifetimes from decay curves generated by FCS measurements of SNARF-ZF5.3 in buffer between pH 4.5 and 7.5. Both the intensity-weighted and amplitude-weighted lifetime values extracted from the observed fluorescence decay curves followed the same trend as observed with FLIM. For SNARF-ZF5.3, $\Delta\tau$ ~ 0.45 ns between pH 4.5 and 7.5 (Fig. 3.5b,c). As noted before, Rho-ZF5.3 exhibited the largest $\Delta\tau$ between pH 6.5 and 7.5 when measured using FLIM alone (0.33 ns compared to 0.07 ns for SNARF-ZF5.3). As cytosolic pH is 7.0 – 7.4, we expect that Rho-ZF5.3 may be a better candidate for lifetime filtering to ensure signal from both early (pH ~6.5) and late (pH ~4.5-5.5) endosomes is removed, though we proceeded with SNARF-ZF5.3 for a proof of concept.

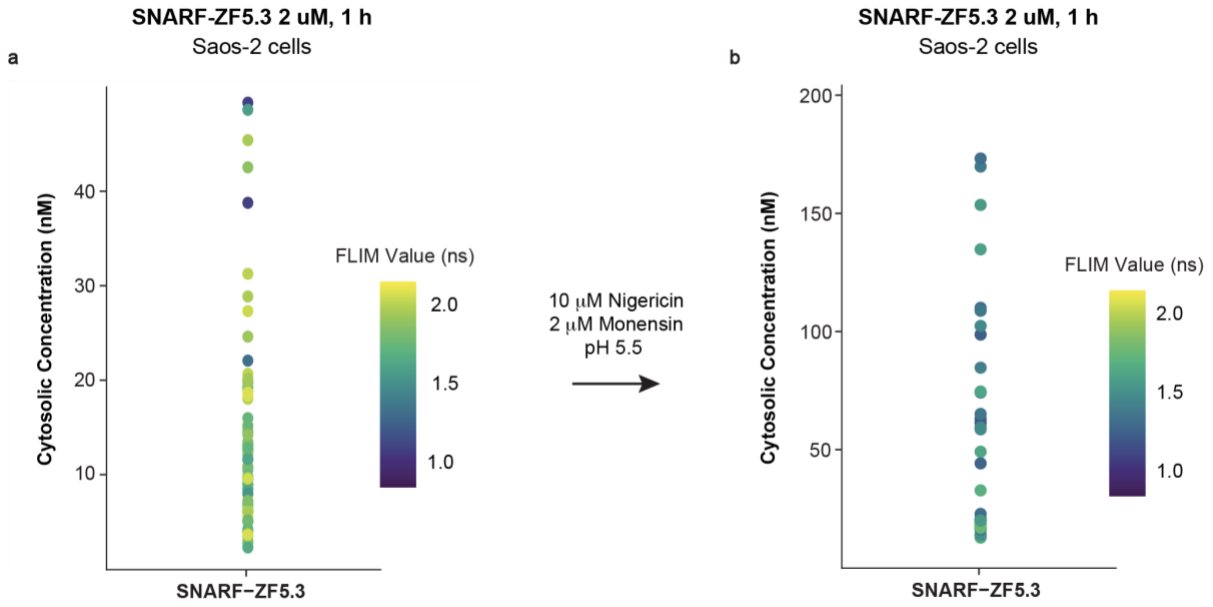

Figure 3.6. Cytosolic FCS measurements of SNARF-ZF5.3 have relatively uniform lifetimes that shorten when intracellular pH is decreased. (A) FLIM-FCS data collected from Saos-2 cells were treated with 2 μM SNARF-ZF5.3 for 1 h. Each point corresponds to a single ten-second autocorrelation trace. Autocorrelation functions and their corresponding exponential decays were fitted using the LasX software (see Methods for more detail). Data are plotted as a function of both concentration (Y-axis) and lifetime (color). Most points have similar lifetimes, with an average lifetime of 2.02 ns. The three darker points represent potential candidates to be filtered out by lifetime. **(B)** FLIM-FCS data collected from Saos-2 cells treated with 2 μM SNARF-ZF5.3 for 1 h followed by pH clamping at 5.5 using 10 μM nigericin and 2 μM monensin for 10 min before measurement. Data were collected in the same manner as **(A)**. Lifetimes are similarly uniform, but significantly shorter than non-pH-clamped cells (average of 1.69 ns).

To demonstrate the utility of FLIM-FCS in living cells, we incubated Saos-2 cells with 2 μM SNARF-ZF5.3 for 1 h, washed with DPBS, trypsinized to remove exogenous

protein, and replated on a fibronectin-coated glass-bottom microscopy dish. Using confocal microscopy images, we positioned the microscope laser in cytosolic regions without visible endosomal puncta and measured five-second FCS traces at a variety of positions. These ACFs and corresponding fluorescence decay functions were fit using algorithms available within the Leica software to obtain a concentration and mean intensity-weighted τ per trace. Each measurement that had reasonable fits (χ^2 <40 for ACF and χ^2 <2 for lifetime) was then plotted as a function of both concentration and fluorescence lifetime (Fig. 3.6a). As expected, the distribution of lifetimes appears uniform for each cytosolic measurement. Without a genuine pH calibration (see **3.3.4**), it is impossible to definitively know that the observed lifetimes derive from a neutral pH. However, we reasoned that pH clamping with ionophores should nonetheless perturb the intracellular pH and thus affect the distribution of cytosolic lifetimes obtained by FLIM-FCFS. We performed the same experiment described above but replaced the imaging media with buffer at pH 5.5 containing 10 μM nigericin and 2 μM monensin. Gratifyingly, nearly all the measurements exhibited a markedly shorter lifetime with the pH clamp (Fig. 3.6b), suggesting that this method can discriminate fluorescence lifetime by pH. These data show that FLIM can be combined with FCS to selectively filter fluorescence arising only from regions at neutral pH, thus increasing the accuracy of cytosolic concentration measurements.

3.4 Conclusions and Discussion

In this chapter, we describe several strategies to exploit the pH gradient generated by the endocytic pathway to gain insights into intracellular delivery of the ZF5.3 peptide. We initially modified ZF5.3 with a pH-sensitive fluorophore (C-SNARF-4F) to develop a high-throughput assay that could directly monitor endosomal escape by quantifying the ratio of fluorescence intensity at acidic and neutral pHs. Unfortunately, the spectral overlap of SNARF-ZF5.3 intensity across the relevant pH range was too high to reliably measure this ratio. This spectral overlap could potentially be reduced by swapping the fluorophore placement, adjusting the linker length, or exploring alternative pH-sensitive dyes (e.g. LysoSensor variants). By integrating such engineering with flow cytometry compensation, a ratiometric delivery assay could be developed from our preliminary work to deconvolute the effects of total endocytic uptake from endosomal escape.

We turned instead to fluorescence lifetime imaging (FLIM) to discriminate SNARF-ZF5.3 signal at varying pHs. FLIM is not currently available with high-throughput applications such as flow cytometry (with the exception of some homemade instruments[65,66]), but it can still provide valuable insights into the microenvironment experienced by exogenously delivered molecules. We report two applications of FLIM in the context of ZF5.3 delivery: tracking the endocytic trafficking via pH microenvironment experienced by ZF5.3, and refining fluorescence correlation spectroscopy measurements by incorporating lifetime analyses.

We found the lifetimes of both SNARF-ZF5.3 and Rho-ZF5.3 to be sensitive to pH, even though Rhodamine B is not expected to be a pH-sensitive fluorophore.[46] Rho-ZF5.3 exhibited a large lifetime shift between pH 7.5 and 6.5 but relatively smaller variations at

lower pH values. Conversely, SNARF-ZF5.3 demonstrated the largest lifetime changes between pH 6.5 and 5.5 and between pH 5.5 and 4.5, and was thus chosen for further endosomal trafficking studies. FLIM analysis of SNARF-ZF5.3-treated cells identified a wide distribution of lifetimes that were responsive to perturbations of intracellular pH by small molecules and knockdown of endosomal maturation machinery. Attempts to calibrate observed lifetimes to known pH values were unsuccessful, but several avenues to do so remain available (see **3.3.4**). With the proper calibration, we envision that FLIM analysis of SNARF-tagged biologics will provide a snapshot of molecular trafficking pathways in a single experiment. This technology could identify endosomal localization without the need for protein markers, detect local pH changes induced by (or necessary for) delivery, and even track membrane- or protein-dependent interactions that induce a reproducible lifetime shift. Integration of single-particle tracking with FLIM would enable multidimensional detection of pH variation among endosomal tethering and fusion events in the presence of exogenously supplied biomolecules. This is of particular importance for mechanistic studies of protein delivery, which currently suggest endosomal fusion may be involved in some endosomal escape pathways but lack definitive evidence.[19,20,28,29]

FLIM-FCS provides an additional layer of information to FLIM studies. The results reported here demonstrate the use of fluorescence lifetime to filter out FCS measurements originating from acidic vesicles and thus refine cytosolic data. This concept could be further applied by applying lifetime gating to FCS measurements, whereby signal from photons emitted within a certain arrival time are omitted from the intensity ACF.[64] For SNARF-ZF5.3 or Rho-ZF5.3, this might enable filtering of photons with short lifetimes characteristic of acidic vesicles simultaneously to data collection. FLIM-FCS can even separate a given autocorrelation function (ACF) into the ACFs contributed by each individual lifetime component, thus providing fluorescence cross-correlation information for fluorescence lifetime rather than intensity.[67] Such an application could discriminate, for instance, DNA-bound from freely diffusing material or other intracellular interactions that shift the observed lifetime. Time-resolved fluorescence correlation data will significantly enhance the sensitivity of our current FCS setup and provide quantitative validation that measurements are derived exclusively from cytosolic signal.

The results in this chapter developed a novel technique to explore pH changes throughout the endocytic pathway and how they relate to the intracellular delivery of a cell-permeant miniature protein. FLIM will provide unique insights into how biologics interact with and influence endogenous trafficking pathways, enabling a quantitative understanding of endosomal transit and escape.

3.5 Supplementary Figures

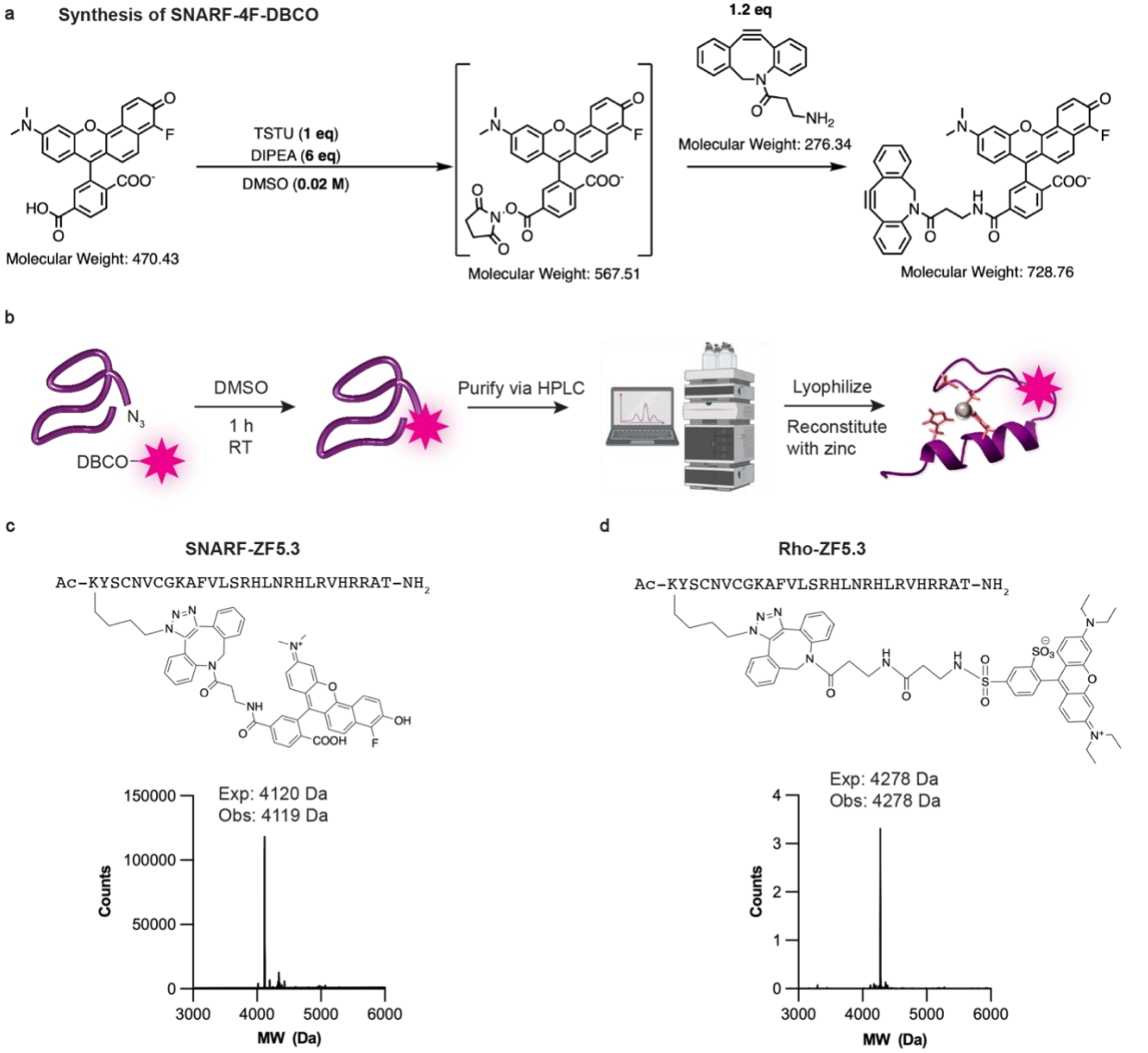

Figure S3.1. Synthesis of SNARF-4F-DBCO, SNARF-ZF5.3, and Rho-ZF5.3. (A) SNARF-4F-DBCO was synthesized by modifying commercially available SNARF-4F 5-(and-6)-Carboxylic Acid with DBCO-Amine. SNARF-4F-PEG2-DBCO and SNARF-4F-PEG4-DBCO were synthesized using DBCO-PEG2-Amine and DBCO-PEG4-Amine, respectively. **(B)** SNARF-4F-DBCO or Rho-DBCO (described previously[19]) were conjugated to ZF5.3 containing an N-terminal azide by incubating five equivalents of dye with N3-ZF5.3 for 1 h at RT in DMSO until reaction reached completion. Dye-labeled ZF5.3 was purified by HPLC, lyophilized, and reconstituted with zinc-containing buffer as described in Methods. **(C)** and **(D)** Structure, sequence, and LC/MS trace for SNARF-ZF5.3 **(C)** and Rho-ZF5.3 **(D)**.

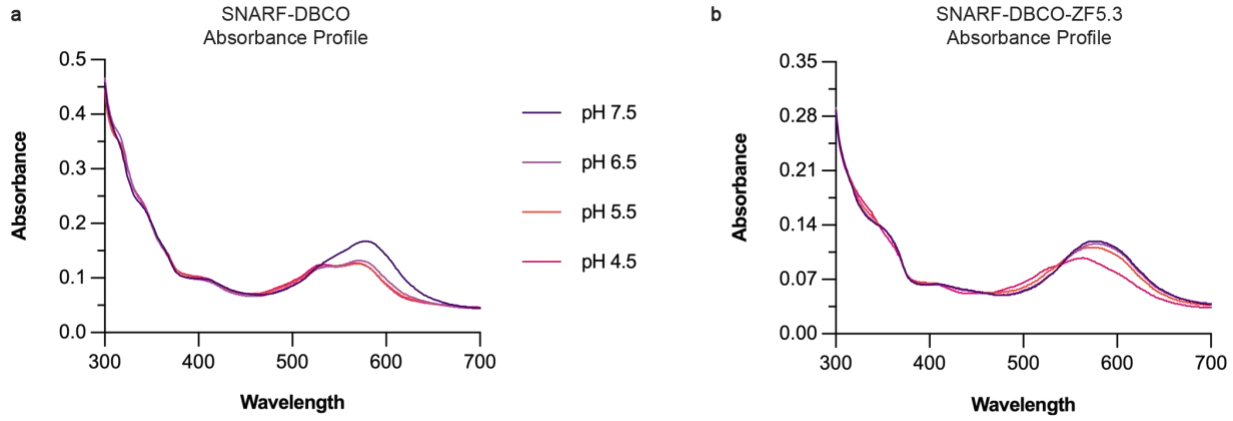

Figure S3.2. *In vitro* absorbance profiles for SNARF-4F-DBCO and SNARF-ZF5.3. Absorbance of SNARF-4F-DBCO and SNARF-ZF5.3 was measured at 10 μM (SNARF-4F-DBCO) or 4 μM (SNARF-ZF5.3) in 20 mM Tris, 150 mM KCl at pH 4.5 – 7.5 using a UV/Vis spectrometer.

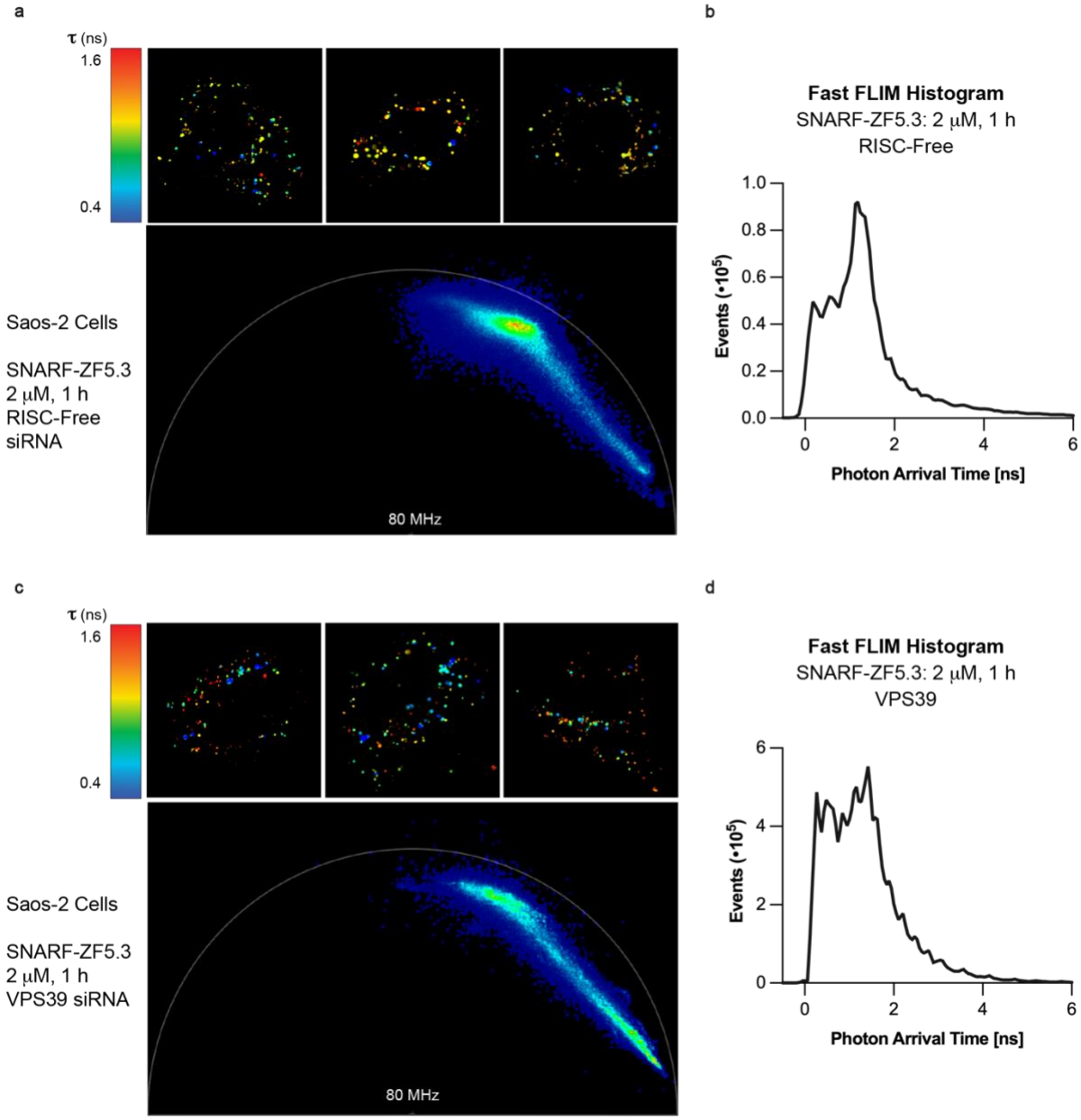

Figure S3.3. The fluorescence lifetime distribution of SNARF-ZF5.3 *in cellula* is impacted by knockdown of the HOPS complex. (A) – (D) Saos-2 cells were transfected with either a RISC-free siRNA (**A** and **B**) or a VPS39 siRNA targeting an essential component of the HOPS complex (**C** and **D**). Cells were then treated with 2 μM SNARF-ZF5.3 for 1 h before FLIM analysis (see Methods for more detail). **(A)** Representative Fast FLIM images pseudocolored by average photon arrival time per pixel and overlaid phasor plot for RISC-free Saos-2 cells treated with SNARF-ZF5.3. **(B)** Representative Fast FLIM histogram analysis of average photon arrival times for RISC-free SNARF-ZF5.3-treated cells. A diverse range of arrival times is observed for all cells. **(C)** Representative Fast FLIM images pseudocolored by average photon arrival time per pixel and overlaid phasor plot for VPS39 knockdown Saos-2 cells treated with SNARF-ZF5.3. **(D)** Representative Fast FLIM histogram analysis of average photon arrival times for VPS39 knockdown SNARF-ZF5.3-treated cells. An increase in shorter arrival times (likely corresponding to a decrease in average pH) is observed.

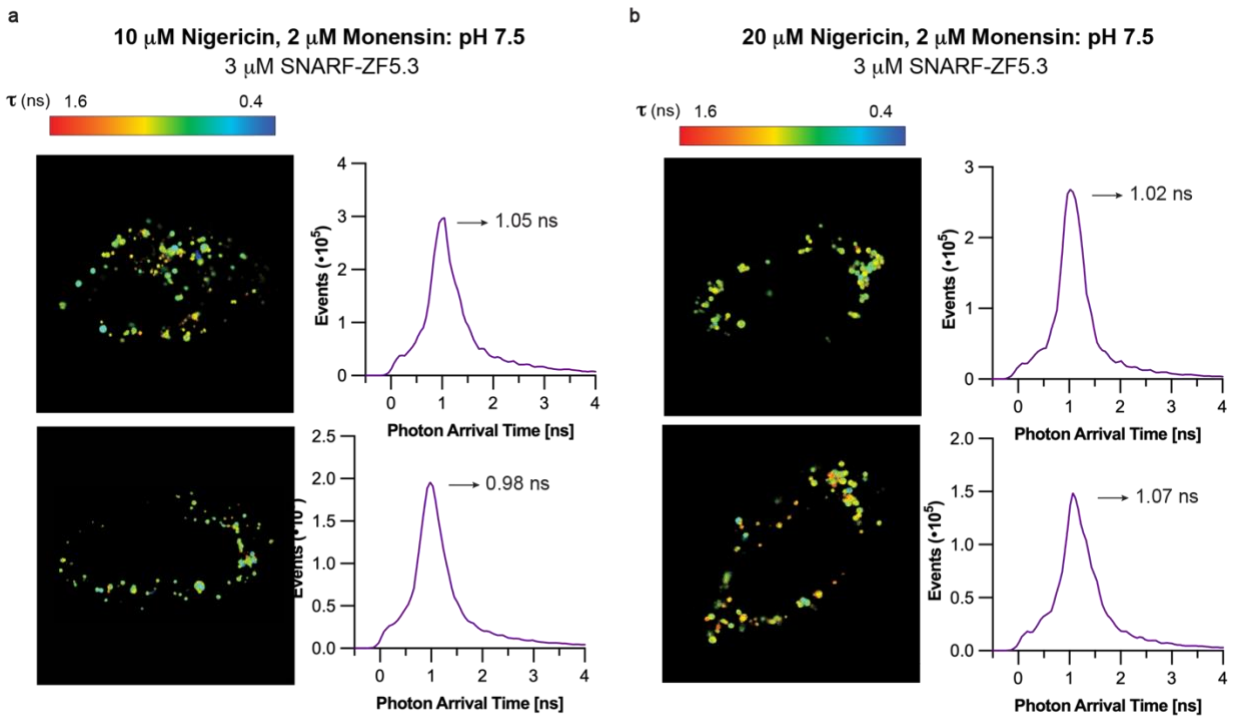

Figure S3.4. Optimization of ionophore concentrations for pH calibration of fluorescence lifetime. (A) and (B) Saos-2 cells were treated with 3 μM SNARF-ZF5.3 for 1 h. After the incubation and workup, media was replaced with high-K+ buffer at pH 7.5 containing either 10 μM nigericin / 2 μM monensin **(A)** or 20 μM nigericin / 2 μM monensin **(B)** for 10 min before imaging. Representative Fast FLIM images pseudocolored by average photon arrival time and representative Fast FLIM histograms are presented. Under both conditions, the photon arrival times become similarly homogenous, with the arrival time of the histogram peak noted for each plot.

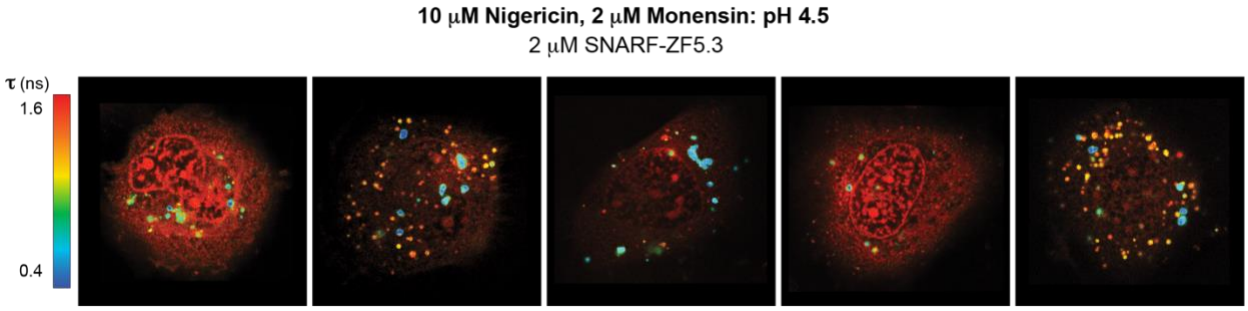

Figure S3.5. Incubation of cells with ionophore-containing buffer at pH 4.5 results in massive vesicular leakage. Saos-2 cells were treated with 2 μM SNARF-ZF5.3 for 1 h. After the incubation and workup, media was replaced with high-K+ buffer at pH 4.5 containing 10 μM nigericin / 2 μM monensin for 5 min before imaging. Representative Fast FLIM images pseudocolored by average photon arrival time are shown.

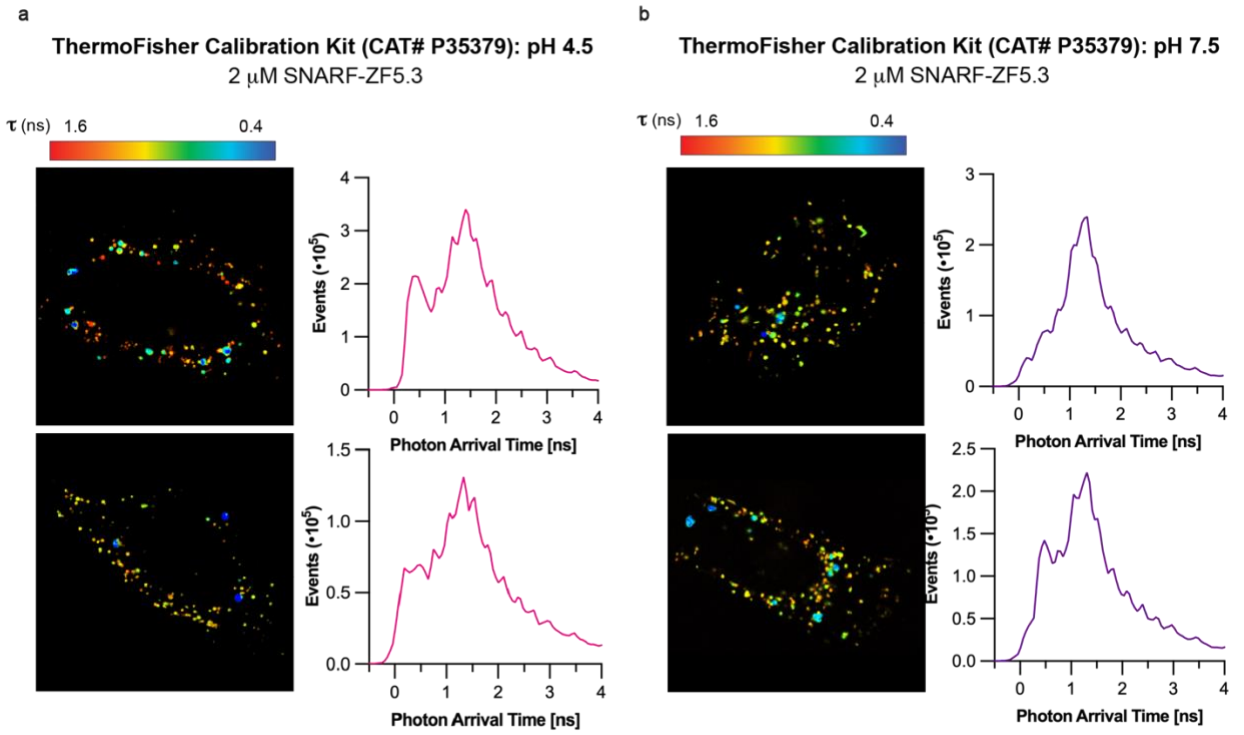

Figure S3.6. Commercially available pH calibration kit is insufficient to calibrate intracellular pH with lifetime. (A) and **(B)** Saos-2 cells were treated with 2 μM SNARF-ZF5.3 for 1 h. After the incubation and workup, media was directly replaced with imaging buffer at pH 4.5 **(A)** or 7.5 **(B)** prepared according to the manufacturer's protocol for the Thermofisher Intracellular pH Calibration Kit (CAT# P35379). Cells were allowed to incubate for 5 min before imaging. Representative Fast FLIM images pseudocolored by average photon arrival time and representative Fast FLIM histograms are presented

3.6 Materials & Methods

3.6.1 Materials

Cell culture/Microscopy: McCoy's 5A Medium without phenol red (#SH30270, Cytiva); all siRNAs (Dharmacon, **Table 3.6.10**); 4-well #1.5H glass bottom coverslip (#80427, Ibidi); Lipofectamine RNAiMAX transfection reagent (#13778150), Intracelluar pH Calibration Buffer Kit (#P35379) (Invitrogen); Fibronectin bovine plasma (#F1141); Gibco™ Dulbecco's modified eagle medium (DMEM) without phenol red, high glucose, with 25 mM HEPES (#21063), Gibco™ GlutaMAX™ Supplement, 200 mM (#35050061), Gibco™ Sodium Pyruvate, 100 mM (#11360070), Gibco™ TrypLE Express Enzyme (1x) with (#12605010) and without (#12604013) phenol red, McCoy's 5a Medium (#16600082), Nunc™ Lab-Tek™ 8-well Chambered Coverglass (#155411) (Thermofisher Scientific); Saos-2 cell stock (UC Berkeley Cell Culture Facility);

Chemicals: SNARF™-4F 5(and-6)-Carboxylic Acid (#S23920, Invitrogen); DBCO NHS ester (#22231), DBCO-Amine (#22066), DBCO-PEG2-Amine (#29733), DBCO-PEG4-Amine (#29732) (BroadPharm); Monensin sodium salt (#M5273), Potassium Chloride (#P3911), Sodium Chloride (#S9888) (Sigma); Lissamine Rhodamine B Ethylenediamine (#T01096, Tenova); Bafilomycin A1 (#J61835), 4-aminopyridine (#J61470), Tris (2-Carboxyethyl) Phosphine Hydrochloride (#50-153-2844) (Thermofisher Scientific); Nigericin sodium salt (#C873Y08, Thomas Scientific); Zinc Chloride (1M aqueous solution, #470303-074, VWR).

3.6.2 Synthesis of DBCO-functionalized rhodamine and SNARF-4F

Rho-DBCO was synthesized by Angel Vázquez Maldonado as described previously.[19] Briefly, Lissamine Rhodamine B ethylenediamine was incubated with 10 equivalents of DBCO NHS ester in DMSO for 1 h at room temperature (RT) and purified by HPLC. SNARF-4F-DBCO, SNARF-4F-PEG2-DBCO, and SNARF-4F-PEG4-DBCO were synthesized by Neville Dadina. SNARF-4F™ carboxylic acid was added to a dry microwaved vial and suspended in DMSO. DIPEA was then added, followed by TSTU. Activation of the acid to the NHS-ester was monitored by LC/MS. Upon complete conversion, DBCO-NH_2 (or DBCO-PEG2-NH_2 / DBCO-PEG4-NH_2) was added to the vial and reaction progress was monitored by LC/MS. Upon completion, the crude was purified by preparative reverse-phase HPLC.

3.6.3 Preparation of Rho-labeled and SNARF-labeled ZF5.3

ZF5.3 containing an N-terminal azide (**Table 3.6.10**) was synthesized as described previously via incorporation of (S)-2-(Fmoc-amino)-6-azidohexanoic acid at the N-terminus followed by acetylation.[19] Purified Ac-Lys(N3)-ZF5.3 was reacted with 10 equivalents of Rho-DBCO or 5 equivalents of SNARF-DBCO / SNARF-PEG2-DBCO / SNARF-PEG4-DBCO in DMSO at RT until the reaction reached completion as monitored by LC/MS (approximately 1 h). Rho-ZF5.3 and SNARF-ZF5.3 were then purified by HPLC and lyophilized. The peptides were reconstituted by dissolving in a buffer comprised of

20 mM Tris pH 7.5 / 150 mM KCl, incubating with 2 molar equivalents of TCEP for 10 min at RT, and adding 2 equivalents of zinc chloride. Peptides were quantified by molar extinction coefficient (Rho-ZF5.3) or Pierce 660 nm protein assay (SNARF-ZF5.3) and stored in working aliquots at -80°C.

3.6.4 SNARF-4F absorbance and fluorescence intensity measurements

Absorbance of SNARF-4F-DBCO between 300 and 700 nm was measured at 10 µM concentration in 20 mM Tris, 150 mM KCl pH 4.5 – 7.5 using a UV/Vis spectrometer (Cary 60 UV-Vis, Agilent Technologies). Absorbance of SNARF-ZF5.3 was measured under the same conditions except the concentration was 4 µM to conserve material. Fluorescence intensity spectra for 10 µM SNARF-4F-DBCO or 4 µM SNARF-ZF5.3 in the same buffers described above were obtained by measuring fluorescence emission between 525 nm and 700 nm when excited at 514 nm or between 560 nm and 700 nm when excited at 550 nm using a spectrofluorometer (PTI, now Horiba, QM400).

3.6.5 SNARF-ZF5.3 and Rho-ZF5.3 *in vitro* fluorescence lifetime measurements

FLIM:

Fluorescence lifetime characterization of SNARF-ZF5.3 and Rho-ZF5.3 was performed at 4 µM final concentration in 20 mM Tris, 150 mM KCl pH 4.5 – 7.5. All samples were warmed to 37°C before fluorescence lifetimes were measured using a STELLARIS 8 microscope (Leica Microsystems) with a Leica DMi8 CS scanhead, a HC Plan-Apo 63x/1.4NA water immersion objective, and a pulsed white-light laser (440 nm-790 nm; 440 nm: > 1.1 mW; 488 nm: > 1.6 mW; 560 nm: > 2.0 mW; 630 nm: > 2.6 mW; 790 nm: > 3.5 mW). All microscopy experiments were performed at 37°C (monitored using Oko-Touch) and 5% CO_2 in a blacked out cage enclosure from Okolab. Before the start of each experiment, the correction collar was optimized to compensate for variations in coverslip thickness. SNARF-4F was excited at either 514 nm or 561 nm and Rho-ZF5.3 was excited at 561 nm, both with a pulse frequency of 80 MHz. Images were acquired with ≥1000 photons per pixel, and mean fluorescence lifetimes were calculated using the LasX software to fit triexponential decay models (*n*-Exponential Reconvolution) to the observed fluorescence decay (χ^2 < 2). Fluorescence lifetime calculations were also performed using phasor analysis by manually placing thresholds around lifetime clusters in the LasX software.[45]

FLIM-FCS:

Before the start of each experiment, the correction collar was optimized to compensate for variations in coverslip thickness. SNARF-ZF5.3 and Rho-ZF5.3 were excited at 561 nm (7% laser intensity for SNARF, 2% laser intensity for Rho) with a pulse frequency of 80 MHz. A 4 µM solution of SNARF-ZF5.3 or 500 nM solution of Rho-ZF5.3 in 20 mM Tris, 150 mM KCl pH 4.5 – 7.5 was used for all measurements. FCS measurements were taken in triplicate for each condition. Autocorrelation functions (ACFs) were fitted using the LasX software (Diffusion with Triplet fit model, Triplet

Amplitude set to zero, Structural Parameter set to 0.17) and discarded if $\chi^2 > 10$. For passing curves, mean fluorescence lifetimes were calculated using the LasX software by fitting triexponential decay models (*n*-Exponential Reconvolution) for the fluorescence decay associated with each ACF. Fits were discarded if $\chi^2 > 2$. All remaining intensity-weighted lifetime values were plotted as a function of pH.

3.6.6 Cellular workup for *in cellula* SNARF-ZF5.3 and Rho-ZF5.3 fluorescence lifetime and fluorescence correlation spectroscopy measurements

SNARF-ZF5.3 FLIM and FLIM-FCS:

The day prior to FLIM or FCS experiments, 80,000 Saos-2 cells were plated in either a 12-well dish or a 4-well glass-bottom Ibidi LabTek microscopy dish. The following day, cells were incubated with 2 µM SNARF-ZF5.3 or 1 µM Rho-ZF5.3 in 500 µL McCoy's 5a medium (no phenol red, no FBS) for 1 h at 37°C. During the incubation, a fibronectin solution diluted into DPBS (0.1 mg/mL) was added to the appropriate number of wells of an 8-well or 4-well Ibidi #1.5H glass-bottom microscopy dish and incubated at 37°C until plating. For FCS experiments, a 100 nM solution of AlexaFluor 594 hydrazide dye in water was also added to one well of the microscopy dish for calibration to calculate the microscope focal volume. After the incubation, cells were washed three times with DPBS, trypsinized for 5 min (400 µL, no phenol red) to lift, and quenched with with 1 mL clear McCoy's 5A medium + 15% FBS. The cells were pelleted in a 15 mL Falcon tube and washed one time with 1 mL of clear DMEM + Hepes. During this centrifugation step, the microscopy dish was removed from the incubator and fibronectin-containing wells were washed three times with DPBS. The DPBS was left in each well until cells were ready to add. The pelleted cells were then resuspended in 600 µL (for 4-well microscopy dish) or 300 µL (for 8-well microscopy dish) DMEM + Hepes, plated on the microscopy dish, and transferred to 37°C, 5% CO_2 to allow the cells to adhere flatly before starting imaging (see **3.6.7**).

SNARF-ZF5.3 FLIM with pH-altering small molecules:

Bafilomycin A1 and 4-aminopyridine were used to alter the intracellular pH for fluorescence lifetime analysis. SNARF-ZF5.3 incubation and cellular work-up steps were performed as described above. To raise the intracellular pH, a 250 nM solution of Bafilomycin A1 in DMEM was incubated with cells for 20 min after allowing them to adhere in the microscopy dish. Cells were then washed once with DPBS before beginning FLIM. To decrease the intracellular pH, a 100 µM solution of 4-aminopyridine in DMEM was incubated with cells for 10 min after allowing them to adhere in the microscopy dish. Cells were then imaged directly with no wash step.

SNARF-ZF5.3 FLIM with siRNA knockdowns:

Knockdowns for VPS39 and a RISC-free control were evaluated using the siRNAs listed in **Table 3.6.10** and were performed as described previously.[50] Four days before delivery, 45,000 Saos-2 cells were plated in a 12-well dish in McCoy's 5A media +15%

FBS (no phenol red, no P/S). The next day, cells were transfected with the siRNA of interest at a final concentration of 100 nM using Lipofectamine RNAi/MAX transfection agent in McCoy's 5A media + 15% FBS (no phenol red, no P/S) and incubated for 4 h at 37°C, 5% CO_2. Cells were then washed three times with DPBS and incubated for 72 h at 37°C, 5% CO_2 in McCoy's 5A media + 15% FBS (2 mL/well, no phenol red, no P/S) before delivery experiments. Cells were treated with SNARF-ZF5.3 and prepared for microscopy as described above.

SNARF-ZF5.3 FLIM with pH calibration:

Calibration of *in cellula* fluorescence lifetimes with pH was performed using ionophores. Calibration imaging buffer[53] was prepared using 140 mM KCl, 1 mM CaCl2, 1 mM MgCl2, 5 mM glucose, and 10% phosphate-citrate buffer at the desired pH (composed of varying ratios of 0.1M citric acid and 0.2M Na2HPO4 as described by Sigma). All buffers were then filter sterilized, pH corrected within 0.1 pH unit, and stored at 4°C. Immediately before use, a working volume of the desired buffer(s) was removed, mixed with nigericin and monensin ionophores at varying concentrations, and warmed to 37°C.

Conditions to equalize intracellular pH were first established by treating 80,000 Saos-2 cells plated the previous day with 3 µM SNARF-ZF5.3 for 1 h, followed by the same cellular workup described above. A higher concentration of SNARF-ZF5.3 than previously described was initially chosen to maximize brightness. After cells adhered to the microscopy dish, the media was replaced with imaging buffer at pH 7.5 containing 2 µM monensin and either 10 or 20 µM nigericin and incubated at 37°C for 10 min before imaging.

For the remaining calibration experiments, a final ionophore concentration of 2 µM monensin and 10 µM nigericin was used. 80,000 Saos-2 cells plated the previous day were incubated with 2 µM SNARF-ZF5.3 for 1 h to be consistent with prior FLIM experiments. The cells were washed and plated as described above. After adhering, the media was replaced with imaging buffer at pH 4.5, 5.5, 6.5, or 7.5 for 10 min before imaging. After cell death was observed at pH 4.5 and 5.5, this incubation period was shortened to 5 min.

For experiments performed with the Thermofisher Intracellular pH Calibration Kit (#P35379), manufacturer's protocols were followed to dissolve ionophores (nigericin and valinomycin) and prepare imaging solutions at pH 4.5 or 7.5. Cells were treated and plated for microscopy as described. A previous group reported that the provided Live Cell Imaging Solution decreased ionophore efficiency,[53] so we replaced the cell media directly with imaging buffer at the desired pH after cells adhered. Cells were allowed to incubate for 5 min before imaging.

3.6.7 *In cellula* SNARF-ZF5.3 fluorescence lifetime measurements

Fluorescence lifetime measurements were carried out using the same

experimental setup as **3.6.5**. SNARF-ZF5.3 was excited at 561 nm with a pulse frequency of 80 MHz and detected with an emission window of 580 – 835 nm. Endosomes varied significantly in brightness, and images were collected such that the dimmest endosomes had ≥100 photons per pixel. Representative Fast FLIM histograms and images pseudocolored by aveage photon arrival time per pixel are presented. For SNARF-ZF5.3 in the presence of pH-altering small molecules and siRNA knockdowns, phasor plots representing the lifetimes overlaid from 5-10 images per condition are also presented.

3.6.8 *In cellula* SNARF-ZF5.3 FLIM-FCS measurements

FCS data was acquired as described previously[28,49,50,59–62] and in **Chapter 2** with some minor modifications. SNARF-ZF5.3 was excited at 561 nm (7% laser intensity) and detected with an emission window of 580 – 835 nm. Each experiment began with the measurement of ten five-second autocorrelation traces using the well containing 100 nM AlexaFluor 594 hydrazide dye. This dye was used to both optimize the motorized correction collar by maximizing counts per molecule and to calculate the focal volume (see **Chapter 2** for more detail on FCS theory). Next, a confocal microscopy image of the cells was used to position the crosshairs of the microscope laser in the cytosol of cells within the frame. Areas with punctate fluorescence indicative of endosomally entrapped protein were avoided. Between five and ten autocorrelation traces (10 s each) were acquired per point, and one point was acquired per cell.

All data was analyzed using the LasX software. Autocorrelation curves from a given experiment were fitted using a Diffusion with Triplet fit model (Triplet Amplitude set to zero, structural factor set to 0.17) with the AlexaFluor 594 measurements as a pre-loaded calibration. For ACF curves with $\chi^2 < 40$, mean fluorescence lifetimes were calculated using the LasX software to fit triexponential decay models (*n*-Exponential Reconvolution) for the fluorescence decay associated with each ACF. Exponential decay fits were discarded if $\chi^2 > 2$. For all measurements that passed both χ^2 thresholds, the concentration and lifetime were plotted simultaneously using a custom Python script.

3.6.9 Statistics

All statistical tests were performed using GraphPad Prism 9 software and are detailed in the appropriate figure legends. Fluorescence lifetime data were analyzed using unpaired t-tests with Welch’s correction.

3.6.10 Relevant Sequences

Peptide Sequences	
ZF5.3	Ac-KYSCNVCGKAFVLSRHLNRHLRVHRRAT-NH_2
siRNA used for RNAi	
RISC-free	siGENOME RISC-Free Control siRNA: D-001220-01 (Dharmacon)
VPS39	siGENOME human SMARTpool siRNA VPS39: M-014052-01 (Dharmacon)

3.7 Acknowledgments

I am so grateful to Neville Dadina for teaching me everything about fluorescence lifetime imaging, performing FLIM experiments with me, and providing many rounds of feedback over the past year. I'm also thankful to Angel Vázquez Maldonado for providing the ZF5.3 peptides for this study, and to Dr. Aurora Alvarez-Buylla for her helpful feedback on this chapter.

3.8 References

(1) Rennick, J. J.; Johnston, A. P. R.; Parton, R. G. Key Principles and Methods for Studying the Endocytosis of Biological and Nanoparticle Therapeutics. *Nat. Nanotechnol.* **2021**, *16* (3), 266–276. https://doi.org/10.1038/s41565-021-00858-8.

(2) Gilleron, J.; Querbes, W.; Zeigerer, A.; Borodovsky, A.; Marsico, G.; Schubert, U.; Manygoats, K.; Seifert, S.; Andree, C.; Stöter, M.; Epstein-Barash, H.; Zhang, L.; Koteliansky, V.; Fitzgerald, K.; Fava, E.; Bickle, M.; Kalaidzidis, Y.; Akinc, A.; Maier, M.; Zerial, M. Image-Based Analysis of Lipid Nanoparticle–Mediated siRNA Delivery, Intracellular Trafficking and Endosomal Escape. *Nat Biotechnol* **2013**, *31* (7), 638–646. https://doi.org/10.1038/nbt.2612.

(3) Bissig, C.; Gruenberg, J. Lipid Sorting and Multivesicular Endosome Biogenesis. *Cold Spring Harb Perspect Biol* **2013**, *5* (10), a016816. https://doi.org/10.1101/cshperspect.a016816.

(4) Stein, M.-P.; Dong, J.; Wandinger-Ness, A. Rab Proteins and Endocytic Trafficking: Potential Targets for Therapeutic Intervention. *Advanced Drug Delivery Reviews* **2003**, *55* (11), 1421–1437. https://doi.org/10.1016/j.addr.2003.07.009.

(5) Shearer, L. J.; Petersen, N. O. Distribution and Co-Localization of Endosome Markers in Cells. *Heliyon* **2019**, *5* (9), e02375. https://doi.org/10.1016/j.heliyon.2019.e02375.

(6) Maxfield, F. R.; Yamashiro, D. J. Endosome Acidification and the Pathways of Receptor-Mediated Endocytosis. *Adv Exp Med Biol* **1987**, *225*, 189–198. https://doi.org/10.1007/978-1-4684-5442-0_16.

(7) Hu, Y.-B.; Dammer, E. B.; Ren, R.-J.; Wang, G. The Endosomal-Lysosomal System: From Acidification and Cargo Sorting to Neurodegeneration. *Transl Neurodegener* **2015**, *4*, 18. https://doi.org/10.1186/s40035-015-0041-1.

(8) Kane, P. M. The Where, When, and How of Organelle Acidification by the Yeast Vacuolar H+-ATPase. *Microbiology and Molecular Biology Reviews* **2006**, *70* (1), 177–191. https://doi.org/10.1128/mmbr.70.1.177-191.2006.

(9) Cipriano, D. J.; Wang, Y.; Bond, S.; Hinton, A.; Jefferies, K. C.; Qi, J.; Forgac, M. Structure and Regulation of the Vacuolar ATPases. *Biochimica et Biophysica Acta (BBA) - Bioenergetics* **2008**, *1777* (7), 599–604. https://doi.org/10.1016/j.bbabio.2008.03.013.

(10) Lafourcade, C.; Sobo, K.; Kieffer-Jaquinod, S.; Garin, J.; van der Goot, F. G. Regulation of the V-ATPase along the Endocytic Pathway Occurs through Reversible Subunit Association and Membrane Localization. *PLoS One* **2008**, *3* (7), e2758. https://doi.org/10.1371/journal.pone.0002758.

(11) Huotari, J.; Helenius, A. Endosome Maturation. *EMBO J* **2011**, *30* (17), 3481–3500. https://doi.org/10.1038/emboj.2011.286.

(12) Prasad, H.; Rao, R. The Na+/H+ Exchanger NHE6 Modulates Endosomal pH to Control Processing of Amyloid Precursor Protein in a Cell Culture Model of Alzheimer Disease *. *Journal of Biological Chemistry* **2015**, *290* (9), 5311–5327. https://doi.org/10.1074/jbc.M114.602219.

(13) Prasad, H.; Rao, R. Amyloid Clearance Defect in ApoE4 Astrocytes Is Reversed by Epigenetic Correction of Endosomal pH. *Proceedings of the National Academy of Sciences* **2018**, *115* (28), E6640–E6649. https://doi.org/10.1073/pnas.1801612115.
(14) Gruenberg, J.; van der Goot, F. G. Mechanisms of Pathogen Entry through the Endosomal Compartments. *Nat Rev Mol Cell Biol* **2006**, *7* (7), 495–504. https://doi.org/10.1038/nrm1959.
(15) Ko, M.; Quiñones-Hinojosa, A.; Rao, R. Emerging Links between Endosomal pH and Cancer. *Cancer Metastasis Rev* **2020**, *39* (2), 519–534. https://doi.org/10.1007/s10555-020-09870-1.
(16) Piot, N.; van der Goot, F. G.; Sergeeva, O. A. Harnessing the Membrane Translocation Properties of AB Toxins for Therapeutic Applications. *Toxins* **2021**, *13* (1), 36. https://doi.org/10.3390/toxins13010036.
(17) Smith, S. A.; Selby, L. I.; Johnston, A. P. R.; Such, G. K. The Endosomal Escape of Nanoparticles: Toward More Efficient Cellular Delivery. *Bioconjugate Chem.* **2019**, *30* (2), 263–272. https://doi.org/10.1021/acs.bioconjchem.8b00732.
(18) Shinn, J.; Kwon, N.; Lee, S. A.; Lee, Y. Smart pH-Responsive Nanomedicines for Disease Therapy. *J Pharm Investig* **2022**, *52* (4), 427–441. https://doi.org/10.1007/s40005-022-00573-z.
(19) Giudice, J.; Brauer, D. D.; Zoltek, M.; Maldonado, A. L. V.; Kelly, M.; Schepartz, A. Requirements for Efficient Endosomal Escape by Designed Mini-Proteins. bioRxiv April 6, 2024, p 2024.04.05.588336. https://doi.org/10.1101/2024.04.05.588336.
(20) Erazo-Oliveras, A.; Najjar, K.; Truong, D.; Wang, T.-Y.; Brock, D. J.; Prater, A. R.; Pellois, J.-P. The Late Endosome and Its Lipid BMP Act as Gateways for Efficient Cytosolic Access of the Delivery Agent dfTAT and Its Macromolecular Cargos. *Cell Chemical Biology* **2016**, *23* (5), 598–607. https://doi.org/10.1016/j.chembiol.2016.03.016.
(21) Boyken, S. E.; Benhaim, M. A.; Busch, F.; Jia, M.; Bick, M. J.; Choi, H.; Klima, J. C.; Chen, Z.; Walkey, C.; Mileant, A.; Sahasrabuddhe, A.; Wei, K. Y.; Hodge, E. A.; Byron, S.; Quijano-Rubio, A.; Sankaran, B.; King, N. P.; Lippincott-Schwartz, J.; Wysocki, V. H.; Lee, K. K.; Baker, D. De Novo Design of Tunable, pH-Driven Conformational Changes. *Science* **2019**, *364* (6441), 658–664. https://doi.org/10.1126/science.aav7897.
(22) Goldbach, N.; Benna, I.; Wicky, B. I. M.; Croft, J. T.; Carter, L.; Bera, A. K.; Nguyen, H.; Kang, A.; Sankaran, B.; Yang, E. C.; Lee, K. K.; Baker, D. De Novo Design of Monomeric Helical Bundles for pH-Controlled Membrane Lysis. *Protein Science* **2023**, *32* (11), e4769. https://doi.org/10.1002/pro.4769.
(23) Behr, J.-P. The Proton Sponge: A Trick to Enter Cells the Viruses Did Not Exploit. *CHIMIA* **1997**, *51* (1–2), 34–34. https://doi.org/10.2533/chimia.1997.34.
(24) Pei, D.; Buyanova, M. Overcoming Endosomal Entrapment in Drug Delivery. *Bioconjugate Chem.* **2019**, *30* (2), 273–283. https://doi.org/10.1021/acs.bioconjchem.8b00778.
(25) Vermeulen, L. M. P.; De Smedt, S. C.; Remaut, K.; Braeckmans, K. The Proton Sponge Hypothesis: Fable or Fact? *European Journal of Pharmaceutics and Biopharmaceutics* **2018**, *129*, 184–190. https://doi.org/10.1016/j.ejpb.2018.05.034.

(26) Bus, T.; Traeger, A.; S. Schubert, U. The Great Escape: How Cationic Polyplexes Overcome the Endosomal Barrier. *Journal of Materials Chemistry B* **2018**, *6* (43), 6904–6918. https://doi.org/10.1039/C8TB00967H.

(27) Paramasivam, P.; Franke, C.; Stöter, M.; Höijer, A.; Bartesaghi, S.; Sabirsh, A.; Lindfors, L.; Arteta, M. Y.; Dahlén, A.; Bak, A.; Andersson, S.; Kalaidzidis, Y.; Bickle, M.; Zerial, M. Endosomal Escape of Delivered mRNA from Endosomal Recycling Tubules Visualized at the Nanoscale. *Journal of Cell Biology* **2021**, *221* (2), e202110137. https://doi.org/10.1083/jcb.202110137.

(28) Steinauer, A.; LaRochelle, J. R.; Knox, S. L.; Wissner, R. F.; Berry, S.; Schepartz, A. HOPS-Dependent Endosomal Fusion Required for Efficient Cytosolic Delivery of Therapeutic Peptides and Small Proteins. *Proceedings of the National Academy of Sciences* **2019**, *116* (2), 512–521. https://doi.org/10.1073/pnas.1812044116.

(29) Brock, D. J.; Kondow-McConaghy, H. M.; Hager, E. C.; Pellois, J.-P. Endosomal Escape and Cytosolic Penetration of Macromolecules Mediated by Synthetic Delivery Agents. *Bioconjug Chem* **2019**, *30* (2), 293–304. https://doi.org/10.1021/acs.bioconjchem.8b00799.

(30) Chatterjee, S.; Kon, E.; Sharma, P.; Peer, D. Endosomal Escape: A Bottleneck for LNP-Mediated Therapeutics. *Proceedings of the National Academy of Sciences* **2024**, *121* (11), e2307800120. https://doi.org/10.1073/pnas.2307800120.

(31) Salim, H.; Pei, D. Assessing the Cellular Uptake, Endosomal EscapeEndosomal Escape, and Cytosolic Entry Efficiencies of Cyclic PeptidesCyclic Peptides. In *Peptide Macrocycles: Methods and Protocols*; Coppock, M. B., Winton, A. J., Eds.; Methods in Molecular Biology; Springer US: New York, NY, 2022; pp 301–316. https://doi.org/10.1007/978-1-0716-1689-5_16.

(32) Sahni, A.; Pei, D. Bacterial Toxins Escape the Endosome by Inducing Vesicle Budding and Collapse. *ACS Chem. Biol.* **2021**, *16* (11), 2415–2422. https://doi.org/10.1021/acschembio.1c00540.

(33) Herling, M. R.; Dmochowski, I. J. Ratiometric, pH-Sensitive Probe for Monitoring siRNA Delivery. *J. Am. Chem. Soc.* **2023**, *145* (17), 9417–9422. https://doi.org/10.1021/jacs.3c01032.

(34) Wilson, D. R.; Routkevitch, D.; Rui, Y.; Mosenia, A.; Wahlin, K. J.; Quinones-Hinojosa, A.; Zack, D. J.; Green, J. J. A Triple-Fluorophore-Labeled Nucleic Acid pH Nanosensor to Investigate Non-Viral Gene Delivery. *Molecular Therapy* **2017**, *25* (7), 1697–1709. https://doi.org/10.1016/j.ymthe.2017.04.008.

(35) Han, J.; Burgess, K. Fluorescent Indicators for Intracellular pH. *Chem. Rev.* **2010**, *110* (5), 2709–2728. https://doi.org/10.1021/cr900249z.

(36) Hausig-Punke, F.; Richter, F.; Hoernke, M.; Brendel, J. C.; Traeger, A. Tracking the Endosomal Escape: A Closer Look at Calcein and Related Reporters. *Macromolecular Bioscience* **2022**, *22* (10), 2200167. https://doi.org/10.1002/mabi.202200167.

(37) Desai, T. M.; Marin, M.; Mason, C.; Melikyan, G. B. pH Regulation in Early Endosomes and Interferon-Inducible Transmembrane Proteins Control Avian Retrovirus Fusion. *J Biol Chem* **2017**, *292* (19), 7817–7827. https://doi.org/10.1074/jbc.M117.783878.

(38) Polli, J. R.; Chen, P.; Bordeau, B. M.; Balthasar, J. P. Targeted Delivery of Endosomal Escape Peptides to Enhance Immunotoxin Potency and Anti-Cancer Efficacy. *AAPS J* **2022**, *24* (3), 47. https://doi.org/10.1208/s12248-022-00698-x.
(39) Sayers, E. J.; Peel, S. E.; Schantz, A.; England, R. M.; Beano, M.; Bates, S. M.; Desai, A. S.; Puri, S.; Ashford, M. B.; Jones, A. T. Endocytic Profiling of Cancer Cell Models Reveals Critical Factors Influencing LNP-Mediated mRNA Delivery and Protein Expression. *Molecular Therapy* **2019**, *27* (11), 1950–1962. https://doi.org/10.1016/j.ymthe.2019.07.018.
(40) Doyen, D.; Poët, M.; Jarretou, G.; Pisani, D. F.; Tauc, M.; Cougnon, M.; Argentina, M.; Bouret, Y.; Counillon, L. Intracellular pH Control by Membrane Transport in Mammalian Cells. Insights Into the Selective Advantages of Functional Redundancy. *Frontiers in Molecular Biosciences* **2022**, *9*.
(41) Pierzyńska-Mach, A.; Janowski, P. A.; Dobrucki, J. W. Evaluation of Acridine Orange, LysoTracker Red, and Quinacrine as Fluorescent Probes for Long-Term Tracking of Acidic Vesicles. *Cytometry Part A* **2014**, *85* (8), 729–737. https://doi.org/10.1002/cyto.a.22495.
(42) Quick, J. D.; Silva, C.; Wong, J. H.; Lim, K. L.; Reynolds, R.; Barron, A. M.; Zeng, J.; Lo, C. H. Lysosomal Acidification Dysfunction in Microglia: An Emerging Pathogenic Mechanism of Neuroinflammation and Neurodegeneration. *J Neuroinflammation* **2023**, *20*, 185. https://doi.org/10.1186/s12974-023-02866-y.
(43) Marcotte, N.; Brouwer, A. M. Carboxy SNARF-4F as a Fluorescent pH Probe for Ensemble and Fluorescence Correlation Spectroscopies. *J. Phys. Chem. B* **2005**, *109* (23), 11819–11828. https://doi.org/10.1021/jp0510138.
(44) Berezin, M. Y.; Achilefu, S. Fluorescence Lifetime Measurements and Biological Imaging. *Chem. Rev.* **2010**, *110* (5), 2641–2684. https://doi.org/10.1021/cr900343z.
(45) Digman, M. A.; Caiolfa, V. R.; Zamai, M.; Gratton, E. The Phasor Approach to Fluorescence Lifetime Imaging Analysis. *Biophysical Journal* **2008**, *94* (2), L14–L16. https://doi.org/10.1529/biophysj.107.120154.
(46) Liu, H.; Maruyama, H.; Masuda, T.; Honda, A.; Arai, F. Multi-Fluorescent Micro-Sensor for Accurate Measurement of pH and Temperature Variations in Micro-Environments. *Sensors and Actuators B: Chemical* **2014**, *203*, 54–62. https://doi.org/10.1016/j.snb.2014.06.079.
(47) Linders, P. T. A.; Ioannidis, M.; ter Beest, M.; van den Bogaart, G. Fluorescence Lifetime Imaging of pH along the Secretory Pathway. *ACS Chem. Biol.* **2022**, *17* (1), 240–251. https://doi.org/10.1021/acschembio.1c00907.
(48) Wang, C.; Zhao, T.; Li, Y.; Huang, G.; White, M. A.; Gao, J. Investigation of Endosome and Lysosome Biology by Ultra pH-Sensitive Nanoprobes. *Adv Drug Deliv Rev* **2017**, *113*, 87–96. https://doi.org/10.1016/j.addr.2016.08.014.
(49) Zhang, X.; Cattoglio, C.; Zoltek, M.; Vetralla, C.; Mozumdar, D.; Schepartz, A. Dose-Dependent Nuclear Delivery and Transcriptional Repression with a Cell-Penetrant MeCP2. *ACS Cent. Sci.* **2023**, *9* (2), 277–288. https://doi.org/10.1021/acscentsci.2c01226.
(50) Zoltek, M.; Vázquez Maldonado, A. L.; Zhang, X.; Dadina, N.; Lesiak, L.; Schepartz, A. HOPS-Dependent Endosomal Escape Demands Protein Unfolding.

ACS Cent. Sci. **2024**, *10* (4), 860–870. https://doi.org/10.1021/acscentsci.4c00016.

(51) van der Kant, R.; Jonker, C. T. H.; Wijdeven, R. H.; Bakker, J.; Janssen, L.; Klumperman, J.; Neefjes, J. Characterization of the Mammalian CORVET and HOPS Complexes and Their Modular Restructuring for Endosome Specificity*. *Journal of Biological Chemistry* **2015**, *290* (51), 30280–30290. https://doi.org/10.1074/jbc.M115.688440.

(52) Van Der Beek, J.; De Heus, C.; Sanza, P.; Liv, N.; Klumperman, J. Loss of the HOPS Complex Disrupts Early-to-Late Endosome Transition, Impairs Endosomal Recycling and Induces Accumulation of Amphisomes. *MBoC* **2024**, mbc.E23-08-0328. https://doi.org/10.1091/mbc.E23-08-0328.

(53) Lazzari-Dean, J. R.; Ingaramo, M. C.; Wang, J. C. K.; Yong, J.; Ingaramo, M. mScarlet Fluorescence Lifetime Reports Lysosomal pH Quantitatively. *Github.io* **2022**.

(54) Nicholls, D. G.; Ferguson, S. J. 2 - Ion Transport Across Energy-Conserving Membranes. In *Bioenergetics (Fourth Edition)*; Nicholls, D. G., Ferguson, S. J., Eds.; Academic Press: Boston, 2013; pp 13–25. https://doi.org/10.1016/B978-0-12-388425-1.00002-6.

(55) Lagadic-Gossmann, D.; Huc, L.; Lecureur, V. Alterations of Intracellular pH Homeostasis in Apoptosis: Origins and Roles. *Cell Death Differ* **2004**, *11* (9), 953–961. https://doi.org/10.1038/sj.cdd.4401466.

(56) Walton, Z. E.; Patel, C. H.; Brooks, R. C.; Yu, Y.; Ibrahim-Hashim, A.; Riddle, M.; Porcu, A.; Jiang, T.; Ecker, B. L.; Tameire, F.; Koumenis, C.; Weeraratna, A. T.; Welsh, D. K.; Gillies, R.; Alwine, J. C.; Zhang, L.; Powell, J. D.; Dang, C. V. Acid Suspends the Circadian Clock in Hypoxia through Inhibition of mTOR. *Cell* **2018**, *174* (1), 72-87.e32. https://doi.org/10.1016/j.cell.2018.05.009.

(57) Schwille, P. Fluorescence Correlation Spectroscopy and Its Potential for Intracellular Applications. *Cell Biochem Biophys* **2001**, *34* (3), 383–408. https://doi.org/10.1385/CBB:34:3:383.

(58) Kim, S. A.; Heinze, K. G.; Schwille, P. Fluorescence Correlation Spectroscopy in Living Cells. *Nat Methods* **2007**, *4* (11), 963–973. https://doi.org/10.1038/nmeth1104.

(59) Knox, S. L.; Steinauer, A.; Alpha-Cobb, G.; Trexler, A.; Rhoades, E.; Schepartz, A. Chapter Twenty-One - Quantification of Protein Delivery in Live Cells Using Fluorescence Correlation Spectroscopy. In *Methods in Enzymology*; Chenoweth, D. M., Ed.; Chemical Tools for Imaging, Manipulating, and Tracking Biological Systems: Diverse Chemical, Optical and Bioorthogonal Methods; Academic Press, 2020; Vol. 641, pp 477–505. https://doi.org/10.1016/bs.mie.2020.05.007.

(60) LaRochelle, J. R.; Cobb, G. B.; Steinauer, A.; Rhoades, E.; Schepartz, A. Fluorescence Correlation Spectroscopy Reveals Highly Efficient Cytosolic Delivery of Certain Penta-Arg Proteins and Stapled Peptides. *J. Am. Chem. Soc.* **2015**, *137* (7), 2536–2541. https://doi.org/10.1021/ja510391n.

(61) Wissner, R. F.; Steinauer, A.; Knox, S. L.; Thompson, A. D.; Schepartz, A. Fluorescence Correlation Spectroscopy Reveals Efficient Cytosolic Delivery of Protein Cargo by Cell-Permeant Miniature Proteins. *ACS Cent. Sci.* **2018**, *4* (10), 1379–1393. https://doi.org/10.1021/acscentsci.8b00446.

(62) Knox, S. L.; Wissner, R.; Piszkiewicz, S.; Schepartz, A. Cytosolic Delivery of Argininosuccinate Synthetase Using a Cell-Permeant Miniature Protein. *ACS Cent. Sci.* **2021**, *7* (4), 641–649. https://doi.org/10.1021/acscentsci.0c01603.
(63) Schwille, P.; Haustein, E. Fluorescence Correlation Spectroscopy.
(64) Lamb, D. C.; Schenk, A.; Röcker, C.; Scalfi-Happ, C.; Nienhaus, G. U. Sensitivity Enhancement in Fluorescence Correlation Spectroscopy of Multiple Species Using Time-Gated Detection. *Biophys J* **2000**, *79* (2), 1129–1138.
(65) Gohar, A. V.; Cao, R.; Jenkins, P.; Li, W.; Houston, J. P.; Houston, K. D. Subcellular Localization-Dependent Changes in EGFP Fluorescence Lifetime Measured by Time-Resolved Flow Cytometry. *Biomed Opt Express* **2013**, *4* (8), 1390–1400. https://doi.org/10.1364/BOE.4.001390.
(66) Garcia Romeu, H.; Deville, S.; Salvati, A. Time- and Space-Resolved Flow-Cytometry of Cell Organelles to Quantify Nanoparticle Uptake and Intracellular Trafficking by Cells. *Small* **2021**, *17* (34), 2100887. https://doi.org/10.1002/smll.202100887.
(67) Ghosh, A.; Karedla, N.; Thiele, J. C.; Gregor, I.; Enderlein, J. Fluorescence Lifetime Correlation Spectroscopy: Basics and Applications. *Methods* **2018**, *140–141*, 32–39. https://doi.org/10.1016/j.ymeth.2018.02.009.

CHAPTER FOUR

Quantification of Cas9 Ribonucleoprotein Delivery in Mammalian Cells

This chapter is based in part on a manuscript in preparation “The impact of gene editor dosage on editing outcomes” and has been adapted with permission from all co-authors.

4.1 Abstract

The delivery of genome editing tools remains a major obstacle to their success in the clinic. Gene editors like Cas9 are large multicomponent complexes whose activity depends on a complex quaternary structure. Delivery of these machineries as intact ribonucleoprotein complexes holds many advantages over nucleic acid and viral delivery strategies, mitigating risks of DNA integration and reducing off-target DNA modifications. Much progress has been made toward the delivery of intact Cas9; however, the ribonucleoprotein dosage required for efficient editing remains an active area of investigation. While it is clear that increased doses of RNP result in undesirable off-target effects and cytotoxicity, the precise amount of Cas9 RNP that must reach the nucleus in order to achieve editing is not known. Here, we use fluorescence correlation spectroscopy (FCS) to measure the absolute concentration of Cas9 RNP that reaches the nucleus when delivered over a range of dosages in multiple mammalian cell lines. We correlate these values to gene knockdown to determine that approximately 1700 molecules of Cas9 must be present in the HeLa nucleus to achieve 90% editing with a high-efficiency guide. We also find that the nuclear concentration of Cas9 RNP when delivered by electroporation is fairly uniform across three cell lines, suggesting that observed differences in gene knockdown potency do not necessarily result from variable delivery efficiency. Finally, we apply a two-component diffusion analysis of nuclear Cas9 to track the fraction of DNA-bound protein across dosages and find that the concentration of bound Cas9 in the nucleus decreases with time and correlates linearly with dosage. Accurate quantitation of nuclear Cas9 will enrich studies related to the effects of dosage on productive versus nonproductive outcomes and provide guidelines for optimization of genome editing delivery strategies.

4.2 Introduction

Genome modification by CRISPR-based gene editors has immense potential to provide curative treatments for diseases with underlying genetic determinants.[1] These impacts now extend beyond knocking out genes with nuclease activity to fine-tuning the expression of biomolecules in the cell through epigenetic and transcriptomic control.[2] These tools have enormous promise not only for genetic diseases, but also for the development of programmable treatments for cancer and autoimmune conditions through targeted immunotherapies.[3–5]

Despite this promise, the safe and efficacious delivery of gene editors remains a major obstacle to their widespread implementation in the clinic.[6,7] Broadly speaking, gene editors can be delivered either as an RNA, by viral vectors such as AAV to be transcribed and translated in the target cell, or as an intact ribonucleoprotein complex (RNP).[6] There are distinct advantages to delivering gene editors as an RNP, including finer control over intracellular lifetime that significantly reduces off-target effects[8] and limits immunogenic responses to the RNP.[9,10] Delivery as an RNP also reduces immunogenicity associated with viral vector delivery strategies, which has been a critical barrier to *in vivo* efficacy of AAV modalities.[11,12] While delivery of proteins to the interior of cells remains an important

therapeutic challenge,[13] widespread efforts to deliver the Cas9 RNP have identified several modalities with *in vivo* efficacy.[6,7]

Through this work, a range of delivery modalities for RNPs have been developed with variable success including virus-like particles (VLPs),[14–16] direct injection of purified proteins,[17] cell-penetrating peptides,[18] and lipid nanoparticles (LNPs).[6,7,19] Given the explosion of CRISPR therapies reaching clinical trials, it is critical to establish the necessary dose to maximize editing while minimizing substantial off-target effects. Significant efforts toward this goal have found that potency varies widely by editing target and delivery strategy, and that excessive doses result in unwanted immunogenicity and off-target edits *in vivo*.[9,20] These studies are typically performed by titrating the amount of exogenously supplied Cas9 and evaluating its activity by analysis of gene knockdown or double-stranded DNA breaks. Given that, in many cases, only a single DNA modification in an individual cell is required for activity, one might expect that the concentration of Cas9 needed in the nucleus would be quite low. However, a quantitative analysis of the physical amount of RNP required in the nucleus of cells to achieve a given editing efficiency has not been performed. Correlating the amount of RNP present in the nucleus to a given editing outcome would provide guidelines for successful delivery strategies and clarify the relationship between dwell time in the nucleus and off-target activity. This information would also fill a critical gap in the field to determine how many molecules of Cas9 in the nucleus are required to achieve editing.

In this chapter, we quantified the doses of the Cas9 RNP required to achieve editing in mammalian cells with multiple delivery strategies. We then used fluorescence correlation spectroscopy, a highly quantitative single-molecule technique,[21] to quantify the concentration of Cas9 RNP in the nucleus of HeLa, U2OS, and HEK293T cells treated with dosages that cover a range of editing efficiencies. We found that only ~1700 molecules of Cas9 RNP are required to achieve 90% editing in HeLa cells; increasing the dose commensurately increases the number of nuclear molecules, but does not improve editing efficiency further. Using a two-component diffusion model, we also evaluated the fraction of RNP that is bound to DNA over these same dosages and found that higher doses result in a larger fraction of DNA-interacting RNP. To our knowledge, these findings represent the first report of the number of Cas9 RNP molecules present in the nucleus of mammalian cells. These results pave the way to investigate whether discrepancies in potency with different delivery strategies arise due to differences in nuclear concentration or activity of the delivered material. We envision these data will enrich analyses of temporal regulation of RNP editing, provide a framework to deconvolute nuclear delivery from editing activity, and guide the development of novel delivery modalities.

4.3 Results

4.3.1 Cas9 gene editing outcomes vary by cell type and delivery method

A successful gene editing event requires the Cas9 RNP to be delivered to the nucleus, remain intact and biochemically active, and have access to the genomic locus of interest. To determine how many molecules in the nucleus are required for efficient

editing, we first needed to establish how much exogenous Cas RNP must be supplied to achieve gene knockdowns in a variety of cell lines. We chose to focus on two delivery strategies: electroporation and enveloped delivery vehicles (EDVs).[22] Electroporation is a standard method for RNP delivery that supplies an electrical pulse to form pores in the plasma membrane through which macromolecules can pass. Though applicable to nearly every cell type and well-established as an *ex vivo* delivery technique, electroporation can induce substantial cell death, is not adaptable for cell-type specific targeting, and cannot be translated *in vivo*.[7,23] EDVs leverage the structural and fusogenic capabilities of HIV but are engineered to package and deliver the Cas RNP. EDVs can be retargeted with single-chain antibody fragments to enable cell-type specific Cas9 delivery and have been applied successfully in live animal models.[22]

We began by establishing dose-response curves for gene knockdown by the Cas9 RNP delivered by electroporation or EDVs in two cell types: HeLa and HEK293T. To control for the impact of guide RNA on editing, we used a single high-efficiency guide targeting the B2M locus for all analyses. For electroporation,
commercially available Cas9 protein was complexed with the B2M cr:tracrRNA and activity was verified by assessing cleavage activity *in vitro*. We then electroporated a range of Cas9 RNP dosages (0.001 pmol – 100 pmol per 100k cells) into HeLa or HEK293T cells and evaluated knockdown of the B2M protein by flow cytometry (Fig. 4.1a,b). The amount of Cas9 RNP required for 50% gene knockdown varied widely by cell type, with ~1.2 pmol required in HeLa and ~0.4 pmol in HEK293T. For EDV delivery, the Cas9 RNP was packaged into EDVs as described previously[22] and the number of Cas9 molecules per EDV was determined by ELISA. Evaluation of B2M knockdown by EDV delivery revealed that significantly less exogenous RNP was required to achieve 50% editing, with only ~0.03 pmol required in HeLa and ~0.009 pmol in HEK293T. We further evaluated knockdown of B2M using a panel of eight guides targeting a 200-base pair (bp) window in the B2M locus in HEK293T cells and found that in all cases, EDV-mediated delivery of the Cas9 RNP yielded more potent knockdown (Fig. 4.1c). Thus, delivery by EDVs is more potent than electroporation by up to two orders of magnitude. Given that a significant proportion of RNP in EDVs is degraded or dysfunctional (data not shown), it is likely the delivery efficiency by EDVs is much higher than that of electroporation.

4.3.2 Fluorescence correlation spectroscopy quantifies the concentration of Cas9 RNP delivered to the nucleus by electroporation

The variation in dose-response curves by cell line and delivery method could reflect differences in delivery efficiency and/or activity of delivered material. We first chose to examine the variability in EC90 by cell type observed when Cas9 is delivered by electroporation. We can reasonably assume that the editing activity of the delivered Cas9 RNP is uniform because the source RNP is the same for all cell lines. Thus, we sought to establish whether differences in the quantity of Cas9 that reaches the nucleus could explain the variable EC90s.

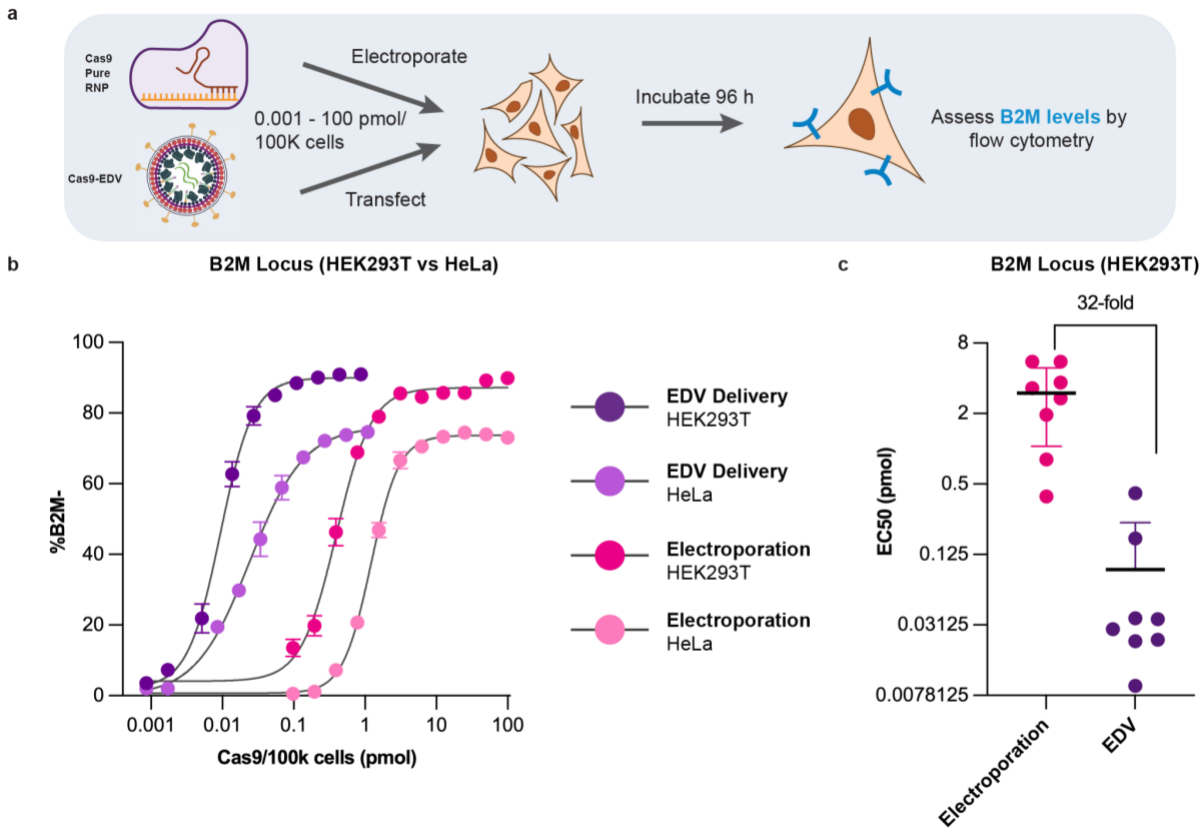

Figure 4.1. Dose-response curves for B2M knockdown reveal EDVs are more potent at delivering the Cas9 RNP than electroporation. (A) Experimental schematic. HEK293T or HeLa cells were either electroporated with purified Cas9 complexed with a B2M guide or transfected with EDVs encapsulating the Cas9-B2M guide RNP. Editing was assessed using flow cytometry to track surface B2M levels. **(B)** Dose-response curves for B2M knockdown. Each point is the mean ± SD of three biological replicates. **(C)** EC50 values for knockdown of B2M in HEK293T cells using a panel of 8 guides targeting a 200-base pair (bp) window in the B2M locus. Cas9 RNP was delivered by either electroporation or EDV, and knockdown was evaluated by flow cytometry.

We turned to fluorescence correlation spectroscopy (FCS), a single-molecule technique that tracks temporal fluctuations in fluorescence intensity to derive an absolute number of molecules in a focal volume generated by a microscope laser.[24–26] By placing the laser in a discrete intracellular location such as the nucleus, the concentration of fluorescent material in that compartment can be calculated provided the focal volume is known.[21] FCS has been applied extensively in living systems and has established the cytosolic and nuclear concentrations of multiple exogenously delivered peptides and proteins.[21,27–34] Because FCS inherently tracks fluctuations in fluorescence resulting from a molecule's diffusion within the focal volume, the resulting data also provides the molecule's lateral diffusion time (e.g. how long the it remains in the focal volume).[25] This value is affected by molecular weight and, in some cases, can distinguish molecules of varying size if their diffusion times are sufficiently different.

For analysis of Cas9 delivery to the nucleus, we were most interested in quantifying the amount of intact (and presumably active) RNP. We chose to use a

fluorescently labeled guide RNA, as we reasoned this may provide a detectable shift in diffusion time between free RNA and RNP. We complexed purified Cas9 with a cr:tracrRNA consisting of a commercially available ATTO^{TM} 550-labeled tracrRNA and a B2M crRNA (Fig. 4.2a). We then used FCS to assess the diffusion time of this Cas9 RNP in buffer and compared this to the diffusion of ATTO^{TM} 550-tracrRNA and ATTO^{TM} 550-annealed cr:tracrRNA alone (Fig. 4.2b). The tracrRNA and cr:tracrRNA both exhibited comparable diffusion time values (τ_{diff}) of 0.126 ms and 0.129 ms, respectively. As expected, τ_{diff} of the intact RNP was greater with a value of 0.253 ms, representing a roughly two-fold increase (Fig. 4.2b). For a typical macromolecule, we expect increases of ~2 – 10-fold in τ_{diff} *in cellula* compared to buffer because of changes in viscosity and interacting partners. Thus, the expected range of τ_{diff} in cells for free RNA is 0.26 – 1.29 ms, and for the Cas9 RNP is 0.5 – 2.5 ms (Fig. 4.2b). Although there is overlap in these ranges, we reasoned that the distribution of diffusion times exhibited by the Cas9 RNP should be more rigorously studied in cells to better reflect any complex diffusive behavior.

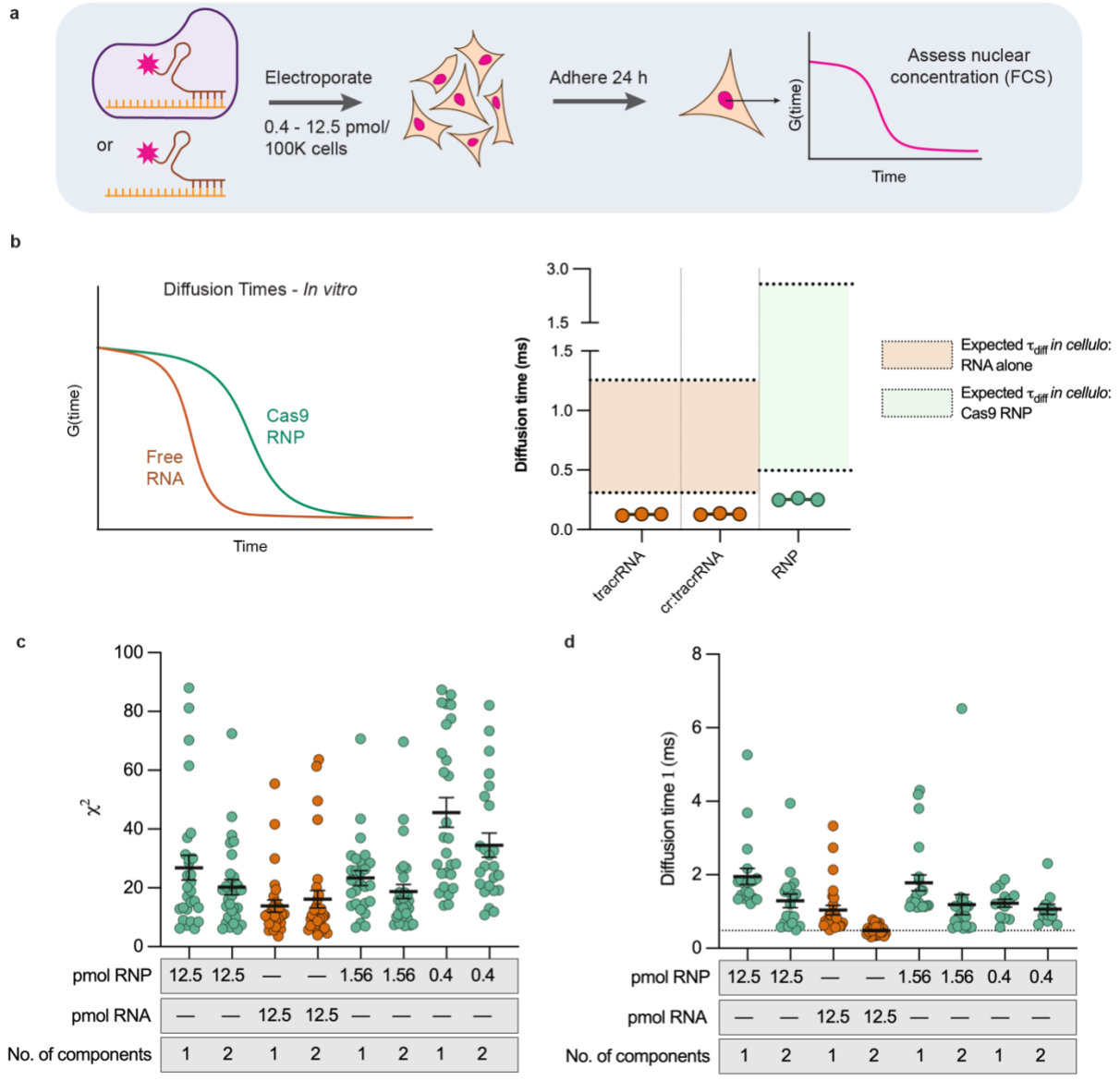

Figure 4.2. Optimization of fitting parameters for measuring Cas9 RNP nuclear concentration by fluorescence correlation spectroscopy. (A) Experimental schematic for experiments *in cellula*. HeLa cells were electroporated with purified Cas9 complexed with a B2M guide and incubated with cells for 24 h before analysis by FCS *in vitro* or in live cells. FCS measurements produce an autocorrelation function, which can be fit to derive both the concentration of delivered material and its diffusion time(s). **(B)** Example FCS traces for free RNA versus an intact Cas9 RNP (left). The diffusion time is calculated as the inflection point of the autocorrelation function. FCS traces were measured for tracrRNA, cr:tracrRNA, and Cas9 RNP *in vitro* (right) to determine diffusion times in buffer. Samples were prepared at a final concentration of 400 nM in DMEM. Each point represents the average diffusion time (τ_{diff}) calculated from ten autocorrelation traces at that point. Average τ for tracrRNA = 0.126 ms, for cr:tracrRNA = 0.129 ms, and for Cas9 RNP = 0.253 ms. **(C)** and **(D)** Comparison of one-component and two-component diffusion fitting equations for FCS data in cells prepared as described in **(A)**. **(C)** Chi-square (χ^2) values for autocorrelation curves fitted with one- or two-component diffusion equations plotted as a function of RNP or cr:tracrRNA dosage. Each point represents the χ^2 for the fitting of an average autocorrelation curve (calculated as the mean autocorrelation function from ten individual traces) obtained from an individual cell. **(D)** Diffusion times for the autocorrelation curves fitted in **(C)**. For a one-component diffusion equation, only one diffusion time is produced. For a two-component diffusion equation, a free diffusion and a slow diffusion time are both calculated; the free diffusion time is plotted here. Each point corresponds to the τ_{diff} derived from each fitted autocorrelation curve in **(C)**.

We delivered ATTO-550-labeled Cas9 RNP or ATTO™ 550-labeled cr:tracrRNA alone to HeLa cells by electroporation at a dosage of 0.4 – 12.5 pmol RNP/100k cells. After 24 hours, fluorescent signal in nuclei was evaluated by FCS (Fig. 4.2a). For each cell, ten FCS measurements were performed, and data was collected for ~30 cells per condition. Although diffusion behavior in buffer is fit by a relatively simple 3-D diffusion equation (see Methods for detail), diffusion in live cells is significantly more complex. Typical *in cellula* diffusion for macromolecules is hindered by the crowded cell interior and can be described effectively by a 3-D anomalous diffusion equation.[21] In the case of DNA-binding proteins like Cas9, however, diffusion can be further complicated by different fractions of protein that are freely or slowly diffusing. In this case, a two-component diffusion equation that incorporates both fast and slower subdiffusive behavior may be more appropriate.[32,35–37] To determine which fitting equation is best for analyzing FCS data of nuclear Cas9, we performed one-component and two-component analyses of nuclear autocorrelation functions obtained by FCS and compared the chi-square values (χ^2) for the respective fits (Fig. 4.2c). For RNP delivery, the χ^2 was lower for the two-component fit for all dosages, representing a better fit of the data; for RNA delivery alone, the χ^2 was essentially identical. We also evaluated the τ_{diff} values obtained in cells for RNP versus free RNA delivery when the data was fit with one component or two (for two-component fits, the "fast" τ_{diff} is reported) (Fig. 4.2d). These data reveal that the average τ_{diff} for RNP in cells is ~1.9-fold higher than that of free RNA when using a one-component fit and ~2.7-fold higher with a two-component fit. We thus proceeded with a two-component diffusion equation for all future nuclear delivery analyses. Given the distribution of *in cellula* and *in vitro* τ_{diff} for free RNA, we employed a lower τ_{diff} filter of 0.5 ms (Fig. 4.2d, dotted line) for Cas9 RNP delivery experiments to avoid fluorescent signal contributed by free RNA.

We note that distinguishing intact RNP from free RNA is particularly suited for analysis by fluorescence cross-correlation spectroscopy (FCCS). A FCCS measurement

excites dually-labeled material with two lasers, separates the fluorescence into two channels, and measures the degree of cross-correlation between them as a direct readout for molecular interaction.[25] In this case, the Cas9 protein must be labeled with a fluorophore spectrally separated from the RNA. Though attempts were made to perform FCCS with Cas9-GFP complexed with cr:tracrRNA labeled with ATTO™ 550, GFP exhibited complex photophysics during FCS measurements that convoluted data interpretation (see **4.3.3**). With a suitable fluorophore, FCCS will likely provide highly sensitive and quantitative information on the concentration of specifically intact Cas9 RNP in the nucleus. For the purpose of this chapter, however, we will continue to discuss only single-fluorophore FCS experiments.

With a proper data analysis pipeline in place, we next measured the nuclear concentration of Cas9 RNP in live cells. We chose to deliver a range of dosages that reflected the entire window in which gene editing was observed by flow cytometry in HeLa cells. We delivered 0.4 – 25 pmol Cas9 complexed with B2M cr:tracrRNA into HeLa cells by electroporation, allowed 24 hours for cells to recover, and used FCS to measure the nuclear concentrations (Fig. 4.3a). Concentration of delivered Cas9 correlated directly and linearly with dosage ($R^2 = 0.9672$) and ranged from 2.9 – 38.5 nM (Fig. 4.3b,c). These concentrations likely reflect a steady-state accumulation of Cas9, as similar values were obtained when measurements were performed 12 h after electroporation instead of 24 (Fig. 4.3b). Near the B2M knockdown EC90 dosage (~1.56 pmol RNP), Cas9 reached a nuclear concentration of 4.2 nM; by assuming a HeLa nuclear volume of 690 μm^3, this corresponds to ~1744 molecules in the nucleus.[38]

The two-component diffusion equation provides not only the concentration of fluorescent material, but also the fraction of that material that is slow-diffusing. Previous analysis of Cas9 diffusion in living cells demonstrated that this slow-diffusing fraction is greatly reduced when a guide RNA is absent,[37] suggesting that slow diffusion is the result of DNA binding. We plotted the slow-diffusing fraction from each cell that produced a valid FCS measurement as a function of Cas9 RNP dosage (Fig. 4.3b, right). There was a wide distribution in the fraction of DNA binding for each condition, although the average slow fraction decreased linearly with decreasing dosage ($R^2 = 0.94$). This suggests that increasing the local concentration of Cas9 RNP in the nucleus also increases the probability of binding to DNA, as expected. Interestingly, the DNA-bound slow fraction of Cas9 was significantly increased for a given dosage when evaluated 12 h after electroporation compared to 24 h. For instance, after 12 h, Cas9 exhibited a slow-diffusing fraction of 0.44 at a dosage of 12.5 pmol, but this fraction decreased to 0.30 after 24 h (Fig. 4.3b; compare 12 h vs 24 h). These results imply that a maximal amount of DNA-bound Cas9 is reached at or prior to 12 h after entry into the cell.

Given the variation in dose-response curves for B2M knockdown among cell lines, we performed the same concentration and diffusion analysis for HEK293T cells electroporated with either 12.5 or 1.56 pmol of Cas9 RNP. We also examined U2OS cells as another reference point for Cas9 delivery, although endogenous B2M expression in U2OS is too low to reliably quantify B2M knockdown efficiency as described for HeLa and

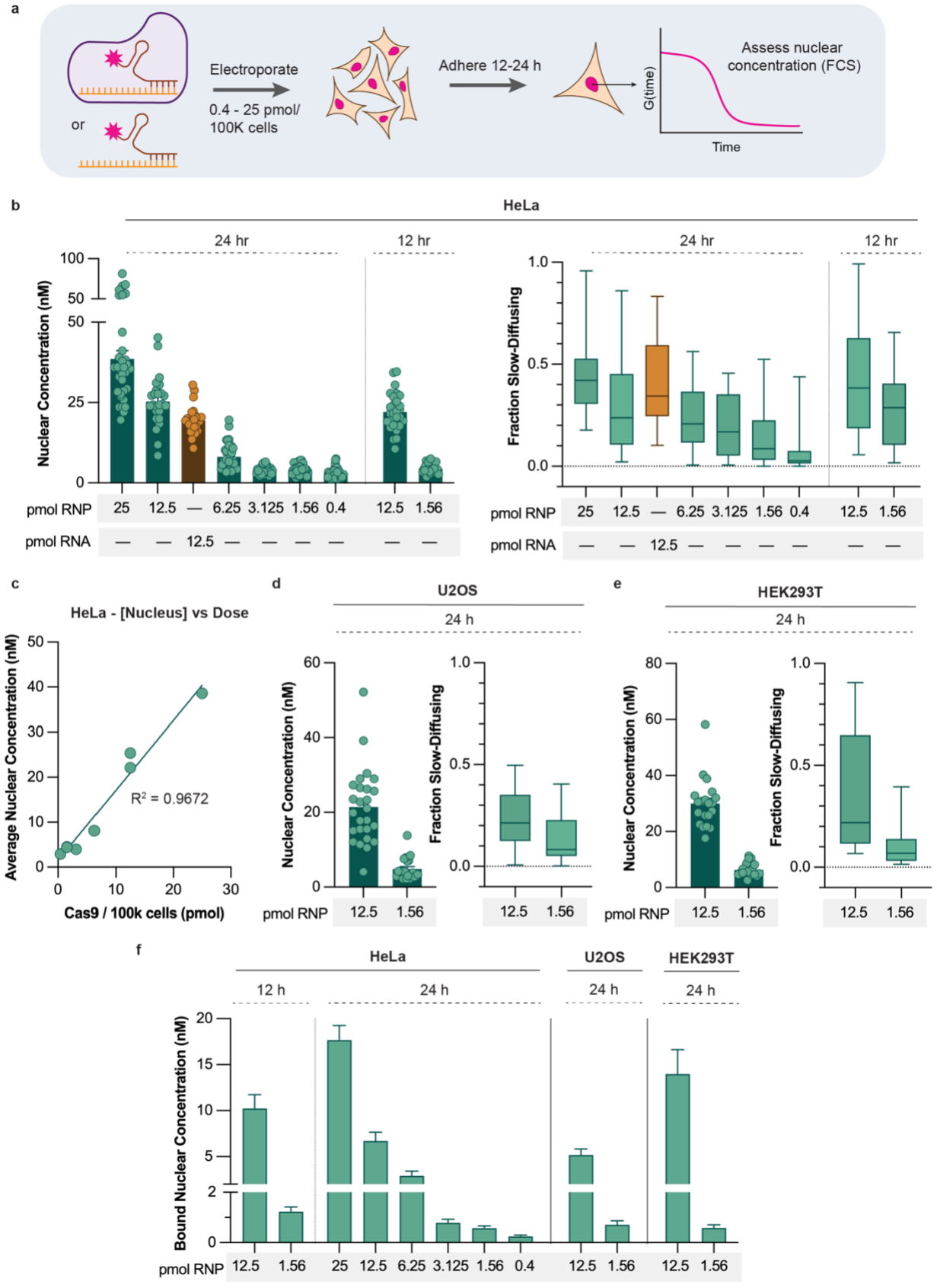
a
Electroporate
0.4 - 25 pmol/
100K cells
or
Adhere 12-24 h
G(time)
Time
Assess nuclear
concentration (FCS)
b
HeLa
24 hr
12 hr
Nuclear Concentration (nM)
Fraction Slow-Diffusing
pmol RNP
pmol RNA
c
HeLa - [Nucleus] vs Dose
Average Nuclear Concentration (nM)
Cas9 / 100k cells (pmol)
R² = 0.9672
d
U2OS
24 h
e
HEK293T
24 h
f
HeLa
U2OS
HEK293T
12 h
24 h
Bound Nuclear Concentration (nM)

Figure 4.3. Nuclear delivery of the Cas9 RNP in HeLa, HEK293T, and U2OS cells. (A) Experimental schematic for experiments *in cellula*. HEK293T, U2OS, or HeLa cells were electroporated with purified Cas9 complexed with a B2M guide and incubated with cells for 12-24 h before analysis of nuclear concentration by FCS. **(B)** FCS analysis of HeLa cells electroporated with the Cas9 RNP. Left: Nuclear concentration of Cas9 RNP or cr:tracrRNA alone as a function of dosage (in pmol per 100k cells). Each point represents the concentration in an individual cell. FCS values provided in nM, n>25 for each FCS condition with at least two biological replicates each (mean ± SEM). Outliers were removed using the ROUT method (Q = 0.1%) See Table 4.5.5 for more detail. Right: Fraction slowly diffusing for the same dosage range depicted on the left. All concentration values and diffusion times were derived by fitting FCS traces with a two-component 3D diffusion equation (see Methods for more detail). **(C)** Average nuclear concentration of Cas9 RNP versus dosage shows a strong linear correlation. **(D)** and **(E)** FCS analysis of nuclear concentration (left) and fraction slowly diffusing (right) for U2OS **(D)** and HEK293T cells **(E)**. FCS values provided in nM, n>20 for each FCS condition with at least two biological replicates each (mean ± SEM). Outliers were removed using the ROUT method (Q = 0.1%). **(F)** Bound nuclear concentration was calculated by multiplying the nuclear concentration of RNP in an individual cell by the slow fraction in that same cell. Concentrations are reported for HeLa, U2OS, and HEK293T cells.

HEK293T. In U2OS cells, Cas9 reached an average nuclear concentration of 21.4 nM when treated with 12.5 pmol and 4.85 nM when treated with 1.56 pmol; this is highly consistent with that observed in HeLa cells (25.4 and 4.51 nM, respectively) (Fig. 4.3d). The fraction of Cas9 that is slow-diffusing in U2OS cells is also identical to that within HeLa cells under similar dosages (Fig. 4.3d vs Fig. 4.3.b). In HEK293T cells, the Cas9 nuclear concentration was somewhat higher than observed for HeLa and U2OS. At a dose of 12.5 pmol/100k cells, the concentration of RNP in the nucleus was 30 nM, which was decreased to 6.3 nM at a dose of 1.56 pmol/100k cells. Correspondingly, the fraction DNA-bound was slightly higher than equivalent doses for HeLa and HEK293T cells as well (Fig. 4.3e).

The slow-diffusing fraction values can be used to extrapolate a “DNA-bound” nuclear concentration of Cas9 by multiplying the slow fraction value by the nuclear concentration for each cell. When plotted as a function of dosage, these data reveal that the average DNA-bound concentration of Cas9 required in the nucleus to achieve 50% editing in HeLa cells (at a dose of 1.56 pmol) is 0.57 nM. At an equivalent dosage in HEK293T and U2OS cells, the nuclear bound concentration is nearly identical at 0.6 nM and 0.7 nM, respectively (Fig. 4.3f).

4.3.3 Attempts at fluorescence correlation spectroscopy to quantify EDV-mediated Cas9 delivery

Given that EDV-mediated delivery is more potent than electroporation (at least for the B2M guide RNA, Fig. 4.1b), we next wanted to quantify the concentration of Cas9 that reached the nucleus when delivered with EDVs. Because EDVs are prepared by genetic tagging of viral packaging proteins with Cas9 and the corresponding guide RNA, the synthetic ATTO-550 cr:tracrRNA could not be used. Instead, we generated a fusion protein between Cas9 and mGreenLantern to track and quantify EDV-mediated delivery. The Cas9-GFP RNP was packaged into EDVs as previously described,[22] and the amount of incorporated Cas9-GFP was determined using an ELISA. We then transfected a fixed

concentration of Cas9-containing EDVs into HeLa cells and incubated for 24 h. After the incubation, the cells were washed twice with DPBS and evaluated by FCS (Fig. 4.4a).

Unfortunately, FCS analysis of HeLa nuclei containing Cas9-GFP revealed unexpected fluorescence behavior that convoluted the data interpretation. Firstly, FCS measurements performed on non-EDV-treated cells detected significant background fluorescence likely due to autofluorescence. Autofluorescence originates from organic molecules, including flavins, NADH, and others containing polycyclic hydrocarbons with delocalized electrons, capable of absorbing photons at the wavelength used to excite GFP. Autofluorescence in FCS can be detected as a non-correlating species that contributes fluorescence intensity without producing an autocorrelation function (ACF) During a measurement, this background can artificially lower the amplitude of the ACF for the fluorophore being analyzed and therefore must be rigorously subtracted from all acquired data. Although there are established equations for this subtraction,[39,40] the FCS data from EDV-treated cells suffered an additional limitation.

An FCS measurement in a single cell is typically performed by positioning the laser in the nucleus, acquiring ten 10-second autocorrelation traces, and using the average of these traces for fitting and further analysis. During measurement of Cas9-GFP in a given cell, we observed that the fluorescence intensity for the last measurement was consistently lower than that of the first (Fig. 4.4b-e, top panels). Although some variation in the ACFs is expected throughout the measurement, the fluorescence intensity should roughly overlap (Fig. 4.4b, ATTO™ 550). The observed depletion in intensity is representative of photobleaching, which is not unexpected for the variant of GFP (mGreenLantern) used for this study.[41] Though photobleaching is not prohibitive for FCS measurements, the relatively slow diffusion of Cas9-GFP (both due to its size and likely interaction with DNA) prevents diffusion of photobleached molecules out of the focal volume in a practical timeframe, magnifying their effect. We additionally observed that the amplitude of the ACFs reliably decreased throughout the duration of the FCS traces in a single cell, with the last trace nearly always lower in amplitude than the first over a range of laser intensities (Fig. 4.c-e). This is indicative of decreasing signal-to-noise levels and is not observed for measurement of Cas9 labeled with ATTO™ 550 (Fig. 4.b). Whether this change in amplitude is related to the photophysics of GFP or solely background autofluorescence is not clear.[25,26,42,43] However, because the y-intercept of the ACF dictates the number of molecules detected during the measurement window, any artifacts may misrepresent Cas9 delivery.

Fluorescent proteins are known to exhibit complex emission behavior related to photobleaching, pH sensitivity, multimerization, and flickering between dark and fluorescent states.[26,44,45] A thorough investigation of the photophysics of mGreenLantern when fused to Cas9, and how these processes contribute to the ACF, is required to proceed with FCS measurements for EDV delivery. The effects of photobleaching and autofluorescence can be controlled for with careful validation,[26,39,40,42] though it may be worthwhile to choose an alternative fluorescent protein for single-molecule applications before proceeding.[46]

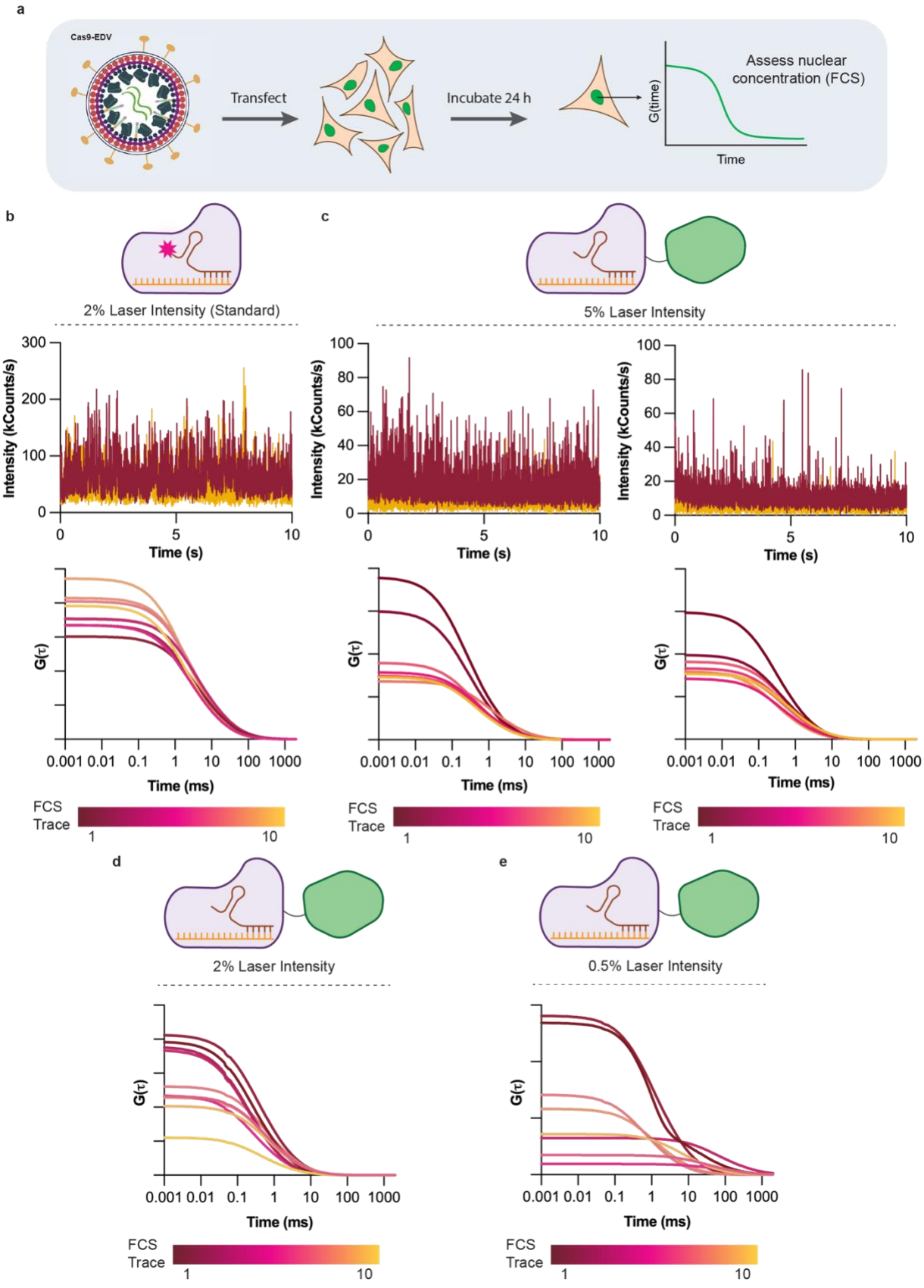
a
Cas9-EDV
Transfect
Incubate 24 h
Assess nuclear concentration (FCS)
G(time)
Time
b
2% Laser Intensity (Standard)
c
5% Laser Intensity
Intensity (kCounts/s)
Time (s)
G(τ)
Time (ms)
FCS Trace
1
10
d
2% Laser Intensity
e
0.5% Laser Intensity

Figure 4.4. Nuclear FCS analysis of EDV-delivered Cas9 RNP in HeLa cells reveals abnormal fluorescence emission patterns. (A) Experimental schematic for experiments *in cellula*. HeLa cells were transfected with EDVs containing Cas9 complexed with a B2M guide and incubated with cells for 24 h before analysis of nuclear concentration by FCS. **(B)** Representative fluorescence intensity trace (top) and autocorrelation curves (bottom) obtained from an individual cell when electroporated with the Cas9 RNP. Ten autocorrelation curves are measured per cell, each with a corresponding intensity trace. The first and tenth intensity traces are plotted on the top. All autocorrelation curves with χ^2<50 are plotted on the bottom, colored by their order during the measurement. For simplicity, autocorrelation curves were fit using the Leica Microsystems LasX software (Diffusion with Triplet fit model, Triplet Amplitude set to zero, Structural Parameter set to 0.17). Calibration with a dye standard was not performed, so absolute y-intercept values are arbitrary. **(C-E)** Representative fluorescence intensity traces (top) and autocorrelation curves (bottom) obtained from cells treated with Cas9 EDVs. In all cases, both the overall fluorescence intensity and the amplitude of the autocorrelation function decreases throughout the duration of the measurement. Laser intensities of 5% **(C)**, 2% **(D)**, and 0.5% **(E)** were tested.

4.4 Conclusions and Discussion

In this chapter, we used fluorescence correlation spectroscopy (FCS) to quantify the absolute concentration of Cas9 RNP that reaches the nucleus of a variety of mammalian cell lines. We found that only ~1700 molecules of Cas9 (~4 nM) are required in the nucleus of HeLa cells to achieve 90% knockdown with a potent guide. We compared the electroporation efficiency across three cell lines and found that nuclear concentrations are fairly consistent at equivalent dosages; this is perhaps surprising, as B2M knockdown in HEK293T cells when Cas9 is delivered by electroporation is more efficient than that in HeLa cells. These results could be explained by differences in nuclear volume between HeLa and HEK293T cells; if HEK293T cells have greater nuclear volume, an equivalent concentration would imply a larger number of Cas9 RNPs present. It is also possible that differences in gene knockdown efficiency by cell line do not arise from variations in delivery, but instead differences in nuclear activity of the RNP (e.g. nuclear crowding and/or accessibility of the target DNA sequence).

We also attempted to quantify the nuclear concentration of Cas9-GFP delivered by enveloped delivery vehicles (EDVs). Unfortunately, the photochemistry of GFP produced artifacts in FCS autocorrelation curves that precluded meaningful data collection. By correcting for these artifacts and/or choosing an alternative fluorophore, we are confident that nuclear concentrations can be established for EDV-mediated Cas9 delivery. It will be interesting to assess whether the increased potency observed for EDV-mediated knockdown of B2M relative to electroporation (Fig. 4.1b,c) corresponds to an increase in delivery efficiency of the RNP. Given that EDVs are engineered to target mammalian cells and actively promote endosomal escape via membrane fusion,[22] one might expect their delivery to be more efficient than passive uptake via nonspecific pores formed during electroporation.

Overall, these data demonstrate how few molecules are required in the nucleus for efficient genome editing. This provides further support for the development of strategies to deliver the intact RNP compared to vector-based approaches, which constitutively express (often unpredictable) levels of protein. Even RNP delivery methods with low efficiency may be successful if they reach this nuclear concentration threshold.

It is important to note that these data are collected with a high-efficiency guide RNA; it is likely that the concentration required for editing specific sequences will vary significantly by target. Nevertheless, these findings represent the first quantitative report on the relationship between the number of Cas9 molecules in the nucleus and gene editing efficiency. The method presented here can be applied toward any target sequence using any adherent cell line (a requisite for FCS analysis). Importantly, these results can deconvolute the comparison of extracellular EC50 values by separating nuclear concentration from editing activity. This will allow for more rigorous studies on the successes and limitations of delivery strategies and facilitate efforts to improve the therapeutic efficacy of gene editors.

4.5 Materials and Methods

4.5.1 Materials

CRISPR Reagents: Alt-R® CRISPR-Cas9 tracrRNA, ATTO™ 550 (#1075928, IDT); B2M crRNA (IDT, sequence: GAGTAGCGCGAGCACAGCTA); *S. pyogenes* Cas9-NLS purified protein (UC Berkeley QB3 MacroLab).

Cell culture/microscopy: 8-well #1.5H glass bottom coverslip (#80801, Ibidi); Fibronectin bovine plasma (#F1141, Millipore Sigma); TransIT-LT1 transfection reagent (#2304, Mirus Bio); Gibco™ Dulbecco's modified eagle medium (DMEM) without phenol red, high glucose, with 25 mM HEPES (#21063, Thermofisher Scientific);

Cell lines & plasmids: HeLa, HEK293T, and U2OS cell lines (UC Berkeley Cell Culture Facility); pCMV-VSV-G (Addgene plasmid #8454), psPax2-U6-sgRNA (Addgene plasmid #12260); LentiX 293T cell stock (#632180, Takara Bio).

Chemicals: AlexaFluorTM 488 NHS Ester (#11820, Lumiprobe); Ethylenediaminetetraacetic acid (EDTA, #E9884), Sodium Chloride (#S9888), Tris-HCl 1M (#DB0339) (Millipore Sigma); Alexa Fluor™ 594 hydrazide (#A10438, ThermoFisher Scientific).

4.5.2 Preparation of Cas9 RNP and Cas9-EDVs for delivery

Preparation of all materials for delivery experiments was performed by Hannah Karp and is detailed in a manuscript in preparation called “The impact of gene editor dosage on editing outcomes.” A summary of relevant procedures is provided below.

Preparation of Cas9 RNP for electroporation experiments

Commercially available *S. pyogenes* Cas9 (QB3 Institute MacroLab, UC Berkeley) was complexed with the B2M guide RNA by combining 40 μM Cas9 with 1.5 molar equivalents of guide RNA for 10 min at RT. For preparation of fluorescently labeled Cas9 RNP, functional guide RNA was first assembled by annealing an ATTO™ 550-labeled

tracrRNA with B2M crRNA in IDT Duplex Buffer at 95°C for 5 min and cooling down to RT. The Cas9 protein was complexed with ATTO™ 550-cr:tracrRNA as described above.

Electroporation of Cas9 RNP into mammalian cells

Cas9 RNPs were electroporated into HeLa, U2OS, or HEK293T cells using a 96-well format 4D-nucleofector (Lonza) with 100,000 cells per well. Dosages were administered as picomoles of RNP per 100,000 cells. HEK293T cells were electroporated using SF buffer and the CM-130 pulse code. HeLa cells and U2OS cells were electroporated with SE buffer and the CN-114 pulse code. After electroporation, all cells were immediately resuspended in pre-warmed media and transferred to fibronectin-treated 8-well microscopy dishes to adhere for 12-24 h.

Preparation of Cas9 EDVs for delivery experiments

Cas9 EDVs were prepared as described previously.[16,22] 4 million Lenti-X cells were seeded into 10 cm dishes and transfected the following day with 1 µg pCMV-VSV-G (Addgene plasmid #8454), 6.7 µg Gag-spyCas9-GFP-U6-sgRNA, and 3.3 µg psPax2-U6-sgRNA (Addgene plasmid #12260) with TransIT-LT1 transfection reagent at a 3:1 TransIT-LT1:plasmid ratio. After two days, supernatants containing Cas9-EDVs were harvested and passed through a 0.45 µm PES syringe filter. Cas9-EDVs were then laid on top of 30% sucrose in 100 mM NaCl, 10 mM Tris-HCl (pH 7.5, and 1 mM EDTA and concentrated by ultracentrifugation at 25,000 rpm for 2 h at 4°C in polypropylene tubes (SW28 rotor, Beckman Coulter). EDVs were resuspended in Opti-MEM at a final concentration of 20x and frozen at -80°C until use.

Delivery of Cas9 EDVs into HeLa cells

The day prior to experiments, HeLa cells were plated at a density of 100,000 cells per well in a fibronectin-treated 8-well microscopy dish. On the day of the experiment, EDVs were thawed on ice and diluted into OptiMEM to a final volume of 200 µL/well. Media in each well was aspirated and replaced with the EDV-OptiMEM solution and incubated at 37°C for 24 h.

4.5.3 Fluorescence correlation spectroscopy

On the day of each FCS experiment, 300 uL of 10 – 100 nM AlexaFluor 594 hydrazide (for electroporation experiments using ATTO™ 550 for Cas9 detection) or AlexaFluor 488 NHS ester (for EDV experiments using mGreenLantern for Cas9 detection), both diluted into MilliQ, was added to one well of the 8-well microscopy dish and incubated at 37°C for at least 30 min. Immediately prior to measurements, a DNA stain was added to the cells to visualize nuclei. For electroporated experiments using ATTO™ 550 for Cas9 detection, 300 nM Hoechst 33342 dye was incubated with cells for 5 min to label nuclei. For EDV experiments using mGreenLantern for Cas9 detection, SiR-DNA dye was diluted 1:1000 in cell media for 20 min to label nuclei. After nuclear dye

incubation, cells were washed 2x with DPBS and incubated with pre-warmed DMEM for imaging.

The procedures used for confocal microscopy and FCS have been generally described previously.[21,32,33] Experiments were performed with a STELLARIS 8 microscope (Leica Microsystems) with a Leica DMi8 CS scanhead, a HC Plan-Apo 63x/1.4NA water immersion objective, and a pulsed white-light laser (440 nm- 790 nm; 440 nm: > 1.1 mW; 488 nm: > 1.6 mW; 560 nm: > 2.0 mW; 630 nm: > 2.6 mW; 790 nm: > 3.5 mW, 78 MHz). All confocal imaging was performed using HyD S or HyD X detectors in counting mode, while FCS measurements were carried out using only a Hybrid HyD X detector in counting mode. All microscopy experiments were performed at 37°C (monitored using Oko-Touch) and 5% CO_2 in a blacked out cage enclosure from Okolab. Before the start of each experiment, the correction collar of the objective was adjusted by maximizing the counts per molecule for the AlexaFluor 594 hydrazide or AlexaFluor 488 NHS ester dye standard; minor fluctuations in the correction collar are expected based on the variable thickness of the glass-bottom microscopy dishes (LabTek™). After correction collar adjustment, ten five-second autocorrelation traces were obtained from the well containing dye standard to calculate the focal volume of the microscope; see **4.5.4** for more detail. AlexaFluor 594 was measured using the same settings as ATTO™ 550; AlexaFluor 488 was measured with the same settings as mGreenLantern (see below).

For electroporation experiments, ATTO™ 550 was excited at 553 nm with an emission window of 570 - 660 nm, and Hoescht 33342 was excited at 405 nm with an emission window of 432 – 509 nm. For EDV experiments, mGreenLantern was excited at 503 nm with an emission window of 510 – 620 nm, and SiR-DNA was excited at 652 nm with an emission window of 670 – 800 nm. Laser intensity for Cas9-ATTO™ 550 and Cas9-mGreenLantern was determined using *in vitro* samples of each respective protein and determining the maximal laser intensity for which the observed counts per molecule (CPM) remained within a linear range. The pinhole S5 of the laser was set to 1 AU. A confocal microscopy image of the cells was used to position the crosshairs of the microscope laser in the nucleus of 10-15 cells within the frame. All FCS measurements consisted of ten ten-second traces. A minimum of 30 cells per condition were measured for each biological replicate, and a minimum of two biological replicates were collected for each condition.

The expected diffusion time (τ_{diff}) for ATTO™ 550-Cas9 RNP was obtained by measuring *in vitro* autocorrelation traces for 400 nM solutions of RNP, annealed ATTO™ 550-tracrRNA:crRNA, or ATTO™ 550-tracrRNA alone in DMEM media (25 mM Hepes, no phenol red) at 37°C. For each sample, ten ten-second autocorrelation traces using the settings described above were measured per point, and three points were obtained per sample. These data were fitted using eq (1) below to derive the average diffusion time (τ_{diff}).

4.5.4 Analysis of FCS Data

Autocorrelation traces obtained from FCS measurements were analyzed using a custom MATLAB script.[32–34] To extract quantitative information from *in cellula* data, the effective confocal volume of the microscope must be known. This value was determined using eqs 1-3 by and the *in vitro* autocorrelation traces for the AlexaFluor 594 hydrazide or AlexaFluor 488 NHS ester standard measured at the start of each experiment, which have known diffusion coefficients in water.[30,47] These traces were fitted to a 3D diffusion equation (eq 1):

$$G(\tau) = \frac{1}{N} \cdot \frac{1}{(1+\frac{\tau}{\tau diff})\sqrt{1+(s^2\frac{\tau}{\tau diff})}} \qquad (1)$$

where N = the average number of molecules detected in the focal volume (V_{eff}), τ_{diff} = the average diffusion time that a molecule requires to cross V_{eff}, and s = the structure factor (the ratio of the radial to axial dimensions of the focal volume). The structure factor was measured to be 0.17 using the autocorrelation function of AlexaFluor 594 in water at 25°C and fixed for all subsequent analysis. V_{eff} can be extracted from these data by inserting the τ_{diff} value derived from eq (1) to calculate ω_1 in eq (2):

$$\omega_1 = \sqrt{4 \cdot D \cdot \tau_{diff}} \qquad (2)$$

where ω_1 = the lateral extension of the confocal volume and D = the known diffusion coefficient of the dye standard in water at 37°C. Note that diffusion coefficients at 25°C are typically reported in the literature and can be used to calculate the diffusion coefficient at 37°C using eq (3):

$$D(T) = D(25°C) \cdot \frac{t+273.15}{\eta(t)} \cdot 2.985 \cdot 10^{-6}\ Pa \cdot s \cdot K^{-1} \qquad (3)$$

where t = 37°C, D(25°C) for AlexaFluor 594 is 3.88 • 10^{-6} cm^2/s (ref.[30]) and for AlexaFluor 488 is 4.14 • 10^{-6} cm^2/s (ref.[47]), and $\eta(t)$ is the viscosity of water at 37°C (6.913 • 10^{-4} Pa · s, ref.[30]). Using this formula, the diffusion coefficient of AlexaFluor 594 at 37° is 5.20 • 10^{-6} cm^2/s and that of AlexaFluor 488 is 5.54 • 10^{-6} cm^2/s.

V_{eff} can then be directly calculated from eq (2):

$$V_{eff} = \pi^{\frac{3}{2}} \cdot ({\omega_1}^3) \cdot \frac{1}{s} \qquad (4)$$

The average V_{eff} for all experiments ranged from 0.25-0.4 fL.

To determine the appropriate fitting equation for data collected in cells, autocorrelation traces derived from *in cellula* measurements of HeLa cells treated with 0.4 – 12.5 pmol Cas9 RNP/100k cells were fitted using two equations. The first was a 3D

anomalous diffusion equation used for previous FCS measurements of proteins in live cells (eq 5)[21]:

$$G(\tau) = \frac{1}{N} \cdot \frac{1}{(1+\frac{\tau}{\tau diff})^{\alpha}\sqrt{1+s^2(\frac{\tau}{\tau_{diff}})^{\alpha}}} + G(\infty) \qquad (5)$$

where N = the average number of molecules in the focal volume, τ_{diff} = the average diffusion time that a molecule requires to cross V_{eff}, α = the anomalous diffusion coefficient, and s = the structure factor (0.17).

The second equation was a two-component diffusion equation previously applied to analysis of DNA-binding transcription factors by FCS.[32,35,36] The equation incorporates both a rapidly and slowly diffusing component to account for biphasic autocorrelation functions. This equation is almost identical to a two-component diffusion equation used for previous single-molecule analysis of Cas9 in live cells,[37] except it incorporates an anomalous diffusion coefficient for the slow-diffusing fraction.[32] Since
Cas9 binds DNA, we expected eq (6) to more accurately fit ACFs in live cells than eq 5:

$$G(\tau) = \frac{1}{N}\left(F_{fast} \cdot \frac{1}{\left(1+\frac{\tau}{\tau_{diff1}}\right)\cdot\sqrt{1+s^2\left(\frac{\tau}{\tau_{diff1}}\right)}}\right)\left(\left(1-F_{fast}\right) \cdot \frac{1}{(1+(\frac{\tau}{\tau_{diff2}})^{\alpha}\sqrt{1+s^2\left(\frac{\tau}{\tau_{diff2}}\right)^{\alpha}}}\right) \qquad (6)$$

where N = the average number of molecules in the focal volume, τ_{diff1} = the average diffusion time for the rapidly-diffusing component, τ_{diff2} = the average diffusion time for the slow-diffusing component, α = the anomalous diffusion coefficient, F_{fast} = the fraction of molecules that are rapidly diffusing, and s = the structure factor (0.17).

From the fittings, a set of parameters specific to individual measurements was obtained, including the diffusion time of the detected molecules (a single τ_{diff} for the 1-component fit or τ_{diff1} and τ_{diff2} for the 2-component fit), the fraction of molecules rapidly diffusing (F_{fast}), the number of molecules detected in the focal volume, and a chi-square (χ^2) value to describe the goodness of fit. The χ^2 values were compared for the one-component vs two-component fits to determine that the two-component diffusion equation most accurately represents the data. All FCS data were therefore fitted by eq (6) and filtered as described previously[32,33] to remove measurements where τ_{diff1} < 0.5 ms (indicative of free RNA), τ_{diff1} > 10 ms (indicative of aggregation), α < 0.3, and χ^2 > 30. We also excluded fits for which a second component was not identified.

For all FCS curves that passed these thresholds, the concentration (C) of protein in the nucleus was then calculated using the value of N derived above in eq (7):

$$C = \frac{N}{N_A \cdot V_{eff}} \qquad (7)$$

where N_A = Avogadro's number (6.023×10^{23} mol^{-1}). At least 20 concentration values from curves that passed all filters were used for each FCS condition.

The number of Cas9 molecules in the nucleus was calculated using the concentration obtained from eq (7) and a HeLa nuclear volume of $6.90 \bullet 10^{-13}$ L (ref.[38]) using eq (8):

$$N_{nucleus} = C \cdot (6.9 \cdot 10^{-13}\ L) \cdot N_A \qquad (8)$$

where N_A = Avogadro's number (6.023×10^{23} mol^{-1}).

Finally, each concentration value derived from eq (7) had a corresponding F_{fast} value describing the fraction of this concentration that was rapidly diffusing. The concentration of DNA-bound Cas9 in the nucleus was then calculated using eq 9:

$$C_{bound} = \frac{1}{F_{fast}} \cdot C \qquad (9)$$

4.5.5 Summary Values for Intracellular Delivery Experiments in Figure 4.3

For all fluorescence correlation spectroscopy (FCS) measurements, *n-BR* refers to the number of biological replicates and *n-Cells* refers to the number of individual cell measurements that passed all final filtering criteria (see **4.5.4** for more details) across all biological replicates. The "FCS Mean" corresponds to the average nuclear concentration in nM measured for that condition. The "FCS SEM" is the standard error of the mean for the corresponding nuclear concentration measurement. Unless specified otherwise, the dosage refers to picomoles of Cas9 ribonucleoprotein complex per 100k cells.

Cell Type	Time post-electroporation (h)	Dosage (pmol per 100k cells)	*n* - BR	*n* - FCS	FCS Mean	FCS SEM
HeLa	12	12.5	2	28	22.1	1.10
HeLa	12	1.56	2	30	4.41	0.245
HeLa	24	25	2	33	38.6	2.58
HeLa	24	12.5	2	25	25.4	1.59
HeLa	24	12.5 – RNA only	2	26	19.4	0.843
HeLa	24	6.25	3	37	8.11	0.650
HeLa	24	3.125	2	28	3.98	0.243

HeLa	24	1.56	2	37	4.22	0.239
HeLa	24	0.4	2	34	2.94	0.287
U2OS	24	12.5	2	26	21.4	1.96
U2OS	24	1.56	2	21	6.86	2.10
HEK293T	24	12.5	2	20	30.0	1.98
HEK293T	24	1.56	2	20	6.28	0.521

4.6 Acknowledgments

I am grateful to Hannah Karp for her generous contributions to the data presented in this chapter, including preparation of all Cas9 materials, generation of B2M knockdown dose-response curves, and helpful feedback throughout this entire collaboration.

4.7 References

(1) Khirallah, J.; Eimbinder, M.; Li, Y.; Xu, Q. Clinical Progress in Genome-Editing Technology and in Vivo Delivery Techniques. *Trends in Genetics* **2023**, *39* (3), 208–216. https://doi.org/10.1016/j.tig.2022.12.001.

(2) Wang, J. Y.; Doudna, J. A. CRISPR Technology: A Decade of Genome Editing Is Only the Beginning. *Science* **2023**, *379* (6629), eadd8643. https://doi.org/10.1126/science.add8643.

(3) Wu, S.-S.; Li, Q.-C.; Yin, C.-Q.; Xue, W.; Song, C.-Q. Advances in CRISPR/Cas-Based Gene Therapy in Human Genetic Diseases. *Theranostics* **2020**, *10* (10), 4374–4382. https://doi.org/10.7150/thno.43360.

(4) Azangou-Khyavy, M.; Ghasemi, M.; Khanali, J.; Boroomand-Saboor, M.; Jamalkhah, M.; Soleimani, M.; Kiani, J. CRISPR/Cas: From Tumor Gene Editing to T Cell-Based Immunotherapy of Cancer. *Front. Immunol.* **2020**, *11*. https://doi.org/10.3389/fimmu.2020.02062.

(5) Song, X.; Liu, C.; Wang, N.; Huang, H.; He, S.; Gong, C.; Wei, Y. Delivery of CRISPR/Cas Systems for Cancer Gene Therapy and Immunotherapy. *Advanced Drug Delivery Reviews* **2021**, *168*, 158–180. https://doi.org/10.1016/j.addr.2020.04.010.

(6) Raguram, A.; Banskota, S.; Liu, D. R. Therapeutic in Vivo Delivery of Gene Editing Agents. *Cell* **2022**, *185* (15), 2806–2827. https://doi.org/10.1016/j.cell.2022.03.045.

(7) Sinclair, F.; Begum, A. A.; Dai, C. C.; Toth, I.; Moyle, P. M. Recent Advances in the Delivery and Applications of Nonviral CRISPR/Cas9 Gene Editing. *Drug Deliv. and Transl. Res.* **2023**, *13* (5), 1500–1519. https://doi.org/10.1007/s13346-023-01320-z.

(8) Jang, H.-K.; Jo, D. H.; Lee, S.-N.; Cho, C. S.; Jeong, Y. K.; Jung, Y.; Yu, J.; Kim, J. H.; Woo, J.-S.; Bae, S. High-Purity Production and Precise Editing of DNA Base Editing Ribonucleoproteins. *Science Advances* **2021**, *7* (35), eabg2661. https://doi.org/10.1126/sciadv.abg2661.

(9) Charlesworth, C. T.; Deshpande, P. S.; Dever, D. P.; Camarena, J.; Lemgart, V. T.; Cromer, M. K.; Vakulskas, C. A.; Collingwood, M. A.; Zhang, L.; Bode, N. M.; Behlke, M. A.; Dejene, B.; Cieniewicz, B.; Romano, R.; Lesch, B. J.; Gomez-Ospina, N.; Mantri, S.; Pavel-Dinu, M.; Weinberg, K. I.; Porteus, M. H. Identification of Preexisting Adaptive Immunity to Cas9 Proteins in Humans. *Nat Med* **2019**, *25* (2), 249–254. https://doi.org/10.1038/s41591-018-0326-x.

(10) Kim, S.; Koo, T.; Jee, H.-G.; Cho, H.-Y.; Lee, G.; Lim, D.-G.; Shin, H. S.; Kim, J.-S. CRISPR RNAs Trigger Innate Immune Responses in Human Cells. *Genome Res.* **2018**, *28* (3), 367–373. https://doi.org/10.1101/gr.231936.117.

(11) Yang, T.; Braun, M.; Lembke, W.; McBlane, F.; Kamerud, J.; DeWall, S.; Tarcsa, E.; Fang, X.; Hofer, L.; Kavita, U.; Upreti, V. V.; Gupta, S.; Loo, L.; Johnson, A. J.; Chandode, R. K.; Stubenrauch, K.-G.; Vinzing, M.; Xia, C. Q.; Jawa, V. Immunogenicity Assessment of AAV-Based Gene Therapies: An IQ Consortium Industry White Paper. *Mol Ther Methods Clin Dev* **2022**, *26*, 471–494. https://doi.org/10.1016/j.omtm.2022.07.018.

(12) Bulcha, J. T.; Wang, Y.; Ma, H.; Tai, P. W. L.; Gao, G. Viral Vector Platforms within the Gene Therapy Landscape. *Sig Transduct Target Ther* **2021**, *6* (1), 1–24. https://doi.org/10.1038/s41392-021-00487-6.
(13) Porello, I.; Cellesi, F. Intracellular Delivery of Therapeutic Proteins. New Advancements and Future Directions. *Front. Bioeng. Biotechnol.* **2023**, *11*. https://doi.org/10.3389/fbioe.2023.1211798.
(14) An, M.; Raguram, A.; Du, S. W.; Banskota, S.; Davis, J. R.; Newby, G. A.; Chen, P. Z.; Palczewski, K.; Liu, D. R. Engineered Virus-like Particles for Transient Delivery of Prime Editor Ribonucleoprotein Complexes in Vivo. *Nat Biotechnol* **2024**, 1–12. https://doi.org/10.1038/s41587-023-02078-y.
(15) Banskota, S.; Raguram, A.; Suh, S.; Du, S. W.; Davis, J. R.; Choi, E. H.; Wang, X.; Nielsen, S. C.; Newby, G. A.; Randolph, P. B.; Osborn, M. J.; Musunuru, K.; Palczewski, K.; Liu, D. R. Engineered Virus-like Particles for Efficient in Vivo Delivery of Therapeutic Proteins. *Cell* **2022**, *185* (2), 250-265.e16. https://doi.org/10.1016/j.cell.2021.12.021.
(16) Hamilton, J. R.; Tsuchida, C. A.; Nguyen, D. N.; Shy, B. R.; McGarrigle, E. R.; Sandoval Espinoza, C. R.; Carr, D.; Blaeschke, F.; Marson, A.; Doudna, J. A. Targeted Delivery of CRISPR-Cas9 and Transgenes Enables Complex Immune Cell Engineering. *Cell Reports* **2021**, *35* (9), 109207. https://doi.org/10.1016/j.celrep.2021.109207.
(17) Staahl, B. T.; Benekareddy, M.; Coulon-Bainier, C.; Banfal, A. A.; Floor, S. N.; Sabo, J. K.; Urnes, C.; Munares, G. A.; Ghosh, A.; Doudna, J. A. Efficient Genome Editing in the Mouse Brain by Local Delivery of Engineered Cas9 Ribonucleoprotein Complexes. *Nat Biotechnol* **2017**, *35* (5), 431–434. https://doi.org/10.1038/nbt.3806.
(18) Sahu, S. U.; Castro, M.; Muldoon, J. J.; Asija, K.; Wyman, S. K.; Krishnappa, N.; Eyquem, J.; Nguyen, D. N.; Wilson, R. C. Peptide-Enabled Ribonucleoprotein Delivery for CRISPR Engineering (PERC) in Primary Human Immune Cells and Hematopoietic Stem Cells. bioRxiv July 16, 2024, p 2024.07.14.603391. https://doi.org/10.1101/2024.07.14.603391.
(19) Kazemian, P.; Yu, S.-Y.; Thomson, S. B.; Birkenshaw, A.; Leavitt, B. R.; Ross, C. J. D. Lipid-Nanoparticle-Based Delivery of CRISPR/Cas9 Genome-Editing Components. *Mol. Pharmaceutics* **2022**, *19* (6), 1669–1686. https://doi.org/10.1021/acs.molpharmaceut.1c00916.
(20) Gangopadhyay, S. A.; Cox, K. J.; Manna, D.; Lim, D.; Maji, B.; Zhou, Q.; Choudhary, A. Precision Control of CRISPR-Cas9 Using Small Molecules and Light. *Biochemistry* **2019**, *58* (4), 234–244. https://doi.org/10.1021/acs.biochem.8b01202.
(21) Knox, S. L.; Steinauer, A.; Alpha-Cobb, G.; Trexler, A.; Rhoades, E.; Schepartz, A. Chapter Twenty-One - Quantification of Protein Delivery in Live Cells Using Fluorescence Correlation Spectroscopy. In *Methods in Enzymology*; Chenoweth, D. M., Ed.; Chemical Tools for Imaging, Manipulating, and Tracking Biological Systems: Diverse Chemical, Optical and Bioorthogonal Methods; Academic Press, 2020; Vol. 641, pp 477–505. https://doi.org/10.1016/bs.mie.2020.05.007.
(22) Hamilton, J. R.; Chen, E.; Perez, B. S.; Sandoval Espinoza, C. R.; Kang, M. H.; Trinidad, M.; Ngo, W.; Doudna, J. A. In Vivo Human T Cell Engineering with

Enveloped Delivery Vehicles. *Nat Biotechnol* **2024**, 1–9. https://doi.org/10.1038/s41587-023-02085-z.
(23) Bloomer, H.; Khirallah, J.; Li, Y.; Xu, Q. CRISPR/Cas9 Ribonucleoprotein-Mediated Genome and Epigenome Editing in Mammalian Cells. *Advanced Drug Delivery Reviews* **2022**, *181*, 114087. https://doi.org/10.1016/j.addr.2021.114087.
(24) Magde, D.; Elson, E.; Webb, W. W. Thermodynamic Fluctuations in a Reacting System—Measurement by Fluorescence Correlation Spectroscopy. *Phys. Rev. Lett.* **1972**, *29* (11), 705–708. https://doi.org/10.1103/PhysRevLett.29.705.
(25) Schwille, P.; Haustein, E. Fluorescence Correlation Spectroscopy.
(26) Schwille, P. Fluorescence Correlation Spectroscopy and Its Potential for Intracellular Applications. *Cell Biochem Biophys* **2001**, *34* (3), 383–408. https://doi.org/10.1385/CBB:34:3:383.
(27) Kim, S. A.; Heinze, K. G.; Schwille, P. Fluorescence Correlation Spectroscopy in Living Cells. *Nat Methods* **2007**, *4* (11), 963–973. https://doi.org/10.1038/nmeth1104.
(28) LaRochelle, J. R.; Cobb, G. B.; Steinauer, A.; Rhoades, E.; Schepartz, A. Fluorescence Correlation Spectroscopy Reveals Highly Efficient Cytosolic Delivery of Certain Penta-Arg Proteins and Stapled Peptides. *J. Am. Chem. Soc.* **2015**, *137* (7), 2536–2541. https://doi.org/10.1021/ja510391n.
(29) Wissner, R. F.; Steinauer, A.; Knox, S. L.; Thompson, A. D.; Schepartz, A. Fluorescence Correlation Spectroscopy Reveals Efficient Cytosolic Delivery of Protein Cargo by Cell-Permeant Miniature Proteins. *ACS Cent. Sci.* **2018**, *4* (10), 1379–1393. https://doi.org/10.1021/acscentsci.8b00446.
(30) Steinauer, A.; LaRochelle, J. R.; Knox, S. L.; Wissner, R. F.; Berry, S.; Schepartz, A. HOPS-Dependent Endosomal Fusion Required for Efficient Cytosolic Delivery of Therapeutic Peptides and Small Proteins. *Proceedings of the National Academy of Sciences* **2019**, *116* (2), 512–521. https://doi.org/10.1073/pnas.1812044116.
(31) Knox, S. L.; Wissner, R.; Piszkiewicz, S.; Schepartz, A. Cytosolic Delivery of Argininosuccinate Synthetase Using a Cell-Permeant Miniature Protein. *ACS Cent. Sci.* **2021**, *7* (4), 641–649. https://doi.org/10.1021/acscentsci.0c01603.
(32) Zhang, X.; Cattoglio, C.; Zoltek, M.; Vetralla, C.; Mozumdar, D.; Schepartz, A. Dose-Dependent Nuclear Delivery and Transcriptional Repression with a Cell-Penetrant MeCP2. *ACS Cent. Sci.* **2023**, *9* (2), 277–288. https://doi.org/10.1021/acscentsci.2c01226.
(33) Zoltek, M.; Vázquez Maldonado, A. L.; Zhang, X.; Dadina, N.; Lesiak, L.; Schepartz, A. HOPS-Dependent Endosomal Escape Demands Protein Unfolding. *ACS Cent. Sci.* **2024**, *10* (4), 860–870. https://doi.org/10.1021/acscentsci.4c00016.
(34) Giudice, J.; Brauer, D. D.; Zoltek, M.; Maldonado, A. L. V.; Kelly, M.; Schepartz, A. Requirements for Efficient Endosomal Escape by Designed Mini-Proteins. bioRxiv April 6, 2024, p 2024.04.05.588336. https://doi.org/10.1101/2024.04.05.588336.
(35) Kaur, G.; Costa, M. W.; Nefzger, C. M.; Silva, J.; Fierro-González, J. C.; Polo, J. M.; Bell, T. D. M.; Plachta, N. Probing Transcription Factor Diffusion Dynamics in the Living Mammalian Embryo with Photoactivatable Fluorescence Correlation Spectroscopy. *Nat Commun* **2013**, *4* (1), 1637. https://doi.org/10.1038/ncomms2657.

(36) Zhao, Z. W.; White, M. D.; Alvarez, Y. D.; Zenker, J.; Bissiere, S.; Plachta, N. Quantifying Transcription Factor–DNA Binding in Single Cells in Vivo with Photoactivatable Fluorescence Correlation Spectroscopy. *Nat Protoc* **2017**, *12* (7), 1458–1471. https://doi.org/10.1038/nprot.2017.051.
(37) Knight, S. C.; Xie, L.; Deng, W.; Guglielmi, B.; Witkowsky, L. B.; Bosanac, L.; Zhang, E. T.; El Beheiry, M.; Masson, J.-B.; Dahan, M.; Liu, Z.; Doudna, J. A.; Tjian, R. Dynamics of CRISPR-Cas9 Genome Interrogation in Living Cells. *Science* **2015**, *350* (6262), 823–826. https://doi.org/10.1126/science.aac6572.
(38) Monier, K.; Armas, J. C. G.; Etteldorf, S.; Ghazal, P.; Sullivan, K. F. Annexation of the Interchromosomal Space during Viral Infection. *Nat Cell Biol* **2000**, *2* (9), 661–665. https://doi.org/10.1038/35023615.
(39) Weidemann, T. Application of Fluorescence Correlation Spectroscopy (FCS) to Measure the Dynamics of Fluorescent Proteins in Living Cells. In *Fluorescence Spectroscopy and Microscopy: Methods and Protocols*; Engelborghs, Y., Visser, A. J. W. G., Eds.; Humana Press: Totowa, NJ, 2014; pp 539–555. https://doi.org/10.1007/978-1-62703-649-8_24.
(40) Zhang, L.; Perez-Romero, C.; Dostatni, N.; Fradin, C. Using FCS to Accurately Measure Protein Concentration in the Presence of Noise and Photobleaching. *Biophysical Journal* **2021**, *120* (19), 4230–4241. https://doi.org/10.1016/j.bpj.2021.06.035.
(41) Petrich, A.; Aji, A. K.; Dunsing, V.; Chiantia, S. Benchmarking of Novel Green Fluorescent Proteins for the Quantification of Protein Oligomerization in Living Cells. *PLOS ONE* **2023**, *18* (8), e0285486. https://doi.org/10.1371/journal.pone.0285486.
(42) Hink, M. A.; Borst, J. W.; Visser, A. J. W. G. [5] Fluorescence Correlation Spectroscopy of GFP Fusion Proteins in Living Plant Cells. In *Methods in Enzymology*; Biophotonics, Part B; Academic Press, 2003; Vol. 361, pp 93–112. https://doi.org/10.1016/S0076-6879(03)61007-4.
(43) *Dynamics of fluorescence fluctuations in green fluorescent protein observed by fluorescence correlation spectroscopy*. https://doi.org/10.1073/pnas.95.23.13573.
(44) Siegel, A. P.; Baird, M. A.; Davidson, M. W.; Day, R. N. Strengths and Weaknesses of Recently Engineered Red Fluorescent Proteins Evaluated in Live Cells Using Fluorescence Correlation Spectroscopy. *International Journal of Molecular Sciences* **2013**, *14* (10), 20340–20358. https://doi.org/10.3390/ijms141020340.
(45) Remington, S. J. Fluorescent Proteins: Maturation, Photochemistry and Photophysics. *Current Opinion in Structural Biology* **2006**, *16* (6), 714–721. https://doi.org/10.1016/j.sbi.2006.10.001.
(46) Dunsing, V.; Luckner, M.; Zühlke, B.; Petazzi, R. A.; Herrmann, A.; Chiantia, S. Optimal Fluorescent Protein Tags for Quantifying Protein Oligomerization in Living Cells. *Sci Rep* **2018**, *8* (1), 10634. https://doi.org/10.1038/s41598-018-28858-0.
(47) Petrov, E. P.; Schwille, P. State of the Art and Novel Trends in Fluorescence Correlation Spectroscopy. In *Standardization and Quality Assurance in Fluorescence Measurements II: Bioanalytical and Biomedical Applications*; Resch-Genger, U., Ed.; Springer: Berlin, Heidelberg, 2008; pp 145–197. https://doi.org/10.1007/4243_2008_032.

CHAPTER FIVE

Conclusions and Outlook

Next-generation protein and RNA therapeutics, or biologics, are capable of achieving unprecedented clinical success for a number of incurable and difficult-to-treat diseases. Most current biologics act in the extracellular space, on the cell surface, or within the endocytic pathway, but few reach the cytosol or nucleus. This is largely the result of inefficient delivery due to endocytic uptake and subsequent lysosomal degradation. To successfully circumnavigate the endocytic pathway, a biologic must encode a discrete signal that enables its passage across the hydrophobic endosomal membrane.

Decades of research, summarized in **Chapter One**, have established numerous vehicles capable of promoting this passage to varying degrees of success. However, their development is hindered by an incomplete understanding of cellular trafficking mechanisms and a lack of quantitative information regarding the fraction of material that reaches a productive cellular location. In this dissertation, we discussed efforts to combat these challenges by applying highly quantitative analyses to the mechanisms, design rules, and dose-response relationships for a variety of protein-based biologics.

In **Chapter Two**, we explored the molecular design rules governing efficient intracellular delivery by a cell-permeant mini protein developed in the Schepartz lab called ZF5.3. ZF5.3 is a synthetic zinc finger modified with five arginine residues that has been demonstrated to escape endosomes with high efficiency, both on its own and when conjugated to therapeutically relevant cargos.[1–4] In this work, we showed that delivery depends on the ability of a protein cargo to unfold using fluorescence correlation spectroscopy (FCS), a single-molecule technique that precisely measures intra-cytosolic protein concentration.[4,5] We showed that regardless of molecular weight and surface charge, the conjugation of low-T_m cargos to ZF5.3 biased its endosomal escape toward a high-efficiency pathway that required endosomal fusion mediated by the HOPS complex. These findings provide clear guidance for the selection or design of optimally deliverable therapeutic cargo for ZF5.3. Similar findings that low thermodynamic stability enhanced intracellular delivery have been reported for toxin-mediated delivery of DARPins[6] and even cytosolic penetration of antisense oligonucleotides,[7] suggesting that the relationship between folding and endosomal escape may apply broadly to the passage of therapeutic macromolecules across cellular membranes.

In **Chapter Three**, we used ZF5.3 as a model to demonstrate the application of fluorescence lifetime measurements to studying intracellular delivery. We exploited the increasingly acidic pH of the endocytic pathway to develop pH-responsive tools for exploring both trafficking and delivery of ZF5.3. Using fluorescence lifetime imaging microscopy (FLIM) in live cells, we demonstrated that ZF5.3 experiences diverse microenvironments within the endocytic pathway that correspond to vesicular pH. With the proper calibration, we envision this analysis will enable sensitive detection of local pH changes as well as identification of endosomes at different stages without the need for colocalized protein markers. We further showed that integration of FLIM into FCS enriched measurements of cytosolic concentration by quantitatively filtering out fluorescent signal derived from acidic vesicles. This lifetime analysis provides a complete snapshot of the localization of biologics within the endocytic pathway in a single

experiment and enables the systematic evaluation of the relationship between pH and biomolecule delivery.

Finally, in **Chapter Four**, we quantified the nuclear delivery of the Cas9 ribonucleoprotein complex (RNP) to determine how many molecules of Cas9 are required in the nucleus for efficient genome editing. Using FCS to establish nuclear concentrations of Cas9 RNP across a broad range of electroporation dosages, we discovered that only ~1700 molecules were required in the HeLa nucleus to observe 90% gene knockdown. We applied a two-component diffusion analysis of nuclear Cas9 to track the fraction of DNA-bound protein across dosages and find that the concentration of bound Cas9 in the nucleus decreased with time and correlated linearly with dosage. To our knowledge, these findings represent the first report of the number of Cas9 RNP molecules present in the nucleus of mammalian cells. These results will clarify whether discrepancies in potency with different delivery strategies arise due to differences in nuclear concentration or activity of the delivered material. We envision these data will enrich analyses of temporal regulation of RNP editing, provide a framework to deconvolute nuclear delivery from editing activity, and guide the development of novel delivery modalities.

These projects discovered design rules to expand the therapeutic scope of ZF5.3 as a delivery modality, developed novel tools to track endocytic trafficking of exogenously supplied macromolecules, and established quantitative metrics for successful delivery of the Cas9 RNP. In the future, there is much to be discovered regarding both ZF5.3 and the trafficking of protein therapeutics as a whole. The mechanism by which ZF5.3 escapes the endosome remains under active investigation, but it is clear that physiological unfolding is critical.[4,8] It will be notable to assess whether ZF5.3 can be re-engineered for new applications, such as binding novel targets on its own. It should also be explored whether thermostable cargos can be modified to unfold by pH and thus improve their delivery by ZF5.3. Mechanistically, the increasing resolution afforded by advanced microscopy techniques will enable a detailed study of ZF5.3's interactions with endosomal membranes and how this relates to endosomal fusion processes. Fluorescence lifetime measurements in particular can both provide information on endosome localization and refine the data quality collected during FCS measurements.

There are significant challenges ahead for the field of macromolecular delivery to substantially progress. Notably, a commitment to rigorously evaluating absolute concentrations of delivered material is critical for standardizing and evaluating the efficiency of delivery strategies in development. Additionally, identifying the appropriate delivery modality for a given therapeutic requires a deep understanding of cellular trafficking mechanisms. Together, the results presented in this dissertation demonstrate the value of highly quantitative techniques to study the mechanisms and efficacy of biological delivery, paving the way for the development of highly efficient and impactful next-generation protein and RNA therapeutics.

References

(1) LaRochelle, J. R.; Cobb, G. B.; Steinauer, A.; Rhoades, E.; Schepartz, A. Fluorescence Correlation Spectroscopy Reveals Highly Efficient Cytosolic Delivery of Certain Penta-Arg Proteins and Stapled Peptides. *J. Am. Chem. Soc.* **2015**, *137* (7), 2536–2541. https://doi.org/10.1021/ja510391n.

(2) Knox, S. L.; Wissner, R.; Piszkiewicz, S.; Schepartz, A. Cytosolic Delivery of Argininosuccinate Synthetase Using a Cell-Permeant Miniature Protein. *ACS Cent. Sci.* **2021**, *7* (4), 641–649. https://doi.org/10.1021/acscentsci.0c01603.

(3) Zhang, X.; Cattoglio, C.; Zoltek, M.; Vetralla, C.; Mozumdar, D.; Schepartz, A. Dose-Dependent Nuclear Delivery and Transcriptional Repression with a Cell-Penetrant MeCP2. *ACS Cent. Sci.* **2023**, *9* (2), 277–288. https://doi.org/10.1021/acscentsci.2c01226.

(4) Zoltek, M.; Vázquez Maldonado, A. L.; Zhang, X.; Dadina, N.; Lesiak, L.; Schepartz, A. HOPS-Dependent Endosomal Escape Demands Protein Unfolding. *ACS Cent. Sci.* **2024**, *10* (4), 860–870. https://doi.org/10.1021/acscentsci.4c00016.

(5) Knox, S. L.; Steinauer, A.; Alpha-Cobb, G.; Trexler, A.; Rhoades, E.; Schepartz, A. Chapter Twenty-One - Quantification of Protein Delivery in Live Cells Using Fluorescence Correlation Spectroscopy. In *Methods in Enzymology*; Chenoweth, D. M., Ed.; Chemical Tools for Imaging, Manipulating, and Tracking Biological Systems: Diverse Chemical, Optical and Bioorthogonal Methods; Academic Press, 2020; Vol. 641, pp 477–505. https://doi.org/10.1016/bs.mie.2020.05.007.

(6) Becker, L.; Singh Badwal, J.; Brandl, F.; Verdurmen, W. P. R.; Plückthun, A. Thermodynamic Stability Is a Strong Predictor for the Delivery of DARPins to the Cytosol via Anthrax Toxin. *Pharmaceutics* **2021**, *13* (8), 1285. https://doi.org/10.3390/pharmaceutics13081285.

(7) Batistatou, N.; Kritzer, J. A. Investigation of Sequence-Penetration Relationships of Antisense Oligonucleotides. *ChemBioChem* **2023**, *24* (9), e202300009. https://doi.org/10.1002/cbic.202300009.

(8) Giudice, J.; Brauer, D. D.; Zoltek, M.; Maldonado, A. L. V.; Kelly, M.; Schepartz, A. Requirements for Efficient Endosomal Escape by Designed Mini-Proteins. bioRxiv April 6, 2024, p 2024.04.05.588336. https://doi.org/10.1101/2024.04.05.588336.